DOT/FAA/AR-xx/xx

Office of Aviation Research
and Development
Washington, DC 20591

# Research for the Electrical Wiring Interconnection System Program

October 2007

Final Report

This document is available to the public through the National Technical Information Service (NTIS), Springfield, Virginia 22161.

U.S. Department of Transportation
**Federal Aviation Administration**

## NOTICE

Technical Report Documentation Page

| | | | |
|---|---|---|---|
| 1. Report No.<br>DOT/FAA/(AR)-xx/xx | 2. Government Accession No. | 3. Recipient's Catalog No. | |
| 4. Title and Subtitle | | 5. Report Date<br>October 2007 | |
| | | 6. Performing Organization Code | |
| 7. Author(s)<br>Robert Kauffman, Rajendra Makote, Patricia Youngerman, Shamachary Sathish | | 8. Performing Organization Report No. | |
| 9. Performing Organization Name and Address<br>University of Dayton Research Institute<br>300 College Park<br>Dayton OH 45469-0161 | | 10. Work Unit No. (TRAIS) | |
| | | 11. Contract or Grant No.<br>DTFACT-040C-00019 | |
| 12. Sponsoring Agency Name and Address<br>U.S. Department of Transportation<br>Federal Aviation Administration<br>Office of Aviation Research and Development<br>Washington, DC 20591 | | 13. Type of Report and Period Covered<br>Final Report, Draft<br>August 2004 – October 2006 | |
| | | 14. Sponsoring Agency Code | |
| 15. Supplementary Notes<br>. | | | |

16. Abstract

This report details the results of a 15-month research program performed by the University of Dayton Research Institute to improve the reliability of aircraft electrical wiring interconnect systems through improved malfunction detection and repair procedures and through improved wiring and support designs. The research was performed in eight separate projects focusing on three main research areas: development of composite polymer wires utilizing adherent metallic films containing carbon nanofibers and analysis of copper cladded aluminum wiring and associated connectors; development of manual and automatic repair techniques for electrical wiring with damaged insulation covered with fibrous material; development of sensing systems for monitoring harness vibration, degradation of electrical connectors and clamp function during installation and breakage.

| | | | |
|---|---|---|---|
| 17. Key Words<br>EWIS, insulation repair, excessive vibration, insulation damage and degraded connector detection | | 18. Distribution Statement | |
| 19. Security Classif. (of this report)<br>Unclassified | 20. Security Classif. (of this page)<br>Unclassified | 21. No. of Pages | 22. Price |

**Form DOT F 1700.7** (8-72) Reproduction of completed page authorized

TABLE OF CONTENTS

LIST OF FIGURES

LIST OF TABLES

LIST OF ACRONYMS

| | |
|---|---|
| A | Amperes |
| AC | Alternating Current |
| AFRL | Air Force Research Laboratory |
| Ag | Silver |
| Al | Aluminum |
| AM | Amplitude modulation |
| Au | Gold |
| AWG | American wire gauge |
| BNC | Bayonet Neill Concelman connector |
| C | Carbon |
| Ca | Calcium |
| °C | Degrees Celsius |
| CCAL | Copper cladded aluminum |
| $cm^{-1}$ | Inverted centimeter |
| CNF | Carbon Nanofibers |
| Cl | Chlorine |
| Cu | Copper |
| dB | Decibels |
| DC | Direct Current |
| º | Degree |
| DFT | Discrete Fourier Transform |
| DPS | Diphenyl silane |
| EDS | Energy dispersive spectrometry |
| EIM | Electromagnetic induction method |
| EIS | Electrochemical impedance spectroscopy |
| EWIS | Electrical wiring interconnection system |
| °F | Degrees Fahrenheit |
| FAA | Federal Aviation Administration |
| Fe | Iron |
| FET | Field effect transistor |
| FFT | Fast Fourier Transform |
| FTIR | Fourier Transform Infrared |
| Gpa | Gigapascal |
| H | Hydrogen |
| Hz | Hertz |
| ” | Inches |
| IBTS | Isobutyltrimethoxy silane |
| ºK | Degrees Kelvin |
| kg | Kilogram |
| km | Kilometer |
| KHz | Kilohertz |
| KΩ | Kiloohms |
| KOH | Potassium Hydroxide |
| Ksi | 1,000 (Kilo) Pounds per square inch |
| lbf | Pound Force |

| | |
|---|---|
| LED | Light Emitting Diode |
| M | Molar |
| MHz | Megahertz |
| MΩ | Megaohms |
| µm | Micrometers/Microns |
| mA | Milliamperes |
| mm | Millimeter |
| mV | Millivolt |
| NaCl | Sodium Chloride |
| NaOH | Sodium Hydroxide |
| ns | Nanoseconds |
| Ni | Nickel |
| nm | Nanometers |
| Ω | Ohms (unit of electrical resistance) |
| O | Oxygen |
| O.D. | Outside Diameter |
| Pa | Pascal |
| PBO | Poly(*p*-phenylene benzobisoxazole) |
| pC | Picocoulombs ($10^{-12}$ coulombs) |
| PEG | Polyethylene glycol |
| PDMS | Polydimethyl siloxanes of variable molecular weight |
| pF | Picofarad ($10^{-12}$ Farads) |
| ppm | Parts per million |
| Φ | Phase in radians |
| psi | Pounds per square inch |
| PTFE | Polytetrafluoroethylene |
| PVAL | Polyvinyl alcohol |
| QTC | Quantum tunneling composite |
| R | Electrical Resistance |
| RMS | Root Mean Square |
| RF | Radio frequency |
| SDTA | Simultaneous Differential Thermal Analysis |
| SEM | Scanning electron microscope |
| Si | Silicon |
| t | Time |
| TBR | Tone Burst Reflectometry |
| TCS | Trichlorosilane |
| TDR | Time Domain Reflectometry |
| TGA | Thermogravimetric analyzer |
| Ti | Titanium |
| TKT | Teflon® Kapton® Teflon® |
| UDRI | University of Dayton Research Institute |
| V | Electrical Voltage |
| Wt. | Weight |
| Zmod | AC impedance |
| Zn | Zinc |

# EXECUTIVE SUMMARY

During the lifetime of an aircraft, the different components of the electrical wiring interconnection system (EWIS) experience a wide range of physical and chemical stresses. Vibration, abrasion, hydrolysis, fatigue, thermal decomposition, and chemical reactions combine to degrade the insulation of wiring and the performance of connectors. Polyimide-type wiring insulation, present in many older aircraft EWIS, are especially susceptible to hydrolytic and chemical degradation reactions. Once degradation of the wiring insulation allows the ingression of moisture, chemicals, and gaseous pollutants, the resulting corrosion of the metallic conductors and connectors increases the potential for control malfunctions, dry and wet arcing, conduit burn-through, and damage to control cables and linkages. The increase in connector resistance due to corrosion and metal surface separation further reduces the signal-to-noise ratios in low-power avionics and increases the risk of local heating and fire hazards in high-power circuits.

This report details the results of a 15-month research program performed to improve the reliability of aircraft electrical wiring interconnect systems through improved malfunction detection and repair procedures and through improved wiring and support designs. The research was performed in eight separate projects focusing on three main areas of research: development of composite polymer wires utilizing adherent metallic films containing carbon nanofibers and analysis of bimetallic (copper cladded aluminum) wiring and associated connectors; development of manual and automatic repair techniques for electrical wiring with damaged insulation covered with fibrous material; development of sensing systems for monitoring harness vibration, degradation of electrical connectors and clamp function during installation and breakage.

The research demonstrated that the composite and bimetallic conductors have both strengths (weight) and weaknesses (maintenance issues) compared to the copper conductors used in aircraft EWIS. Although the metallized polymer wires have the additional advantages of improved strength and fatigue resistance, research to date indicates significant improvements in electrical conductivity and long-term metal film adherence studies are still required prior to consideration for future aircraft designs. The copper cladded aluminum wires are already in use and their performance issues (galvanic corrosion, intermetallics) appear resolved by the design of the associated connectors.

The manual repair technique was based on easy to apply solutions containing volatile solvents that produced a hydrophobic, modified polyimide film capable of filling microcracks/gouges as well as reconditioning degraded Kapton® surfaces. The viscosity of the repair solution and curing temperatures were modified for coating wires to develop a methodology better-suited for maintenance actions. Longer term heating studies were also performed to evaluate the effects of temperature on the stability of the repair films. The research again showed that electrochemical impedance spectroscopy was the most effective analysis tool for evaluating the hydrolysis resistance of the different modified polyimide surfaces.

As opposed to the solvent based manual repair techniques, the self-repairing solutions are water based with low toxicity. Water sprays or condensed water allow detection of remote wire bundles with damaged insulation through detection of the generated radio frequencies by hand-held, directional devices inside the compartment or by non-directional, portable antennas from

outside the aircraft. Low concentrations of salts or stable emulsions must be added to the self-repairing solutions prepared with distilled water solutions to produce water insoluble films on the exposed, powered conductor. In addition to water based coating methods, electrical wiring with the capability to perform self-repair of damaged insulation was developed using water-insoluble, organic films containing low concentrations of suspended particles. Based on the success of the research a patent was filed on the self-repairing wire concept.

The analyses of the submitted wire dirt samples indicated that they were basically organic fibers with a small amount of inorganics present and so would not require special/chemical cleaning methods for removal prior to applying the repairing solutions. In fact, the wire "dirt" layer may act as a water/solution reservoir for the aqueous self-repairing solutions. The different samples were primarily cellulose in composition and appeared to have a common source regardless of aircraft or location. The cellulose (wool and nylon also present) would support combustion directly (fuel) and indirectly (decomposition products are combustible gases and carbon-like residues).

During this study, the piezo cable was combined with a stand-alone signal conditioning board capable of determining clamp failure by monitoring the "normal" vibration levels of the wiring system during flight. The effects of position and geometry on the piezo cable signal with respect to input acceleration and cable length were studied on a shaker table using a variety of random and sine wave vibrational profiles. It was determined that the calculated ratio (baseline acceleration value / acceleration value after simulated clamp failure) provided the signal conditioning board the capability to detect clamp failure when the inputted values were obtained at the frequency of the maximum acceleration value recorded after clamp failure.. The method is relatively inexpensive, has low to moderate weight penalty, and a low volume penalty making the piezo cable potentially suitable for aircraft use.

Although not as fully developed as the vibration technique using piezoelectric cables, a promising technique based on an electromagnetic induction method to monitor the degradation of unopened connectors was identified. The technique wraps loose wires with stripped ends tightly around the EWIS wires to form coils on both sides of the connector of interest. When a continuous electromagnetic signal passes through the connector, the phase difference between the voltages detected by the hand wound coils can be measured using a lock in amplifier to detect connector degradation (abrasion, chemical and vibration). The entire methodology is quite simple and could be implemented at the maintenance facility level.

Although preliminary, the initial results produced for smart clamp and rattle demonstration devices indicated that the simple designs have potential for development into sensors for detecting wire harnesses with loose/broken clamps prior to insulation damage. The smart clamps also have potential for ensuring proper clamp installation. Other than miniaturization, future efforts would focus on the techniques used to power and process the data outputs of the smart sensors.

# 1. LIGHTER-WEIGHT, HIGHER-STRENGTH CONDUCTORS.

Due to the miles of wiring used by aircraft EWIS, composite or bimetallic conductors with weight/strength advantages compared to copper conductors would provide weight/space savings for current and future aircraft designs. In addition to overall weight savings, the lighter-weight conductors would improve EWIS reliability by reducing the fatigue of clamps and connections. Two different types of lighter-weight, higher-strength conductors were studied during this project for use in the EWIS of current and future aircraft: copper cladded aluminum and metallized polymer.

The main focus of the copper cladded aluminum (CCAL) wire testing was on the occurrences of galvanic corrosion and intermetallics layer formation at the aluminum:copper interface. While the intermetallics formation required elevated temperatures, the galvanic corrosion was studied at room temperature in the presence of moisture, especially salt or basic water. A connector specifically designed for CCAL wiring was also characterized to study the connector's mechanical features designed to inhibit galvanic corrosion of CCAL wiring by protecting any exposed aluminum:copper interfaces from the corrosive aircraft environment.

The metallized polymer wires being evaluated during this research were poly(p-phenylene benzobisoxazole) (PBO) polymer fibers covered with a strongly adherent silver film. The research focused on the effects of the silver metallization process and film composition on the adherence of the silver film to the PBO polymer during fatigue and tensile strength tests. Copper wires of similar diameter were also fatigue tested for comparison with the silver coated PBO wires.

## 1.1 CHARACTERIZATION OF COPPER CLADDED ALUMINUM WIRING.

Although CCAL wires have the electrical properties required for use on aircraft, the concerns with CCAL wires are galvanic corrosion and the formation of a brittle intermetallics layer at the copper (Cu):aluminum (Al) interface. Two types of CCAL wiring (insulated, aircraft wiring and non-insulated, commercial wires) as well as connectors designed specifically for use with CCAL wiring were studied during this project.

### 1.1.1 Commercial CCAL Wire.

Commercial, non-insulated CCAL (10% Cu cladding) wire was encased in epoxy and cross-sectioned to study the physical and elemental characteristics of the Cu:Al interface. The cross-sectioned surface of the 34 AWG CCAL [160 micron (μm) diameter] wire was photographed at high magnification using a scanning electron microscope (SEM). As shown in figure 1, the copper cladding of the wire was measured as a 5-6 um layer of Cu (supplier specifications: 4 μm cladding).

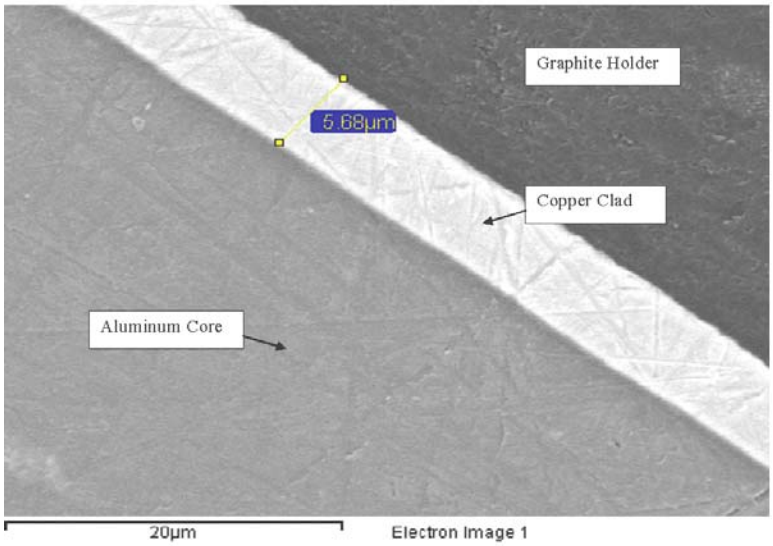


FIGURE 1. SEM PHOTOGRAPH OF CROSS-SECTIONED COMMERCIAL WIRE

To better illustrate the interface of the Cu and Al surfaces, an energy dispersive spectrometric (EDS) line scan was performed across the Cu:Al interface. As shown in figure 2, the Cu:Al interface is sharp with less than 1 µm Cu:Al overlap.

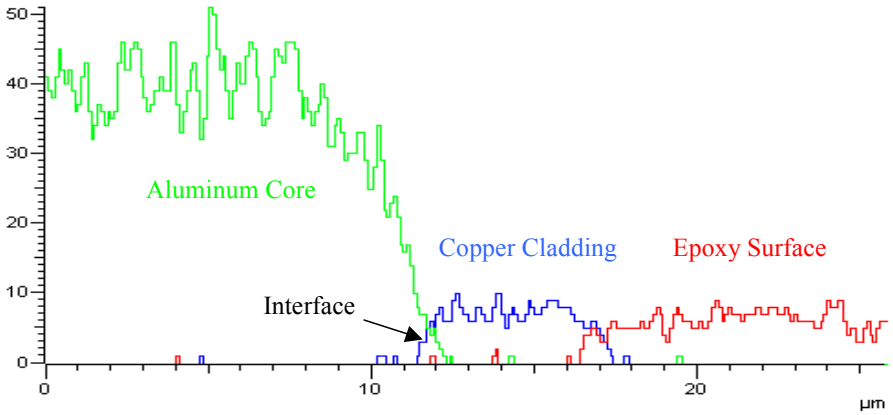


FIGURE 2. EDS LINE SCAN OF CCAL WIRE CU:AL INTERFACE

1.1.2 CCAL Aircraft Wiring.

Three different sizes of insulated CCAL aircraft wiring (20, 22 and 24 AWG) were provided by the FAA for physical/chemical characterizations. A piece of the 24 AWG aircraft wiring was cross-sectioned and photographed at low magnification using a SEM. As shown in figure 3, the insulated wiring is constructed from composite insulating

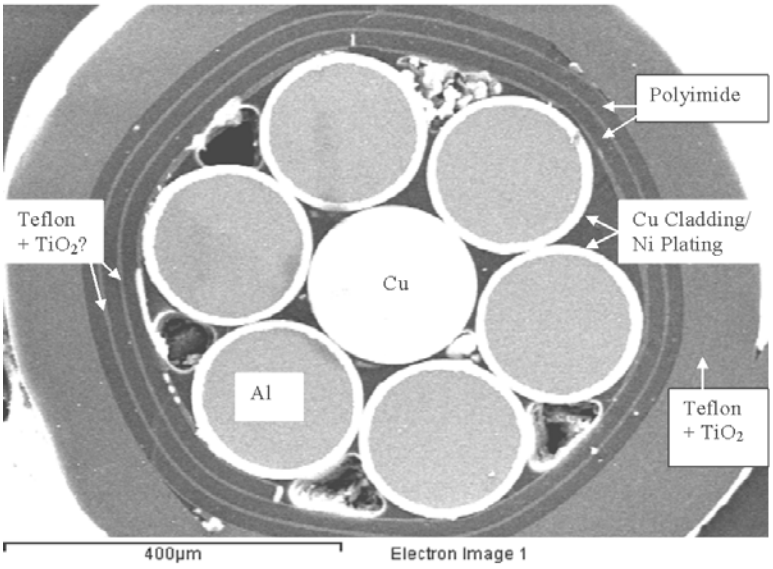


FIGURE 3. SEM PHOTOGRAPH OF CROSS-SECTIONED 24 AWG AIRCRAFT WIRING

materials and metals. The metal conductor is made of 6 nickel (Ni) plated CCAL wires and 1 centered, unplated Cu wire (wires have ~200 µm diameters). The insulation has a 90 – 130 µm outer layer of a fluorinated polymer containing titanium (Ti) (e.g., Teflon containing $TiO_2$ for markability) and two to three alternating inner layers of a non-fluorinated, oxygen containing polymer (~20 µm thickness) and fluorinated polymer (~ 4 µm thickness), e.g., polyimide and Teflon, respectively ("TKT" insulation). The inner fluorinated polymer layers may contain $TiO_2$ but detection capabilities are limited by the thinness of the polymer layers.

A piece of the 22 AWG aircraft wiring was also cross-sectioned and photographed at low magnification using a SEM. The 22 AWG wiring system is virtually identical to the 24 AWG system in Figure 3, i.e., conductor is 6 Ni plated CCAL wires and 1 centered, unplated Cu wire and the insulation has an outer layer of Teflon and $TiO_2$ and two to three alternating inner layers of a polyimide and Teflon. The main difference between the 22 and 24 AWG wiring is the diameter of the CCAL and Cu wires, approximately 200 µm in the 24 AWG wiring and 250 µm in the 22 AWG wiring.

In contrast to the 22 and 24 AWG wiring designs, the cross section of the 20 AWG aircraft wiring photographed at low magnification using a SEM determined that the wiring contains 19 CCAL wires (approximately 200 µm diameter) with no center Cu wire as shown in figure 4. The insulation of the 20 AWG wiring system appears identical to those of the 22 and 24 AWG systems in Figure 3, i.e., outer layer of Teflon and $TiO_2$ and two to three alternating inner layers of a polyimide and Teflon (TKT insulation).

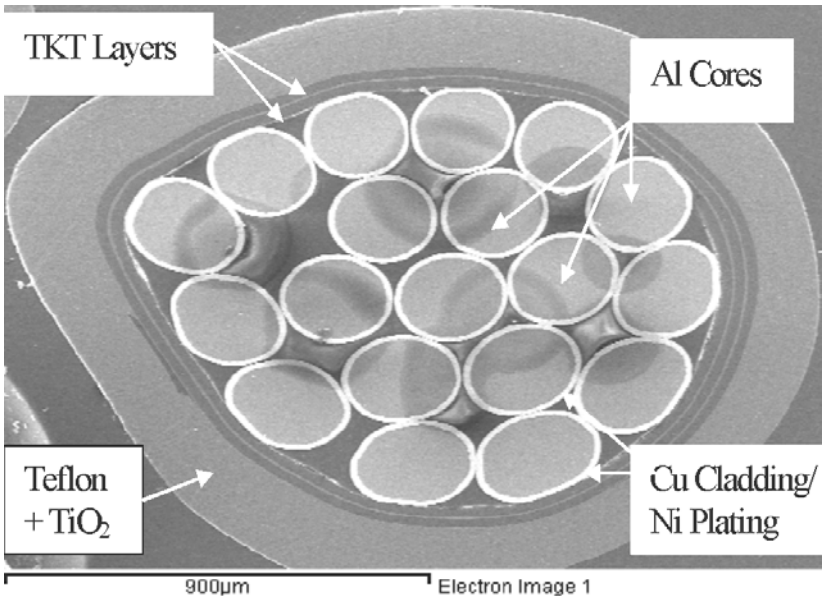


FIGURE 4. SEM PHOTOGRAPH OF CROSS-SECTIONED 20 AWG CCAL AIRCRAFT WIRING

To better illustrate the various interfaces of the insulation and metal conductors, an EDS line scan was performed across the inner insulation and one of the CCAL wires (figure 4) of the 20 AWG aircraft wiring as shown in figure 5. The EDS line scan was able to distinguish between the different polymeric layers by plotting the fluorine response from Teflon and the carbon response from the polyimide (PI in figure 5) versus analysis distance as the EDS scanned across the inner insulation layers toward the edge of the CCAL wire which is distinguished by the increase in the Ni response (Ni plating). Then the Ni, Cu and Al responses successively increase/decrease as the EDS analysis proceeds across the CCAL wire. The EDS line scans of the inner insulations/CCAL wires of the 22 and 24 AWG aircraft wiring produced EDS line scans similar to figure 5, i.e., similar insulation systems.

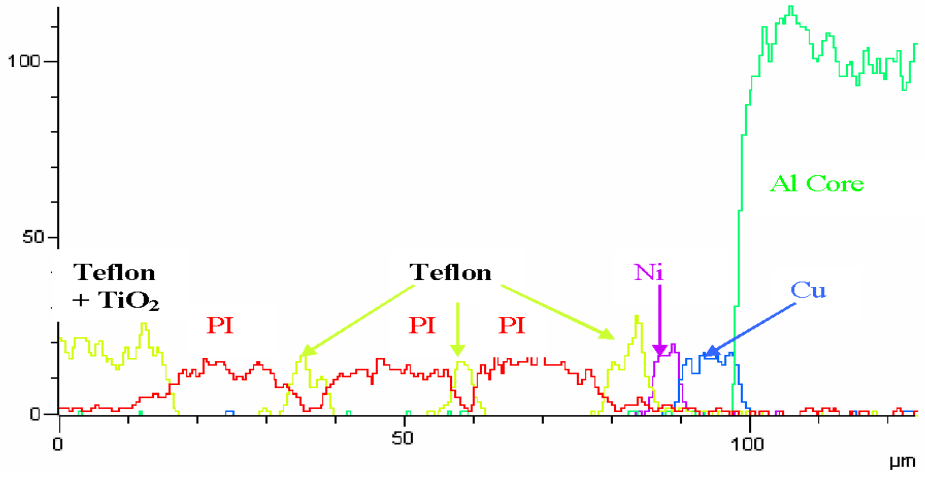


FIGURE 5. EDS LINE SCAN OF CROSS-SECTIONED INSULATION AND CCAL WIRE

For direct comparison with the commercial CCAL wire in Figures 1 and 2, a much higher magnification SEM photograph and EDS line scan were performed on a single CCAL wire from the 24 AWG insulated aircraft wiring as shown in figures 6 and 7, respectively.

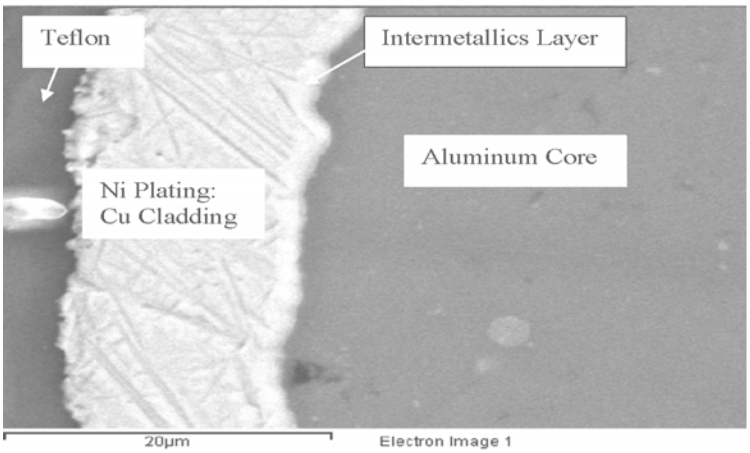


FIGURE 6. SEM PHOTOGRAPH OF CROSS-SECTIONED CCAL WIRE FROM 24 AWG AIRCRAFT WIRING

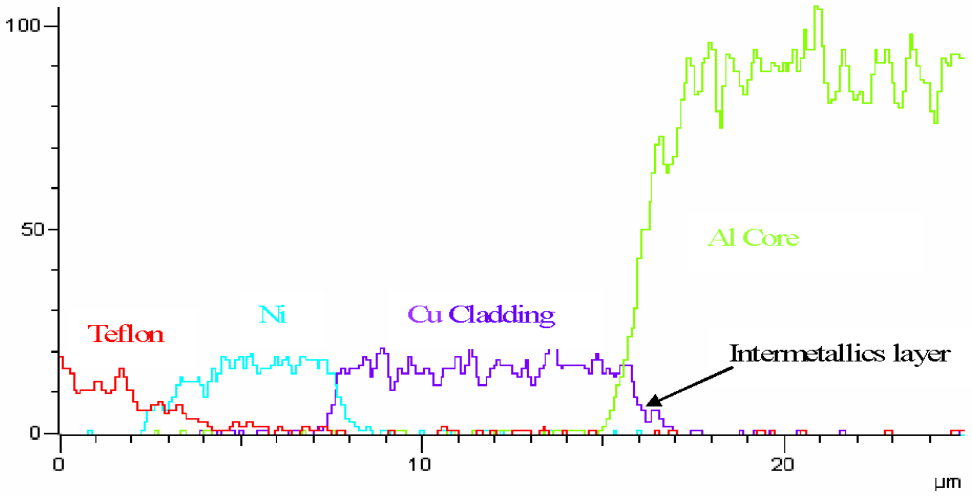


FIGURE 7. EDS LINE SCAN OF CROSS-SECTIONED CCAL WIRE FROM 24 AWG AIRCRAFT WIRING

The SEM photograph in figure 6 shows that the Cu:Al interface of the CCAL wire removed from the 24 AWG aircraft wiring is much rougher than the interface of the commercial CCAL wire in figure 1. The SEM photograph shows that the total thickness of the Ni plating/Cu cladding layer was 14 – 17 µm. The SEM photographs of the CCAL wires removed from the 20 and 22 AWG aircraft wiring were very similar to figure 6, i.e., similar total Ni plating/Cu cladding thickness and Cu:Al interface roughness.

The EDS line scan of the CCAL wire from the 24 AWG aircraft wiring in figure 7 shows that the thicknesses of the Ni plating and Cu cladding were 5 – 6 and 9 – 11 µm, respectively. The Cu cladding in figure 7 is about twice as wide as the cladding on the commercial 10% CCAL wire in

figure 1. The EDS line scans of the CCAL wires removed from the 20 and 22 AWG aircraft wiring were very similar to figure 7, i.e., similar individual Ni plating and Cu cladding thicknesses.

In figure 6, the Cu:Al interface of the wire removed from the 24 AWG aircraft wiring is ~ 2 μm wide and lighter in color (no polishing marks) than the cladding region. The EDS line scan in figure 7 of the same region of the Cu:Al interface determined that the 2 μm wide interface consisted of intermetallics containing different ratios of Al and Cu (the roughened interface and intermetallics both indicate that the CCAL wires used in the aircraft wiring were heated/annealed during manufacture). Representative EDS analyses of different regions of the intermetallics layer are shown in figure 8. The EDS analyses of the CCAL wires removed from the 20 and 22 AWG aircraft wiring determined that intermetallics were also present at their Cu:Al interfaces in a thickness similar to figure 7 and with Al:Cu ratios bounded by those shown in figure 8.

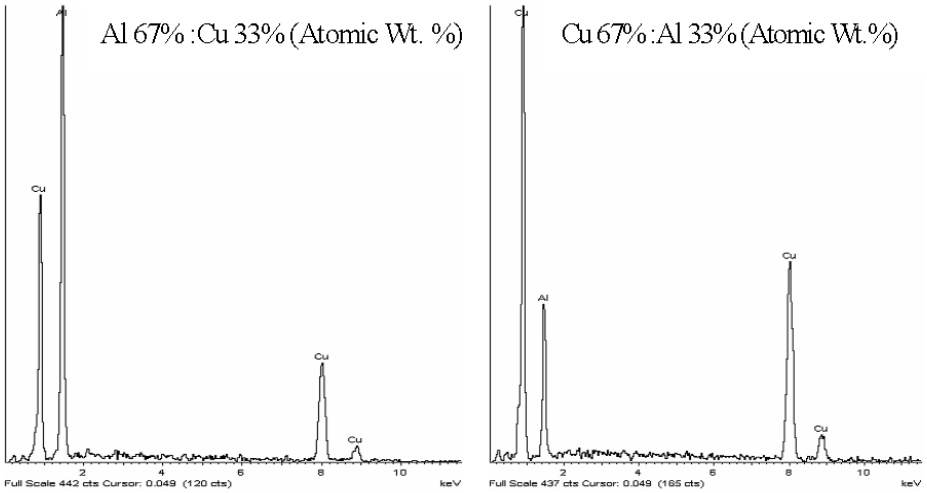


FIGURE 8. EDS SPECTRA OF INTERMETALLICS AT CU:AL INTERFACE OF CCAL WIRE FROM 24 AWG AIRCRAFT WIRING

The intermetallics layer was not seen in figure 1 (no light layer at Cu:Al interface) or detected by the EDS line scan in figure 2 (interface below 1 μm in width) indicating the commercial CCAL wire was not heated to the same degree as those in the aircraft wiring.

## 1.2 CHARACTERIZATION OF CCAL AIRCRAFT WIRING CONNECTORS.

In addition to the different sizes of insulated CCAL aircraft wiring, wires with crimped connectors were also provided by the FAA for physical/chemical characterizations. The connectors were crimped by the FAA using specially designed tools. The connectors were specially designed to have multiple mechanical and electrical contacts as well as a sealing barrier to negate the potential problems associated with long-term use of CCAL wiring. Several of the crimped connectors were length-sectioned and photographed at low magnification using a SEM. The representative SEM photographs of the connector sections securing the stripped wire ends in figure 9 show that the connectors each contain a silver (Ag) cup. The Ag cup is crimped onto the

stripped wire surfaces to provide multiple Ag/Cu electrical contacts and a nearly continuous mechanical seal to protect the cut wire ends from contaminants that could enter the connector through the hole designed to allow air to escape during the crimping process. The excess Ag apparent in the upper connector in Figure 9 caused the Cu cladding to fail producing a direct electrical contact between the Ag surface of the connector and Al core of the CCAL wire as shown in figure 10.

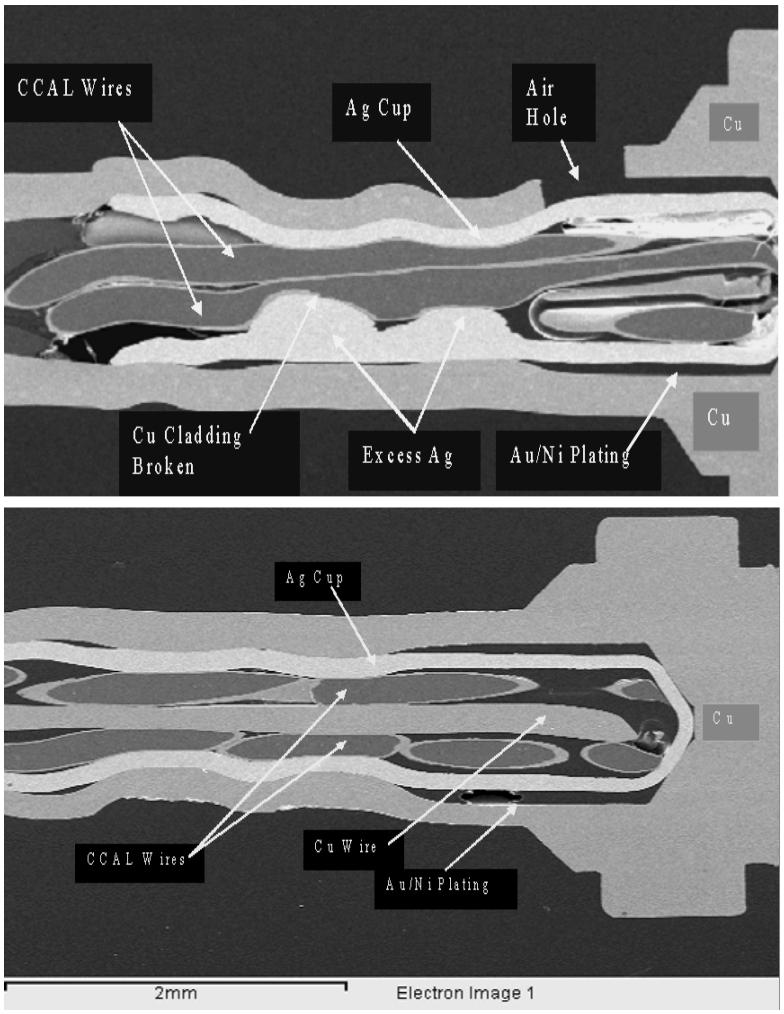


FIGURE 9. SEM PHOTOGRAPHS OF STRIPPED CCAL AIRCRAFT WIRING IN LENGTH-SECTIONED, CRIMPED CONNECTORS

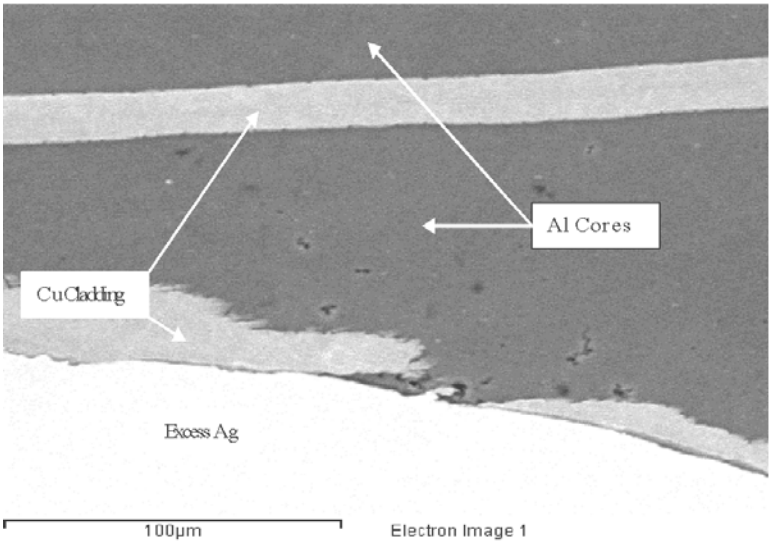


FIGURE 10. SEM PHOTOGRAPH OF SILVER LAYER OF THE CONNECTOR AND AL CORE OF THE CCAL WIRE

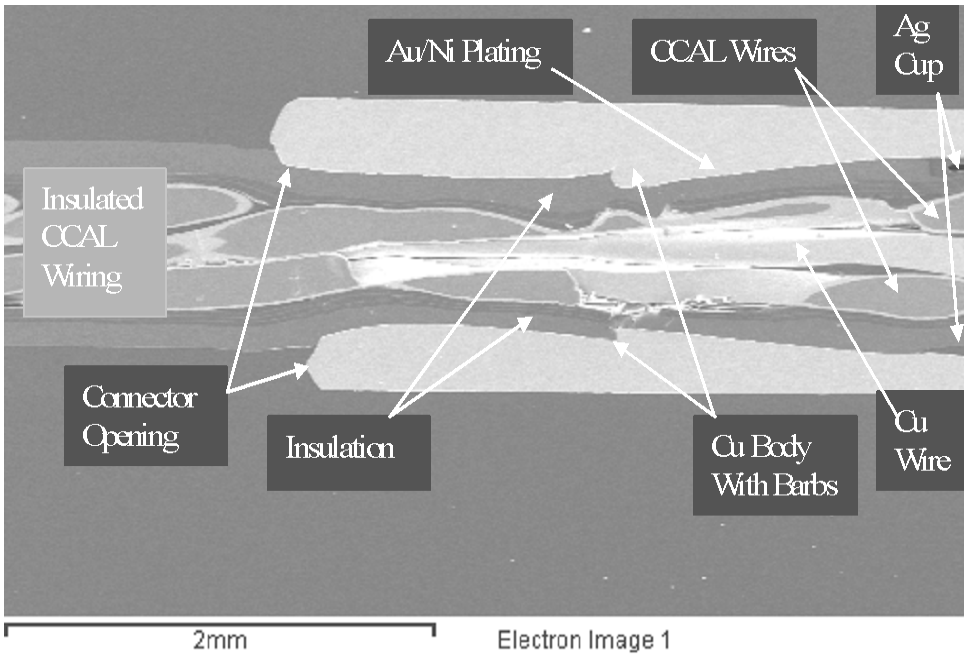


FIGURE 11. SEM PHOTOGRAPH OF INSULATED PORTION OF CCAL AIRCRAFT WIRING IN LENGTH-SECTIONED, CRIMPED CONNECTOR

In contrast to the connector sections securing the stripped wire ends, the representative SEM photograph in figure 11 shows that the surface of the connector section securing the insulated CCAL wiring contains a reversed barb. The barb is forced into the insulation during the crimping process to form a mechanical seal that protects the stripped wire surfaces in the silver cup (figure 9) from the contaminants that would enter through the connector opening. To prevent internal corrosion of the connector, the entire internal surface of the connector is gold

(Au)/Ni plated as indicated in figures 9 and 11 and as determined by the representative EDS line scan across a CCAL wire in contact with the interior wall of a length-sectioned connector as shown in figure 12.

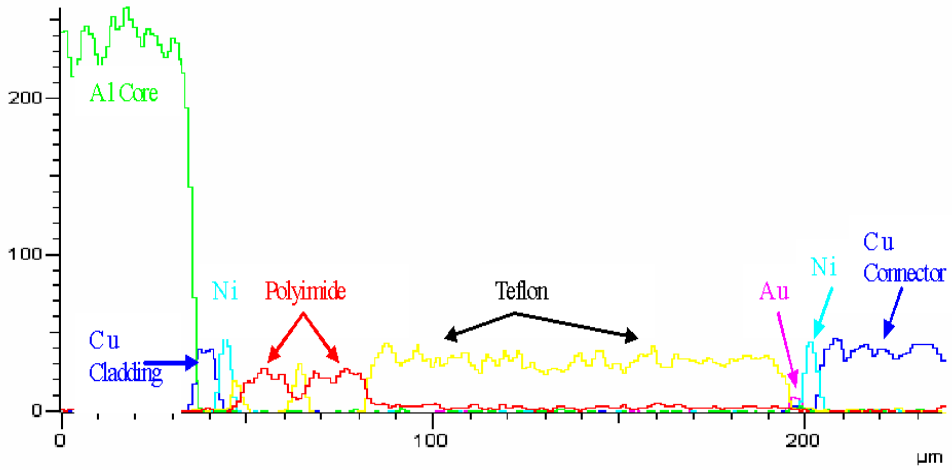


FIGURE 12. EDS LINE SCAN ACROSS CCAL WIRE, INSULATION AND INTERNAL SURFACE OF CRIMPED CONNECTOR

To view the shape of the crimped CCAL wires, the connector was cross-sectioned and photographed with a microscope as shown in figure 13. The photograph was taken with side lighting to highlight any gaps between the CCAL wiring and Ag cup and between the Ag cup and the exterior body of the connector. The photograph shows that the 7 CCAL wires are no longer circular conforming to the crimped shape of the connector. In contrast to the CCAL wires, the centered Cu wire retains its circular shape during the crimping process. Except for a small gap in one corner in figure 13, there is continuous contact between the CCAL wiring and Ag surface for the entire circumference of the crimped cup. There is also continuous contact between the Ag cup and exterior body of the crimped connector except for one, possibly two, gaps in the crimped corners.

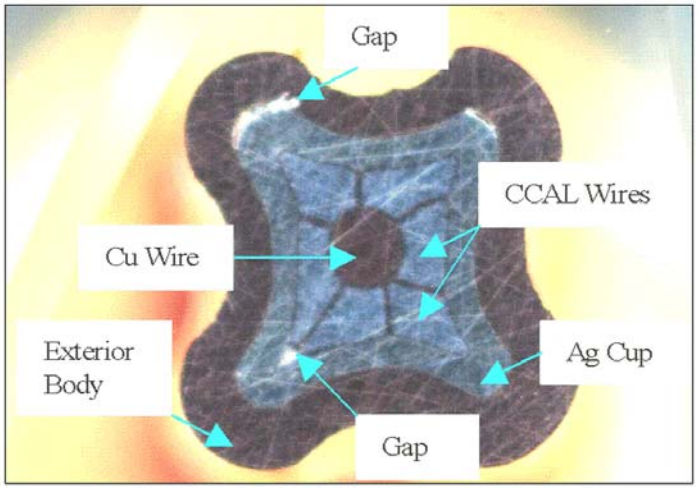


FIGURE 13. MICROSCOPE PHOTOGRAPH OF THE CCAL AIRCRAFT WIRING IN CROSS-SECTIONED, CRIMPED CONNECTOR

Consequently, the analyses of the crimped connectors in figures 9 – 13 indicate that the design of the connectors includes multiple mechanical contacts/seals to prevent the corrosive contaminants present in the aircraft environment from entering a properly crimped connector to react with the cut ends of the CCAL wires. Even bare CCAL wires with Cu:Al interfaces exposed by damage during improper stripping procedures would be protected from galvanic corrosion by the crimped connector. The continuous nature of the interfaces between the CCAL wiring/Ag cup and Ag cup/connector body should ensure good electrical contact between the aircraft wiring and crimped connector.

## 1.3 NON-APPROVED STRIPPING OF CCAL AIRCRAFT WIRING .

To test the ruggedness of the CCAL aircraft wiring during non-approved stripping procedures and tight bends, the insulation was stripped from the 24 AWG aircraft wiring using common wire strippers (24 AWG gap) and the exposed CCAL wires were bent around a 1/8 inch metal rod. The sharp bending caused several breaks in the Ni plating of the bent wire. The EDS line scan performed on the damaged Ni plating was transposed on the SEM photograph in figure 14 to show Al was not detected near or in the hole.

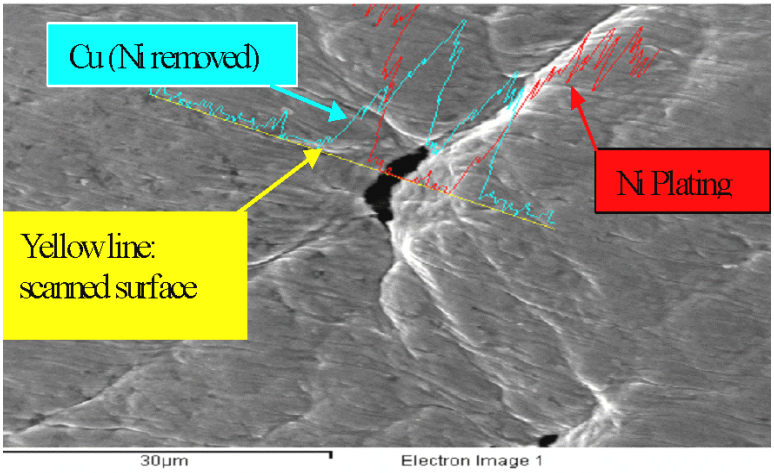


FIGURE 14. SEM PHOTOGRAPH AND EDS LINE SCAN OF HOLE IN NICKEL PLATING ON BENT CCAL WIRE

The aircraft wiring stripped of its insulation shown in figure 15 had the expected gouges in its CCAL wire surfaces that were produced when the insulation was cut/removed with a common stripping tool. EDS analyses of the gouges detected Al indicating the damage was deeper than the 17 µm total thickness of the Ni plating/Cu cladding layer.

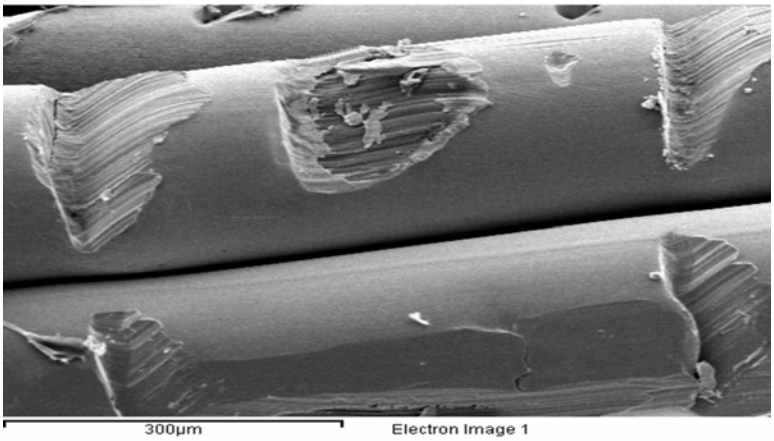


FIGURE 15. SEM PHOTOGRAPH OF STRIPPED 24 AWG AIRCRAFT WIRING

Although the gouges in figure 15 were expected, the damage to the CCAL wires caused when the stripping tool was used to pull the insulation along/off the wires was not expected. The SEM photograph in figure 16 (with transposed EDS line scan) shows two different types of damage to the CCAL wire surfaces. The first level of damage changes the physical appearance/decreases the thickness of the Ni plating (Cu detected by EDS in figure 16) as the stripping tool is pulled along the surface of the wire. The second level of damage is more severe and occurs when Cu cladding is removed completely from the Al surface leaving behind large holes in the Cu cladding (Al detected by EDS and drawing marks on Al surface are visible in figure 16).

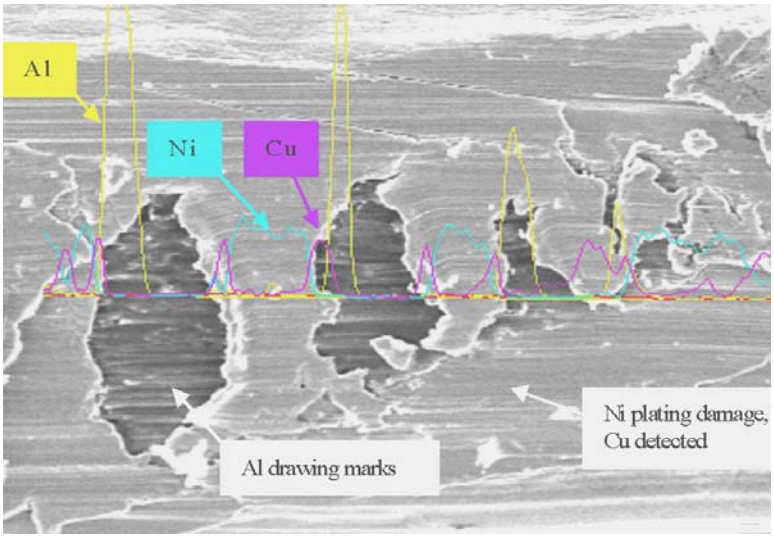


FIGURE 16. SEM PHOTOGRAPH OF NI PLATING DAMAGED BY STRIPPING

## 1.4 FATIGUE TESTING OF COMMERCIAL CCAL WIRE.

To study the fatigue resistance of the CCAL wire, the fatigue tester described in Appendix A was used to bend the weighted wire 90º in two directions supporting a 0.5 pound weight. Bending the wire clockwise then counterclockwise to the beginning position constituted one cycle. Using the described fatigue tester, the commercial 34 AWG CCAL wire physically broke after 4 cycles. For a general point of reference, a 36 AWG copper wire (0.125mmdiameter, annealed, 99.9% purity purchased from Goodfellow Corp.) broke after 10 cycles.

Although the SEM photograph of the bent CCAL wire in figure 17 appears to have broken into layers, the EDS analysis only detected Cu in the cracks indicating the broken Cu layer did not separate enough to allow EDS detection of the Al core of the wire.

Since the CCAL wires in the aircraft wire contained intermetallics layers (figures 6-8), which are known to be brittle (2), the commercial CCAL wires were heated at 350ºC for 4 hours and 250ºC for 1 week to produce layers of intermetallics for fatigue testing. The heated CCAL wires were cross-sectioned and SEM/EDS analyses were performed to characterize the Cu:Al interfaces.

As opposed to the smooth Cu:Al interface of the unheated, commercial CCAL wire in figure 1, the interfaces of the 250 and 350ºC heated wires were roughened similar to those of the CCAL wires in the aircraft wiring (figure 6). A SEM photograph of the Cu:Al interface (intermetallics layer darker than Cu cladding) for the 250ºC heated CCAL wire is shown in figure 18

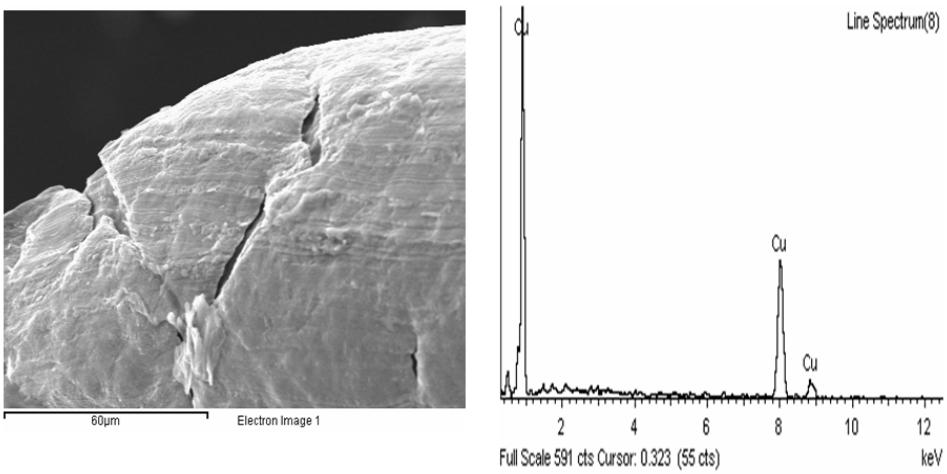


FIGURE 17. SEM PHOTOGRAPH AND EDS SPECTRUM OF BENT CCAL WIRE

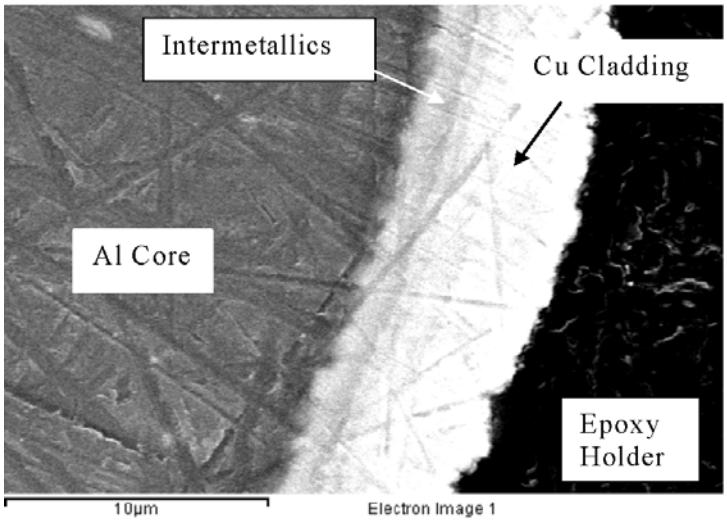


FIGURE 18. SEM PHOTOGRAPH OF CROSS-SECTIONED COMMERCIAL CCAL WIRE HEATED 250°C FOR 1 WEEK

To quantitate the intermetallics layers, EDS line scans of the CCAL wires heated at 250 and 350ºC were performed as shown in figures 19 and 20, respectively.

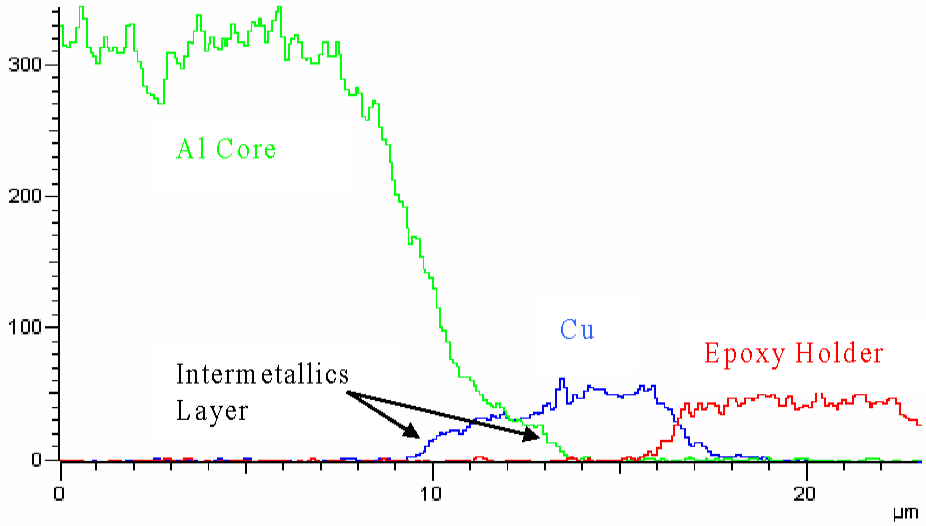


FIGURE 19. EDS LINE SCAN OF CROSS-SECTIONED COMMERCIAL CCAL WIRE HEATED AT 250°C FOR 1 WEEK

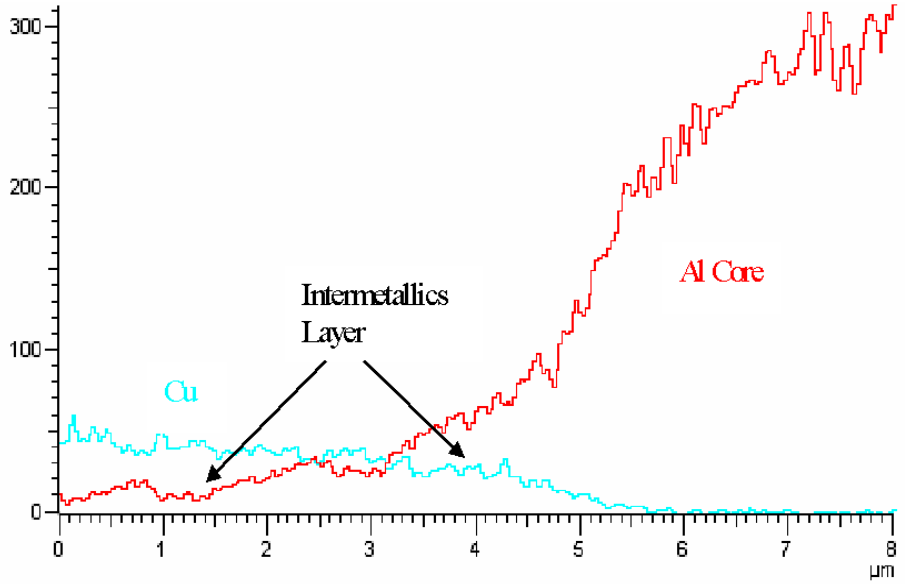


FIGURE 20. EDS LINE SCAN OF CROSS-SECTIONED COMMERCIAL CCAL WIRE HEATED AT 350°C FOR 4 HOURS

The data in figures 19 and 20 show that the heated CCAL wires contain intermetallics layers that are approximately 4 and 6 microns wide, respectively. In fact, at 350ºC the intermetallics layer consumed the entire Cu cladding of the CCAL wire, i.e., Al detected on wire surface (figure 20).

To determine the effects of the intermetallics formation on the fatigue resistance of the CCAL wire, the wire heated 350ºC for 4 hours was placed on the fatigue tester (Appendix A). However, the initial 90º bending of the heated CCAL wire caused the wire to break. The SEM photograph of the broken wire in figure 21 shows that the intermetallics layer separated from the Al core greatly reducing the fatigue resistance of the heated CCAL wire. Reported research (2)

demonstrated an inversely proportional relationship between breaking load and intermetallic layer thickness.

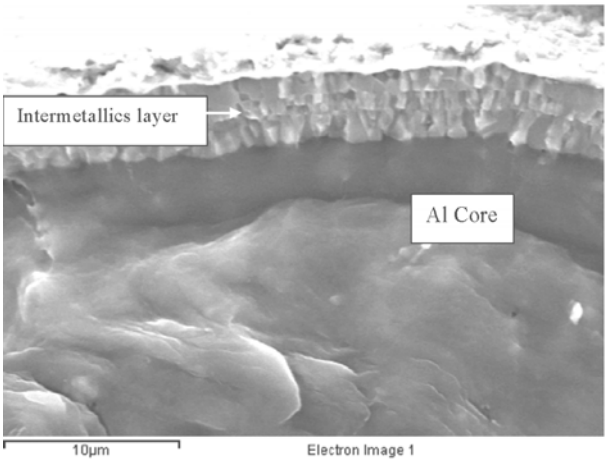


FIGURE 21. SEM PHOTOGRAPH OF 350°C HEATED/BROKEN CCAL WIRE

Based on these preliminary tests, the formation of intermetallics layers in the commercial CCAL wires by heating (already present in CCAL aircraft wiring) will reduce the fatigue resistance/breaking load of the aircraft wiring and will eventually increase the contact resistance of the wires' surfaces, i.e., Al on wire's surface will form highly resistive Al oxides. Since research has demonstrated that intermetallics form at temperatures below 160ºC (3), research at temperatures below 150ºC is still needed to evaluate the importance of long-term intermetallic formation at the operating temperatures of aircraft wiring.

## 1.5 CORROSION TESTING OF CCAL WIRES.

Since Al and Cu form a galvanic couple, a Cu:Al interface exposed to water by improper maintenance actions (physical testing report), insulation damage or connector failure would be expected to undergo accelerated electrochemical corrosion, not experienced by either pure Al or Cu wires. To study the effects of the Cu:Al interface on the corrosion of exposed CCAL surfaces, single commercial CCAL wires and insulated aircraft wiring were suspended in an epoxy casting material and cross-sectioned. Aqueous solutions containing different concentrations of salts or alkalines were then dispensed on the exposed ends of the CCAL wires for different lengths of time. SEM/EDS analyses were then performed to quantitate the induced corrosion of the exposed wire ends.

### 1.5.1 Commercial CCAL Wires.

The first study dispensed drops of 1% sodium chloride (NaCl) in deionized water onto the exposed ends of the CCAL wires. A glass slide was placed over the salt water layer allowing the corrosion to be followed under a microscope or using video equipment. After 3 hours, the surfaces of the CCAL wires and epoxy holder were washed off with deionized water, dried and analyzed with SEM as shown in figure 22. Although the decrease in the Al surface in figure 22 indicates that corrosion did take place, the corrosion at the Al surface and Cu:Al interface (including intermetallics) are similar in extent so the galvanic differences between Al and Cu had

minimal effect on the overall corrosion rates. The effects of electrochemical corrosion on the CCAL wire ends appeared to be inhibited by the formation of a protective film on the Al surface that contained Al, O and Cl. The larger white deposits on the Al core surface in figure 22 are located where the bubbles escaped through the film.

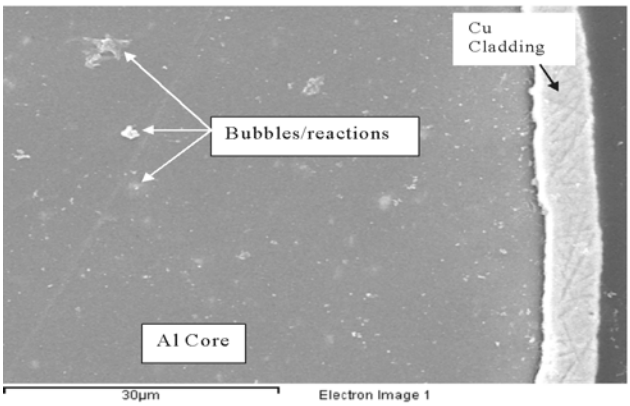


FIGURE 22. SEM PHOTOGRAPH OF CROSS – SECTIONED CCAL WIRE AFTER 3 HOUR 1% NACL SOLUTION TEST

The second study dispensed drops of 200 ppm sodium hydroxide (NaOH) in deionized water onto the exposed ends of the CCAL wires. After 3 days (ends wetted the entire exposure period), the surfaces of the CCAL wires and epoxy holder were washed off with deionized water, dried and analyzed with SEM/EDS. The SEM photographs of the different CCAL wire ends at different magnifications in figure 23 show that significant electrochemical reactions took place at the Cu:Al interface, i.e., the deep crevice produced at, and the furrows in the Al surface extending from, the Cu:Al interface occur since the rate of galvanic corrosion of the Al surface at the Cu:Al interface in figure 23 is significantly greater than the corrosion rate of the isolated Al core surface. Even away from the Cu cladding, the Cu appeared to be responsible for the electrochemical corrosion of the Al core surface, i.e., EDS detected Cu in the corrosion pits (figure 23) formed in the Al core surface.

Due to the protective coating produced by the 1% NaCl solution in figure 22 and the severe corrosion produced with the 200 ppm NaOH solution in figure 23, corrosion tests with dilute (20 ppm NaOH and NaCl) aqueous solutions were then performed with commercial CCAL wires in an attempt to better define the effects of galvanic corrosion on the overall Al corrosion processes. As described above, several CCAL wires were suspended in an epoxy casting material, cross-sectioned, exposed to a dilute aqueous solution for 3 days, rinsed off with distilled water and analyzed by SEM/EDS to quantitate the resulting corrosion.

As opposed to the 1% NaCl aqueous test in figure 22, the commercial CCAl wire ends exposed to the 20 ppm NaCl underwent severe corrosion at the Cu:Al interface as evidenced by the accumulation of Al oxide/hydroxide crystals ( no Cl detected) at the interface in figure 24. The 20 ppm NaCl solution did not form a protective layer as in figure 22 as evidenced by the removed (with respect to Cu cladding), furrowed Al core surface in figure 24. As opposed to the NaCl produced crystals present on the Cu:Al interface, the 20 ppm NaOH galvanic corrosion produced a deep crevice at, and deep furrows extending from, the Cu:Al interface in figure 24.

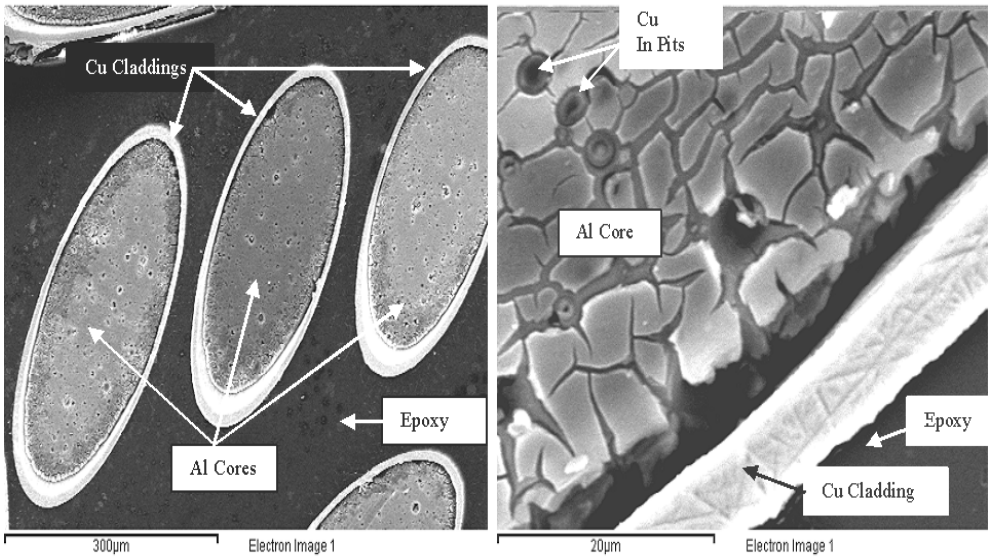


FIGURE 23. SEM PHOTOGRAPHS OF CROSS-SECTIONED COMMERCIAL CCAL WIRES AFTER 3 DAY EXPOSURE TO 200 PPM NAOH SOLUTION

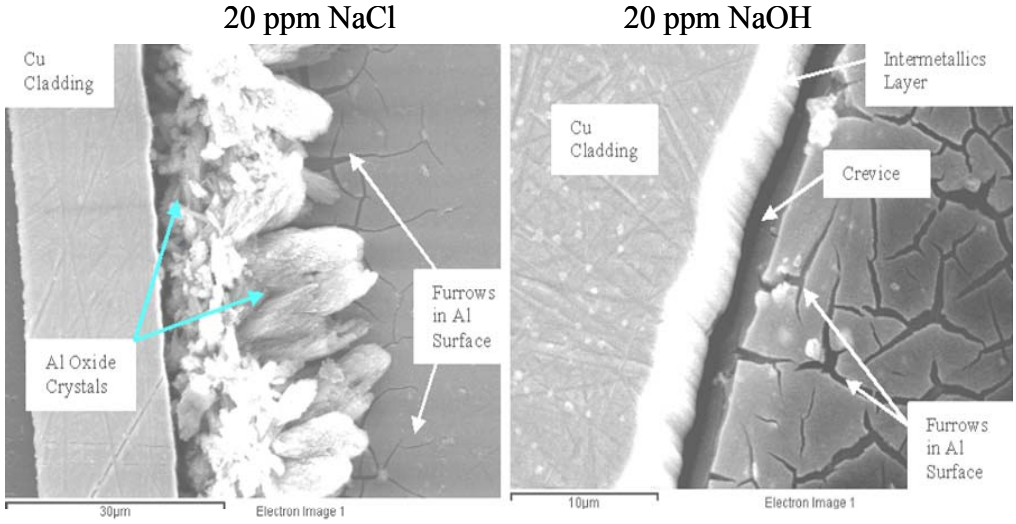


FIGURE 24. SEM PHOTOGRAPHS OF CROSS-SECTIONED CCAL WIRES AFTER 3 DAY EXPOSURES TO 20 PPM NACL AND NAOH SOLUTIONS

Consequently, the initial corrosion studies with the salt and basic water solutions indicate that dilute (20 ppm) aqueous solutions are best suited for promoting the effects of galvanic corrosion at the Cu:Al interface of commercial CCAL wires. The NaOH corrosion products were soluble regardless of solution concentration while those produced by NaCl had limited solubility, resulting the formation of deposits at the Cu:Al interface.

1.5.2 Corrosion Testing Of CCAL Aircraft Wiring.

To study the effects of Ni plating and the pure Cu wire at the center of the 24 AWG aircraft wiring (figure 4) on the electrochemical reactions of exposed Al surfaces, different pieces of CCAL aircraft wiring were suspended in an epoxy casting material, cross-sectioned and exposed to 200 ppm NaOH solution for 2 days. The corroded surfaces were then washed off with distilled water and analyzed using SEM/EDS. The inner Cu wire, Ni plating and Cu claddings of the CCAL wires did not show any signs of corrosion. However, significant amounts of the Al cores had been corroded from the interior of the CCAL wires and Al oxides were present on the lowered Al core surfaces as shown by the SEM photograph in figure 25.

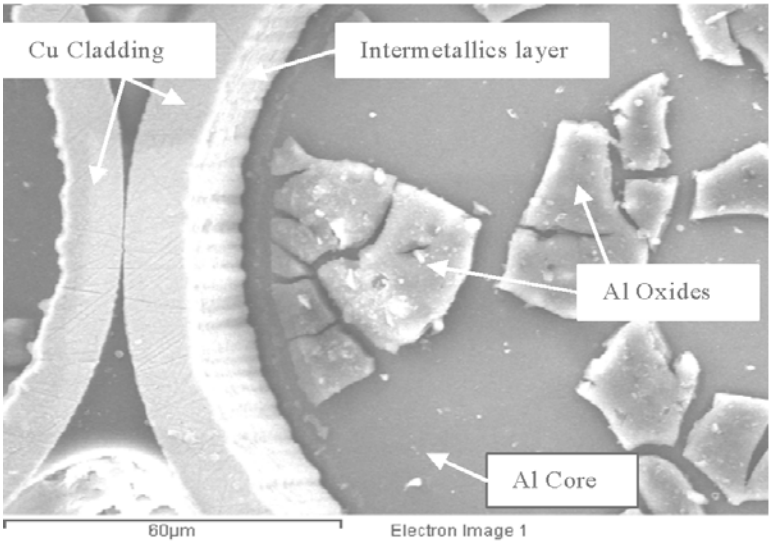


FIGURE 25. SEM PHOTOGRAPH OF CROSS-SECTIONED CCAL AIRCRAFT WIRING AFTER 2 DAY EXPOSURE TO 200 PPM NAOH SOLUTION

The intermetallics layer on the interior of the Cu cladding in figure 25 is visible due to the Al core removal indicating the Al and Cu composition of the intermetallics layer corroded at a much slower rate in the NaOH solution corrosion than the Al core.

The severity of the corrosion exhibited in figure 25 makes the contribution of the galvanic corrosion at the Al:Cu interface to the overall corrosion rates undetectable. Therefore, additional corrosion tests with 20 ppm NaOH and NaCl aqueous solutions were then performed with the 20 and 24 AWG CCAL aircraft wiring in an attempt to better define the effects of galvanic corrosion on the overall Al corrosion processes.

For the first study, pieces of the 20 and 24 AWG CCAL aircraft wiring were suspended in an epoxy casting material, cross-sectioned and exposed to 20 ppm NaOH for 6 days. The corroded surfaces were then washed off with distilled water and analyzed using SEM/EDS. The Al surfaces of the CCAL wires in the 20 AWG wiring underwent much less corrosion than those of the CCAL wires in the 24 AWG wiring (centered Cu wire) as shown in figure 26.

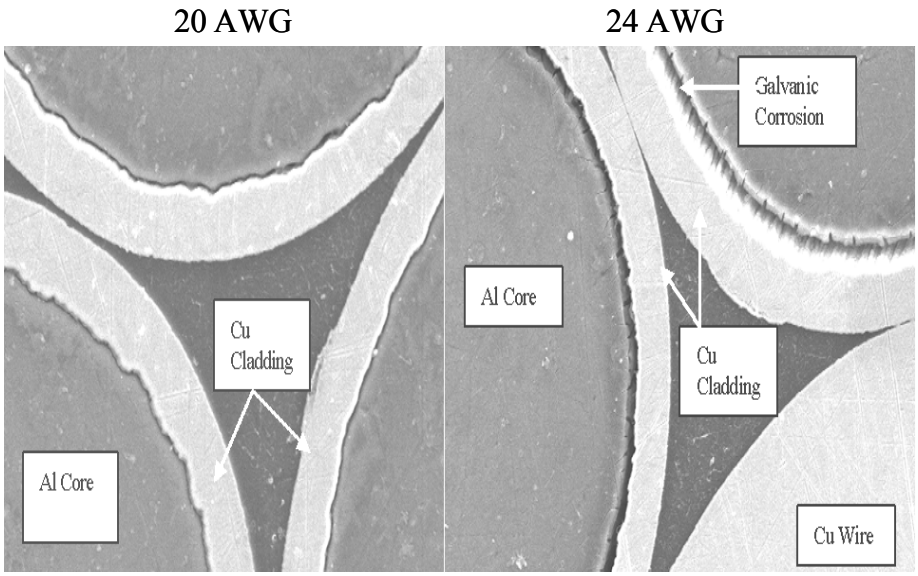


FIGURE 26. SEM PHOTOGRAPHS OF CROSS-SECTIONED CCAL AIRCRAFT WIRING AFTER 6 DAYS WITH 20 PPM NAOH SOLUTION

A higher magnification SEM photograph of the 24 AWG CCAL wire in figure 26 was recorded as shown in figure 27 and shows that the 20 ppm NaOH galvanic corrosion at the Al:Cu interface is similar in appearance to the 20 ppm NaOH corrosion in figure 24, i.e., crevice at Al:Cu interface and furrows in Al surface. The Cu:Al interface in figure 27 is much more uneven than in figure 24 due to the thicker intermetallics layer in the CCAL aircraft wiring compared to the commercial CCAL wires.

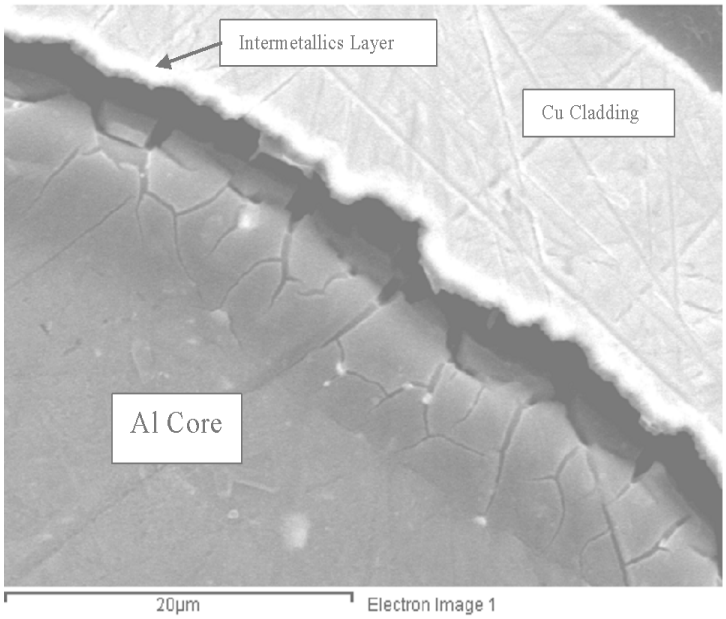


FIGURE 27. SEM PHOTOGRAPH OF CROSS-SECTIONED CCAL WIRE FROM 24 AWG AIRCRAFT WIRING AFTER 6 DAYS WITH 20 PPM NAOH SOLUTION

Since the first study using 1% NaCl in deionized water formed a protective gel on the exposed ends of the commercial CCAL wires, a 20 ppm NaCl solution was used to corrode cross-sectioned pieces of the 20 and 24 AWG CCAL aircraft wiring suspended in an epoxy casting material for 4 days. The corroded surfaces were then washed off with distilled water and blown dry (to remove any heavy deposits) before SEM/EDS analysis. The corrosion of the Al surfaces was less concentrated on the Al:Cu interfaces for the 20 AWG wiring than for the 24 AWG wiring as shown in figure 28.

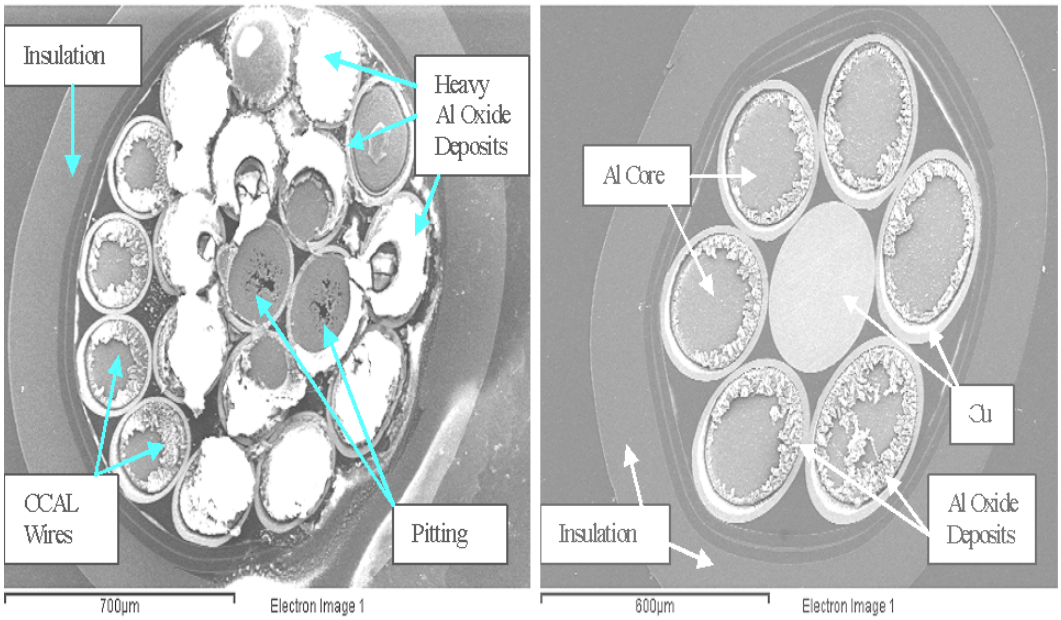


20 AWG 24 AWG

FIGURE 28. SEM PHOTOGRAPHS OF CROSS-SECTIONED CCAL AIRCRAFT WIRING AFTER 4 DAYS WITH 20 PPM NACL SOLUTION

As opposed to the 20 ppm NaOH tests (Al dissolves in alkaline solutions), deposits formed on the Al surfaces and Al:Cu interfaces during the corrosion test. The Al surfaces of the CCAL wires where the deposits were blown off prior to EDS analysis were heavily pitted for the 20 AWG wiring as shown in figure 28. As with the NaOH solution tests, the galvanic corrosion rate at the Al:Cu interface appeared to be promoted more for the CCAL wires of the 24 AWG wiring than the 20 AWG as shown by the higher magnification SEM pictures in figure 29; i.e., there is a crevice and heavier deposits at the Al:Cu interface of the 24 AWG CCAL wires.

## 1.6 PHYSICAL TESTING OF SILVER METALLIZED POLYMER WIRES

For the past two decades, considerable research effort has been spent on electrically conducting polymers for various electrical, electronic, and electro-optical applications. Although these conducting polymers possess advantages over metal conductors in weight reduction, chemical structure tailorability, and low-temperature processability, they have limited applications due to their poor environmental stability and low mechanical properties. In contrast to the conducting polymers, poly(p-phenylene benzobisoxazole) PBO polymer wires have very good mechanical properties but very low conductivity.

Previous research [1] indicated that the addition of carbon nanofibers (CNF) to the PBO dope used to make the wires did not produce conductive wires. However, adherent Ag metal films could be formed on the CNF/PBO wires if Ag metallization inks containing CNF were used to produce the conductive CNF metal films. To quantitate the adherence of the Ag films t6o the PBO wires with and without CNF present in the PBO and/or Ag ink, fatigue resistance and tensile tests were performed. A Cu wire of similar diameter to the PBO filaments (0.125 mm, 36 AWG) was also tested to establish a reference value for evaluating the coatings' performances.

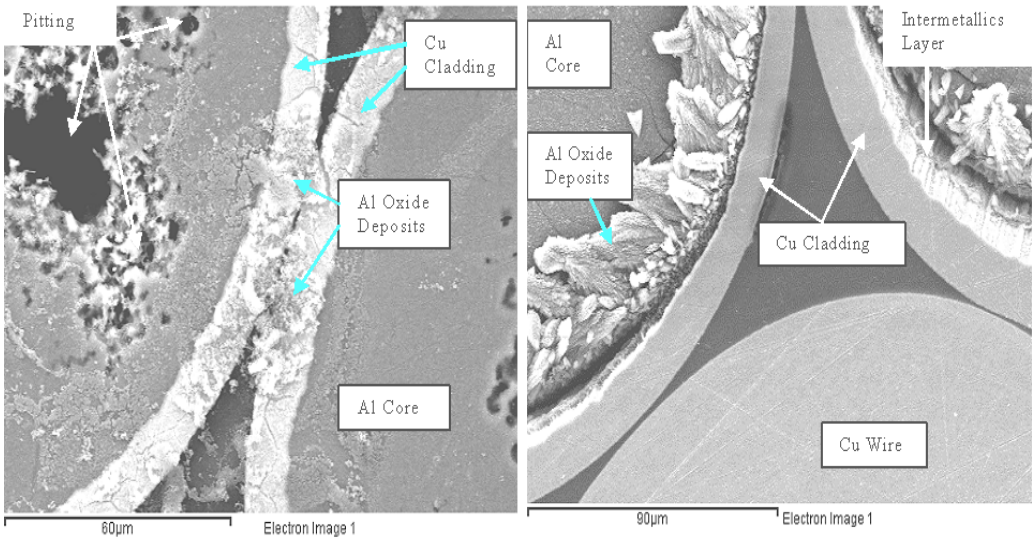


20 AWG 24 AWG

FIGURE 29. SEM PHOTOGRAPHS OF CROSS-SECTIONED CCAL AIRCRAFT WIRING AFTER 4 DAYS WITH 200 PPM NACL SOLUTION

1.6.1 Fatigue Resistance Tests.

To determine the fatigue resistances of the different Ag coated PBO wires made with and without CNF, PBO wires containing 0, 5 and 10% CNF were coated or infiltrated with the different Ag inks and then fatigue tested (procedures described in Appendix A). Based on the previously described results [Ag coatings on the rubber sheet (1)], the CNF was added at 5% to the Ag ink to obtain improved adhesion while minimizing the decrease in the coating conductivity. Although preliminary, the data in table 1 indicates that adding CNF to the conductive ink or PBO filament improves the adherence of the conductive coating to the PBO filament. The failures of the PBO coated wires were always due to coating failure and not the breakage of the PBO filament. The PBO filaments were unbreakable (>20 cycles) even when the fatigue test parameters were made more severe, bending was increased to 10º and the weight was increased to 1 pound.

Under the test conditions used to generate the data in table 1, the fatigue resistances (cycles to coating failure) of the conductive Ag coatings were similar to the fatigue resistance of the Cu wire when 5% CNF was added to the Ag coating or PBO wire. However, when the CNF was added to both the PBO wire (10%) and conductive ink (5%), the metallized PBO had a fatigue

resistance far superior to that of the Cu wire and the formed Ag film could not be failed (stopped at 24 cycles) under the fatigue test conditions in Appendix A.

In an attempt to further improve the Ag coating adherence to the PBO filament, the PBO filament was swelled during the coating process to allow infiltration of the Ag ink into the filament. The preliminary results in table 1 indicate that until 10% CNF was added to the PBO, the infiltration process appears to have had a detrimental effect on the fatigue resistance of the conductive film, i.e., for comparable amounts of CNF in the PBO and/or Ag ink, the cycles to failure were much higher for Ag films produced with the coating process than with the infiltration process. As with the Ag ink coated PBO wires, when the PBO filament contained 10% CNF and the Ag ink contained 5% CNF, the Ag coating produced by infiltration had a fatigue resistance over 24 cycles under the test conditions in Appendix A.

TABLE 1. FATIGUE TESTING RESULTS FOR SILVER CONDUCTIVE COATINGS

| Wire | % CNF in PBO | % CNF in Silver Conductive Coating | Application Technique | Cycles* to Coating Failure |
|---|---|---|---|---|
| Copper | - | - | - | 10 (Wire broke) |
| PBO | 0 | 0 | Coating | 3 |
| PBO | 0 | 5 | Coating | 8 |
| PBO | 5 | 0 | Coating | 12 |
| PBO | 10 | 5 | Coating | >24 |
| PBO | 0 | 0 | Infiltration | 5 |
| PBO | 0 | 5 | Infiltration | 3 |
| PBO | 5 | 5 | Infiltration | 4 |
| PBO | 10 | 5 | Infiltration | >24 |

* Each cycle:
Wire supporting a 0.5 pound weight was bent 90º around a rod (3 mm diameter)
Wire straightened and then bent 90º in opposite direction around second rod
Wire re-straightened and then bent 90º around first pin back into initial position

1.6.2 Tensile Strength Tests.

In addition to the fatigue test used to bend the Cu and metallized PBO wires, a tensile strength test rig was used to determine the strength of the Cu and metallized PBO wires. The resistances of the wires were measured using a 4-probe method to both quantitate the resistances of the wires and to determine when the Cu wire or Ag coating failed (coating becomes nonconductive as shown in figures 30 and 31).

20060824 4-Probe using Nanovoltmeter, 100mA
Copper wire 2

| LCD Panel | Load (lbf) | Displacement (inch) | Resistance (Ohm) | | |
|---|---|---|---|---|---|
| | | | Forward | Backward | Average |
| 0 | 0 | 4.06 | 0.154 | 0.154 | 0.154 |
| 1 | 0.25 | | 0.155 | 0.154 | 0.1545 |
| 2 | 0.5 | 4.24 | 0.165 | 0.164 | 0.1645 |
| 1 | 0.25 | 4.44 | 0.181 | 0.182 | 0.1815 |
| 1 | 0.25 | 4.56 | 0.191 | 0.192 | 0.1915 |

Resistivity estimation
Resistivity form literature (Ohm.cm)
1.7240E-06
Initial diameter (m & cm)
1.2500E-04 1.2500E-02
Initial length (inch & cm)
4.0600E+00 1.0312E+01
Initial resistance (Ohm)
1.5400E-01
Resistivity (Ohm.cm)
1.8317E-06

Stress estimation (ksi) (1 lbf assumed)
52.5990318

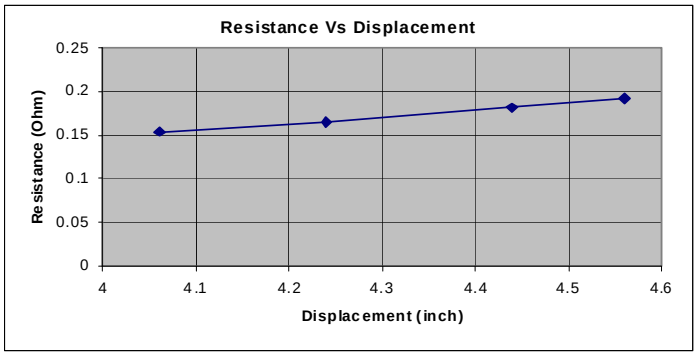


FIGURE 30. TENSILE TEST DATA FOR CU WIRE (36 AWG)

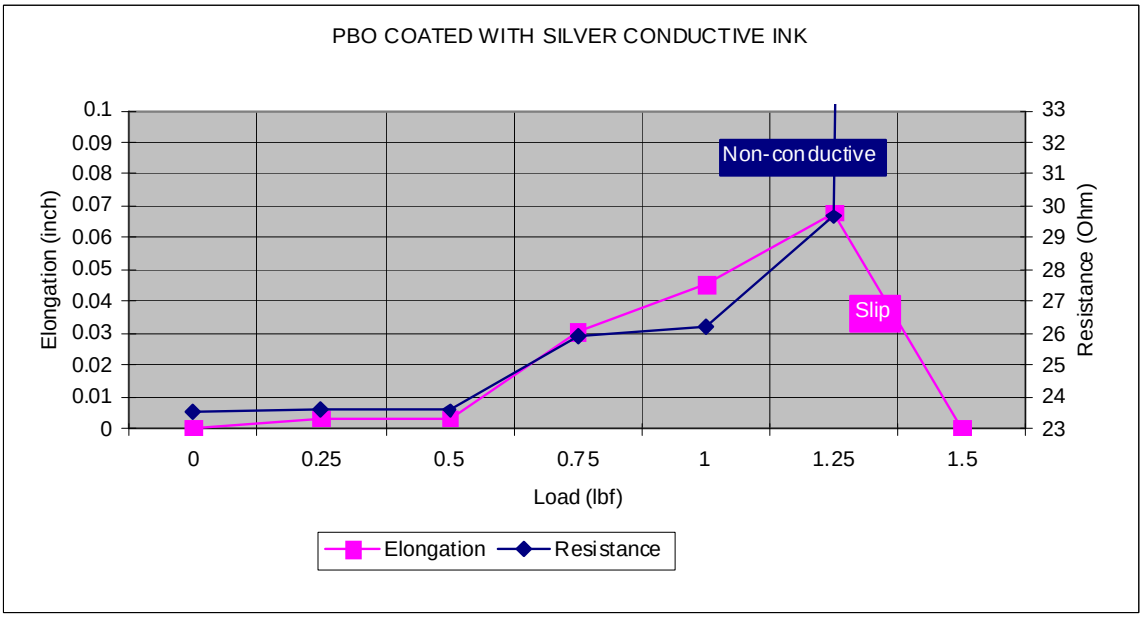


FIGURE 31. TENSILE TEST DATA FOR PBO WIRE COATED WITH AG CONDUCTIVE INK – 0% CNF

The plot in Figure 30 indicates that the Cu wire had a resistance of 0.15 ohms while the Ag coated PBO wires ranged from 8.5 to 30 ohms. The resistances of the Ag films were not dependent on the CNF content (most likely dependent on Ag film thickness and curing time). The Cu wire increased 0.5 inch in length and was estimated to have a tensile strength of 52 ksi (manufacturer data: 32-45 ksi). The literature value for commercial PBO wire is 840 ksi and previous FAA research (1) reported 230 ksi for lab produced PBO wires. The strength of the PBO filaments appeared to increase with CNF content but the increased strength was probably

more a consequence of filament diameter differences than CNF strengthening of the PBO [previous research (1) demonstrated that the addition of CNF caused a small decrease in PBO strength]. The tensile test data was in general agreement with the fatigue resistance data in table 1, i.e., when the CNF was added to both the PBO wire (10%) and conductive ink (5%), the Ag film on the PBO filament was able to withstand a much elongation (0.125 inches) prior to film failure than the other tested PBO wires (failed in 0.065 – 0.09 inch range). Basically, the Ag films formed with the coating method had longer elongations prior to failure than those formed with the infiltration method and the Ag films containing CNF had longer elongations prior to failure than those without CNF regardless of the PBO wire composition.

1.6.3 Analysis of Stressed UDRI PBO Wires

Since both the fatigue resistance and tensile strength tests indicated that CNF help anchor the coating to the PBO surface and improve the flexibility of the formed Ag coating, SEM/EDS analyses of the Ag coated PBO wires that failed after less than 12 cycles and the two PBO wires that exceeded 24 cycles without failure (table 1) on the fatigue test rig were performed. The SEM/EDS analyses focused on the physical changes that occurred at the Ag coating:PBO interface that could account for the improved film adhesion in the presence of CNFs. The SEM photographs of the failed Ag coated PBO wire without CNF present (failed after 3 cycles) in figure 32 show that the PBO wire surface is smooth and the Ag coating left the entire circumference of the PBO filament in sections.

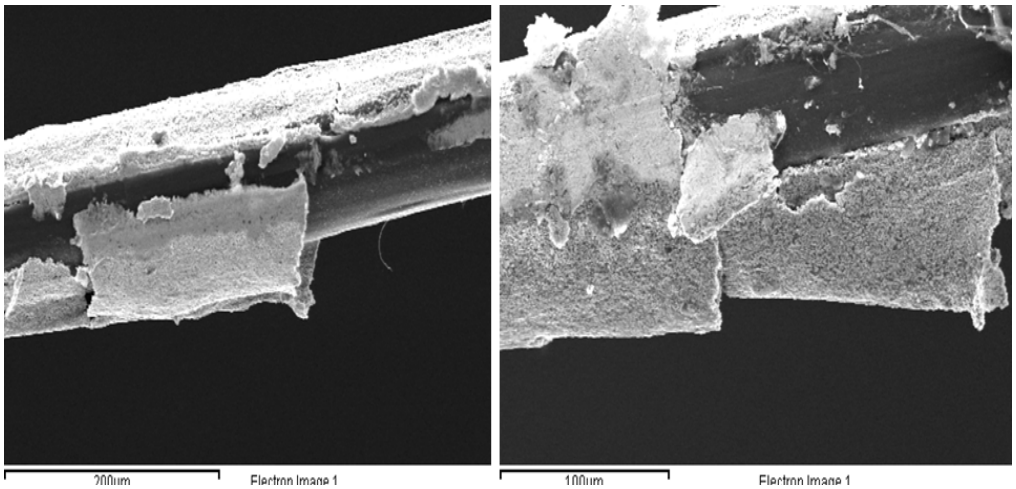


FIGURE 32. SEM PHOTOGRAPHS OF PBO FIBERS COATED WITH AG FILM AFTER 3 TEST CYCLES – NO CNF PRESENT

The SEM microphotographs of the failed Ag infiltrated PBO wire with %5 CNF in both the PBO filament and Ag coating (failed at 4 cycles) are shown in figure 33. The SEM photographs in figure 33 show that the PBO wire surface is smooth and the Ag coating left the entire circumference of the PBO surface in sections even though several CNFs are apparent extending out of the upper edges of the broken Ag film. The SEM photographs in figure 34 of the failed Ag coated PBO wire with 5% CNF only in the PBO filament (failed after 12 cycles) show that the Ag film did not fail the entire circumference of the PBO filament and that the PBO surface contained furrows/grooves. Since the PBO wires in figures 33 and 34 both contain 5% CNF, the results indicate that the infiltration process reduces the roughness/number of grooves in the PBO

surface and the increased surface smoothness likely accounts for the reduction in the number of cycles prior to film failure, i.e., 12 cycles for coated versus 4 for infiltrated.

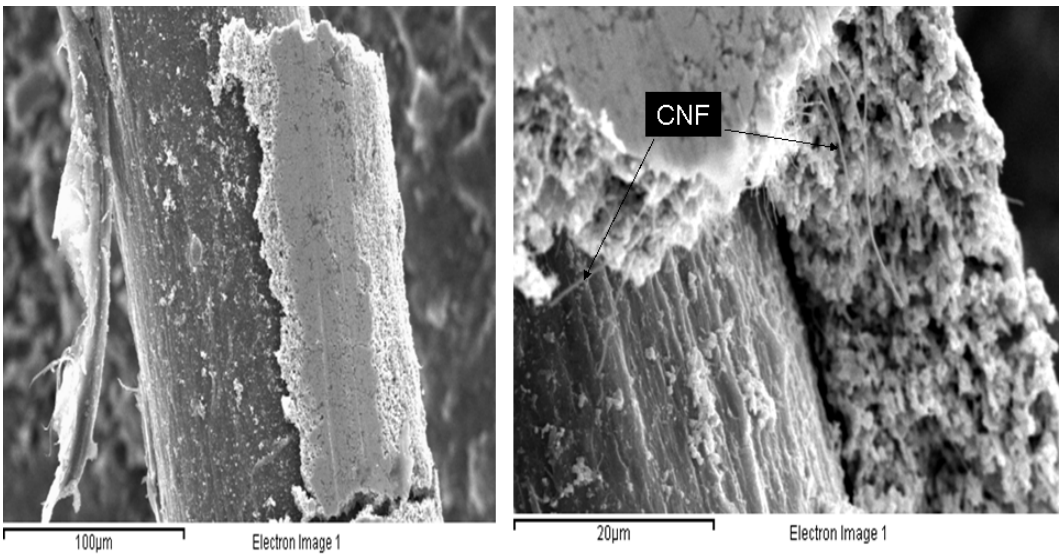


FIGURE 33. SEM PHOTOGRAPHS OF PBO FIBERS (5% CNF) INFILTRATED WITH AG FILM (5% CNF) AFTER 4 TEST CYCLES

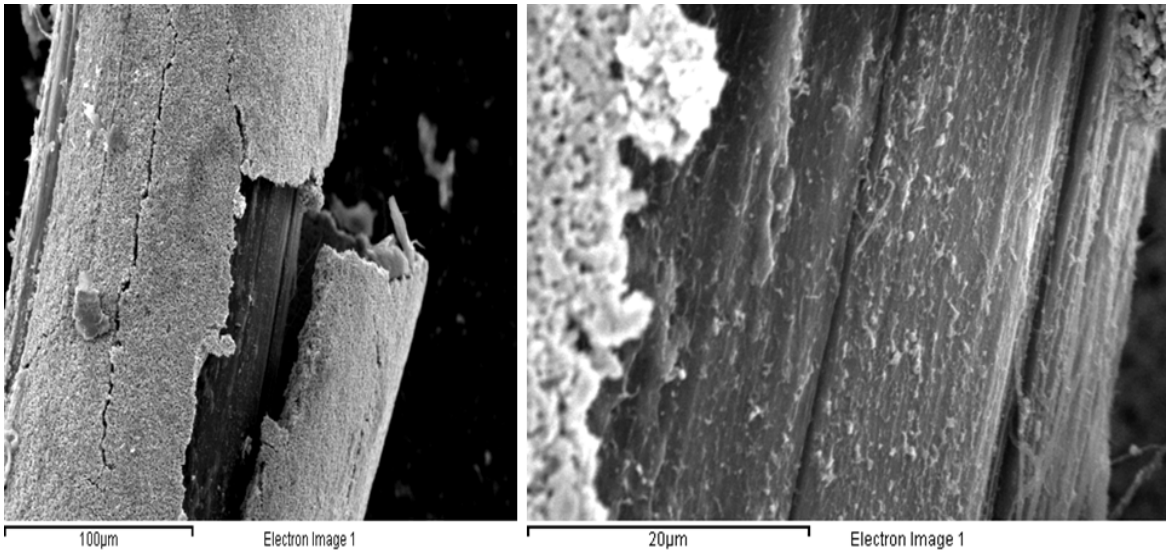


FIGURE 34. SEM PHOTOGRAPHS OF PBO FIBERS (5% CNF) COATED WITH AG FILM (NO CNF PRESENT) AFTER 12 TEST CYCLES

Since their Ag films did not fail after 24 cycles on the bending fatigue test, the PBO wires with 10% CNF in the PBO filament and 5% CNF in the Ag film were cross sectioned to reveal the PBO surface:Ag film interface for SEM analysis. The SEM photographs of the cross sectioned PBO filaments in figure 35 show that the PBO surface:Ag film interfaces of the coated and infiltrated PBO filaments are uneven, i.e., the 10% CNF in the PBO filament roughened the filament surface, regardless of the Ag film forming process, contributing to the strong adherence

of the Ag films that was undamaged after 24 cycles of the bending fatigue test. The cross-sectioned Ag films indicate there are voids in the films, which may also contribute to the flexibility of the films.

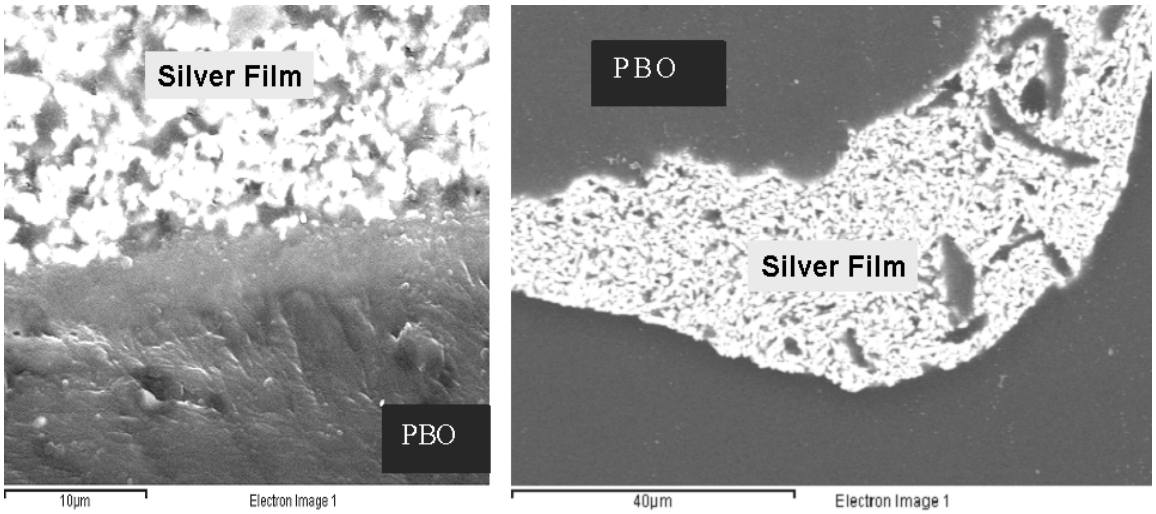


INFILTRATED COATED

FIGURE 35. SEM PHOTOGRAPHS OF CROSS-SECTIONED PBO FIBERS (10% CNF) WITH AG FILM (5% CNF) AFTER 24 TEST CYCLES

## 1.7 SUMMARY

The preliminary results indicate that a simple coating process suitable for high speed wire production could be used to produce robust, conductive PBO wires as long as CNF are present in both the PBO filament and conductive ink. Although Ag conductive ink was used in this research, conductive inks to thermally produce Cu and Ni coatings are also commercially available and would be expected to also produce rugged metal films upon modification with the CNF.

The composite or bimetallic conductors have both strengths (weight) and weaknesses (maintenance issues) compared to the Cu conductors used in aircraft EWIS. Although the Ag metallized PBO polymer wires have the additional advantages of improved strength and fatigue resistance, the preliminary research indicates they will require significant improvements in electrical conductivity and long-term metal film adherence studies prior to consideration for future aircraft designs. In contrast to the metallized polymer wires, the CCAL wires are already used in current and future aircraft designs and the preliminary research presented in this paper indicates that many of CCAL wires' performance issues (galvanic corrosion, intermetallics) appear resolved by the connector designed for aircraft EWIS.

## 2. INSULATION REPAIR TECHNIQUES AND ENVIRONMENT OF AGING EWIS.

The potential safety hazards resulting from aged or damaged insulation require that prompt maintenance actions be taken to ensure reliable EWIS performance. However, the miles of inaccessible, bundled wiring of aircraft EWIS reduce the effectiveness of repair technologies

currently in use today. Therefore, a research program was performed to develop self-repairing insulation and manual insulation repair procedures to improve the reliability of aging aircraft EWIS.

The self-repairing insulation techniques incorporate a non-toxic, water based solution that can be misted into inaccessible compartments, sprayed/brushed onto accessible wire bundles or used to produce a self-repairing insulation layer during electrical wire manufacture. When the solution droplets come into contact with a powered wire with damaged insulation, the solution reacts with the exposed metal conductor to produce an adherent, insulating film to repair the damaged insulation. The self-repairing solutions were developed for both Cu and plated Cu conductors and to perform independent of the insulation damage mechanism, insulation composition or power characteristics. Hand-held devices to locate the damaged insulation and to ensure the self-repair of the wiring insulation is complete were also studied.

The manual insulation repair techniques use brushable chemical solutions to repair different types of damaged insulation and to modify aged polyimide surfaces to make them permanently water repellent and hydrolytically stable. Interpenetrating network polymer solutions based on chemically modified polyimide resin were developed to coat cracked polyimide insulation with an adherent, flexible insulating film with enhanced hydrolytic and chemical stabilities. The hydrolytic and chemical degradation resistances of the new and modified polyimide surfaces were evaluated using long-term exposure to alkali solutions and other chemicals.

In addition to the insulation repair studies, research was also performed to characterize the "dirt" present on aircraft wiring that would have to be removed prior to the application of the repair solutions. The research was performed to both determine the composition of the wire "dirt" and to determine the potential of the "dirt" to support combustion during wiring arcing events.

## 2.1 SELF-REPAIRING INSULATION REPAIR.

Previous research [1] has shown that water-soluble polyvinyl alcohol (PVAL) dissolved in water will rapidly form water-insoluble, insulating polymer layers during the electrolysis of the water matrix by powered, exposed Cu wire conductors. However, the location of the insoluble polymer layer was dependent on the type of water used to dissolve the PVAL. When the PVAL was dissolved in distilled or deionized water, the water-insoluble polymer formed between the Cu wires. However when the PVAL was dissolved in water obtained from a dehumidifier, the water-insoluble polymer formed directly on the positive Cu wire when dc powered and on both Cu wires when ac powered. Therefore, research was performed to determine the species present in dehumidifier water responsible for the water-insoluble layer forming directly on the Cu wire. Once the species were identified then research was performed to identify compounds that could be added to distilled water to form the water-insoluble polymer directly on the Cu wires.

### 2.1.1 Analysis of Dehumidifier Water.

To determine the species present in the dehumidifier water responsible for directing the water-insoluble polymer formation onto the Cu wires, drops of the dehumidifier water were dried on a graphite holder. The EDS spectrum representative of the dried dehumidifier water films is shown in figure 36 and the elemental analyses indicate there are two types of solids dissolved in

the dehumidifier water. The first type includes aluminum (Al), Cu (Cu), zinc (Zn) and iron (Fe) representing construction metals of the dehumidifier. The second type are carbon (C), calcium (Ca), chlorine (Cl), oxygen (O) and sodium (Na) representing species from the surrounding area that were deposited on the dehumidifier coils by the air flow and washed into the condensed water reservoir. The thin deposit with distinct areas of different crystal structures formed by the evaporating dehumidifier water shown in figure 37 indicates that the species are present in ppm levels and have a wide range of water solubilities [most likely, low solubility organics/carbonates (metal, C, O) and high solubility chlorides (metal, Cl)]. The dissolved metal species present in the dehumidifier water are most likely responsible for directing the water-insoluble polymer onto the powered Cu wires, i.e., the dissolved metal species combine with the dissolved Cu species produced during electrolysis to cross-link the dissolved PVAL producing the water-insoluble polymer on the Cu wires.

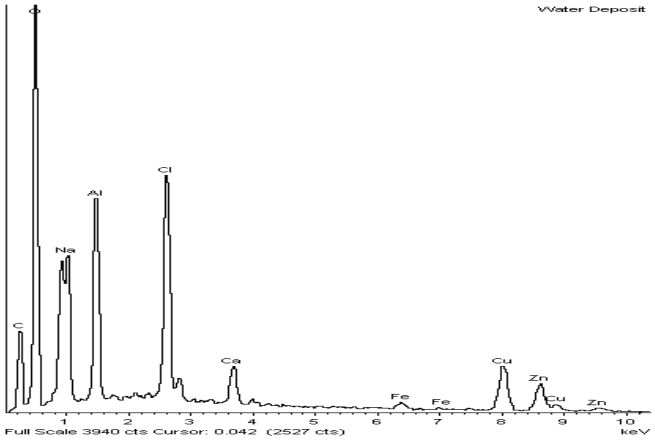


FIGURE 36. EDS ANALYSIS OF DEHUMIDIFIER WATER DEPOSIT

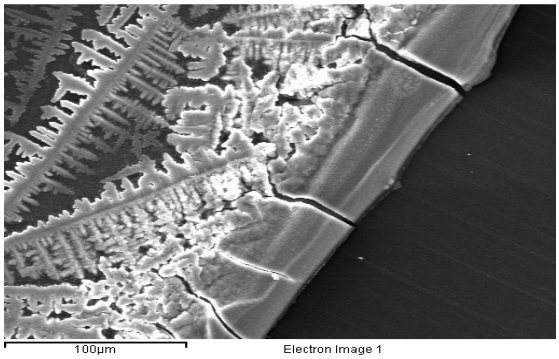


FIGURE 37. SEM PHOTOGRAPH OF DEHUMIDIFIER WATER DEPOSIT

2.1.2 Modification of Distilled Water Used in PVAL Solutions.

Based on the analyses in figures 36 and 37, studies which evaluated the effects of adding dissolved metal species and stable nonmetallic suspensions to the distilled water used to produce the 10% PVAL water solutions were performed next. Cu and Fe chlorides and carbonates were dissolved into the distilled water as well as hydrochloric acid (HCl) to provide sources of dissolved metals and chlorides and to clean the Cu oxides (dissolved Cu chlorides) from the Cu wires. In addition to the dissolved species, stable suspensions of particles were produced by

adding fumed silica and Elmer's School glue (polyvinyl acetate suspension) to 10% PVAL (PVAL: 80% hydrolyzed, molecular weight 8,000) water solutions.

A series of bare Cu wire pairs (Appendix B) were prepared for testing the capabilities of the modified PVAL solutions to direct the formation of a water-insoluble film onto the positively charged wire of the selected wire pair connected to 27 Vdc. Representative results of the studied 10% PVAL solutions and the resistances of the produced water-insoluble films (measured with a 4-point probe) are listed in table 2.

TABLE 2. TEST RESULTS FOR 10% PVAL SOLUTIONS

| Compound Added (Concentration in Solution) | Film Formed on (+) Wire? | Adherent Film? | Resistance of Film (GΩ) |
|---|---|---|---|
| $FeCl_3$ (0.5%)<br>HCl (0.09M) | No | No | 0.05 |
| $CuCl_2$ (0.5%)<br>HCl (0.01M) | Yes | Yes | 0.1 |
| Elmer's Glue (2%) | Yes | Yes | 500 |
| Elmer's Glue (1%)<br>$CuCl_2$ (0.05%)<br>HCl (0.005M) | Yes | Yes | 100 |
| Elmer's Glue (2%)<br>$FeCl_3$ (0.05%)<br>HCl (0.009M) | Yes | No | 1 |
| Elmer's Glue (25%) | No | No | 10 |
| Fumed Silica (1%) | Yes | No | 1000 |

Of the various compounds added to the 10% PVAL solutions in distilled water, the solutions containing low concentrations of $CuCl_2$/HCl (dissolved species) and/or Elmer's School glue produced the best candidates for the self-repairing solutions, i.e., adherent water-insoluble film with high resistance formed directly on positively charged wire. The fumed silica identified during the previous program [1] produced a water-insoluble film with high resistance directly on the positively charged wire but reduced the adherence of the film to the covered wire.

2.1.3 Modification of Distilled Water to Detect Damaged Insulation.

In addition to the ability to direct the formation of the water-insoluble polymer, research also evaluated the different added species as catalysts to maximize radio frequency (RF) output/rate during the electrolysis of water solutions used to identify unobserved areas of insulation damage. To determine if the dissolved metals used to control the formation of the water-insoluble polymer could also be used to increase the electrolysis rate at exposed, powered Cu wire conductors, distilled water containing different concentrations of $CuCl_2$/HCl were dispensed onto bare Cu wires connected to 27 Vdc. The current flow and RF output of the unrestricted electrolysis reactions were measured as described in Appendix B. Regardless of the concentration of the $CuCl_2$/HCl and other dissolved metal salts, the presence of the salts increased the rate of electrolysis and current while appearing to decrease the measured RF output as shown in figure 38. Consequently, any salts to be used in the self-repair methodology would

be dissolved into the PVAL repairing solution and not in the water used to detect damaged insulation. In every case, seconds after a drop of 10% PVAL solution was added to the water layer undergoing electrolysis, the RF output decreased to a level equal to the background noise in figure 38, a water-insoluble film formed on the positively charged wire and the current flow decreased from greater than 0.5 A to less than 15 mA.

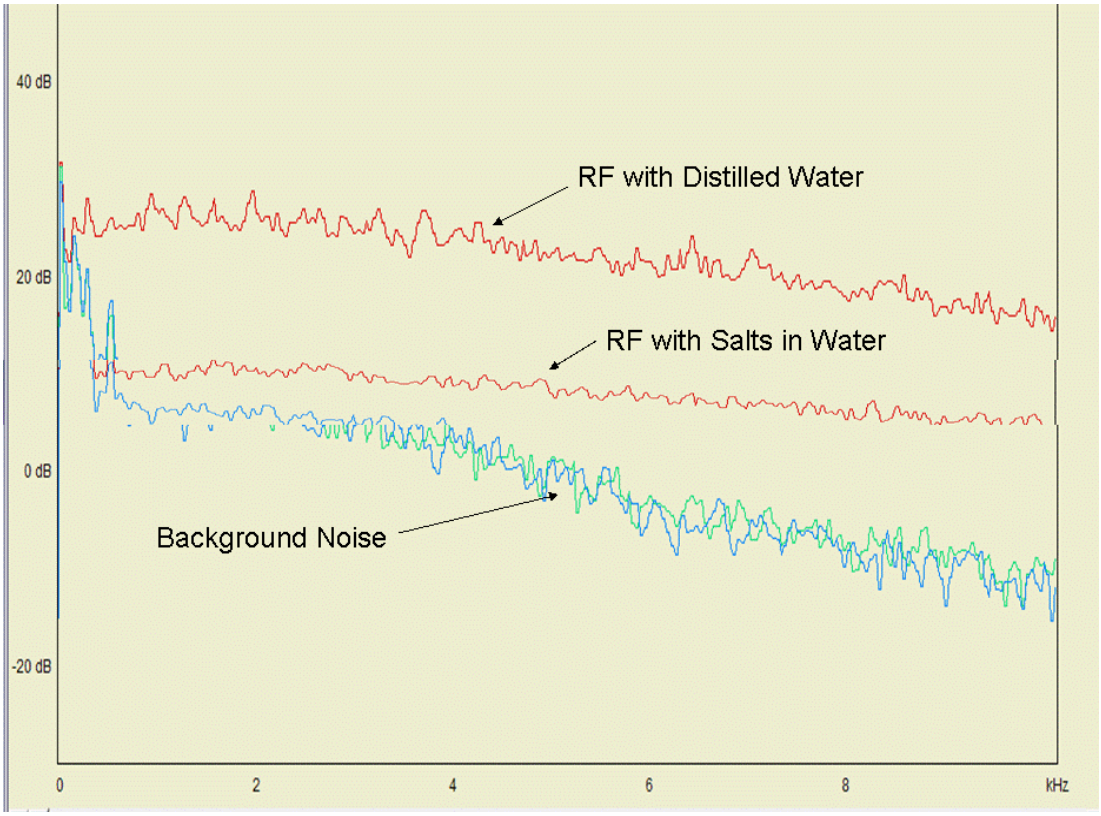


FIGURE 38. BACKGROUND NOISE AND RF PRODUCED BY ELECTROLYSIS OF DIFFERENT WATER SOLUTIONS

2.1.4 Effects of PVAL Structure on Water-Insoluble Polymer Formation.

In addition to the electrolytic composition of the water solution, the degree of hydrolysis and molecular structure of the PVAL used to produce the 10% PVAL solutions were also studied. The degrees of hydrolysis varied from 80 - 96% and the molecular weights varied from 8,000 – 145,000 for the tested PVAL. The PVALs with degrees of hydrolysis above 92% and/or molecular weights above 70,000 required heating at 80ºC with stirring for 6 hours to dissolve completely. Although a wide range of water solubilities, molecular weights and degrees of hydrolysis were studied, the water-insoluble films created during electrolysis at bare Cu wires were similar in appearance and toughness. The most water-soluble PVAL (80% hydrolysis and 8,000 – 10,000 molecular weight) was selected for the self-repairing solution since it produced the least viscous solution (suitable for spraying) and the most flexible, adherent water-insoluble layer.

To determine if chemical modification of the PVAL molecule could be used to improve the production of the water-insoluble layer during electrolysis, two different types of modified

PVAL were obtained R-2105 and KL-318 (Kuraray America, New York). R-2105 contains silanol groups in its PVAL molecular structures. The silanol groups are reactive with inorganic substances such as silica or alumina and can be easily cross-linked by changing the pH of the solution or by mixing with inorganic substances to form water resistant films. In contrast to R-2105, the KL-308 PVAL (85% hydrolysis) has been carboxylated making the polymer more hydrophilic (improves water solubility) and the carboxyl groups are available for interacting with/removing the oxides on the exposed Cu surfaces. The 10% solutions of the unmodified PVAL (80% hydrolysis), R-2105 and KL-308 were prepared in distilled water with and without $CuCl_2$ (0.05%) and were used to produce water-insoluble layers on bare Cu wires connected to 27 Vdc. The modifications of the PVAL molecule appeared to inhibit the formation of the water-insoluble polymer layer as shown in figure 39. The water-insoluble polymer layers produced by KL-318 and R-2105 did not provide completer coverage of the positively charged wires (bottom wire in figure 39) and were brittle and poorly adhering compared to the water insoluble polymer formed by the unmodified PVAL, i.e., modification of PVAL molecule inhibited the polymerization process at the surface of the bare Cu wire.

2.1.5 Evaluation of Optimized PVAL Solution (Commercialization).

Based on the research to date, the unmodified 10% PVAL (80% hydrolysis) solution prepared with distilled water containing $CuCl_2$ (0.05%) or Elmer's School glue (1%) was selected as the best candidate (least viscous solution, most adherent/flexible film) for development into a sprayable self-repairing solution. As further evaluation of the PVAL solution, the insulation of a lamp cord was cut away with a razor blade and the damaged cord was plugged into an 115Vac, 20A outlet. When a drop of distilled or tap (salts) water was placed on the exposed Cu strands, within seconds the produced dendrites [1] shorted the circuit causing the circuit breaker to open. When the test was repeated with the candidate PVAL solution, a clear water-insoluble layer formed immediately on both exposed wires as shown in figure 40 and the current flow rapidly fell to below 3 mA.

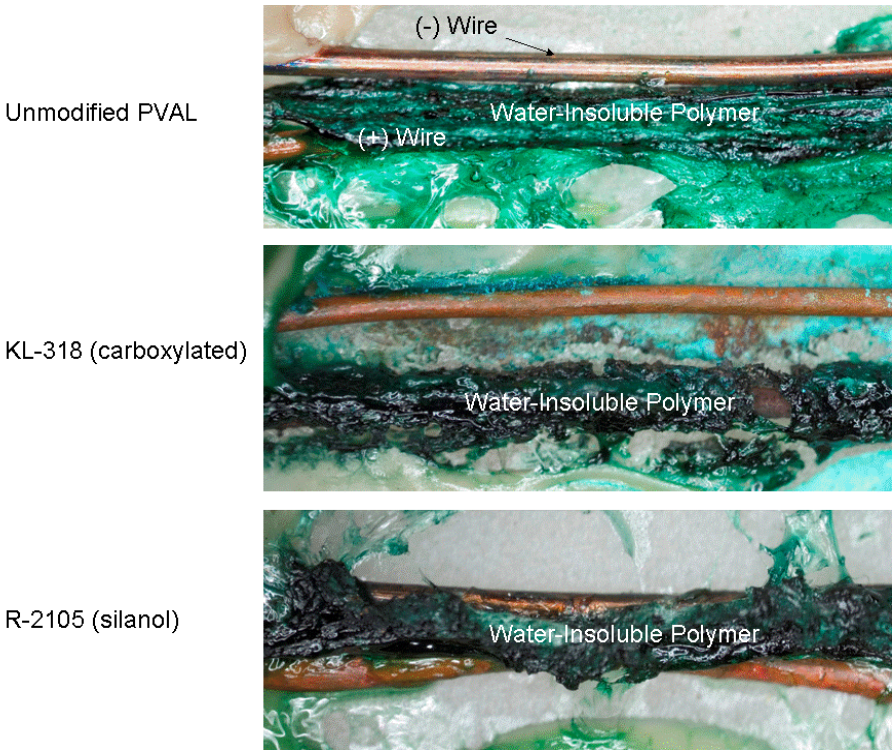


FIGURE 39. WATER INSOLUBLE POLYMERS PRODUCED BY UNMODIFIED AND MODIFIED PVAL SOLUTIONS

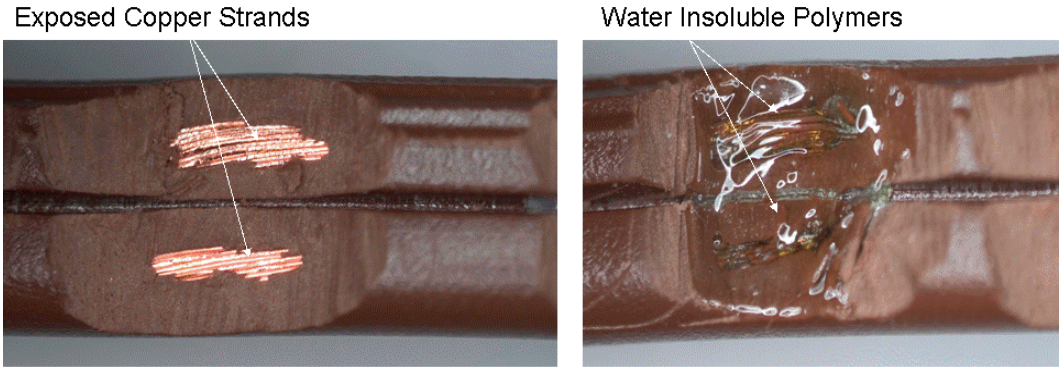


FIGURE 40. DAMAGED AND SELF-REPAIRED LAMP CORDS

Since one of the successful self-repairing wire solution contained 1% Elmer's School glue and the solution would have home/industrial repair possibilities in addition to aircraft wiring, the self-repairing solution technology was presented at the research headquarters of Elmer's Products in Columbus, Ohio. Discussions with Elmer's for home repair and CRC Industries (Warminster, PA) for industrial applications have been initiated to commercialize the self-repairing solution(s).

## 2.2 DETECTION OF RF OUTPUT OF ELECTROLYSIS.

In addition to the self-repairing solution development, research was also initiated to identify/construct a RF detection system for locating exposed, adjacent Cu conductors causing

electrolysis of adhering water droplets. At the beginning of this project, portable spectrum analyzers were identified which had been developed specifically for low frequency (below 10 kHz) RF signals so as to be sensitive to the RF range produced by electrolysis (figure 38). However, the analyzers are still not commercially available.

In addition to the portable spectrum analyzers, the low frequency RF detection capabilities of purchased or constructed antenna were evaluated using the computer based spectrum analyzer described in Appendix B. A simple AM radio tuned to a local station (1410 AM) was used to confirm that RF was being produced during the antenna evaluations.

### 2.2.1 Evaluation of Distance on RF Detection Of Cu Coil Antenna

To initiate the evaluation of the selected antenna, the AM radio was situated 6 inches from a pair of bare Cu wires attached to a 27Vdc battery supply. When a drop of water was placed between the Cu wires, electrolysis occurred and the produced RF caused strong static blocking out the signal of the selected radio station. When the radio was moved to 12 inches from the Cu wires, the signal of the selected radio was clear (no static). So the AM radio was placed 6 inches from the bare Cu wires for all the following experiments. The output of the spectrum analyzer was time averaged (500 milliseconds) in an attempt to cancel out the background noise (sporadic, averaging decreases) and improve the RF detection (constant, averaging increases).
The wound Cu wire coil described in Appendix B was placed directly above the Cu pair with the coil held vertically (open end toward wires) and was slowly moved from 0.5 to 12 inches above the Cu wire pair during electrolysis (static heard on AM radio). The overlaid spectra shown in figure 41 are representative of the spectrum analyzer outputs as the Cu coil antenna was moved from 0.5 inches to 6 inches away from the Cu wire pair. The RF detected by the spectrum analyzer decreased dramatically with increasing distance and equaled the background noise by 9 inches. Consequently, the wound Cu coil antenna and the radio (static not heard at 12 inches) had similar capabilities for detecting the RF produced by electrolysis.

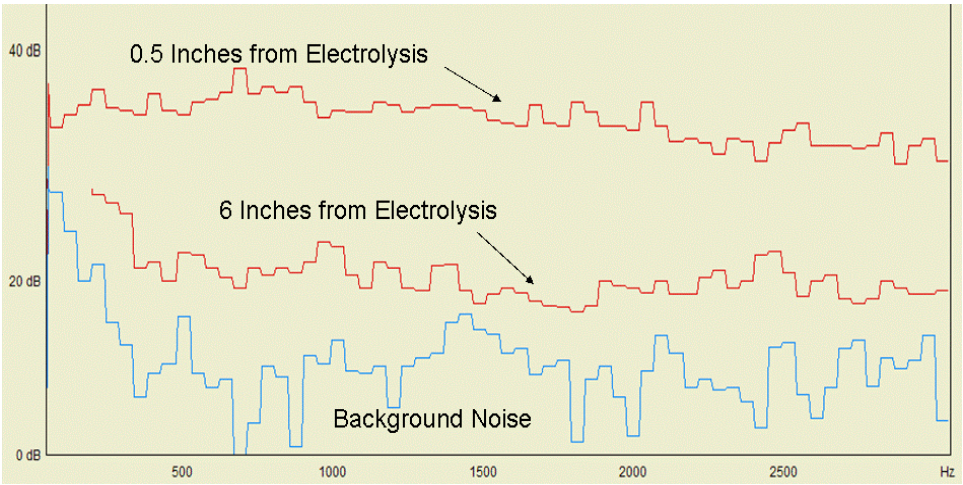


FIGURE 41. EFFECTS OF DISTANCE ON RF DETECTED BY CU COIL ANTENNA

2.2.2 Evaluation of Distance and Metal Obstructions on RF Detection of Loop Antenna.

A commercial loop antenna designed to detect low frequency RF is shown in figure 42. The loop is 48 inches in diameter and comes with an amplifier and connectors allowing its use with the computer based spectrum analyzed. Although cumbersome, the antenna is portable and was used more to evaluate the possibility of detecting RF from outside the aircraft than inclusion into a portable, self-repair maintenance procedure. As opposed to the Cu coil antenna, the RF detection capabilities of the loop antenna did not change significantly when moved 12 inches from the Cu pair undergoing electrolysis. The overlaid spectra in figure 43 are representative of the spectrum analyzer outputs as the loop antenna was moved in steps of 12 inches from the Cu pair. The overlaid spectra in figure 43 also includes the spectrum analyzer outputs when the Cu pair undergoing electrolysis was placed on a steel plate and then covered with either an aluminum or steel pan. Since it could not be confirmed visually, electrolysis during the covered tests was confirmed by the static detected by the radio placed 6 inches from the covered wire pair.

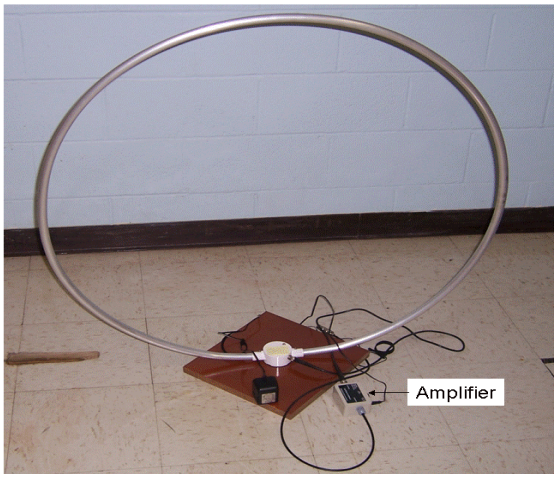


FIGURE 42. LOOP ANTENNA FOR LOW FREQUENCY RF

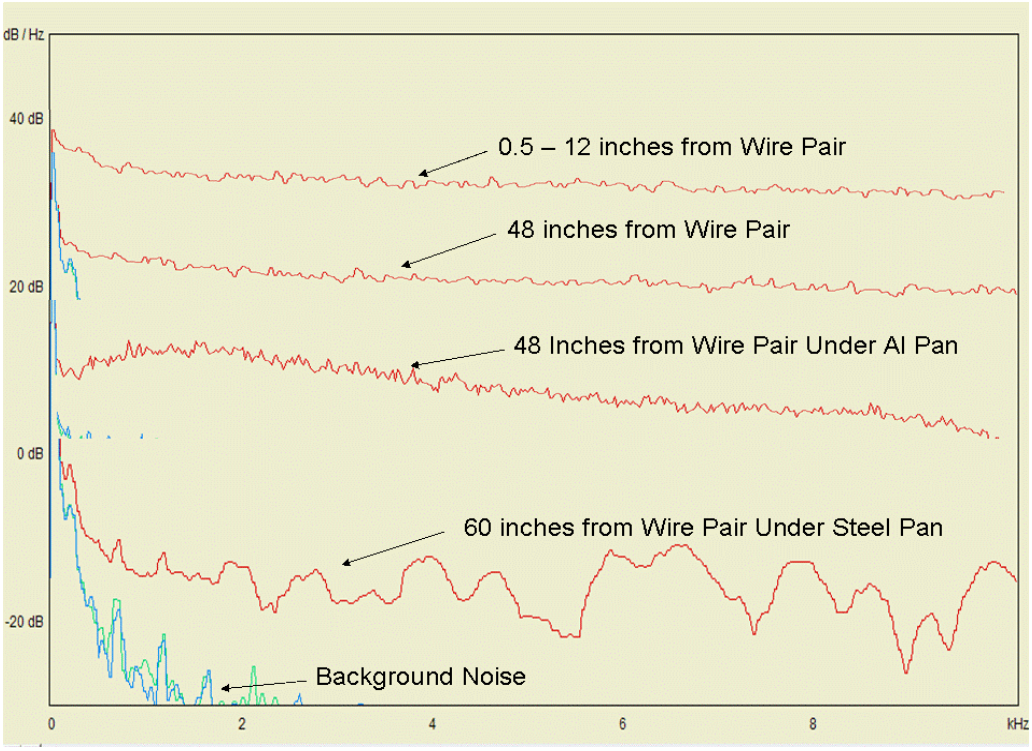


FIGURE 43. EFFECTS OF DISTANCE AND METAL OBSTRUCTIONS ON THE RF DETECTED BY THE LOOP ANTENNA

The first difference between the spectra in figures in 41 and 43 is the background noise in figure 43 was suppressed by the loop antenna amplifier (background noise similar to figure 41 when the amplifier was not used). The second main difference is the effect of distance was minimal up to 60 inches from the Cu pair undergoing electrolysis for the loop antenna compared to the Cu coil antenna. Both the AM radio (6 inches) and loop antenna (60 inches) were able to detect the electrolysis produced RF through either the aluminum and steel covers.

Therefore, these preliminary results indicate that maintenance personnel could use portable antenna with distance limitations inside the aircraft to detect/locate exposed, powered conductors producing electrolysis RF (condensed or sprayed water) and could use supported/stationary large antenna without distance limitations to identify recently landed aircraft with exposed conductors (condensed water) in need of further examination.

## 2.3 EVALUATION OF SELF-REPAIR SPRAY ON BUNDLE OF WIRES TEST.

To make the evaluation of the self-repairing repair method more realistic, 10 lengths (each 1 foot long) of 24 AWG aircraft wiring were bundled together using wire wraps as shown in figure 44. The insulations of several wires were damaged with a razor blade and

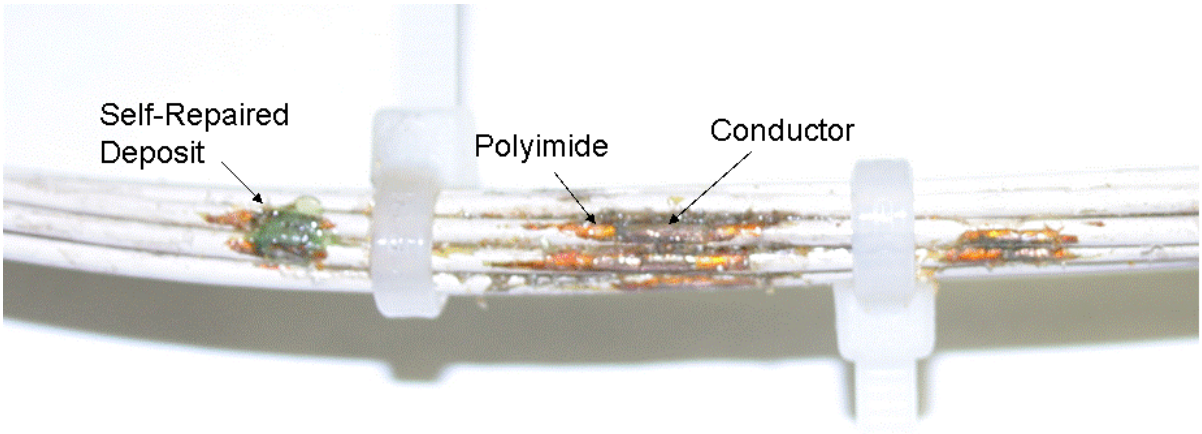


FIGURE 44. BUNDLE OF WIRING WITH DAMAGED AND SELF-REPAIRED INSULATION

Wetted with distilled or dehumidifier water for the electrolysis experiments using either 27 Vdc, 1A or 115 Vac, 20A. Once RF was detected by the AM radio (static) or spectrum analyzer confirming electrolysis was occurring, 10% PVAL aqueous solutions (also contained 1% Elmer's School glue) were sprayed on the areas of insulation damage. Within a few seconds the RF became undetectable, the current flow fell to below 2 mA and a water-insoluble deposit formed on top of the bundle covering the site of insulation damage (figure 44). Consequently, the self-repairing solution will form water-insoluble polymers on bundled aircraft wiring with damaged insulation as well as bare Cu wire pairs when ac or dc current is applied.

## 2.4 SELF-REPAIR WIRES WITH PVAL COATINGS.

In addition to the self-repairing sprays, work was also performed on designing methods for incorporating the self-repairing PVAL film directly into wiring insulation systems. Conversations with an aircraft wiring manufacturer (Thermax/CDT, Connecticut) indicated that the required PVAL film could be formed on the conductor by a simple operation in which the conductor was moved through an aqueous PVAL solution then a drying tower to remove all of the water prior to the normal insulation operations (PVAL based adhesives could be used in adhering wrapped wire insulations). The aqueous dipping process would be expected to produce a PVAL film similar to the dipping process described in previous research [1]. In case the film produced by the aqueous solution dipping process was excessive for the self-repair process, research was also performed to study the effectiveness of PVAL dispersed in insulating polymer matrices.

### 2.4.1 Water-Soluble Polymer Matrix

The first matrix investigated during the study was the water-soluble polymer polyethylene glycol (PEG). A 9% PEG, 1% PVAL aqueous solution was prepared, dispensed onto a bare Cu wire pair and allowed to dry overnight to produce a film covering the wires that was 90% PEG and 10% PVAL. The wire pair was connected to a 27 Vdc battery source and drops of distilled water were dispensed onto the film. Both the PEG matrix and dispersed PVAL polymer dissolved into the dispensed water inhibiting electrolysis (no RF detected and current below 10 mA). Although

no detectable electrolysis occurred, no water-insoluble film was apparent on either Cu wire, i.e., dissolved PEG molecules interfered with the polymerization of the PVAL at the Cu wire surface.

### 2.4.2 Water-Insoluble Polymer Matrix

Since the initial results indicated that a water-soluble matrix may interfere with the self-repair process, water-insoluble matrices were then investigated. The water-insoluble matrices selected were low molecular weight polyethylene and beeswax due to their melting points being below 150ºC and differences in polarity to affect the solubility of the PVAL in the matrices, i.e., PVAL would be expected to have a higher level of solubility in polar beeswax than in nonpolar polyethylene. After the polyethylene and beeswax were melted, PVAL crystals were mixed into the melted polymers to produce polymer mixtures containing 10, 1 or 0.1% PVAL.

To simulate cuts in the wiring insulation, bare Cu wires were dipped in the melted polyethylene and beeswax mixtures containing 1 and 0.1% PVAL then allowed to cool/harden overnight. The coated wires were paired, connected to a 27 Vdc battery source, cuts were made in the coatings with a razor blade to expose the wires (sparks occurred whenever the blade touched both wires confirming the cut was complete) and drops of distilled water were dispensed onto the cuts. As in previous research [1], the self-repair was rapid regardless of the PVAL concentration or polymer matrix and the current flow never exceeded 2 mA.

To simulate large removal of the wiring insulation, the melted polymer mixtures containing different levels of PVAL were then poured onto opposite ends of bare Cu wire pairs. The wires were then connected to 27 Vdc and drops of distilled water were placed between the hardened polymers containing different levels of PVAL. For the polyethylene mixtures containing 10%, 1% and 0.1% PVAL, electrolysis was inhibited (no RF detected and current below 2 mA) and water-insoluble polymer films formed on the positively charged Cu wire (10% PVAL also produced heavy film between the wires) as shown in figure 45. For the beeswax mixture containing 10% PVAL, electrolysis again was inhibited and water-insoluble polymer films formed on the positively charged Cu wire. For the beeswax mixtures containing 1 and 0.1% PVAL, electrolysis was inhibited to a lesser degree (no RF detected but current levels reached 30 mA prior to decreasing to 5 mA) and the water-insoluble polymer films formed on the positively charged Cu wires were incomplete (debris between wires in figure 45). Consequently, these results indicate that polyethylene was a better matrix for supporting the PVAL molecules for self-repair than beeswax. Whether the polyethylene was better than beeswax because the PVAL had lower solubility in the nonpolar matrix or because the beeswax contained water-soluble components (low molecular weight components) that interfered with the PVAL polymerization process at the Cu surfaces (similar to the PEG) was not determined.

Consequently, these results show that the self-repairing PVAL component of a wiring insulation system can be present as an underlying coating formed from aqueous PVAL solutions or as suspended particles in a meltable, water-insoluble polymer.

## 2.5 MANUAL INSULATION REPAIR METHODS.

One type of well known insulation polymer for electric current carrying Cu wires is polyimide insulating material. Polyimide materials like Kapton® (®registered trademark of DuPont) have been a favorable choice as insulation material for electrical wiring inside aircraft due to its excellent properties of a low dielectric constant, high temperature resistance, etc. The weakness of polyimides is that they undergo ring openings in the presence of moisture and the hydrolysis lowers the mechanical strength of the damaged polymer. The penetration of moisture, cleaning solutions, oil, grease through the polyimide film and subsequent film degradation reactions reduce the polyimide's insulation properties over time resulting in a safety hazard. Mechanical deterioration of degraded polyimide further increases safety issues because of rubbing of wires on steel frames, unusual clamping or pinching of connectors or wire-to-wire abrasions and related factors. The effective maintenance of these wiring systems requires frequent inspections; wire stripping and rewiring techniques resulting in an enormous cost and extensive maintenance schedules and operational delays. Therefore, a need has emerged for a rapid curing liquid formulation to repair damaged polyimide insulation surfaces or to coat exposed metal conductors that produces an insulating film that exceeds the insulation properties of the original polyimide material.

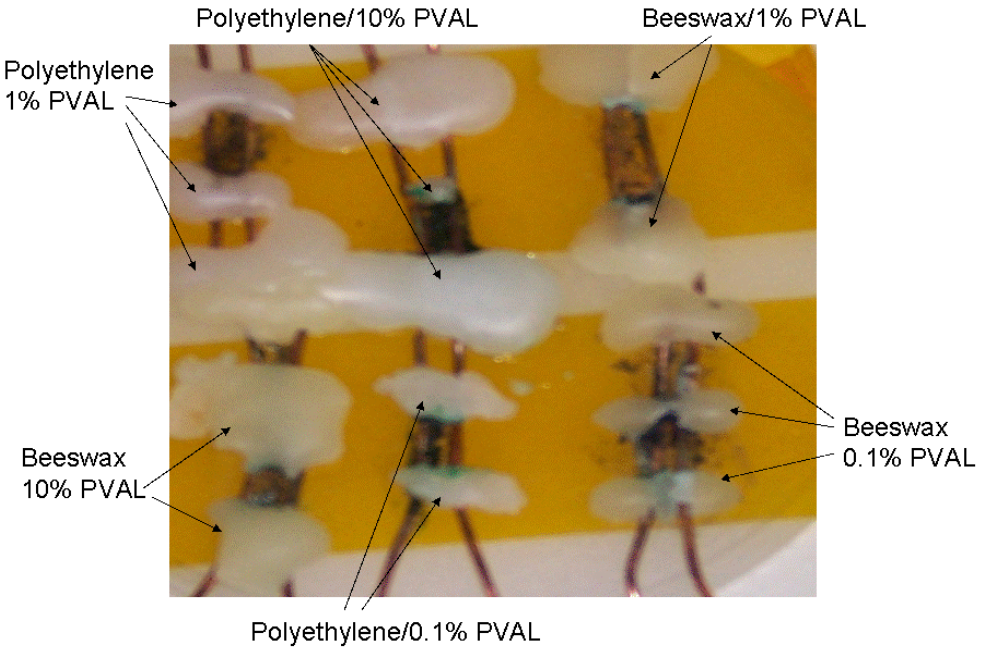


FIGURE 45. ELECTROLYSIS EXPERIMENTS WITH PVAL SUSPENDED IN WATER-INSULUBLE POLYMER MATRICES

Based on the chemical degradation mechanism of polyimides, chemical solutions were developed to rejuvenate areas of damaged polyimide insulation through chemical modification of the affected areas [1]. Additional formulations were developed in which polyimide resin and modifying compounds were dissolved in solvents to produce modified polyimide coatings with improved hydrolytic stability for repairing damaged insulation of any composition as well as exposed conductors.

2.5.1 Wire Coating Formulations.

The liquid insulation formulations previously developed to improve the hydrolytic stability of polyimides [1] were low viscosity and were evaluated by forming coatings on dipped Cu plates. Since the repair solutions are intended for wires with small diameters, research was performed to improve the viscosity characteristics of the liquid formulations. Also studies were performed to increase the application temperatures to decrease the polymer curing/solvent evaporating times of the liquid formulations.

Typical formulations had polyimide resin material dissolved in organic solvents as the base substrate. Siloxanes and fluoropolymers were dissolved with the polyimide in the organic solvent in various ratios. The maximum compound:resin ratio used was the highest ratio that still produced a clear solution without any particulate formation. The silanes used in the formulation to impart hydrophobicity to the formed polyimide film included diphenyl silane (DPS), isobutyltrimethoxy silane (IBTS), trichlorosilane (TCS) and polydimethylsiloxanes (PDMS). Fluoropolymers including polyvinyledene fluoride or trifluoroalkanes were also added to some of the polyimide resin solutions. In some of the cases, epoxy resin was added to the final formulation to improve the adhesion properties of the formed polyimide for Cu metal surfaces of different geometries, flat panel or round metallic wire.

To initially test the insulation repair capabilities of the modified polyimide solutions for wire applications, two standard hookup wires (M81381/11-20-9 “C”) with an aromatic polyimide jacket were damaged to partially or completely expose a polyimide tape (brown) wrapped around a metal conductor wire (white: Ag plated Cu) as shown in figure 46. When the damaged wire was coated with a polyimide resin:DPS in figure 46, the coating was adherent to the polyimide jacket, inner polyimide tape and exposed metal conductor. However, repeated bending produced cracks in the repair coating. The second damaged wire was coated with a polyimide resin:PDMS system. Again the modified polyimide film was adherent to all of the exposed surfaces of the damaged wire, but in contrast to the DPS system, the film remained intact after multiple bends as shown in figure 46. Therefore, the initial results indicate that the modified polyimide resin solutions are suitable for coating wires as well as flat surfaces and the adherence/flexibility of the modified polyimide coating can be defined by the silanes selected to modify the polyimide resin.

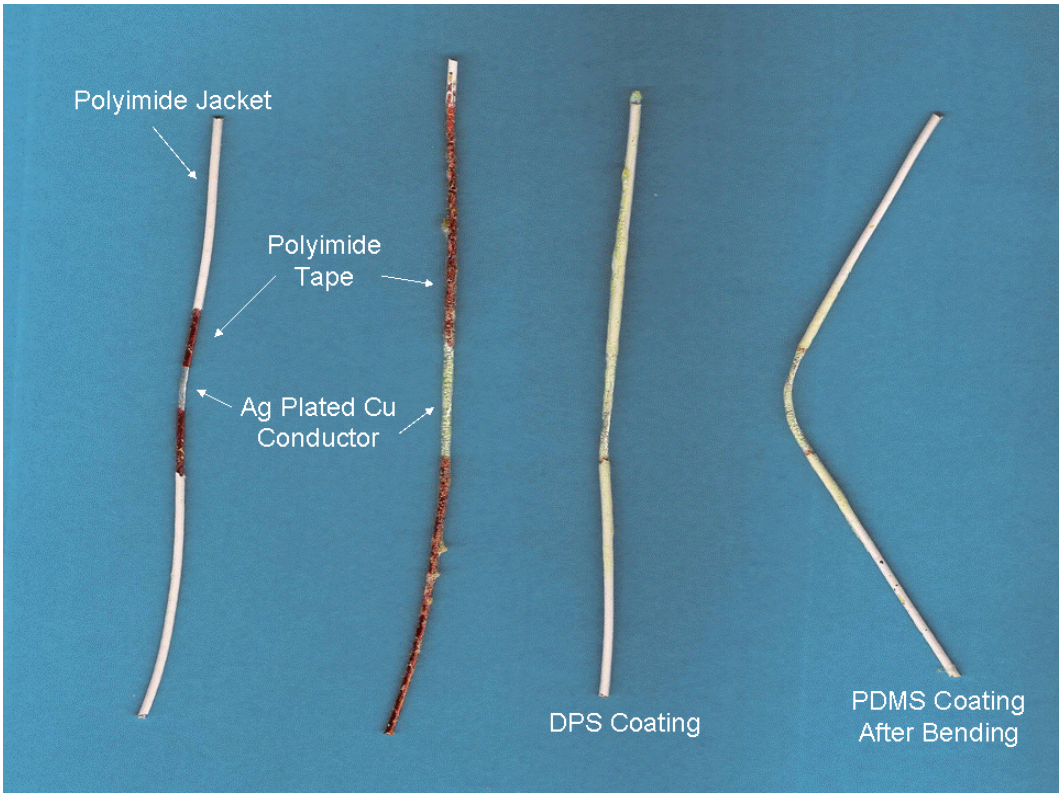


FIGURE 46. DAMAGED STANDARD HOOKUP WIRES BEFORE AND AFTER COATING WITH REPAIR SOLUTIONS

2.5.2 Temperature Studies.

For on-board maintenance actions, the application temperatures will need to be increased to decrease the polymer curing/solvent evaporating times of the liquid formulations for repairing wires with damaged insulation. Therefore, the effects of elevated (120ºC) temperatures on the characteristics of the modified polyimide films were studied. To decrease the curing time from hours to a few minutes, various formulations were investigated that employed different volatile solvents (more rapid solvent evaporation). However, adding more volatile solvents or different silanes made no appreciable difference in the curing times of the various coating formulations.

The primary evaluations of the produced insulation coatings were carried out by electrical impedance spectroscopy (EIS) measurements. Flat Cu panels of 3x3 inch size were coated with liquid insulation formulations using the dip coating method (Appendix C). Bare and polyimide insulated Cu wires were also coated with the same formulations. The coated panels/wires were held at room temperature for 1 hour to allow the solvents to evaporate (minimize pore formation) and then were heated at 60$^{o}$C for 2 hrs to fully cure the modified polyimide polymer.

Each Cu panel with an adherent/uniform coating was clamped to a standard paint cell which was then filled with aqueous 2% potassium hydroxide (KOH) solution for EIS studies (Appendix C). The electrical impedance of the coated panel immersed in KOH solution was scanned periodically for seven days to evaluate the short- and long-term hydrolytic stabilities of the coating. The higher the impedance (Zmod) of the coating during the first day of testing, the

better the insulating capabilities of the initial coating. The coatings with the best hydrolytic stability show the least changes in Zmod with reaction time and the highest Zmod at the end of the EIS experiment, i.e., a decrease in Zmod is indicative of KOH solution contact with the Cu surface due to polyimide film degradation resulting in increased film porosity.

2.5.2.1 Cu Panel EIS Stability Studies.

The first experiment was performed to determine the effects of adding PDMS to the polyimide resin in 1:1 and 1:2 ratios. The coated Cu panels, coatings approximately 1 mil (20 micron) thick, produced by the two formulations were immersed in 2% KOH solution and monitored by EIS for five days. The EIS spectra produced at 1, 3 and 5 days for the 1:1 and 1:2 polyimide to PDMS coatings (epoxy added to improve Cu surface adhesion) on Cu panels are shown in figures 47 and 48, respectively.

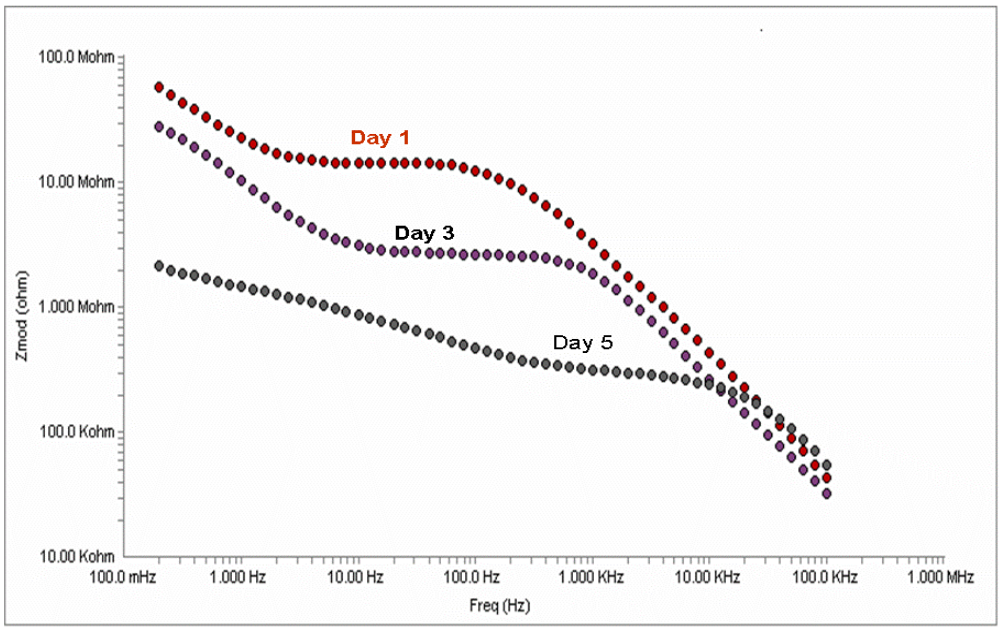


FIGURE 47. EIS SPECTRA OF 1:1 FORMULATION IN 2% KOH SOLUTION

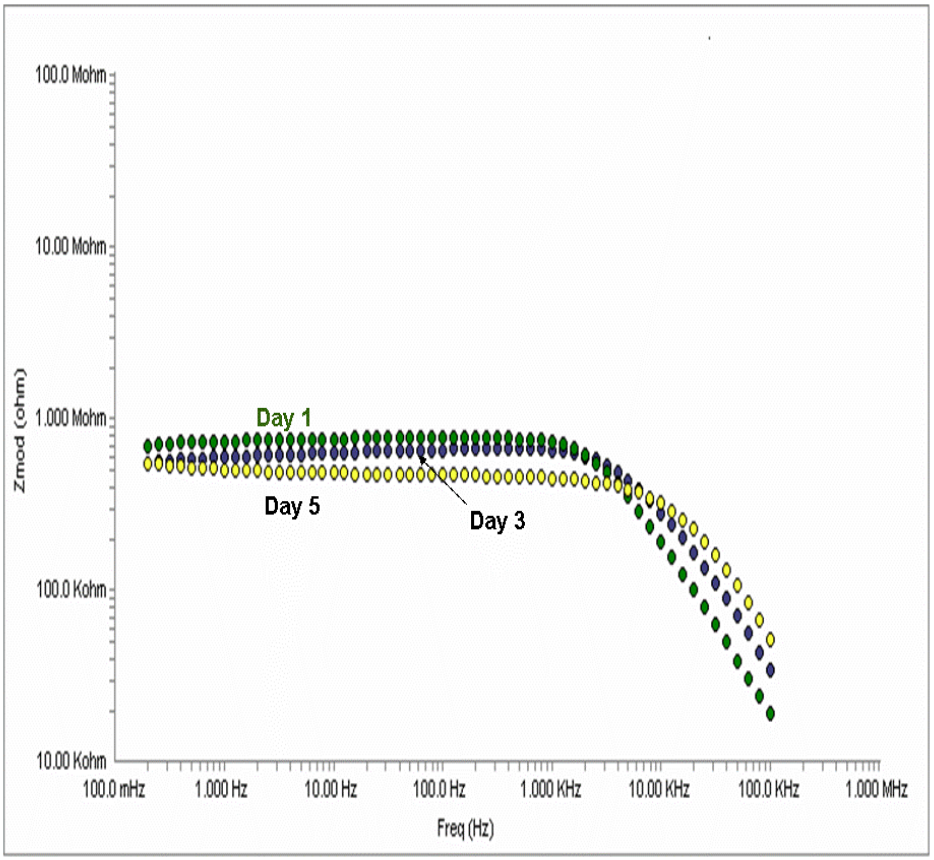


FIGURE 48: EIS SPECTRA OF 1:2 FORMULATION IN 2% KOH SOLUTION

For the polyimide:PDMS coatings on Cu panels, the Zmod measured at day 1 is much higher for the 1:1 formulation than for the 1:2 formulation. However, with exposure time to the 2% KOH solution, the 1:1 formulation degrades rapidly (Zmod decreases) while the 1:2 formulation is stable (Zmod unchanged). For the polyimide:PDMS formulations, increasing the PDMS concentration decreases the initial resistance, but greatly increases the hydrolytic stability, of the polyimide film.

Since elevated temperatures will shorten the polymer curing/solvent evaporating times of the modified polyimide coatings, the coatings produced on Cu panels with the 1:2 polyimide polymer:PDMS formulation (epoxy included) were heated at 120ºC for 2 days. After the extended heat treatment, the panels were exposed to 2% KOH solution in the EIS system for 7 days. The initial EIS spectrum and the EIS spectra of the heated panel recorded after 1, 3, 5 and 7 days of exposure to the 2% KOH solution are shown in figure 49. The initial EIS spectrum indicates that heating the polyimide coating at 120$^{o}$C develops some porosity in the film, presumably because of disorientation of polymer chains and driving off residual solvents in the film, allowing some 2% KOH solution penetration to the Cu surface. During the first day of 2% KOH solution exposure, the initial corrosion reactions insulate the Cu surface so that the EIS spectra of the 1:2 coatings in figures 48 (60ºC for 2 hours) and 49 (120ºC for 2 days) are very similar. However, the EIS spectra in figures 48 and 49 indicate that the hydrolytic stability of

the 1:2 coating is decreased by heating at 120ºC for 2 days, i.e., the EIS spectra of the unheated films are stable versus exposure time but decrease with time for the heated coatings.

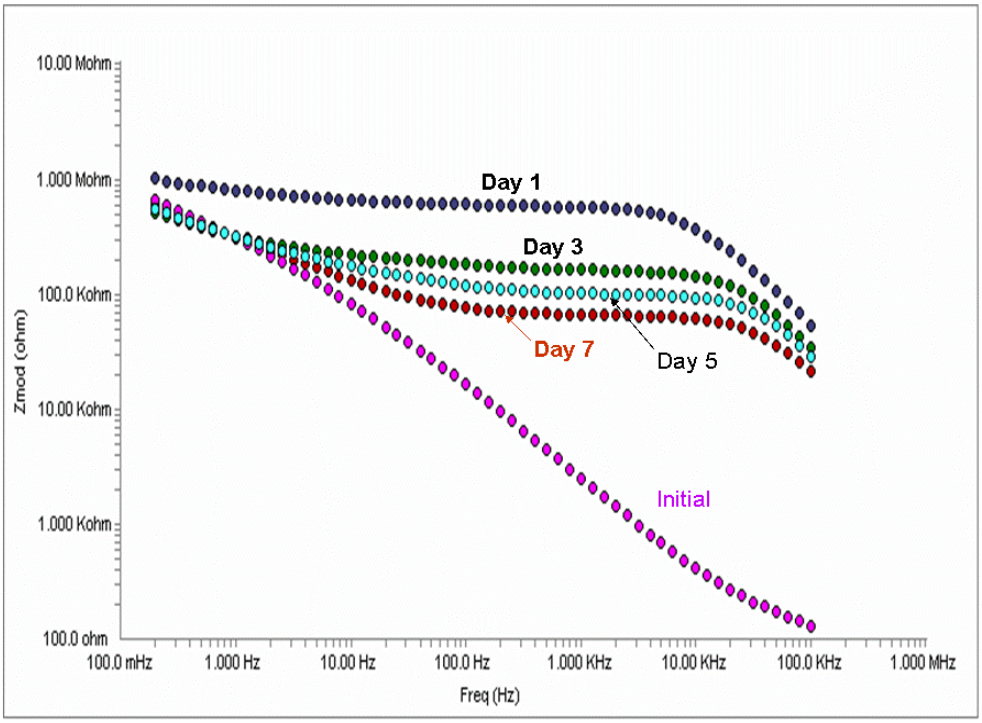


FIGURE 49. EIS SPECTRA OF HEATED 1:2 FORMULATION IN 2% KOH SOLUTION

2.5.2.2 Cu Wire EIS Stability Studies

In addition to the Cu panels, Cu wires were brush coated with polyimide formulations containing different silanes. The coated wires were held at ambient temperature for 1 hour to allow the solvents to evaporate (minimize pore formation) and then were heated at 60°C for 2 hrs to fully cure the modified polyimide polymer. The specimens were placed in an oven for 2 days at 120°C to evaluate the effects of elevated temperatures on the hydrolytic stabilities of different coating formulations. The paint cell of the EIS was modified to accommodate the coated wires (Zmod of panels and wires can not be compared). The initial EIS spectra of the Cu wires coated with the different formulations were recorded upon immersion in the 2% KOH solution as shown in figure 50.

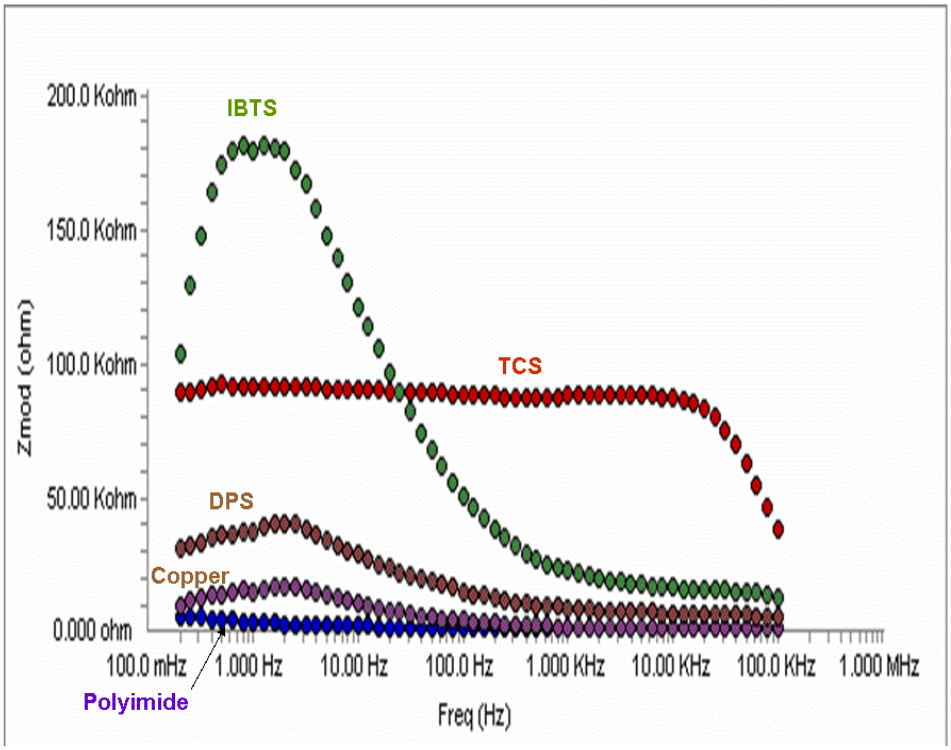


FIGURE 50. INITIAL EIS SPECTRA OF HEATED FORMULATIONS IN 2% KOH SOLUTION

Of the silanes tested in the polyimide coating formulations, isobutyltrimethoxy silane (IBTS) produces an EIS spectrum with the highest initial resistance with a maximum at the lower frequencies. Even though an initial EIS spectrum, trichlorosilane (TCS) produces a spectrum similar in shape to those in figure 48 (minimum number of pores to be inerted by initial corrosion reactions). Phenyl silane (DPS), which failed the bending test in figure 46, produces the initial EIS spectrum with the lowest resistance indicating a very poor coating and/or high number of pores.

In order to demonstrate the improvement in the hydrolytic stability of the polyimide resin by the silane modifications, the initial EIS spectra of the heated coating produced by polyimide (polyimide) without the addition of silanes and of a bare Cu wire (Cu) are also shown in figure 50. The EIS spectra indicate that under the severe conditions of the 2% KOH solution, the unmodified polyimide offers minimal protection for the Cu wire.

Consequently, the EIS spectra in figures 49 and 50 indicate that any of the silane modified polyimide formulations would provide magnitudes of order improvements in the hydrolytic stability of wiring insulation, even after heating at 120ºC for 2 days, compared to the original polyimide wiring insulations. The EIS spectra also indicate that the nature of the organic functional group on the silane backbone and the polyimide to silane formulation ratio both strongly affect the hydrolysis resistant properties of the modified polyimide coatings.

2.5.2.3 Cu Wire Visual Stability Tests.

In addition to the bare Cu panels and wires, polyimide insulated wiring was coated with the silane:polyimide formulations used for the EIS tests in figure 50 to visually evaluate the different formulations for use in repair solutions. The coated wires were heated in an oven at 120°C for 2 days and then immersed in 2% KOH for 2 days. Even though they were heated prior to the 2% KOH solution exposure, the insulated wires coated with the DPS and IBTS modified polyimides shown in figure 51 did not undergo hydrolysis when


FIGURE 51. PHOTOGRAPHS OF HEATED, COATED CU WIRES AFTER 2 DAYS IN 2% KOH SOLUTION.

compared to the insulated wire coated with the unmodified polyimide, i.e., underlying insulation apparent for unmodified polyimide, and possibly TCS modified polyimide, wires.

2.5.3 Resistivity Measurements.

Generally, resistivity of $10^{11}$ ohms and above is considered to be excellent for insulation material . Polyimide materials offer excellent resistivity when coated on Cu wirings. The resistivities of the modified polyimide insulation materials were measured by 2-point and concentric ring type of probes according to ASTM STD D-257. Polyimide tape wrapping materials were measured in the resistance range of $10^{-12}$-$10^{-15}$ ohms. Regardless of the modification to the polyimide, all of the liquid insulation coatings prepared in the laboratory have resistances equivalent to those of the polyimide tape or jacket materials of standard M81381 wires as listed in Table 3.

TABLE 3. SURFACE RESISTIVITY MEASUREMENTS

| Coatings Formulation | Surface Resistivity (ohms) |
|---|---|
| Aromatic Polyimide Jacket (Mil81381) | 8.7 E+12 |
| Polyimide tape (Mil81381) | 1.2 E+12 |
| Formulation Polyimide + silane | 1.10 E+13 |
| Formulation Polyimide + silane + epoxy | 1.56 E+13 |

## 2.6 CHARACTERIZATION OF WIRE "DIRT".

Before the self-repairing and manual repair methods can be used on aircraft wiring, the surfaces of the wires must be cleaned of any "dirt". To determine the composition of the "dirt" present on aircraft wiring, eight samples of wire "dirt" obtained from different locations of commercial aircraft and one sample of dryer lint were submitted by FAA personnel for analysis. The spectra produced by the thermal gravimetric analysis/simultaneous differential thermal analysis (TGA/SDTA) and Fourier Transform Infrared Spectrophotometry (FTIR) are presented in Appendix D. The wire "dirt" samples with the UDRI designation and aircraft location (if available) are listed in table 4.

TABLE 4. WIRE "DIRT" SAMPLES

| UDRI # | Sample Description | UDRI # | Sample Description |
|---|---|---|---|
| 1 | 747 - Projection | 6 | AC 4629 Zone 131 & 132 |
| 2 | 747 - Rear | 7 | Dryer Lint |
| 3 | 4006 12/05 | 8 | N429UA FGR 55 to 56 |
| 4 | AC 4626 AFT PIT | 9 | Ring Air Dirt |
| 5 | AC 4626 FWD PIT | | |

The TGA/DSC analyses were performed to evaluate the flammability potential of the "dirt" samples as well as their compositions through comparison with TGA/SDTA analyses of reference compounds such as dryer lint, cellulose (paper), nylon and wool.

### 2.6.1 TGA/SDTA Analyses.

Since the wire "dirt" samples appeared to be fibrous in nature, small pieces of cellulose and dryer lint were heated in air at a rate of 20ºC/minute from room temperature up to 600ºC using TGA/SDTA. The TGA plots in the Appendix D show that the cellulose undergoes a small (~5%) weight loss when heated from room temperature up to 250ºC (loss of water), and then from 250 to 350ºC, the cellulose decreases to 5% of its original weight. Finally, the cellulose undergoes its final weight loss from 350 - 500ºC leaving a clean pan (no residue). In similar fashion to the cellulose standard, the dryer lint undergoes a small (~5%) weight loss when heated from room temperature up to 250ºC (loss of water), and then from 250 to 350ºC, the lint decreases to 25% of its original weight (70% of lint is cellulose similar in structure to Kimwipe). The dryer lint undergoes a second weight loss from 350 - 500ºC decreasing to ~5% of its original weight [different type of cellulose or different type of material] and does not undergo further

weight loss up to 600ºC leaving a residue in the pan. The dryer lint underwent a similar weight loss when the TGA was performed in nitrogen, i.e., thermal degradation of polymers into volatile species is mainly responsible for the weight losses of the TGA analyses.

Also shown in Appendix D are the SDTA plots for the cellulose and dryer lint TGA tests. For cellulose, there is a strong (sample pan increases 20ºC in comparison to reference pan), sharp exotherm that occurs during the rapid weight loss that occurs from 250 to 350ºC. A small (1ºC rise), sharp exotherm occurs when the final weight loss occurs between from 350 to 500ºC. In contrast to the cellulose SDTA plot, the dryer lint plot only has two small (1ºC), broader exotherms accompanying the large weight losses during the TGA test. When run in nitrogen, the dryer lint undergoes a very slow, broad exotherm that causes the sample pan to increase 5ºC during the test. These results indicate that the cellulose and dryer lint are undergoing oxidation reactions when heated in air, in addition to the thermal degradation reactions, and that in the case of the cellulose, the oxidation reactions are highly exothermic, indicating combustion is possible.

Of the different wire samples, the sample 8 TGA/SDTA plots in air (Appendix D) are the most similar to the cellulose standard, i.e., Sample 8 loses ~75% of its weight by 320ºC and produces a strong, sharp exotherm similar to cellulose plot. The primary difference is sample 8 produces a residue in air (10% of weight) indicating the presence of other materials (inorganics, other organic materials). In nitrogen, the residue increases to over 20% of the original amount (residue for dryer lint was ~5%, regardless of environment).

Since wool is used in airliner flooring and seat covers, pieces of wool were tested in air. In air, wool loses 40% of its weight prior to 350ºC then loses the final 60% of its weight by 500ºC producing a clean pan (no visible residue). In contrast to the cellulose sample, the wool produces a weak, broad exotherm at 350ºC followed by a strong, sharp exotherm at 490ºC corresponding with the 60% weight loss. In nitrogen, wool has a 60% weight loss by 400ºC but above 400ºC the weight loss rate slows leaving a large residue corresponding to 25% of the sample's original weight. The wool in nitrogen produces a very slow, broad exotherm that causes the sample pan to increase 4ºC during the test. These results indicate the first weight loss in air or nitrogen is due to thermal degradation of the wool while the second weight loss in air occurs due to oxidation of the remaining carbon based residue (in nitrogen wool carbonizes similar to polyimide carbon tracking).

Samples 5 and 6 (different aircraft) appear to be a combination of the cellulose and wool samples. In air, samples 5 and 6 undergo a 50% weight loss by 320ºC accompanied by a sharp exotherm and then undergo a rapid weight loss at 500ºC accompanied by a second sharp exotherm. As opposed to cellulose or wool, the residues are 15% in air (inorganics, other organic materials). In agreement with wool, the residues increase to 30% in nitrogen. Presence of wool could also explain increase in residue amount for sample 8 in nitrogen.

Samples 1-4 in Appendix D, all undergo 50% weight loss by 320ºC (cellulose), a rapid, small weight loss around 500ºC (wool), both weight losses are accompanied by small, distinct exotherms and the produced residues are ~10% of the original sample weight. However, the residue amounts do not increase for samples 1 and 4 when the tests are run in nitrogen. Also, SDTA plots of samples 1, 2 and 4 contain an exotherm that is 50ºC higher than the wool exotherm.

Sample 9 is similar to samples 1 – 4 except the weight loss is lower occurring by 350ºC, the exotherms are smaller in size, and the % residue is 30% regardless of the environment (indicates higher amount of inorganics).

2.6.2 SEM/EDS Analyses.

Since the TGA data indicated the samples contained inorganics (residues 10 - 30% of original weights), the original fibers and TGA residues of the fibers were analyzed by SEM/EDS. The SEM photographs in Appendix D show that the samples consist of a wide assortment of fibers. The EDS analyses of the fibers indicate that carbon and oxygen make up 96 – 98% of the sample indicating that inorganics make up only 2 – 4% of the sample. Of the inorganics present in the ash, aluminum, calcium, oxygen, potassium, silicon and sodium total ~ 80 -90% indicating sand, clays, and other dirt species make up the majority of the residue. The EDS analyses of the sample ashes also show that sulfur (~4%) is present in all of the residues indicating that oxidized hairs, wool and other natural fibers (carbon peak minimal) probably make up the remainder of the residue.

2.6.3 Pyrolysis Fourier Transform Infrared Spectrophotometry (FTIR).

In pyrolysis FTIR, the sample is placed into the bottom of an open test tube and the test tube is heated using the flame of a Bunsen burner until a residue condenses on the upper inside surfaces of test tube. The FTIR spectra of the cellulose sample prepared as a potassium bromide (KBr) pellet (no heating involved) and the residue produced by pyrolysis shown in Appendix D are very similar except that the pyrolysis residue spectra contains a much stronger peak at 1700 $cm^{-1}$ (indicates residue contains oxidation products since heated in open tube).

In contrast to the cellulose sample, the KBR pellet and pyrolysis residue spectra of sample 5 in Appendix D are quiet different. The KBR pellet has much larger peaks at 3400 and 1100 $cm^{-1}$ indicative of cellulose while the pyrolysis has stronger peaks at 1700 $cm^{-1}$ indicative of oxidation or a carbonyl containing compound such as nylon or urethane. So the FTIR spectra indicate that the cellulose content of the pyrolysis condensation residue is lower than that of the original sample and that oxidation occurs during the pyrolysis process or the concentration of another compound is increased. The increase in the peak at 2900 $cm^{-1}$ indicates that the residue has a higher alkyl ($CH_x$) content most likely due to the concentration increase of another compound such as nylon in the residue.

The pyrolysis spectra for cellulose and dryer lint in Appendix D are very similar indicating the lint is primarily cellulose in agreement with the TGA data in slide 1. The pyrolysis spectra of sample 8, cellulose and wool indicate that sample 8 is similar to wool but contains some of the characteristics of cellulose (smaller peak at 1700 $cm^{-1}$ but larger peak at 1100 $cm^{-1}$). The pyrolysis spectra of samples 3 – 5 in Appendix D are very similar to the wool spectrum indicating the samples contain a higher amount of wool than sample 8 in agreement with the TGA plots in Appendix D.

To determine the thermal characteristics of the pyrolysis residues, the pyrolysis residue of sample 6 was run on the TGA/STDA system in air as shown in Appendix D. The TGA plot shows the residue undergoes 80% weight loss up to 350ºC (expected since residue composed of

condensed volatile compounds) accompanied by a small exotherm followed by continuous weight loss up to 600ºC accompanied by a second small exotherm at 550ºC. The TGA residue was less than 5% (no inorganics since residue condensed volatiles) of the original amount added.

2.6.4 Nylon Presence.

In an attempt to find a possible compound to explain the peak at 2900 $cm^{-1}$, polyester and polyurethane compounds were analyzed by TGA/SDTA and pyrolysis FTIR but did not produce the peaks in the required areas of the FTIR spectrum. Nylon 6,6 which is used with wool, did produce strong peaks at 2900 and 1700 $cm^{-1}$ as well as reinforced the peak at 3200 $cm^{-1}$ as shown in Appendix D. Also the nylon produced TGA/SDTA plots that agreed well with those produced by the wire dirt samples.

2.6.5 Summary of "Dirt" Analyses.

The analyses indicate that the wire dirt samples are basically organic in nature with a small amount of inorganics present (Sample 9 has the highest amount of inorganics). The organics consist of cellulose (Rayon or natural fiber such as cotton, paper, etc.), wool and probably nylon. The dryer lint is primarily cellulose and so only is a partial match for Sample 8 which has the highest (75%) cellulose content of the wire dirt samples. The rest of the dirt samples are ~50% cellulose. Looking at the TGA and FTIR results, its interesting the compositions of the different samples are so similar even though they were sampled from different parts of different planes, i.e., appears wire dirt has common source regardless of aircraft or location.

The cellulose would support combustion directly (fuel) and indirectly (decomposition products are combustible gases such as hydrogen, methane, etc.). The wool and nylon, if present, would support combustion through the formation of combustible gases/volatile fragments and carbon-like residues.

2.7 SUMMARY.

The manual repair technique was based on easy to apply solutions containing volatile solvents that produced a hydrophobic, modified polyimide film capable of filling microcracks/gouges as well as reconditioning degraded Kapton® surfaces. The viscosity of the repair solution and curing temperatures were modified for coating wires in an attempt to develop a methodology better-suited for maintenance actions. Longer term heating studies were also performed to evaluate the effects of temperature on the stability of the repair films. The research again showed that EIS was a more effective analysis tool than FTIR or visual observations for evaluating the hydrolysis resistance of the different modified polyimide surfaces.

As opposed to the solvent based manual repair techniques, the self-repairing solutions are water based and the low toxicity of PVAL is demonstrated by the fact that it is used in eye drops, school paste and other consumer goods. Water sprays or condensed water allow detection of remote wire bundles with damaged insulation through detection of the generated RF by hand-held, directional devices inside the compartment or by non-directional, portable antennas from outside the aircraft. Low concentrations of salts or stable emulsions must be added to the distilled water solutions of PVAL to produce water insoluble films on the exposed, powered

conductor. Modifications of the PVAL molecular structure or increases in the degree of hydrolysis or molecular weight of the unmodified PVAL had detrimental effects on the water-insoluble film formation. In addition to water based coating methods, electrical wiring with the capability to perform self-repair of damaged insulation was developed using water-insoluble, organic films containing low concentrations of suspended PVAL particles. Based on the success of the research a patent was filed on the self-repairing wire concept and initial discussions to commercialize the concept were initiated with companies involved in PVAL products.

The analyses of the submitted wire dirt samples indicate they are basically organic fibers with a small amount of inorganics present and so would not require special/chemical cleaning methods for removal prior to applying the repairing solutions. In fact, the wire "dirt" layer may act as a water/solution reservoir for the aqueous self-repairing solutions. The organics consist of cellulose (50 – 80). The compositions of the different samples were similar even though they were sampled from different parts of different planes, i.e., appears wire "dirt" has common source regardless of aircraft or location.

The cellulose would support combustion directly (fuel) and indirectly (decomposition products are combustible gases such as hydrogen, methane, etc.). The wool and nylon, if present, would support combustion through the formation of combustible gases/volatile fragments and carbon-like residues.

## 3. TECHNIQUES TO MONITOR SUPPORT AND CONNECTOR FAILURES IN AIRCRAFT EWIS

During the lifetime of an aircraft, the different components of the EWIS experience a wide range of physical and chemical stresses. Vibration, abrasion, hydrolysis, fatigue, thermal decomposition and chemical reactions combine to degrade the performance of wiring insulation, clamps and connectors. The deterioration and breaking of clamps results in excessive vibration and increased rubbing further accelerating the rates of insulation and connector degradation. Once degradation of the wiring insulation allows the ingression of moisture, chemicals and gaseous pollutants, the resulting corrosion of the connectors increases the potential for control malfunctions, dry and wet arcing, conduit burn through and damage to control cables and linkages. The increase in connector resistance due to corrosion and metal surface separation further reduces the signal-to-noise ratios in low-power avionics and increases the risk of local heating and fire hazards in high-power circuits.

The research to detect excessive harness vibration levels due to support failure identified and evaluated the capabilities of triboelectric and piezoelectric sensors to detect an increase in wire harness vibration levels when clamps and ties were removed from wire bundles undergoing vibrational testing. Based on the initial findings, a vibration monitoring system and circuit to analyze the system output was constructed based on a piezoelectric cable. During vibration tests performed to simulate flight vibration, the circuit acquired vibration data on a continuous basis during each simulated flight and then calculated a statistical baseline for specific frequency bins. The circuit detected clamp breakage and other support failures based on abrupt and permanent changes in the baseline vibrational characteristics of wire bundles containing wiring of different or similar gauges. The circuit was able to detect excessive vibration either when attached to (retrofit) or incorporated in (future) the wire harness.

To be suitable for measuring the corrosion degradation occurring inside an electrical connector, the technique must be performed without opening the connector. The researched techniques were evaluated using experimentally simulated partial pin contact, lumped impedance changes and corrosion at the connector. Of the different techniques researched to date, the method based on the propagation of continuous electromagnetic signals through the connector and determining the differences in the induced electromagnetic signals measured on both sides of the connector appears to have the best potential for success. The results also indicate that impedance measurements and analysis will most likely be more sensitive to connector corrosive degradation than simple contact resistance measurements

To compliment the remote vibration research, research to develop a smart clamp was initiated during the project. By developing a smart clamp with prognostic/diagnostic capabilities, maintenance personnel can be alerted to imminent/recent support failure so that insulation damage resulting from the unrestricted movement of unsupported wiring bundles can be avoided. Two different types of smart clamps were investigated: sensing capability incorporated directly into clamp versus sensing capability built into a small film/compartment adhered to the wiring/clamp/tie prior to applying support. A smart rattle was also investigated as a simple sensor that is able to differentiate between supported, vibrating wires and unsupported, swaying wires.

## 3.1 REMOTE VIBRATION DETECTION: PIEZO CABLE CHARACTERIZATION.

Gaining more knowledge about the capabilities and limitations of the piezoelectric cable would provide a better understanding of how best to implement this technology. It was recommended a research effort be conducted to address the following issues:

- Investigate the effect on the cable to varying random and sine acceleration levels as above while varying the length (12.5 inches or 25 inches), by the positioning of attachments (3 or 2).

- Evaluate the cable response to varying random and sine acceleration levels when bent or curved, at the same lengths.

- Testing of piezo cable was performed using equipment, fixtures, conditioning circuitry, and vibration profiles as described in Appendices A.1 and A.2.

### 3.1.1 Random Profiles-Straight Cables

Initial testing of the random profiles covered piezo cable sensitivity settings ranging from 1 mV/g to 1500 mV/g. The piezo cable overloaded at all sensitivities under 50 mV/g and the response was effectively zero over 500 mV/g. Therefore, analysis was performed at piezo cable sensitivities between 50 mV/g and 500 mV/g.

During the past month, research continued based on a new test plan in which an accelerometer was added to the test set-up to control the vibration input during the piezo cable vibrational tests. Initial reporting of results follows.

To evaluate the effects of piezo cable positioning, the remote vibration detection research was performed with the piezo cable positioned either on the top or side of the aluminum fixture (1" x 13" x 25") which was bolted to the vibration table. The cable positioning tests were repeated several times using three random profiles (C, C1 and C2) and acceleration levels ranging from 4 – 8.5g. The piezo cable was attached to the aluminum fixture (Appendix E) using three attachments positioned at 12.5" intervals. Clamp failure was simulated in the tests by removing the center attachment effectively increasing the length of the vibrating cable from 12.5" to 25".

When the piezo cable was located on the side of the fixture and the length of cable was increased from 12.5" to 25" by removing the center attachment, a significant increase in acceleration was exhibited at the lower vibration frequencies with all three random profiles (C, C1, and C2). To provide the vibration detector with the ability to ignore vibrations with minimal acceleration (normal movement), the piezo cable signal conditioning board was set to different sensitivities. When the piezo sensitivities were set to ignore signals below 50 - 100 mV/g (calibrated board converts mV into acceleration), the acceleration feedback of the cable was overloaded for the majority of the tests (overload in Table 5). However, when the piezo sensitivity was set at 500 mV/g, the signal conditioning board did not detect any signals above the input acceleration (<g rms input in Table 5) for the majority of the tests. Consequently, sensitivity values of 150 - 250 mV/g are the preferred settings in Table 5 since they produce the highest possible maximum acceleration signal without overloading the system in Table 5.

Although the input acceleration levels ranged between 4 – 8.5 g RMS for the different random profiles (4 for profile C, 6 for profile C1 and 8.5 for profile C2), the signal output of the cable was basically unaffected by the input acceleration level, e.g., test side 2 results in the 150 mV/g column are basically the same for profiles C, C1 and C2. However, the data in Table 1 does demonstrate that cable position and number of attachments have a large effect on the maximum acceleration results. For the cables attached to the side of the fixture, the maximum acceleration test results are always larger for the cables with an attachment removed (side 2 rows in table 1) than for the shorter cables with all three attachments in place (side 3 rows). The signal maxima generated with attachments removed are always higher for the cables on the side of the fixture than those with the cable on top. With the cable on top, the removal of attachments had an inconsistent effect on the measured acceleration maxima.

TABLE 5. RANDOM PROFILE MAXIMUM ACCELERATION TEST RESULTS.

| Random max $g^2$/Hz | Piezo set at 50 mV/g | Piezo set at 100 mV/g | Piezo set at 150 mV/g | Piezo set at 200 mV/g | Piezo set at 250 mV/g | Piezo set at 500 mV/g |
|---|---|---|---|---|---|---|
| **test C top full** | 5.91 | 0.73 | < g rms input | < g rms input | < g rms input | < g rms input |
| **test C top 3** | overload | 1.29 | 0.91 | 0.39 | < g rms input | < g rms input |
| **test C top 2** | overload | 2.56 | 1.18 | 0.82 | < g rms input | < g rms input |
| **test C side 3** | overload | overload | 19.23 | 11.13 | 6.63 | 1.93 |
| | overload | overload | 24.09 | 4.67 | 2.73 | not run |
| **test C side 2** | overload | overload | 83.52 | 22.65 | 17.09 | 2.39 |
| | overload | overload | 96.05 | 19.60 | 10.41 | not run |
| **test C curve A & B side 3** | not run | not run | 2.34 | 1.24 | 0.79 | not run |
| **test C curve A side 2** | not run | not run | < g rms input | < g rms input | < g rms input | not run |
| **test C curve B side 2** | not run | not run | 21.73 | 7.31 | 6.76 | not run |
| | | | | | | |
| **test C1 top full** | overload | 5.91 | 8.59 | 2.60 | 1.73 | < g rms input |
| **test C1 top 3** | overload | overload | 12.64 | 7.04 | 4.77 | < g rms input |
| **test C1 top 2** | overload | overload | 10.42 | 4.15 | 5.67 | < g rms input |
| **test C1 side 3** | overload | overload | 13.57 | 10.74 | 6.40 | 2.68 |
| | overload | overload | 17.32 | 13.16 | 8.03 | not run |
| **test C1 side 2** | overload | overload | 57.23 | 21.41 | 11.36 | 2.01 |
| | overload | overload | 86.28 | 42.76 | 28.62 | not run |
| **test C1 curve A & B side 3** | not run | not run | 10.91 | 5.51 | 3.06 | not run |
| **test C1 curve A side 2** | not run | not run | < g rms input | < g rms input | < g rms input | not run |
| **test C1 curve B side 2** | not run | not run | 33.92 | 13.55 | 9.31 | not run |
| | | | | | | |
| **test C2 top full** | overload | overload | 21.93 | 9.63 | 5.52 | 1.69 |
| **test C2 top 3** | overload | overload | overload | 25.94 | 13.80 | 3.74 |
| **test C2 top 2** | overload | overload | overload | 29.42 | 5.16 | 4.38 |
| **test C2 side 3** | overload | overload | 54.15 | 14.60 | 8.48 | 2.16 |
| | overload | overload | 34.47 | 24.77 | 19.46 | not run |
| **test C2 side 2** | overload | overload | 88.71 | 27.46 | 17.99 | 2.82 |
| | overload | overload | 109.00 | 43.75 | 33.40 | not run |
| **test C2 curve & B side 3** | not run | not run | 23.27 | 10.39 | 6.87 | not run |
| **test C2 curve A side 2** | not run | not run | < g rms input | < g rms input | < g rms input | not run |
| **test C2 curve B side 2** | not run | not run | 28.05 | 28.00 | 15.05 | not run |

To expand on the data in table 1, the relative magnitude of acceleration was plotted versus frequency (converted from bins) for each test run. Representative acceleration versus frequency plots for the random profile C2 with the 8.5 g rms input acceleration for the piezo cable attached to the side and top of the fixture, respectively, are shown in figures 52 and 53 (R in legend stands for repeat). All other graphs are in the Appendix E. Although the input acceleration levels ranged between 4 – 8.5 g RMS for the different random profiles (4 for profile C, 6 for profile C1 and 8.5 for profile C2), the signal output of the cable was basically unaffected by the input acceleration level, e.g., test side 2 results in the 150 mV/g column are basically the same for profiles C, C1 and C2. However, the data in Table 1 does demonstrate that cable position and number of attachments have a large effect on the maximum acceleration results. For the cables attached to the side of the fixture, the maximum acceleration test results are always larger for the cables with an attachment removed (side 2 rows in table 1) than for the shorter cables with all three attachments in place (side 3 rows). The signal maxima generated with attachments removed are always higher for the cables on the side of the fixture than those with the cable on top. With the cable on top, the removal of attachments had an inconsistent effect on the measured acceleration maxima.

The vibration C2 profiles in Figure 52 illustrate that the maximum accelerations for the cable on the side of the fixture occur at a higher magnitude and lower frequency for the cable with 2 attachments (broken clamp) than those for the cable with 3 attachments. The vibration profiles in Figure 53 demonstrate there is only a small difference in the magnitude or frequency of the maximum acceleration results for the cable attached to the top of the fixture. To summarize the relative magnitude of acceleration versus frequency plots for the performed tests, the frequency of the maximum acceleration response for each test is listed in Table 6.

Regardless of the cable length (full 2 vs. 3 attachments) attached to the top of the fixture, the frequency of the maximum frequency was very low (2-6 Hz). In contrast to the top of fixture data, the cable length attached to the side of the fixture had a strong effect on the maximum acceleration frequencies regardless of the input acceleration [only frequency studied in previous work (1)]. For each random profile, the frequency of the maximum acceleration for the side tests with two attachments was between 12 to 22 Hz, with the majority of the maxima at 12 or 14 Hz. The maximum acceleration frequencies for the side test results with 3 attachments had a larger range (4 to 58 Hz) and there was no one particular frequency at which the majority of the maximum acceleration values occurred.

In an effort to optimize the capability of the signal conditioning board to detect clamp failure, the acceleration values of the 25 and 12.5" length cables were recorded for each test at the frequency at which the 25" cable acceleration maximum occurred. Then the acceleration value for the 25" cable (maximum) was divided by the 12.5" acceleration value (may or may not be maximum) to produce a ratio that would take into account vibrational changes in both frequency and acceleration of wire bundles experiencing clamp failure. The ratios calculated for all of the cable position vibrational tests are listed in Table 7 (ratio of 1: no change detected).

Regardless of the random profile (C, C1 and C2) used for the vibration test, all of the tests using the 150 – 250 mV/g sensitivity and the cable attached to the side of the fixture produce ratios well above 1 (3 – 59) indicating a high sensitivity to cable length, and consequently, clamp failure. Not surprisingly, the ratios for all of the tests with the cable attached to the top of the fixture were approximately 1 since the acceleration values and frequencies of maximum frequency were independent of cable length.

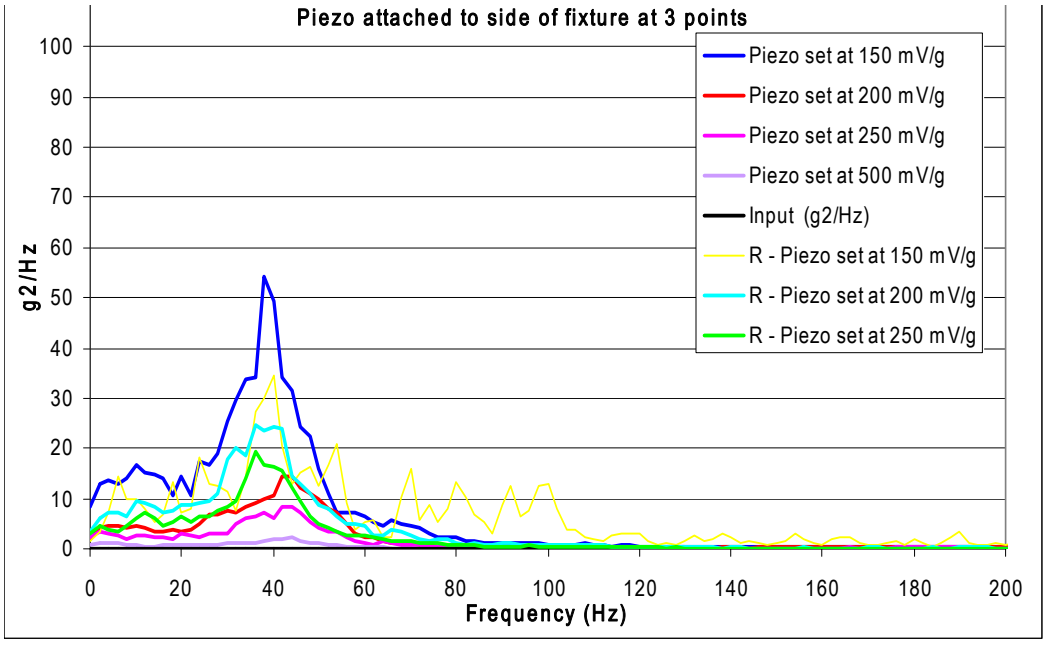


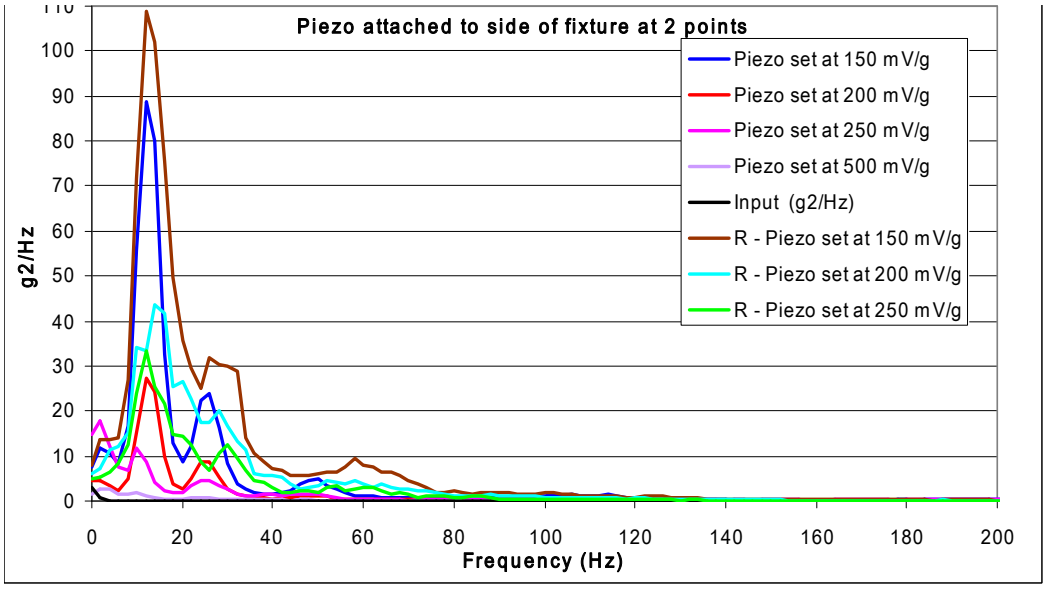


FIGURE 52. C2 RANDOM PROFILE TEST GRAPHS FOR PIEZO CABLES POSITIONED ON THE SIDE OF THE FIXTURE.

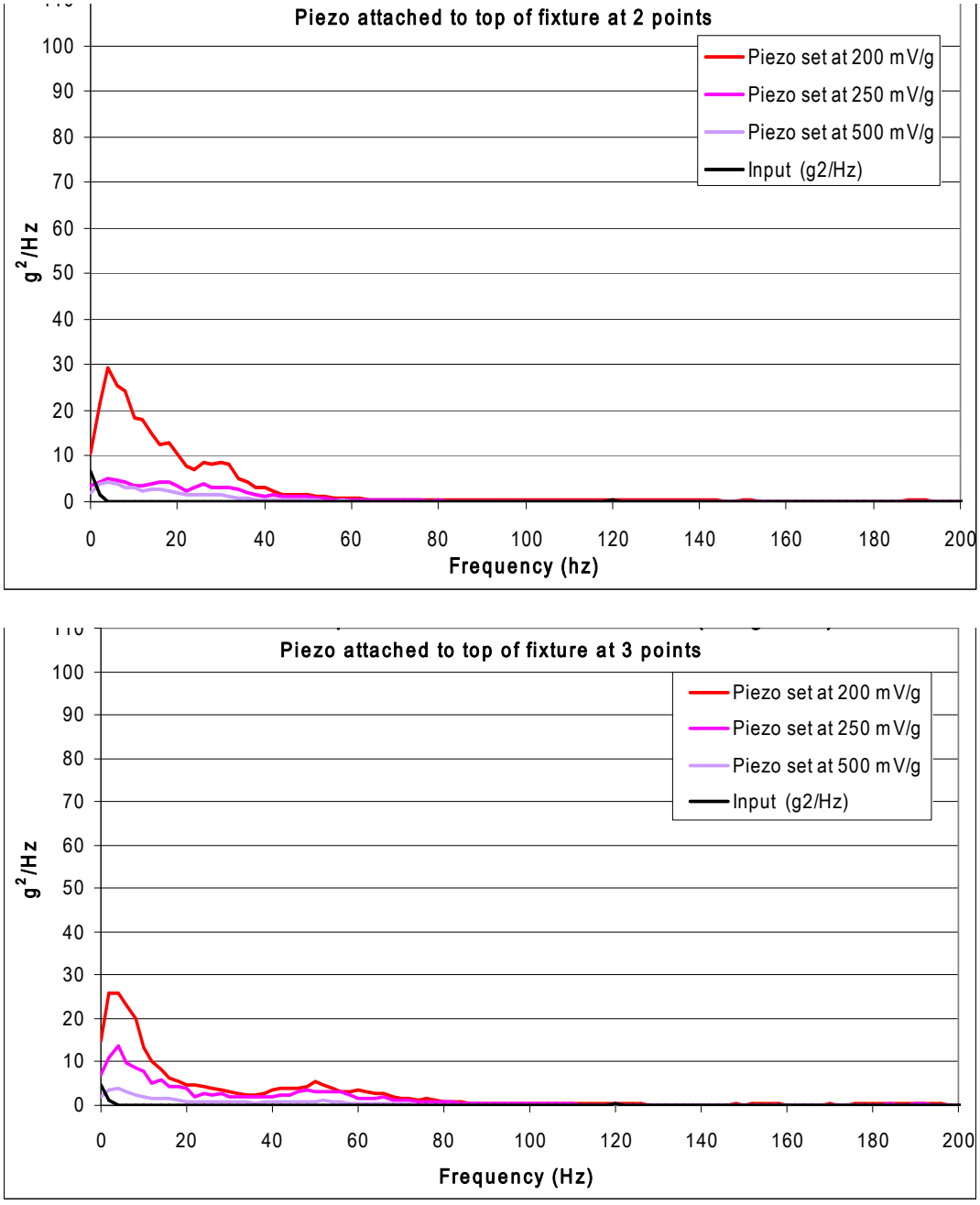


FIGURE 53. C2 RANDOM PROFILE TEST GRAPHS FOR PIEZO CABLES POSITIONED ON TOP OF THE FIXTURE.

TABLE 6. RANDOM PROFILE FREQUENCY LOCATIONS OF MAXIMUM ACCELERATION

| Random at Frequency | Piezo set at 50 mV/g | Piezo set at 100 mV/g | Piezo set at 150 mV/g | Piezo set at 200 mV/g | Piezo set at 250 mV/g | Piezo set at 500 mV/g |
|---|---|---|---|---|---|---|
| **test C top full** | 4 | 6 | < g rms input | < g rms input | < g rms input | < g rms input |
| **test C top 3** | overload | 62 | 4 | 6 | < g rms input | < g rms input |
| **test C top 2** | overload | 2 | 4 | 4 | < g rms input | < g rms input |
| **test C side 3** | overload | overload | 26 | 50 | 22 | 16 |
| | overload | overload | 52 | 58 | 58 | not run |
| **test C side 2** | overload | overload | 14 | 12 | 14 | 14 |
| | overload | overload | 22 | 22 | 22 | not run |
| **test C curve A & B side 3** | not run | not run | 4 | 52 | 48 | not run |
| **test C curve A side 2** | not run | not run | < g rms input | < g rms input | < g rms input | not run |
| **test C curve B side 2** | not run | not run | 2 | 2 | 2 | not run |
| | | | | | | |
| **test C1 top full** | overload | 4 | 4 | 4 | 4 | < g rms input |
| **test C1 top 3** | overload | overload | 2 | 4 | 4 | < g rms input |
| **test C1 top 2** | overload | overload | 4 | 6 | 6 | < g rms input |
| **test C1 side 3** | overload | overload | 4 | 4 | 4 | 4 |
| | overload | overload | 52 | 54 | 52 | not run |
| **test C1 side 2** | overload | overload | 12 | 12 | 14 | 2 |
| | overload | overload | 12 | 12 | 14 | not run |
| **test C1 curve A & B side 3** | not run | not run | 6 | 4 | 6 | not run |
| **test C1 curve A side 2** | not run | not run | < g rms input | < g rms input | < g rms input | not run |
| **test C1 curve B side 2** | not run | not run | 2 | 2 | 2 | not run |
| | | | | | | |
| **test C2 top full** | overload | overload | 4 | 4 | 2 | 2 |
| **test C2 top 3** | overload | overload | overload | 4 | 4 | 4 |
| **test C2 top 2** | overload | overload | overload | 4 | 4 | 4 |
| **test C2 side 3** | overload | overload | 38 | 44 | 44 | 44 |
| | overload | overload | 40 | 36 | 36 | not run |
| **test C2 side 2** | overload | overload | 12 | 12 | 2 | 4 |
| | overload | overload | 12 | 14 | 12 | not run |
| **test C2 curve A & B side 3** | not run | not run | 6 | 4 | 4 | not run |
| **test C2 curve A side 2** | not run | not run | < g rms input | < g rms input | < g rms input | not run |
| **test C2 curve B side 2** | not run | not run | 2 | 2 | 2 | not run |

3.1.2 Random Profiles - Curved Cables.

To test the effects of curvature on the vibration sensing of the piezo cable, two curve directions were tested on the side of the fixture. Curve A was in a vertical direction and curve B was horizontal as shown in Figure 54. The cable responses of curves A and B were essentially identical at 12.5" (3 attachments) for all input levels in Table 5 with the measured acceleration increasing with the input for profiles C to C2. Curve A results at the 25" length (2 attachments) showed no amplification of acceleration, i.e., did not detect any signals above the input acceleration (<g rms input in Table 5). This implies that loss of clamps in aircraft areas with wiring configurations similar to curve A (i.e. parallel to the direction of vibration) may not be detectable. Curve B results at the 25" length (2 attachments) increased, as the input increased, but there were two distinct frequencies. For curve B the acceleration levels were only slightly higher than the 12.5" lengths (3 attachments) at the lower frequency but were higher by a factor of 2 – 3 at the higher frequency as shown in figure 55. All other graphs are in the Appendix E. A lower piezo sensitivity setting would provide a better signal for curved wiring but the ability to monitor other situations would be lost due to overloading of the signal.

TABLE 7. RANDOM PROFILE RATIOS OF MAXIMUM ACCELERATION TEST RESULTS

| Random ratio of 2 vs 3 | Piezo set at 50 mV/g | Piezo set at 100 mV/g | Piezo set at 150 mV/g | Piezo set at 200 mV/g | Piezo set at 250 mV/g | Piezo set at 500 mV/g |
|---|---|---|---|---|---|---|
| **test C top** | overload | 3.09 | 1.30 | 2.36 | < g rms input | < g rms input |
| **test C1 top** | overload | overload | 0.95 | 1.10 | 1.59 | < g rms input |
| **test C2 top** | overload | overload | overload | 1.13 | 0.37 | 1.17 |
| **test C side** | overload | overload | 13.14 | 7.39 | 3.74 | 1.72 |
| | overload | overload | 58.98 | 50.54 | 43.31 | not run |
| **test C curve A** | not run | not run | < g rms input | < g rms input | < g rms input | not run |
| **test C curve B** | not run | not run | 11.77 | 7.83 | 15.22 | not run |
| **test C1 side** | overload | overload | 12.70 | 9.56 | 7.64 | 0.88 |
| | overload | overload | 11.33 | 11.43 | 18.11 | not run |
| **test C1 curve A** | not run | not run | < g rms input | < g rms input | < g rms input | not run |
| **test C1 curve B** | not run | not run | 4.91 | 4.43 | 4.94 | not run |
| **test C2 side** | overload | overload | 5.88 | 6.43 | 5.06 | 2.61 |
| | overload | overload | 13.82 | 5.29 | 4.64 | not run |
| **test C2 curve A** | not run | not run | < g rms input | < g rms input | < g rms input | not run |
| **test C2 curve B** | not run | not run | 1.80 | 2.93 | 2.86 | not run |

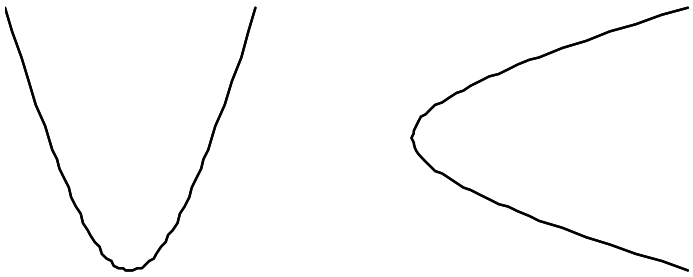

FIGURE 54. IMAGES OF CURVES A (LEFT) AND B (RIGHT)

Table 6 also lists the frequencies at which the maximum acceleration responses occurred for the curved piezo cables. The maximum acceleration occurred from 4 – 6 Hz for the 12.5” lengths of curves A and B and at 2 Hz for the 25” lengths of curve B (curve A (<g rms input). Most of the inconsistencies in determining the maximum frequencies within profile groups occurred when there was no obvious peak. As with the straight cables, the frequency of the maximum acceleration is lower for the long (25”) lengths of piezo cable simulating clamp failure than for the short (12.5”) lengths simulating proper clamping.

Table 7 also lists the ratios calculated by dividing the acceleration value for the 25” length cable (maximum) by the 12.5” acceleration value at the same frequency (may or may not be maximum) for the curved piezo cables (ratio = 1: no change). For the curve B there is a large

increase in $g^2$/Hz for the 25" lengths of piezo cable (i.e. loss of a clamp) compared to the 12.5" lengths. Since the acceleration values for the curve A cables were below the input value for the 25" length cable, the calculated ratios would be below 1 and have to be calculated at a preselected frequency since the acceleration value has no maximum.

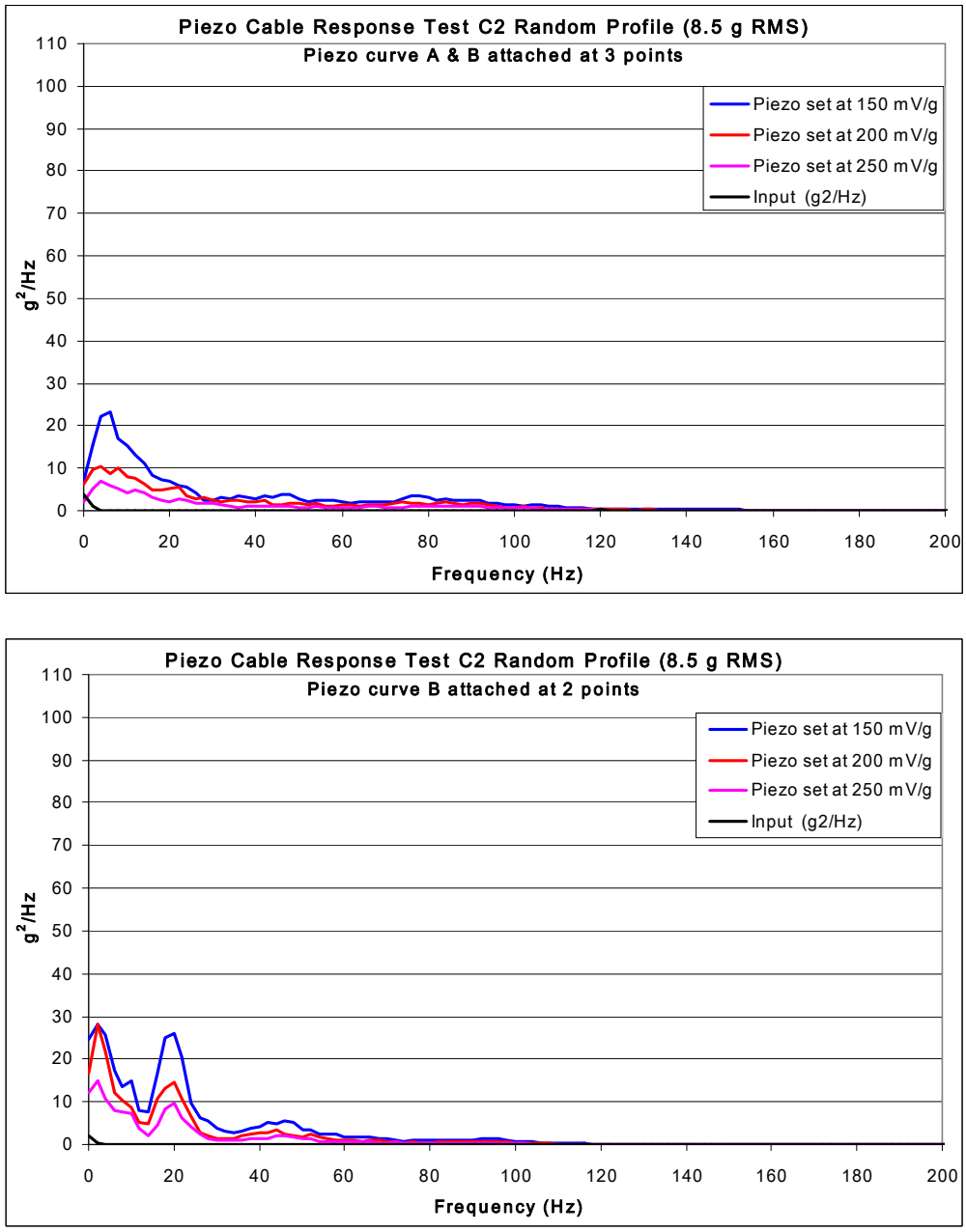


FIGURE 55. C2 RANDOM PROFILE TEST GRAPHS FOR CURVED PIEZO CABLES POSITIONED ON THE SIDE OF THE FIXTURE.

3.1.3 Sine Profile – Straight Cables.

Based on the random profile tests, the sine profiles were performed at the piezo cable sensitivities of 150 mV/g, 200 mV/g, and 250 mV/g using three acceleration inputs (1, 2 and 6g). When the piezo cable was located on the side of the fixture and the length of cable was increased from 12.5" to 25" by removing the center attachment, a small increase in acceleration was which was independent of the input acceleration as listed in table 8.

TABLE 8. SINE PROFILE MAXIMUM ACCELERATION TEST RESULTS

| Sine max g | Piezo set at 150 mV/g | Piezo set at 200 mV/g | Piezo set at 250 mV/g |
|---|---|---|---|
| 1 g top full | < g input | < g input | < g input |
| 1g top 3 | < g input | < g input | < g input |
| 1 g top 2 | < g input | < g input | < g input |
| 1 g side 3 | 58.29 | 43.35 | 35.03 |
| | 57.27 | 34.71 | 34.70 |
| 1 g side 2 | 62.67 | 47.10 | 37.49 |
| | 62.80 | 45.69 | 38.07 |
| 1 g curve A & B side 3 | 5.90 | 5.34 | 3.28 |
| 1 g curve A side 2 | 15.01 | 13.28 | 12.40 |
| 1 g curve B side 2 | 17.61 | 13.99 | 19.60 |
| | | | |
| 2.5 g top full | < g input | < g input | < g input |
| 2.5g top 3 | < g input | < g input | < g input |
| 2.5 g top 2 | < g input | < g input | < g input |
| 2.5 g side 3 | 61.30 | 45.93 | 36.80 |
| | 59.08 | 44.57 | 35.71 |
| 2.5 g side 2 | 63.01 | 46.93 | 37.60 |
| | 74.16 | 55.41 | 44.67 |
| 2.5 g curve A & B side 3 | 5.17 | 4.81 | 3.88 |
| 2.5 g curve A side 2 | 17.13 | 12.70 | 9.56 |
| 2.5 g curve B side 2 | 25.19 | 17.50 | 12.91 |
| | | | |
| 5 g top full | < g input | < g input | < g input |
| 5 g top 3 | < g input | < g input | < g input |
| 5 g top 2 | < g input | < g input | < g input |
| 5 g side 3 | 62.79 | 47.30 | 37.70 |
| | 59.27 | 44.27 | 34.35 |
| 5 g side 2 | 62.55 | 47.36 | 37.64 |
| | 64.38 | 48.09 | 39.16 |
| 5 g curve A & B side 3 | 6.59 | 5.22 | 4.10 |
| 5 g curve A side 2 | 16.13 | 12.60 | 10.98 |
| 5 g curve B side 2 | 45.56 | 36.56 | 28.50 |

Similar to the random profile results, when the cable was located on the top of the fixture the measured acceleration was less than the input for both the lengths of cable.

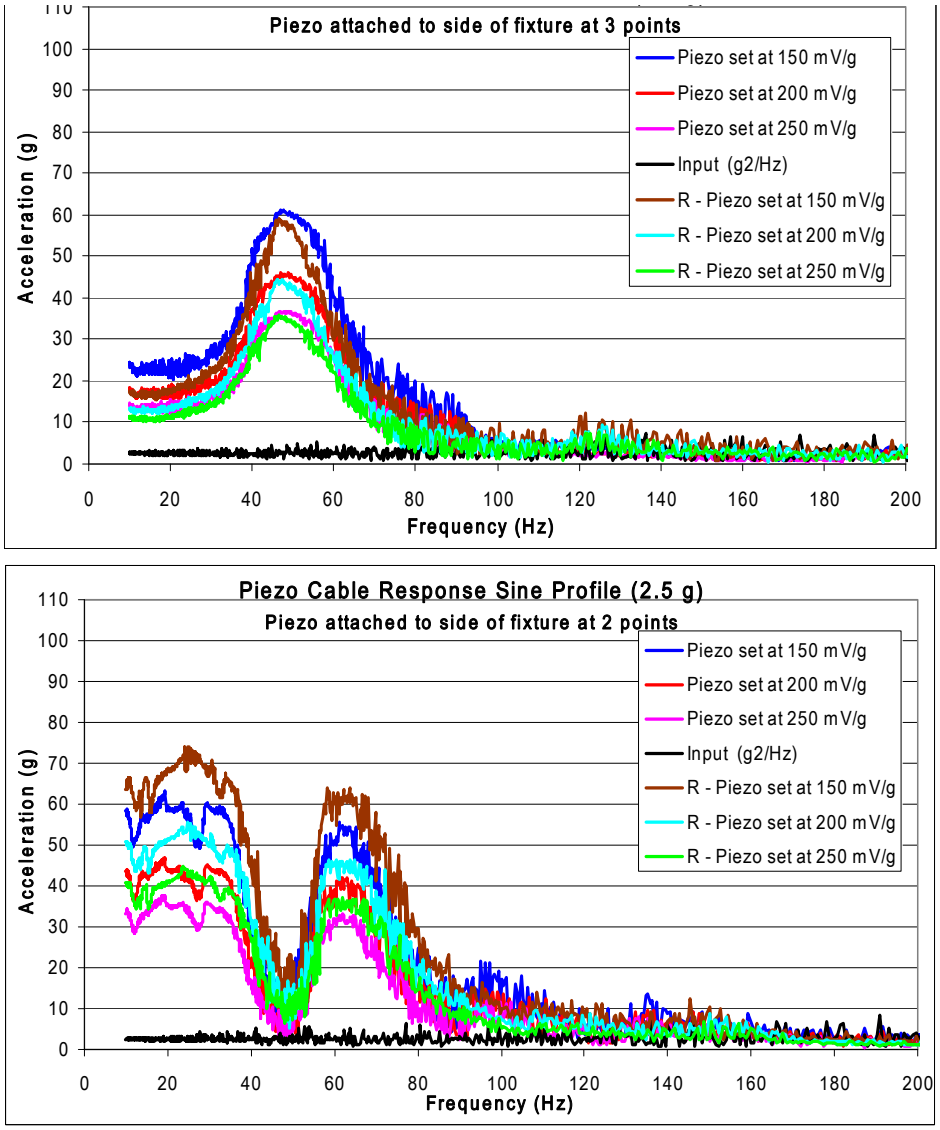


FIGURE 56. SINE PROFILE TEST (2.5 G) GRAPHS FOR PIEZO CABLES POSITIONED ON THE SIDE OF THE FIXTURE

To expand on the data in table 8, the relative magnitude of acceleration was plotted versus frequency (converted from bins) for each test run as shown in figure 56. Labels starting with "R" are repeat tests. The rest of the graphs are in the Appendix E. Although the maximum acceleration values in table 8 are similar for the 12.5" and 25" piezo cables placed on the side of the fixture, the maximum responses were at different frequencies as shown in figure 56. The piezo cables had an increased response in the range of 40 Hz to 60 Hz for the 12.5" length (3 attachments) and a decreased response in the same range for the 25" length (2 attachments). In contrast to the random profile graph in figure 52, the 25" length cables on the side of the fixture exhibited two maxima, approximately 10 to 30 Hz (similar to random profile results) and 50 to 60 Hz. Again, the length of the cable did not affect the frequency of the maximum acceleration results when attached to the top of the fixture. To summarize the relative magnitude of acceleration versus frequency plots for the performed tests (Appendix E), the frequency of the

maximum acceleration response for each test is listed in Table 9. In agreement with figure 56 and the random profile results in table 7, the frequency at which the acceleration maximum occurs was always lower for the 25" length cables (2 attachments, i.e., broken clamp) than for the 12.5" length cables (2 attachments) for the straight cables attached to the side of the fixture. The frequencies of the acceleration maxima were unaffected by the input acceleration vales of 1, 2.5 and 5g. No maxima were listed for the cables attached to the top of the fixture since the measured acceleration was below the input value.

TABLE 9. SINE PROFILE FREQUENCY LOCATIONS OF MAXIMUM ACCELERATION

| Sine at Frequency | Piezo set at 150 mV/g | Piezo set at 200 mV/g | Piezo set at 250 mV/g |
|---|---|---|---|
| **1 g top full** | < g input | < g input | < g input |
| **1g top 3** | < g input | < g input | < g input |
| **1 g top 2** | < g input | < g input | < g input |
| **1 g side 3** | 49 | 49 | 50 |
| | 50 | 48 | 49 |
| **1 g side 2** | 21 | 21 | 21 |
| | 22 | 22 | 22 |
| **1 g curve A & B side 3** | 56 | 57 | 57 |
| **1 g curve A side 2** | 37 | 37 | 37 |
| **1 g curve B side 2** | 10 | 10 | 10 |
| | | | |
| **2.5 g top full** | < g input | < g input | < g input |
| **2.5g top 3** | < g input | < g input | < g input |
| **2.5 g top 2** | < g input | < g input | < g input |
| **2.5 g side 3** | 47 | 49 | 49 |
| | 47 | 46 | 47 |
| **2.5 g side 2** | 19 | 19 | 19 |
| | 25 | 25 | 24 |
| **2.5 g curveA & B side 3** | 56 | 55 | 55 |
| **2.5 g curve A side 2** | 36 | 36 | 36 |
| **2.5 g curve B side 2** | 10 | 10 | 10 |
| | | | |
| **5 g top full** | < g input | < g input | < g input |
| **5 g top 3** | < g input | < g input | < g input |
| **5 g top 2** | < g input | < g input | < g input |
| **5 g side 3** | 46 | 46 | 47 |
| | 45 | 45 | 45 |
| **5 g side 2** | 18 | 19 | 18 |
| | 16 | 16 | 22 |
| **5 g curve A & B side 3** | 54 | 55 | 55 |
| **5 g curve A side 2** | 36 | 36 | 35 |
| **5 g curve B side 2** | 10 | 10 | 10 |

For comparison with the random profile results, the acceleration values of the 25 and 12.5" length cables were recorded for each test at the lower frequency at which the 25" cable acceleration maximum occurred. Then the acceleration value for the 25" cable (maximum) was divided by the 12.5" acceleration value (may or may not be maximum) to produce a ratio that would take into account vibrational changes in both frequency and acceleration of wire bundles experiencing clamp failure. The ratios calculated for all of the cable position vibrational tests are listed in Table 10 (ratio of 1: no change detected).

TABLE 10. SINE PROFILE RATIOS OF MAXIMUM ACCELERATION TEST RESULTS

| Sine ratio of 2 vs 3 | Piezo set at 150 mV/g | Piezo set at 200 mV/g | Piezo set at 250 mV/g |
|---|---|---|---|
| **1 g top** | na | na | na |
| **2.5 g top** | na | na | na |
| **5 g top** | na | na | na |
| **1 g side** | 4.98<br>3.98 | 5.10<br>5.30 | 4.06<br>4.34 |
| **1 g curve A** | 11.53 | 16.76 | 28.27 |
| **1 g curve B** | 19.24 | 18.15 | 47.51 |
| **2.5 g side** | 2.82<br>3.72 | 2.73<br>3.85 | 2.87<br>3.97 |
| **2.5 g curve A** | 43.56 | 43.56 | 43.56 |
| **2.5 g curve B** | 13.02 | 24.79 | 14.47 |
| **5 g side** | 2.40<br>3.29 | 2.32<br>3.41 | 2.21<br>3.32 |
| **5 g curve A** | 9.37 | 11.05 | 12.62 |
| **5 g curve B** | 63.69 | 71.65 | 68.84 |

Since the outputs were below the acceleration inputs for the cables attached to the tops of the fixtures, the ratios were not calculated for table 10. As with the random profile results, the ratios were well above 1 (i.e., detected loss of clamp) for the cables attached to the side of the fixture regardless of the input acceleration.

3.1.4 Sine Profile – Curved Cables.

To test the effects of curvature on the vibration sensing of the piezo cable for the sine profile, two curve directions were tested on the side of the fixture. Curve A was in a vertical direction and curve B was horizontal as shown in Figure 54. As opposed to the random profile results in table 5, Curve A results at 25" (2 attachments) exhibited significant acceleration peaks of 10 to 17 g, which remained steady even with increased input levels. Acceleration g levels for curve B did increase with greater input g. The values ranged from 20 g to 45 g. Representative graphs are in figure 57. All other graphs are in the Appendix E.

Table 9 also lists the frequencies at which the maximum acceleration responses occurred for the curved piezo cables. The maximum acceleration occurred from 55 - 57Hz for the 12.5" lengths of curves A and B. The maximum acceleration responses for the 25" lengths of curve B occurred at lower frequencies, 36 – 37Hz for curve A and 10Hz for curve B. As with the straight cables, the frequency of the maximum acceleration is lower for the long (25") curved lengths of piezo cable simulating clamp failure.

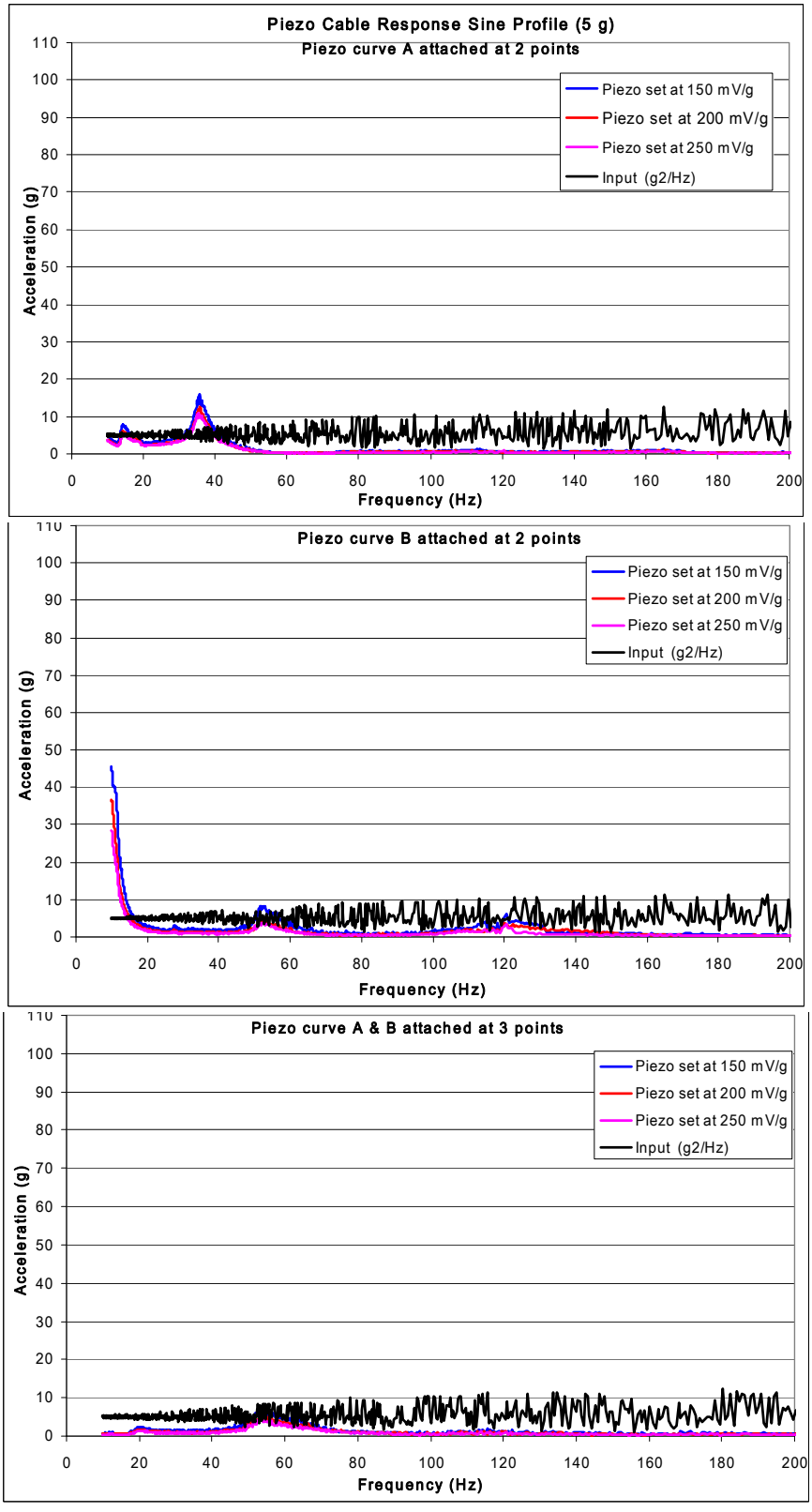


FIGURE 57. SAMPLE GRAPHS OF 5 G SINE PROFILE TEST RESULTS WITH CURVES A AND B.

Table 10 also lists the ratios calculated by dividing the acceleration value for the 25" length cable (maximum) by the 12.5" acceleration value at the same frequency (may or may not be maximum) for the curved piezo cables (ratio = 1: no change). For both curves A and B in Table 10 there is a large increase in $g^2$/Hz for the 25" lengths of piezo cable (i.e. loss of a clamp) compared to the 12.5" lengths. In fact, the ratios for the curved cables are significantly larger than the ratios for the straight cables in table 10.

## 3.2 CONNECTOR DEGRADATION MONITORING TECHNIQUES.

Connectors are an integral part of the electrical wiring system in aircraft as they carry electrical power and communication signals for proper operation of the aircraft. The connectors and wiring also route and branch electrical signals into different parts of the electrical subsystems of the aircraft. Connectors introduce additional resistance into the EWIS system which must be controlled. Any change in resistance that reduces the amounts of current or voltage being carried from one electrical subsystem to another is critical for the continuing safety of the aircraft.

The connector is held together by the connector shell and the contact force between the mating parts. In general, any mechanism that causes reduction in this force ruins the intimacy of the contact between the mating surfaces and thereby degrades the connector. This can happen due to many reasons, e.g., the corrodibility of the environment, gaseous pollutants, less external pressure at high altitudes and temperature differences between the mating surfaces. Mechanical vibration during a flight can exacerbate these factors. The fretting caused by mechanical vibration can generate a debris layer of oxide between the surfaces. In the presence of moisture, the fretting process will produce corrosion leading to further reduction of the electrical contact area. Formation of corrosion byproducts will shorten the life of connectors. Loss of contact area and increases of dielectric material between the mating surfaces increases the resistance to the flow of current and causing localized heating with the heat transferring to surrounding regions of the electrical contact. If severe, the heating will melt and char the polymeric insulator of the electrical connector creating a potential fire hazard.

Degradation of connectors causes a gradual change in the resistance at the mating interface. Generally, it takes a long time for a connector to degrade enough to lose complete contact. This long term durability has led to a general belief that it may not be necessary to inspect or replace connectors. Although connectors may be highly reliable electrical components, a problem in a single connector can cause tremendous delay and ground an aircraft. The problems due to connectors are more prevalent in older airplanes.

The inevitable presence of degradation in connectors and the resulting adverse effects on EWIS performance are a major problem for the aircraft industry. Due to a lack of knowledge of the approximate usable life of connectors, under different environmental conditions, or lack of established inspection techniques to precisely determine the rate of degradation of electrical connectors in service, there is hardly any maintenance currently scheduled for electrical connectors. Therefore, the aim of this research is to detect the degradation of a connector without the need for opening the connector (as explained below).

### 3.2.1 Established Degradation Evaluation Techniques.

#### 3.2.1.1 Contact Resistance Measurements.

One of the most well established techniques to evaluate the degradation of the connector is to measure the resistance across the connector, which is defined as the "contact resistance". Most often this resistance is quite small, and to measure small resistances a large current is sent through the connector and the voltage across the connector is measured. This requires access to both sides of the connectors. In many situations, this also requires, puncturing the insulation of the wire to make contact with the conductor. Although partially destructive, contact resistance measurements have been instrumental in the research, design and development of materials for connectors. It has also been the test of choice to evaluate connector degradation.

#### 3.2.1.2 Time Domain Reflectometry.

In order to examine the connector degradation when access is available from only one side, electromagnetic wave propagation methods can be used. Time Domain Reflectometry (TDR) [4] has been one of the oldest and best-established methods in the evaluation of wiring integrity. In this method, an electromagnetic square pulse is injected into the wire. The propagating electromagnetic wave reflects back to the source whenever it encounters a change in the impedance. The reflected signals are separated in time from the input signal and the distance at which a change in impedance occurs can be determined based on the velocity of propagation of the electromagnetic wave. Although TDR is a well-established technique, it has been very successful in detection of "hard opens" when the contact has been lost. When the contact area between the mating surfaces of the connector is completely lost, the connector appears to be electrically open. An electromagnetic wave propagating through the open connector experiences an infinite impedance change, and hence, is completely reflected and a 180-degree phase change occurs at the interface. This technique can also locate wiring and connector shorts. On the other hand, small changes in resistance due to gradual contact and insulation degradation are difficult to observe with the TDR technique.

Recently, several alternative wave propagation methods [5-7], along with advanced signal processing techniques [8-11], have been developed for wire integrity. As in the case of the TDR technique, almost all of the wave propagation methods detect hard opens or shorts and have limitations in the measurement of small changes in contact resistance at the connector interfaces undergoing slow, long-term degradation.

#### 3.2.1.3 Tone Burst Phase Lock-in Reflectometry.

Another electromagnetic wave propagation method that can be used for monitoring connector condition is Tone Burst Phase Lock-in Reflectometry. A monochromatic pulse is propagated through the connector and the reflected signal from the connector interface is detected. The basic concept of this methodology is to compare the phase of the reflected signal from the connector with the input signal. An RF tone-burst of known frequency is generated by chopping a continuous wave RF sinusoidal signal from a signal generator. This RF tone-burst is sent through a directional coupler and then propagated through a cable. The use of a directional coupler prevents the reflected signals from interfering with the input signals. The tone-burst

signal is reflected by any defects (open/ short or a load) present along the length of the cable. The reflected signal is amplified and displayed on the oscilloscope, along with the transmitted signal. The reflected signal may contain multiple reflections from defects. A particular reflection is selected and gated out for further evaluation. The gated and amplified reflected signal and the reference signal from the function generator are fed to an RF lock-in amplifier. The lock-in amplifier compares the two signals and measures the precise phase difference between the transmitted and reflected signal [12].

This method has been applied in the laboratory to detect degradation in connectors. Although the results are encouraging, several limitations were detected [1]. The reflected signals are quite weak at early stages of degradation. The kinks and bends in the wire bundles and changes in the wire insulation conditions can also cause changes in the signal making it difficult to ascertain the degree of degradation in the connector.

3.2.2 Electromagnetic Induction Degradation Evaluation Technique - Description.

The techniques of contact resistance measurements, basic electromagnetic wave propagation method, the signal processing enhanced wave propagation techniques, and the improved instrumentation methodology of tone burst reflectometry all have limited applicability in connector degradation evaluation. Moreover, these techniques require specialized instrumentation and sophisticated signal processing algorithms. Therefore, the electromagnetic induction method (EIM) based on currents induced in sensor coils placed on the two sides of a connector when a sinusoidal current passes through the connector was investigated due to its practicality and applicability to connector degradation monitoring.

The EIM for detecting connector degradation is based on the basic principles of Ampere's law and Biot-Savart law. Ampere's law relates the direction and amplitude of the magnetic field to the current flowing through a conductor. On the other hand, the Biot-Savart law provides a relation between the magnitudes of the induced magnetic field at a distance from a current carrying conductor (figure 58). In particular, if the differential element of the current is defined as $Id\mathbf{l}$ then the corresponding differential element of a magnetic field is

$$d\mathbf{B} = K_m \frac{Id\mathbf{l} \times \hat{\mathbf{r}}}{r^2} \qquad K_m = \frac{\mu_0}{4\pi} \tag{1}$$

Where:

$\boldsymbol{\mu_0}$ is the magnetic constant

$I$ is the current, measured in amperes

$d\mathbf{l}$ is the differential length vector of the current element

$\hat{\mathbf{r}}$ is the unit displacement vector from the current element to the field point and

$r$ is the distance from the current element to the field point.

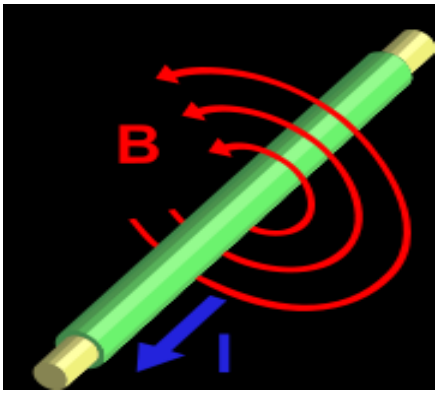


FIGURE 58. ILLUSTRATION OF BIOT-SAVART LAW

For a straight conductor carrying a current I, the magnetic field B at a radial distance r from the wire the equation reduces to

$$\mathbf{B = \mu_0 I / (2 \pi r)} \qquad (2)$$

The magnetic field varies inversely with distance from the current carrying wire. When the current through the wire is a sinusoidal varying signal, the magnetic field oscillates with the same frequency. If a coil is wrapped around the conductor carrying an oscillating current, the varying magnetic field around the conductor, induces a current in the coil. By placing two coils around the wire, one on each side of the connector (figure 59), the induced current in the coils can be detected and compared. The characteristics of the induced currents in the coils (amplitude and phase) on the two sides of the connector are expected to be different and to change as the connector degrades.

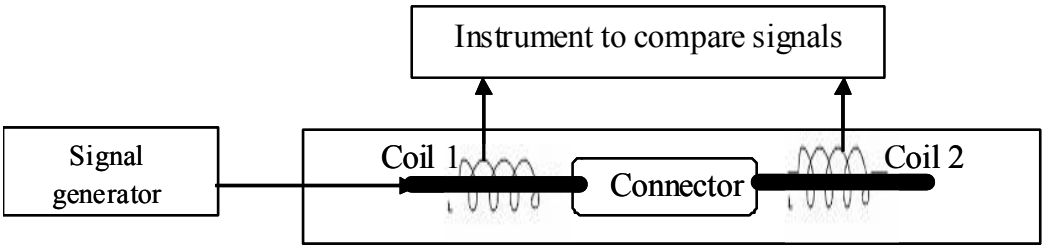


FIGURE 59. BLOCK DIAGRAM FOR ELECTROMAGNETIC INDUCTION

To investigate the potential of the EIM for connector degradation monitoring, three different approaches were developed and tested. The first technique involved the use of a network analyzer with hand wound coils on plastic tubing. In the second approach, a signal generator was used to send a sinusoidal signal through the connector and the induced signals from each of the commercial coils were compared using a lock-in amplifier. In the final approach, simple coils tightly wound around the connector wires were used in place of the commercial coils.

3.2.3 EIM Degradation Evaluation Technique: Network Analyzer.

The first evaluated EIM employed a network analyzer and hand wound coils on plastic tubing located on each side of the connector to determine the $S_{21}$ parameters of continuous

electromagnetic waves inputted through pristine (as received) and degraded connectors as illustrated in figure 60. The network analyzer was set to transmit continuous wave signals from 10 kHz – 500 MHz. The long wires soldered to the connector pins were pushed through the central tubing of the hand made coil sensors and the coil sensors were then adjusted to be in close proximity to the opposite ends of the connector. The RF input from the network analyzer was connected to the wire on one end of the connector to transmit continuous electromagnetic waves through the connector. One of the sensing coils was connected to the second port of the network analyzer.

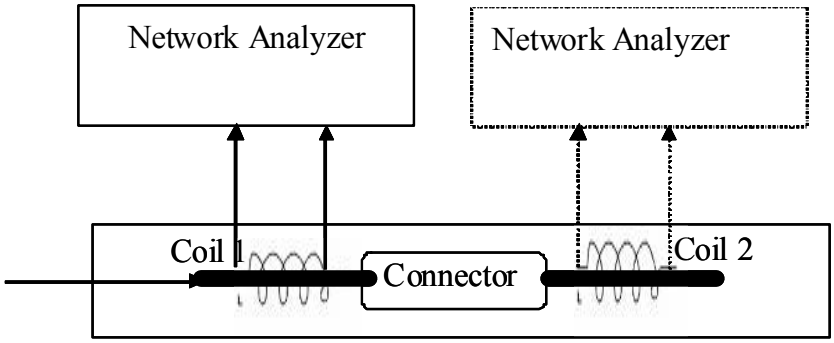


FIGURE 60. NETWORK ANALYZER FOR CONNECTOR DEGRADATION

The net work analyzer treats the wire, connector and the coil sensor as a two port network. The wire to the connector is connected to port 1 and the sensor is connected to port 2 of the network analyzer and the $S_{21}$ parameter (the ratio of output of port two to the incident wave of port 1) is measured as a function of the frequency. After storing the data from the coil from one side, the second coil is connected to port 2 of the analyzer and data is collected from the second coil. The $S_{21}$ parameter measured for the coils on both sides of a pristine connector is shown in figure 61. The transmission coefficients as a function of frequency for both coils are expected to be similar, i.e., the plots in figure 61 are expected to be identical. The small differences in the $S_{21}$ plots are attributed to the differences in the two coils that are hand wound.

Figure 61 also shows the data for a corroded connector. The reflection coefficients from the two coil sensors show significant differences in the amplitude of the peaks and the frequencies at which they occur, e.g., the peaks at point 881. The differences in the features observed between the virgin and corroded connector pins indicate that the EIM employing the network analyzer is sensitive and feasible to detect connector degradation.

Although there were positive signs in the applicability of the network analyzer EIM, there are several limitations. It is quite difficult to make both coils identical. Even when they were made to be close in resistance, diameter and number of turns, significant differences were still observed in their responses. Although coils with 700 - 1000 turns showed more stability than coils with 100-200 turns, significant cross-talk between the coil sensors occurs at frequencies of 100 – 500 MHz making positioning of the coils with respect to connector position an important factor in producing a reproducible technique.

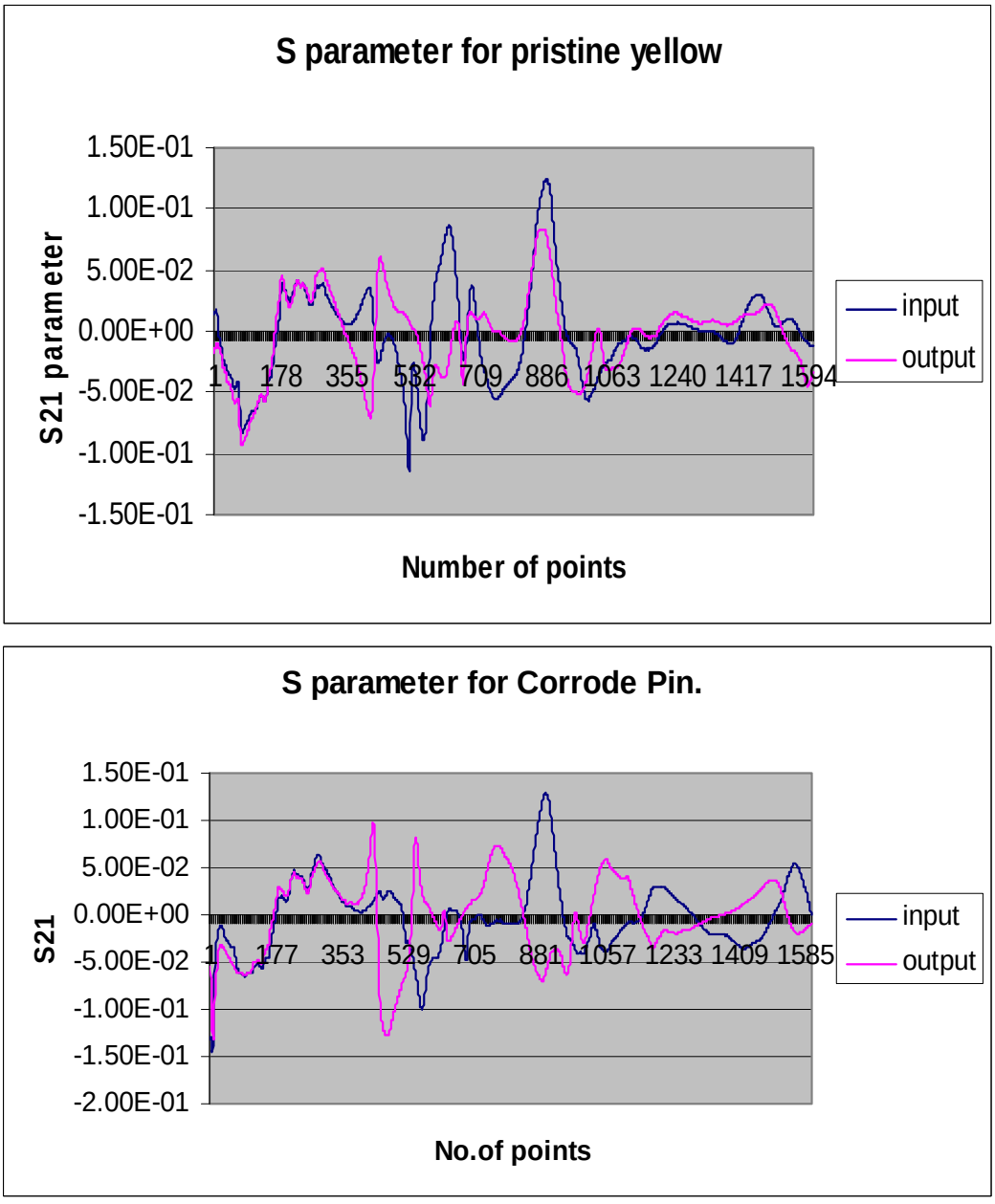


FIGURE 61. NETWORK ANALYZER $S_{21}$ RESPONSES FOR PRISTINE AND DEGRADED CONNECTORS

3.2.4 EIM Degradation Evaluation Technique: Commercial-Coils and Lock-in Amplifier.

Due to the limitations of the cross talk and poor reproducibility of hand wound coil sensors, commercial coil sensors were used in place of the hand wound coils. The commercial coil resonance and peak sensitivity were found to be at about 25 kHz as shown in figure 62). To operate at low frequencies of 25 kHz, the network analyzer in figure 61 was replaced by an

Agilent 3685 function generator and a SRS 830 Lock-in Amplifier. A block diagram and photograph of the instrumentation are shown in Figure 63.

A sinusoidal signal of appropriate amplitude and frequency is propagated through the wires connected to the connector. When current passes through the wire, a small magnetic field is generated around the wire. The electromagnetic field induces a current through the coil surrounding the wire thus generating a small voltage. The signal from the coil is amplified and fed to one arm of a lock-in amplifier. The voltage induced in the second coil across the connector is also amplified and fed to the other arm of the lock-in amplifier. Since the frequency and amplitude of the signal passing thorough the wire are the same and the amplification factor for both amplifiers is the same, the phase and the amplitude differences between the two coil sensors can be measured. It was expected that as the degradation of the connector progresses, the phase and amplitude differences between the two sensors would increase proportionally**.**

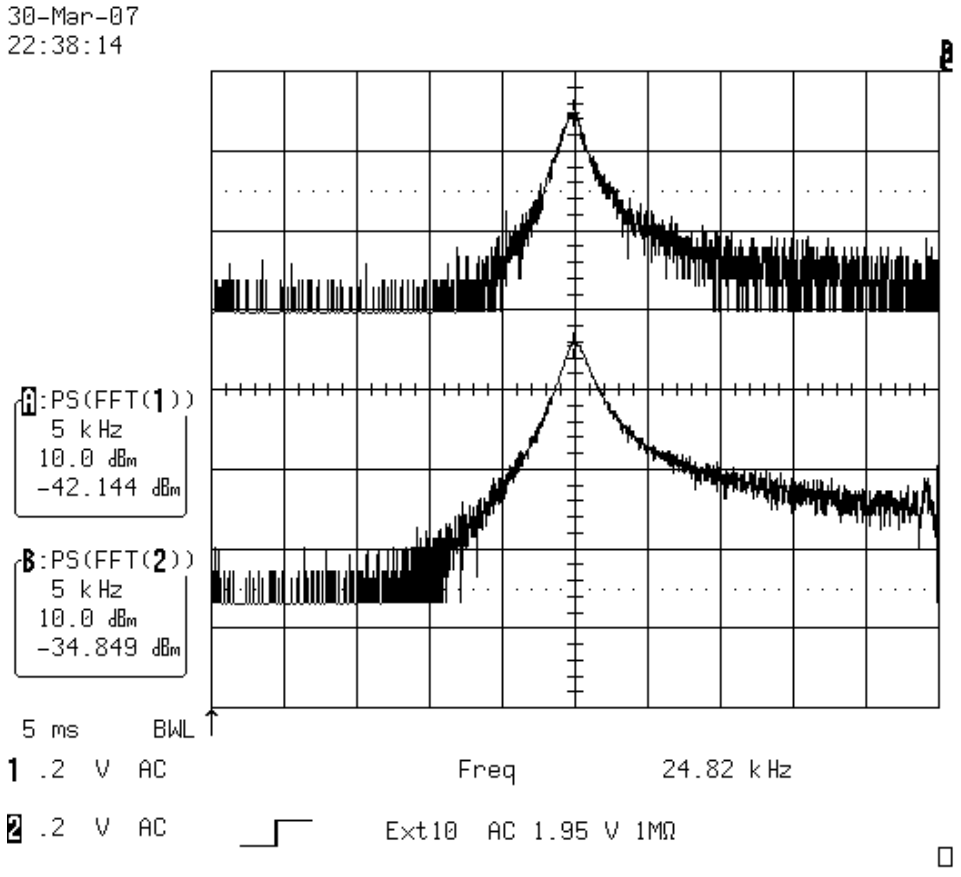


FIGURE 62. COMMERCIAL COIL PEAK RESONANCE AT 24.82 HZ

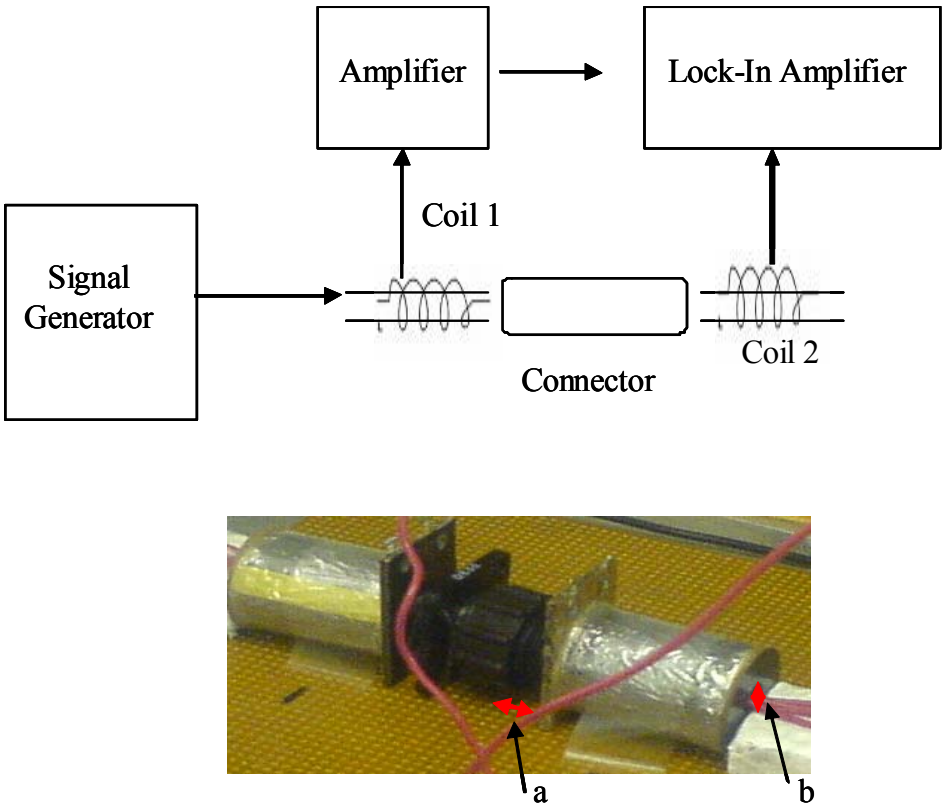


FIGURE 63. BLOCK DIAGRAM OF THE LOCK-IN AMPLIFIER SETUP AND PHOTOGRAPH OF CONNECTOR AND COMMERCIAL COILS

The difference between the phase and amplitude for virgin and degraded connector pins were found to be significantly different. The methodology was found to be very sensitive to changes in the condition of the connector. Although the methodology was simple and could be applied, again drawbacks and limitations were identified. The signals changed significantly when the wires were touched were quite sensitive to the positioning and orientation of the coils with respect to the wires.

The changing signals and wire/coil positioning were attributed to the induced magnetic fields. The cylindrical opening in the center of the commercial coil had a much larger diameter than the bundle of four wires used in the experiment. When the distance between the wire and the coil inner surface changes, the induced magnetic field changes according to the Biot-Savart law. Similarly, if the wire is not laying parallel to the axis of the coil, the characteristics of the induced magnetic field also changes the signal. To overcome some of these problems, the coil was affixed firmly to the connector but the repeatability remained poor. Another practical drawback is that the wire bundle must be cut or a connector opened so that the wiring can be passed through the central cylindrical hole before installation.

3.2.5 EIM Degradation Evaluation Technique: In-Situ Coils and Lock-in Amplifier.

To overcome the limitations with the commercially available coils, two coils were hand wound around the wire bundle and used as sensors. Since the coil can be wound quite tightly around

wire bundles of different sizes, the space between the coil and each wire is eliminated. According to the Biot-Savart law, the direct contact should increase the magnetic field induction and resulting signals. Secondly, the direct contact also eliminated the effect of wire bundle handling on the produced signals.

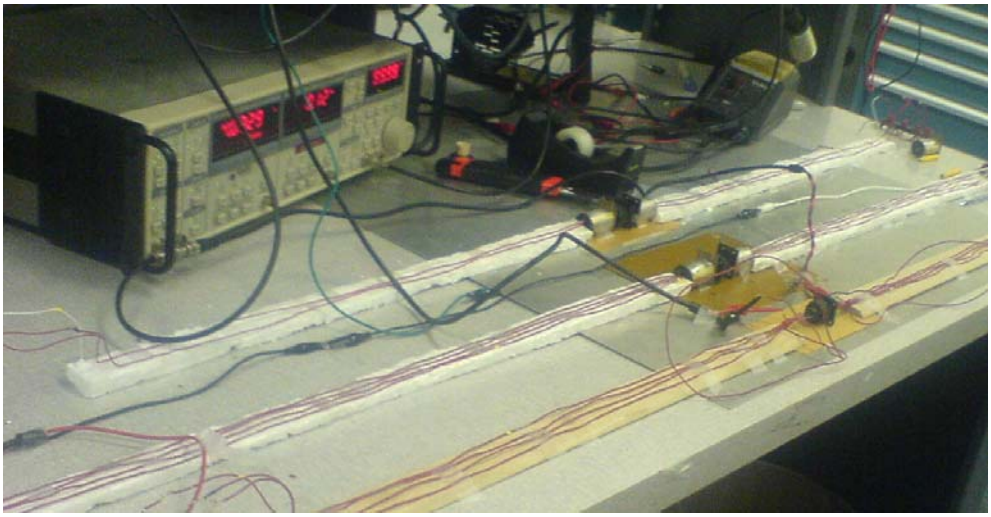

FIGURE 64. PHOTOGRAPH OF THE LOCK-IN AMPLIFIER SETUP USING THE HAND WOUND COIL SENSORS

In order to test this methodology, a 10 V pk-pk signal was set at the generator output with a frequency range of 25 KHz-1 MHz which was applied and propagated throughout the wiring. Most of this signal amplitude is attenuated inside the signal generator's 50 ohm output resistance due to the low ohm resistance of the tested contacts and wiring. The signal from the first sensor coil was amplified using a low noise SRS amplifier. The amplified signal from the coil was displayed on a Lecroy Oscilloscope and the phase and amplitude difference between the two sensors was measured using the SRS Lock-in amplifier as shown in figure 64.

The EIM measurements were performed on pristine and degraded contacts (described in Appendix F) at three different frequencies: 75 kHz, 100 kHz and 250 kHz. The amplification factor (gain) was kept constant at 2000 for all the tests. The results are presented in Tables 11 – 12.

TABLE 11. EIM MEASUREMENTS FOR SINUSOIDAL SIGNAL AT 75 KHZ

| Type of Degradation | Voltage(mv) | Phase |
|---|---|---|
| Pristine Pin | 0.2250 | Zeroed (Within -/+ 1) |
| Grit Paper | 0.4242 | -18.45 deg |
| Nitric Acid (Long Duration) | 0.0061 | No-Lock in |
| Nitric Acid (Short Duration) | 0.3781 | -18.31 |
| Vibration test | 0.3534 | -20.45 deg |
| Pristine pin | 0.2250 | Within (-/+ 1 deg) |

TABLE 12. EIM MEASUREMENTS FOR SINUSOIDAL SIGNAL AT 100 KHZ

| Type of Degradation | Voltage(mv) | Phase (Deg) |
|---|---|---|
| Pristine Pin | 0.3176 | Zeroed (Within -/+ 1) |
| Grit Paper | 0.5466 | -16.66 |
| Nitric Acid (Long Duration) | ~ 0 | No-Lock in |
| Nitric Acid (Short Duration) | 0.4921 | -16.69 |
| Vibration test | 0.4507 | -18.35 deg |
| Pristine pin | 0.3160 | Within (-/+ 1 deg) |

TABLE 13. EIM MEASUREMENTS FOR SINUSOIDAL SIGNAL AT 250 KHZ

| Type of Degradation | Voltage(mv) | Phase(Deg) |
|---|---|---|
| Pristine Pin | 0.843 | Zeroed (Within -/+ 1) |
| Grit Paper | 1.236 | -13.10 |
| Nitric Acid (Long Duration) | ~ 0 | No-Lock in |
| Nitric Acid (Short Duration) | 1.110 | -12.78 |
| Vibration test | 0.979 | -14.16 |
| Pristine pin | 0.842 | Within (-/+ 1 deg) |

The phase difference between the two coil sensors placed on both sides of the connector for pristine connector was found to be close to zero at all of the frequencies examined. On the other hand, the signals could not be locked on the pin degraded by corrosion in acid for 5 minutes (long duration), i.e., the connector was an open circuit so that no current was flowing to induce a magnetic field and the lock-in amplifier had no signal to lock on to provide a phase measurement. All other pins with less degradation showed a significant change in the phase and amplitude of the signals as compared to the pristine pins. The phase differences for the chemically and physically degraded pins were found to be 10 to 20 degrees which was an order of magnitude larger than the 1 degree phase changes of the pristine connectors.

Although more experimentation with systematically degraded connectors is needed to draw firm conclusions, the preliminary data shows significant differences between the pristine connector and the degraded connectors (abrasion, chemical and vibration). These results show that this methodology has the potential to be used as a practical method to detect connector degradation. The methodology is quite simple and requires two pieces of wire that are wound around a wire bundle as tightly as possible. Two coil windings are made on opposite sides of the connector with an equal number of turns. When a sinusoidal current is passed though the wires, the phase difference between the voltages detected by these coils can be measured using a lock in amplifier to detect connector degradation. The entire methodology is quite simple and can be implemented at the maintenance facility level.

### 3.2.6 Comparison of EIM Connector Degradation Detection Techniques.

Experimental techniques to detect connector degradation without opening the connector have been developed. The approaches are based on the detection of electromagnetic field induced signals in coils placed on either side of a connector encircling the wires. The amplitude and the phase difference between the two coils are measured by different types of instrumentation, either a network Analyzer or a lock-in-amplifier. Different types of hand wound and commercial coils were used to test the feasibility and practical implementation of the EIM. A summary of the techniques is presented in table 14.

TABLE 14. COMPARISON OF DIFFERENT TECHNIQUES DEVELOPED FOR CONNECTOR DEGRADATION DETECTION

| Sensor-type | Experimental Setup | Limitations |
|---|---|---|
| Network Analyzer<br>Coil: >100 turns on tube | Network Analyzer<br>(S Parameter) | 1. Difficulty in making identical coils.<br>2. Orientation of coils.<br>3. High frequency of operation. |
| Lock-in amplifier<br>Coil: commercial | Lock-in Amplifier<br>(Phase Change) | 1. Orientation of coils affected the phase.<br>2. Sensors must be installed even before the wiring is laid. |
| Lock-in Amplifier<br>Coil: 10 turns on wires | Lock-in Amplifier<br>(Phase Change) | 1. Availability of wires |

The hand wound coils with hundreds of turns have been found to be suitable for high frequency (500 – 1 GHz) measurements with a network analyzer. The induced signals were noisy, sensitive to mechanical movement of the wire. The difficulty is attributed to electromagnetic interference between the two coil sensors and to the orientation of the coil with respect to the current carrying wire bundle. The coils were wound around a tube through which the wire was passed. Although commercial coils operate at low MHz frequency range and can be used with a lock-in analyzer, the coils have a large central cylindrical opening and hence had reproducibility problems similar to hand wound coils. The ten turn coils wound directly on the wire bundle using ordinary wiring eliminated most of the reproducibility problems while simplifying the measuring methodology. Stable signals were observed and different types of degradation of connectors were monitored by using the lock-in-amplifier approach. The phase difference between the signals between the coils was found to sensitive to the connector degradation. The methodology was found to be simple and also quite practical to implement since it does not require opening of the connector and minor disturbance of the wiring bundle by the maintenance personnel. .

## 3.3 SMART CLAMP INVESTIGATION.

To complement the remote vibration research, research to develop a smart clamp was initiated during the project. By developing a smart clamp with prognostic/diagnostic capabilities,

maintenance personnel can be alerted to imminent/recent support failure so that insulation damage resulting from the unrestricted movement of unsupported wiring bundles can be avoided. Two different types of smart clamps were investigated: sensing capability incorporated directly into clamp versus sensing capability built into a small film/compartment adhered to the wiring/clamp/tie prior to applying support. A smart rattle was also investigated as a simple sensor that is able to differentiate between supported, vibrating wires and unsupported, swaying wires.

### 3.3.1 Smart Clamp With Embedded Sensing Capability.

The initial smart clamp design considered in this investigation was based on microampere radiotelemetry transmitters designed to be swallowed or implanted for continuous temperature measurements [15]. Temperature sensitive resistors were added to the oscillator circuits to make the frequency of the transmitter directly proportional to temperature. The electronics of the transmitters were inexpensive and suitable for miniaturization, two requirements for smart clamp designs.

For this investigation, the temperature sensitive resistor was replaced with two parallel resistors as shown in figure 1. In this design, the plastic clamp is made conductive by printing metal traces on its surface or by molding metal wires into its body. The smart clamp could be designed as one complete component built entirely into the clamp or as two separate components. In the two component system, the conductive clamp is installed similar to a non-modified clamp and then a second component containing the oscillation and transmission electronics is electrically connected/clipped to the closed clamp. In either case, the conductive clamp electrically completes one of the parallel resistance legs in figure 65. The electronics could be configured to differentiate between a clamp that needed retightening (clamp separating at closed end) from one in which the body of the clamp was cracking/had broken. Regardless of the exact design, the frequency output of the oscillator will be directly dependent on the health of the clamp, i.e., when the clamp in figure 65 opens/breaks, the affected resistance leg becomes open causing the resistance of the system to increase [double if the two kilo-ohm (KΩ) resistors are of equal resistance] and the frequency of the oscillator to decrease.

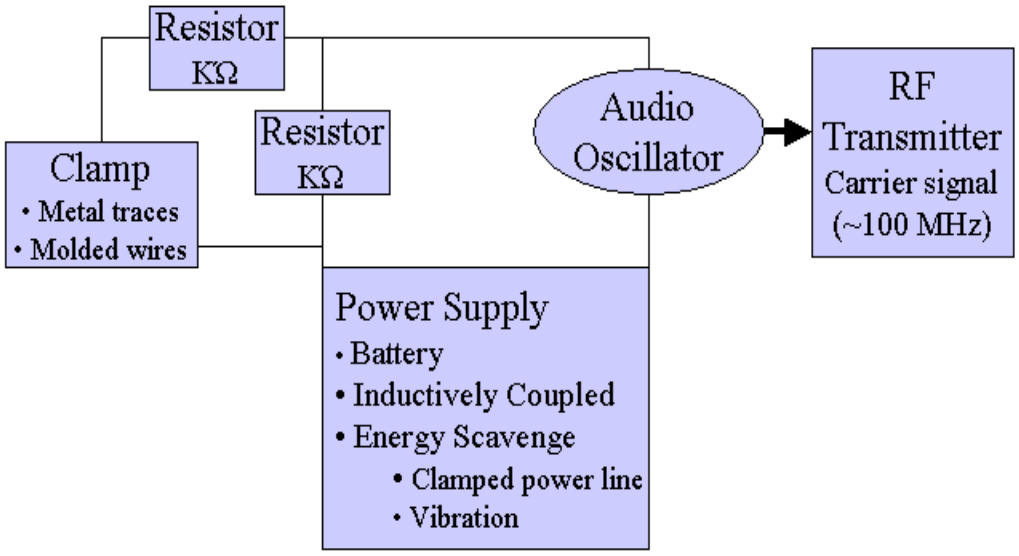


FIGURE 65. BLOCK DIAGRAM OF SMART CLAMP WITH VARIABLE FREQUENCY TRANSMITTER

To demonstrate the capability of the variable oscillator to produce a frequency dependent on clamp health, a simple circuit based on figure 1 was constructed in which high resistance resistors (333 KΩ to make resistance of conductive clamp negligible) were placed in the parallel resistance legs and a switch was used to repeatedly simulate an intact (switch closed)/broken (switch open) clamp. As shown in figure 66, the output of the oscillator decreased from approximately 1400 hertz (Hz) down to 800 Hz each time the switch was opened, i.e., clamp broke. The changes in the oscillator output frequency caused a change in the tone (spectrum analyzer needed to fully characterize the signal) of the transmitted RF frequency of approximately 160 megahertz (MHz).

The power for the smart clamp circuitry could be obtained from on-board power sources such as batteries, mechanical or electrical energy scavenging systems, etc. or from inductively coupled power such as the RFID tag technologies being studied by the aircraft industry for tracking parts. If the RFID included in the smart clamp design transmitted the aircraft location of the installed smart clamp, the information could be used to help identify the location of a remote clamp that has broken. A simple experiment in which power was inductively coupled through 1 inch of polymer or 0.25 inches of aluminum to illuminate a red LED (RF transmission discussed in section 1. ) is shown in figure 67.

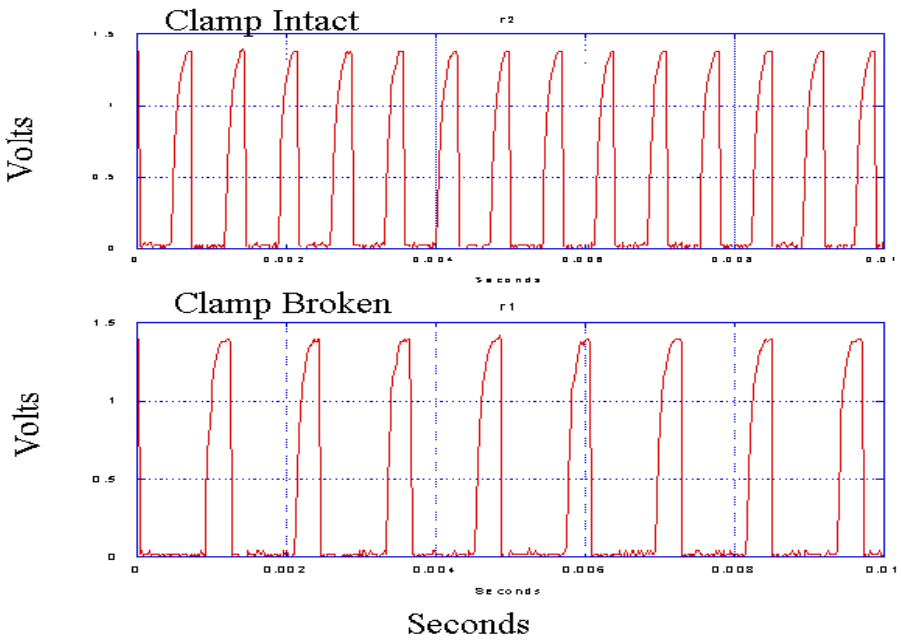


FIGURE 66. OSCILLATOR OUTPUTS WITH SWITCH CLOSED (CLAMP INTACT) AND OPEN (CLAMP BROKEN).

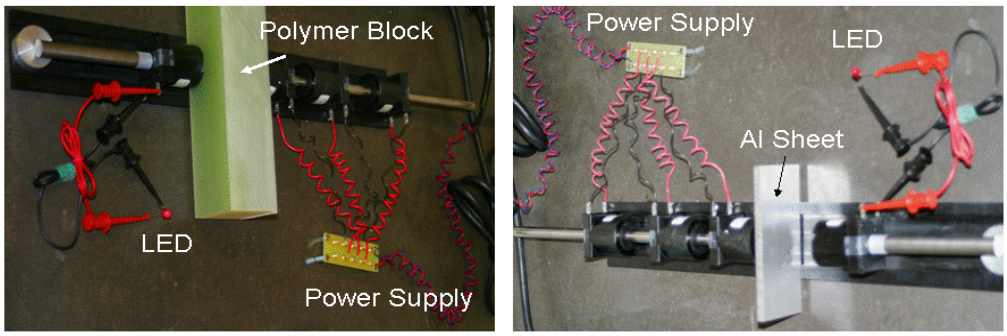


FIGURE 67. PHOTOGRAPHS OF INDUCTIVELY COUPLED POWERED LED

### 3.3.2 Smart Clamp Design Without Clamp Modification

As opposed to the design in figure 65, the non-clamp modification designs do not require clamp modification and so could be used with existing clamping systems, both metal and plastic bodies. The alternate smart clamp designs are based on the use of a switch that automatically changes state (closes/opens) when the clamp breaks. The alternate smart clamp designs can also use either a RF transmitter or LED to signal clamp breakage. The simplest smart clamp circuit is illustrated in figure 68. When the monitored clamp is closed/intact, the single loop circuit (e.g., RFID tag) has an opening/break in its circuitry so that no power is used. When the clamp breaks, a spring-loaded switch closes completing the circuit in figure 68, power is drawn and an audio or visual signal is outputted. A 9Vdc battery-powered circuit with a bent steel coupon as a switch and a red LED was built to demonstrate the simple concept.

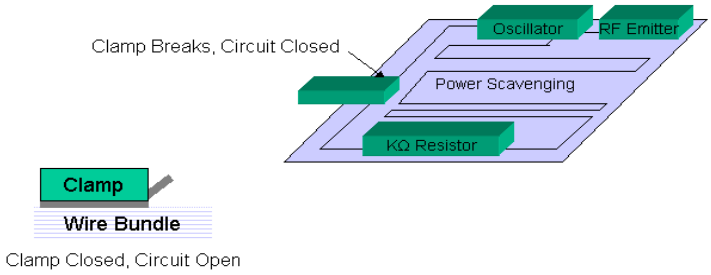


FIGURE 68. SCHEMATIC OF SMART CLAMP CIRCUIT THAT OUTPUTS SIGNAL WHEN CIRCUIT IS CLOSED BY CLAMP BREAKING

As an alternate to the circuit in figure 68, the pictures in figure 69 demonstrate the operation of a field effect transistor (FET) based circuit in which closing the clamp compresses a small piece of quantum tunneling composite (QTC - rubber filled with iron particles that becomes conductive when compressed) to complete the circuit between the power supply and the gate of the FET. When the clamp opens/breaks, the QTC expands and becomes non-conductive. The increase in the QTC resistance lowers the potential applied at the gate of the FET and the FET changes state from OFF to ON illuminating the red LED in figure 69. Any type of pressure sensitive resistor or switch would work in place of the QTC piece. As opposed to the circuits in figures 65 and 68, the FET based circuit would require a continuous power supply such as a small battery to supply the nanoamps of power to maintain the FET in the OFF state.

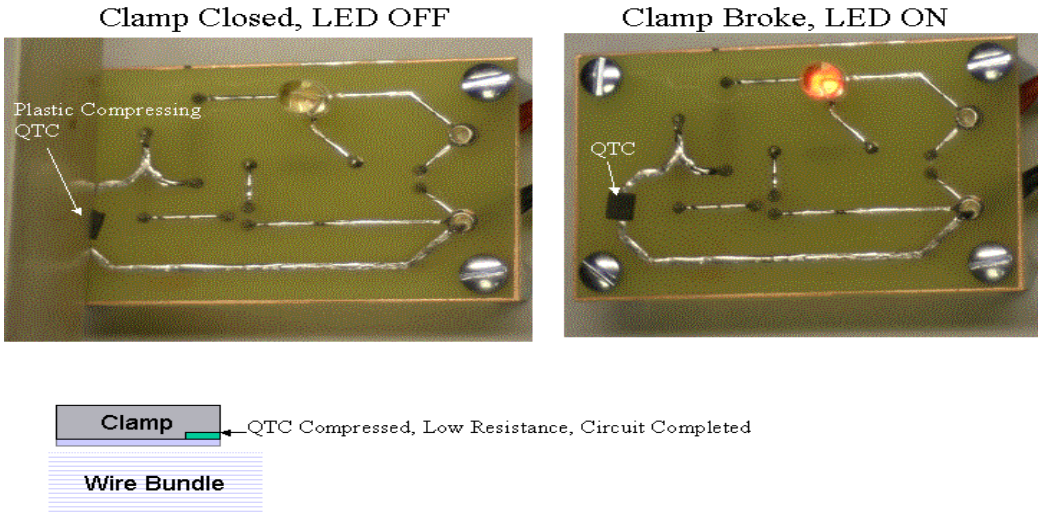


FIGURE 69. SMART CLAMP CIRCUIT WITH QTC SWITCH, FET AND LED

As opposed to the circuit in figure 65 which allows all clamps to be identified/assessed regardless of clamp condition, only the broken/open clamps will be identified by the circuits in figures 68 and 69. Obviously, adding a second resistance leg parallel to the clamp controlled switches in figures 68 and 69 would allow both circuits to produce a variable frequency transmission similar to figure 66 or a two LED visual check (green bright, red dim: clamp closed

versus red bright, green OFF: clamp broken, clamp leg with green LED very low resistance compared to second resistance leg with red LED) to allow all clamps to be identified/assessed.

The selection of the smart design most suitable for aircraft applications will depend on three main factors:

- Is it better to identify/assess the condition of all clamps or just the clamps that are loose/broken?
- Does the power for the associated electronics need to be on-board/scavenged (remote/accessible) or can be provided by hand held probe (accessible only)?
- Is the modified clamp (figure 65) or mechanical switch (figures 68 and 69) more reliable?

### 3.3.3 Smart Rattle Design Without Clamp Modification

In addition to the smart clamp designs, a smart "rattle" was also designed and initially tested. The idea behind the smart rattle is that a tightly bound wire harness will experience higher frequency vibrations than a loose/swinging harness with broken clamps/supports. Instead of stringing a piezo cable the entire length of a wire harness to monitor its vibrational environment, individual smart rattle circuits could be placed at a few select sites (lower weight/cost than piezo cable). The smart rattle could be positioned to monitor the vibrations of a wire harness regardless of support integrity (perpendicular to aircraft motion) or to only monitor unbound, swaying electrical harnesses (horizontal to aircraft motion) as they impact with structures.

For this initial work, the smart rattle was simply a small, cylindrical magnet placed inside an iron coil with electrical connections for monitoring the magnet position. As the magnet moves parallel to the iron core, the voltage output of the core changes both in magnitude and sign. To demonstrate the performance of the smart rattle concept, the magnet/iron core was shaken by hand in the 1-20 Hz range (10 Hz: vibrational speed of shaking table) to produce voltage versus time plots. A representative voltage versus time plot for 1 second of shaking is shown in figure 70. During the shaking process, the magnet moves back and forth in the mid section of the iron core and the produced voltages stays within the voltage range of ± 0.2V.

After a few minutes of shaking, the times between the voltage maxima were calculated and placed into individual frequency bins (1 Hz resolution). The ratio (number of voltage maxima in frequency bin/total number of maxima recorded) was then calculated for each frequency bin to determine the rate at which the core had been shaken. The amplitude (calculated ratio) versus frequency bin plot in figure 71 demonstrates that the majority of the voltage maxima occurred between 4-12 Hz (with the highest amplitudes occurring at 5 and 11 Hz) in agreement with the attempted frequency of the hand shaking. These results indicate that the response time of the simple magnet/iron core setup was sufficient to monitor the expected vibrations of aircraft wire harness. As the clamps on a wire harness fail, the frequency of the wire harness vibrations will be expected to decrease shifting the plot in figure 71 to the left.

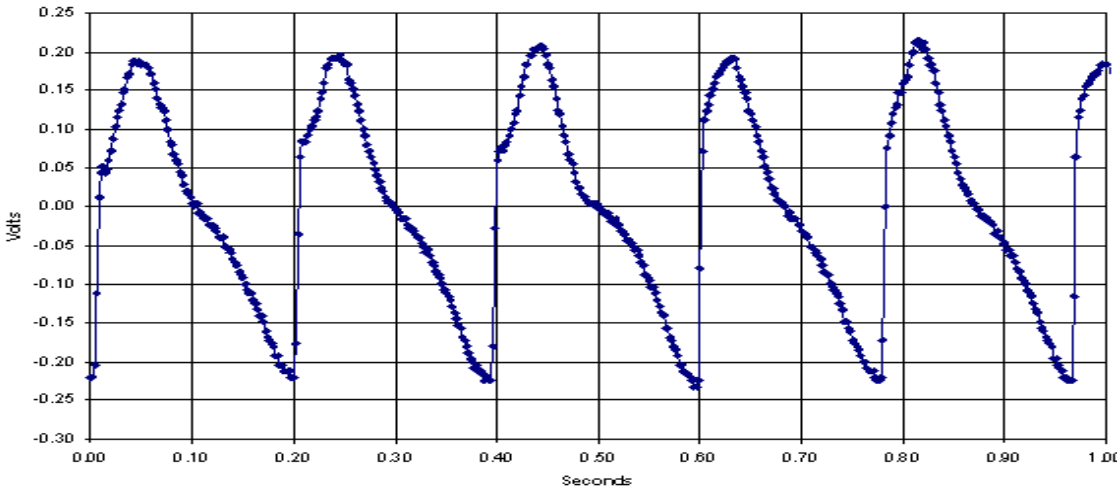


FIGURE 70. REPRESENTATIVE VOLTAGE VERSUS TIME PLOT PRODUCED BY THE SMART RATTLE DURING 1 SECOND OF HAND SHAKING

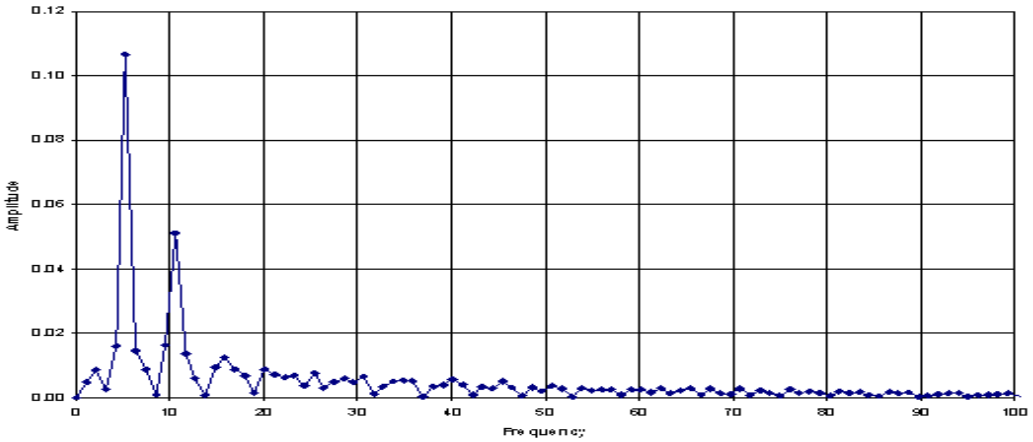


FIGURE 71. PLOT OF AMPLITUDE VERSUS FREQUENCY BIN PRODUCED BY THE SMART RATTLE DURING HAND SHAKING EVALUATION

To determine the magnet/iron core response for a loose wire harness impacting a structure, the magnet in the iron core was held in one hand and then hit against the palm of the other hand. The representative voltage versus time plot in figure 72 produced by hitting the iron core against a surface shows that the initial voltage output maxima are higher than in figure 71 (magnet moved further toward end of core by impact) followed by voltage maxima that decrease rapidly at a higher frequency than figure 71 (magnet restored to original position by magnetic force). To obtain full differentiation between normal vibrations and impact with structures, the iron core would be placed horizontal with the aircraft motion, e.g., normal vibrations would not change magnet position with respect to the core (no voltage output) while the swinging motion would create small voltage outputs that would increase suddenly with each harness impact of the aircraft structures.

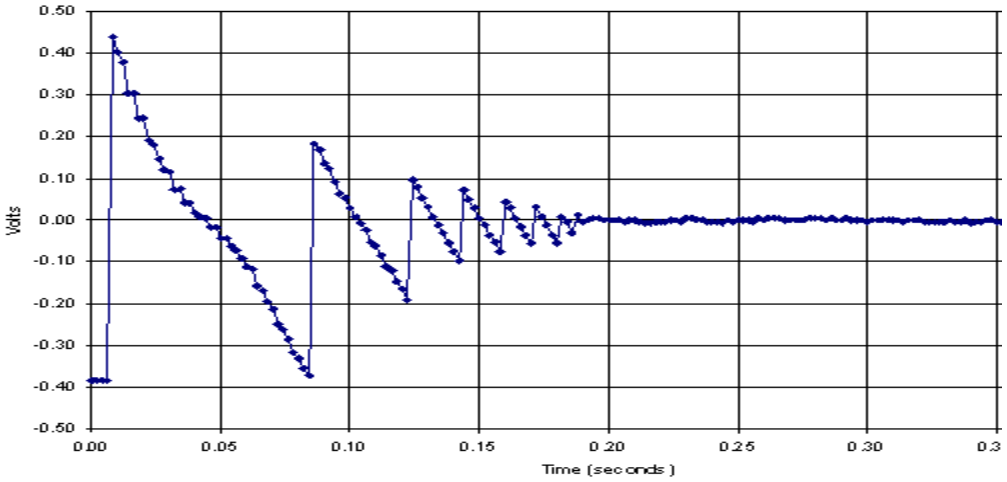


FIGURE 72. REPRESENTATIVE VOLTAGE VERSUS TIME PLOT PRODUCED BY THE SMART RATTLE HITTING AGAINST PALM OF HAND

## 3.4 SUMMARY

During this study the piezo cable was considered as both a short detector (detects breach of wire insulation) and vibration-induced fault sensor (figures 8 – 12). Using the piezo cable as a short detector is not practical at this time as it would require multiple cables and much more complex signal conditioning circuitry and electrical connections. A stand-alone signal conditioning board is capable of determining clamp failure by monitoring the "normal" vibration levels of the wiring system during flight. When the vibration signature changes from "normal" or the low frequency signal magnitude/high frequency signal magnitude ratio increases (5 – 25 Hz versus 30 – 60 Hz for the shaker table used in this study), it would be an indication of clamp failure or possibly tie loosening/breakage. The method is relatively inexpensive, has low to moderate weight penalty, and a low volume penalty making the piezo cable potentially suitable for aircraft use. Some of the remaining issues to be evaluated before flight testing the piezo cable are the relationship between cable length and signal-to-noise ratio, reparability, temperature effects, feasibility of using networked cables, and a defined time for the circuit to learn the normal baseline signature of different vibrational profiles. A patent application has been filed titled: Method for Detecting Vibration-Induced Failures in Wiring Bundles.

Although not as fully developed as the vibration technique using piezoelectric cables, a promising technique based on an electromagnetic induction method, EIM, to monitor the degradation of unopened connectors was identified. The technique wraps loose wires with stripped ends tightly around the EWIS wires to form coils on both sides of the connector of interest. When a continuous electromagnetic signal passes through the connector, the phase difference between the voltages detected by the hand wound coils can be measured using a lock in amplifier. Although more experimentation with systematically degraded connectors is needed to draw firm conclusions, the preliminary data shows significant differences between the pristine connector and the degraded connectors (abrasion, chemical and vibration). These results show

that this methodology has the potential to be used as a practical method to detect connector degradation and is suitable for development into a maintenance facility level technique.

Although preliminary, the initial results produced for the smart clamp and rattle demonstration devices indicate that the simple designs have potential for development into sensors for detecting wire harnesses with loose/broken clamps prior to insulation damage. The smart clamps would also have potential in ensuring proper clamp installation. Other than miniaturization, future efforts would focus on the techniques used to power and process the data outputs of the smart sensors.

## 4. REFERENCES


1. Previous FAA Report

2. Voropai, N. and Shiyaev, A., "Influence of heating on diffusion processes and properties of bimetallic joints of aluminum and copper," Institute of Metallurgy of the academy of Sciences of the USSR. Translated from Metallovedenie I Termicheskaya Obrahotka Metallov, No. 12, pp. 55-57, December 1967.

3. Hentzell, H., Thompson, R. and Tu, K., "Interdiffusion in copper-aluminum thin bilayers. I. Structure and kinetics of sequential compound formation," J. Appl. Phys. V. 54(12), pp. 6923-6928, December 1983.

4. Advanced TDR techniques, Hewlett Packard Application Note 62-3, May 1990.

5. Mackay, N. A. and Penstone, S. R, "High sensitivity narrow-band time domain reflectometer,' IEEE Trans. Instrum. Meas., 23, 155-158 (1974).

6. Furse, C., Chung, Y. C, Dongoal, Nielsen, Maney, G, and Woodward, R. "Frequency – Domain Reflectometry for on-Board Testing of Aging Aircraft Wiring," IEEE Trans. Electromag. Compat. 45, 306-315 (2003).

7. Tsai, P.; Chet Lo; You Chung Chung; Furse, C. "Mixed-signal reflectometer for location of faults on aging wiring," IEEE Sensors Journal v 5 n 6 2005 p.1479-82.

8. You Chung Chung; Furse, C.; Pruitt, "Application of phase detection frequency domain reflectometry for locating faults in an F-18 flight control harness," J. IEEE Transactions on Electromagnetic Compatibility v 47 n 2 2005 p.327-34.

9. Chet Lo; Furse, C, "Noise-domain reflectometry for locating wiring faults," IEEE Transactions on Electromagnetic Compatibility v 47 n 1 2005 p.97-104.

10. Smith, P.; Furse, C.; Gunther, "Analysis of spread spectrum time domain reflectometry for wire fault location," J. IEEE Sensors Journal v 5 n 6 2005 p.1469-78.

11. Yong-June Shin, Choe, T, Song, E., Park, J., Yook, J., Powers, E. J., " Joint Time Frequency Domain reflectometry for diagnostics of coaxial cables, " Eighth Joint NASA/FAA/DoD Conference on Aging Aircraft, Feb. 2005.

12. Walz, M. J., Huang, M. E., Sadock, M., “Hilbert Huang Transform for single wire diagnostics,” Proceedings of Ninth Joint NASA/FAA/DoD Conference on Aging Aircraft, March. 2006.

13. Doorn, E.v., Tolani, D., “Radical extension of TDR for detection and location of flaws in aircraft wiring system,” Proceedings of Ninth Joint NASA/FAA/DoD Conference on Aging Aircraft, March. 2006.

14. http://en.wikipedia.org/wiki/Amperes_Law

15. Jones, D.L. and Wang, L.C., “A Microampere Radiotelemetry Transmitter for Measurement of Temperature from Unrestrained Subjects,” Journal of Applied Physiology, Vol. 44 (4), pp. 607- 610.

# APPENDIX A - FATIGUE TEST OF WIRES

To determine the fatigue resistance of the Cu and CCAL wires and different conductive silver coatings on PBO wires, the fatigue tester developed during this work and shown in figure A1 was used to bend the weighted wires 90º in two directions.

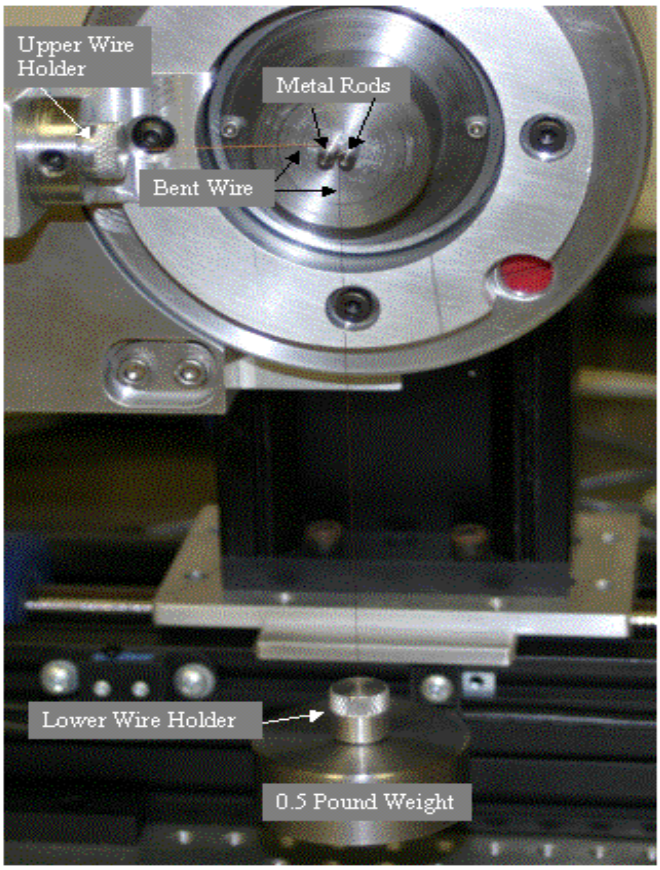


FIGURE A-1. INITIAL POSITIONING OF BENT WIRE IN FATIGUE TESTER

The wire to be tested was threaded through the upper wire holder and then through the lower wire holder attached to the 0.5 pound weight. The middle of the wire was then placed on the left metal rod and the weight was slowly lowered until the wire was taut and a 90º angle in the wire was obtained. The left wire holder was then mechanically rotated clockwise around the circumference of the metal face until the wire was bent at a 90º angle around the right metal pin. The upper wire holder was then rotated counterclockwise until the wire was again bent 90º around the left pin (initial starting position). Bending the wire clockwise then counterclockwise to the beginning position constituted one cycle.

Since the PBO wires did not break under the test conditions shown in figure A-1, the coating failure was determined visually and by resistance measurements after each cycle. A coating was deemed failed when the black surface of the PBO filament was visible and/or the resistance of the conductive film exceeded 100 KΩ.

APPENDIX B- SELF-REPAIRING WIRE EXPERIMENTAL

## B.1 ELECTRICAL SET-UP AND PROCEDURE.

In order to initially evaluate the potential of the different materials for use in the self-repairing solution concept, two electrically isolated metal or alloy wires were placed in one of the basic geometries illustrated in figure B-1.

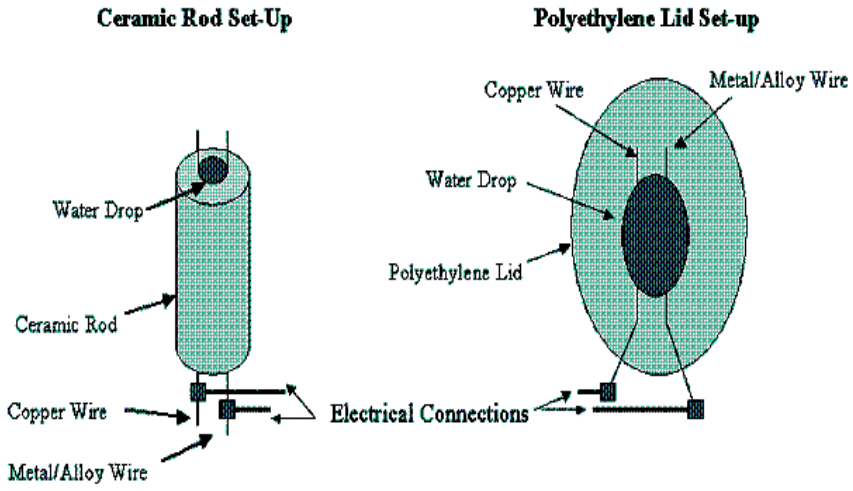


FIGURE B-1. EXPERIMENTAL SET-UPS TO SUPPORT A WATER DROP BETWEEN TWO METAL WIRES

In each geometry, the metal wire pair was spaced approximately 1 mm apart and kept electrically isolated by the ceramic rod or by the polyethylene lid. For each wire pair, one set of ends were connected to a 27Vdc voltage electrical source (three 9Vdc batteries in series) and a water or aqueous solution drop was used to complete the electrical circuit by bridging the isolated wires.

To supply the electrical power to the metal wire pairs in figure B-1 and to measure the electrical current between the metal pairs as the water or aqueous solution drop was electrolyzed by the flowing current, the electrical set-up shown in figure B-2 was used.

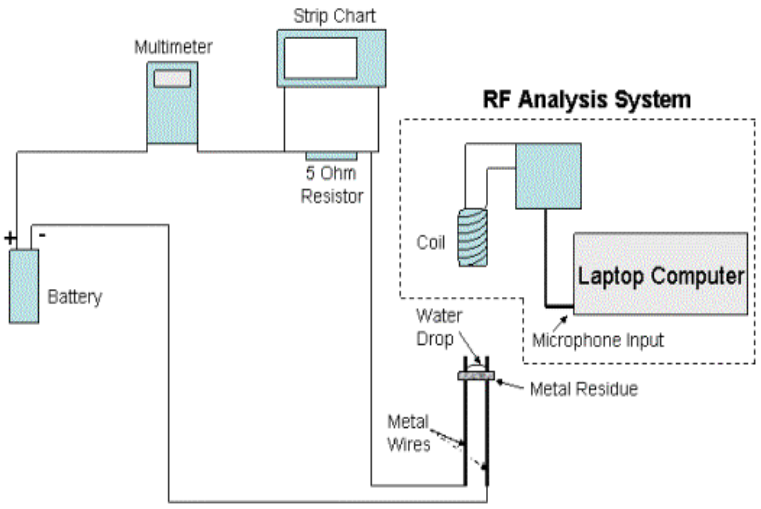


FIGURE B-2. ELECTRICAL CIRCUIT USED IN ELECTROLYSIS EXPERIMENTS

The electrical current was measured in series with a digital multimeter and in parallel (voltage drop across a 5-ohm resistor) by a stripchart recorder. In addition to measuring the electrical current, a spectrum analyzer was set-up as shown in figure B-2 to determine if radio frequencies (RF) were produced by the electrolysis of the water between the metal wires. In earlier research for the FAA [1], an AM radio was used to show that the electrolysis of water drops between silver and copper wire pairs produced measurable levels of RF causing static on the selected AM radio station broadcast channel. The production of RF during electrolysis indicates that miniature sparks/ignition of hydrogen bubbles (small flashes of light observed during hydrolysis) are occurring.

The following procedure was used to evaluate the different self-repairing solutions and RF detection candidates as follows:

1. With the dc battery disconnected, make the electrical measurement connections to the selected metal pair in figure B-1

2. Connect the dc battery to the circuit in figure B-2 and turn ON the multimeter and stripchart recorder to verify that there is no current flow (below 1 μA)

3. Turn ON the spectrum analyzer and position its antenna directly above the wire pair. Turn ON the AM radio and position its antenna side towards the wire pair.

4. Add a drop of water, water suspension or water solution to the ceramic or polyethylene surface between the wires. Record any observations (deposit formation, hydrogen bubbles on negatively charged wire, static on AM radio, etc.)

5. When the current decreases to below 1 mA due to electrolysis of the water, repeat steps 4 and 5 until four drops of water/solution have been added to the wire pair. In the case of poorly performing solutions, stop the test when 0.5 A is reached.

6. Disconnect the wire pair and battery from the circuit and immediately measure the resistance of the wet deposit formed by the electrolysis of the water drop. After 48 hours at room temperature, measure the resistance of the dried deposit, add a drop of water to the deposit and remeasure the resistance of the rewetted deposit.

The initial tests were performed with water obtained from a home dehumidifier (contained 200 – 300 ppm of metals) to simulate the water condensing on wires inside landing aircraft and to increase the conductivity of the original water drop. The metal and metal oxide powders were prepared as 20% by weight suspensions in the dehumidifier water. The organic compounds and polymers were dissolved in the dehumidifier or distilled water to produce 6-10% by weight aqueous solutions as described below.

## B.2 WATER SOLUBLE POLYMERS.

The PVAL polymers used in the research were obtained from Aldrich Chemical Company and ranged from 80 – 98% hydrolyzed (20 – 1% acetate groups remaining). The PVAL molecular weights ranged from 8,000 to 124,000 grams per mole: decreasing molecular weight increases film adhesion and water solubility while the increasing molecular weight increases film strength and water insolubility. The 80 – 89% hydrolyzed PVAL polymers dissolved rapidly into room temperature water with continuous stirring. The PVAL polymers with a degree of hydrolysis greater than 95% were heated to 75ºC with continuous stirring for at least 20 minutes to obtain complete dissolution into the water.

The two different types of modified PVAL polymers used in the research were obtained from Kuraray America (New York, NY) and were labeled R-2105 and KL-318. R-2105 contains silanol groups in its PVAL molecular structures. The silanol groups are reactive with inorganic substances such as silica or alumina and can be easily cross-linked by changing the pH of the solution or by mixing with inorganic substances to form water resistant films. In contrast to R-2105, the KL-308 PVAL (85% hydrolysis) has been carboxylated making the polymer more hydrophilic (improves water solubility) and the carboxyl groups are available for interacting with/removing the oxides on the exposed Cu surfaces

## B.3 DIFFERENT TYPE WATER SOLUTIONS.

The initial water used to produce the PVAL containing test solutions was obtained from a dehumidifier in an attempt to simulate the water condensing on cold aircraft wires and nearby surfaces. Since different batches of dehumidifier water would vary in metal and bacteria content, self-repairing test solutions were also made using distilled water in place of the dehumidifier water to ensure the test solutions were repeatable and stable. Different levels of water-soluble salts and compounds such as cuprous and cupric chlorides, ferric chloride, potassium and sodium chlorides, polyethylene glycol polymers, etc. (Aldrich Chemical Company) were dissolved in the distilled water to produce “synthetic” dehumidifier water that could be used to produce self-repairing PVAL solutions which formed water-insoluble layers on exposed, powered conductors.

In addition to the water-soluble species, water-insoluble species such as magnesium oxide (325 mesh), fumed silica (submicron) and polyvinyl acetate (Elmer’s School glue – 10% solids) were

also investigated in distilled water in an attempt to control where the water-insoluble polymer layered formed when exposed to dc or ac power.

## B.4 PVAL SUSPENSIONS

The water-insoluble matrices selected to suspend the PVAL crystals were low molecular weight polyethylene and beeswax (obtained from Aldrich Chemical Company) due to their melting points being below 150ºC and differences in polarity to affect the solubility of the PVAL in the matrices, i.e., PVAL would be expected to have a higher level of solubility in polar beeswax than in nonpolar polyethylene. After the polyethylene and beeswax were melted, PVAL crystals were mixed into the melted polymers/suspended to produce homogeneous polymer mixtures containing 10, 1 or 0.1% PVAL.

## B.5 INSULATION DAMAGE PROCEDURES FOR PVAL SUSPENSIONS.

To simulate cuts in the wiring insulation, bare Cu wires were dipped in the melted polyethylene and beeswax mixtures containing 1 and 0.1% PVAL then allowed to cool/harden overnight. The coated wires were paired using the polyethylene lid set-up in figure A-1 and connected to a 27 Vdc battery source, cuts were made in the hardened polymers with a razor blade to expose the wires (sparks occurred whenever the blade touched both wires confirming the cut was complete).

To simulate large removal of the wiring insulation, the melted polymer mixtures containing different levels of PVAL were then poured onto opposite ends of bare Cu wire pairs supported by the polyethylene lid set-up as shown in figure A-1. The wires were then connected to 27 Vdc and drops of distilled water were placed between the hardened polymers containing different levels of PVAL.

# APPENDIX C - POLYIMIDE REGENERATION EXPERIMENTAL

## C.1 POLYIMIDE SURFACE PRETREATMENT MATERIALS.

All the chemicals were procured from Aldrich or Alfa-Aesor and used as received. Polyimide resin powder was obtained from Alfa Aesor. Polyvinyledene fluoride (PVDF) and solvents were obtained from Aldrich while siloxane materials were procured from Gelest Inc and used without any further purifications. Siloxanes used under present study were, isobutyltrimethoxy silane (IBTS); trichlorosilane; phenyl silane, diphenyl silane (DPS), and polydimethylsiloxanes (PDMS)

## C.2 SURFACE DAMAGE AND GRAFTING MODIFICATIONS

In a typical procedure, polyimide powder resin was dissolved in an appropriate solvent and siloxanes (5-20% w/w of polyimide) were added to the same solution to produce a homogeneous formulation solution. Addition of siloxanes or fluoropolymers to dissolved polyimide in various ratios was optimized carefully to keep the resulting liquid clear without any noticeable particulate matter. The following formulations were investigated for liquid insulation materials:

- Polyimide resin + IBTS or DPS
- Polyimide resin + PDMS
- Polyimide resin + IBTS or DPS + epoxy
- Polyimide resin + PDMS + epoxy

In some cases, epoxy resin was added to the final formulation to improve the adhesion properties of the final coating to Cu metal when coated either on flat panels or over round metallic Cu wires.

All polyimide experiments were performed on cut Kapton® 500HN (obtained from DuPont) pieces that were 127 μm thick and 4x6 cm in area. Kapton® 500HN has similar physical and chemical characteristics in terms of dielectric constant, tensile strength and hydrolytic stability as those of polyimides used in aircraft wiring insulation manufacturing. To simulate hydrolytic degradation of aircraft wiring, the Kapton® 500HN surfaces were exposed to 2-4% aqueous alkali (sodium or potassium hydroxide) solutions at ambient temperature for 1 day. After the alkali solution treatment, the Kapton® 500HN specimens were rinsed with water and dried in air for 1 day prior to analysis or the coating experiments.

Degraded pieces were dipped in the silane reaction mixtures for 30 minutes and then dried in air without rinsing with any solvent. After curing for 1 day in air, surface treated Kapton® 500HN sheets were evaluated/analyzed using different techniques. In the case of the IPN coatings, the solution was warmed to 45°C and the Kapton® 500HN pieces were dipped in or brushed with the heated coating solution. The coated Kapton® 500HN pieces were then dried in the oven for about 3 hrs. Also small disks were casted by solvent evaporation from the IPN coating formulations to study bulk polymer properties.

In the case of the hook-up wires, the formulations were applied on an exposed metal area or degraded polyimide area by brush or dip coating. Multiple passes of coatings were required in

certain formulations in order to obtain the thickness of the original wire gauge. The coated polymers were cured at 60°C in the oven for about 2 hrs or at 100°C for 10 min. Also small flat panel disks were casted by solvent evaporation from these formulations to study bulk polymer properties

## C.3 ELECTRICAL IMPEDANCE SPECTROSCOPY TEST METHODS.

Evaluations of insulation coatings were carried out by electrical impedance spectroscopy (EIS) measurements. The coated flat coupons or wires were clamped in a standard paint cell and filled with aqueous 2% potassium hydroxide solution as shown in figure C-2. A standard calomel

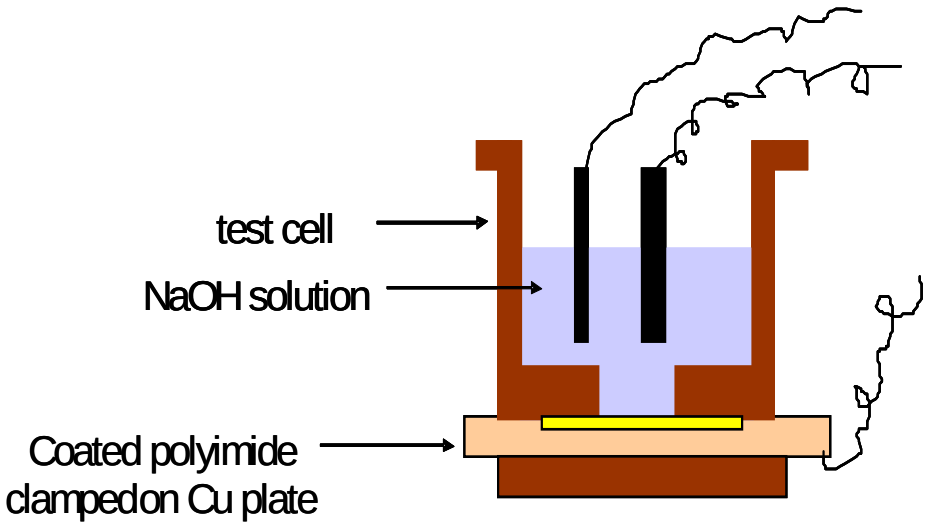


FIGURE C-1. TEST CELL USED IN EIS MEASUREMENTS

electrode (reference electrode) and a platinum wire mesh (auxiliary electrode) were also immersed in the alkali solutions. The copper plate was isolated from the alkali solution by the polyimide sheet and was used as the working electrode. The current densities ranged from 10nA to 1mA/cm$^2$. The electrochemical measurements were performed by using a Gamry electrochemical workstation and the data curves were analyzed with electrochemistry software provided by Gamry.

The EIS measurements monitored the development of microcracks and pores in the immersed polyimide material or insulation coating. Penetration of alkali through the coating or polyimide substrate due to microcracks or pores was reflected by a decrease in the impedance measurements at lower frequencies.

## C.4 RESISTANCE MEASUREMENTS

The resistivities of the_of the fresh and coated Kapton® 500HN materials were measured using 2-point and concentric ring type of electrodes as described in ASTM STD D-257.

APPENDIX D-ANALYTICAL TEST RESULTS FOR WIRE “DIRT”

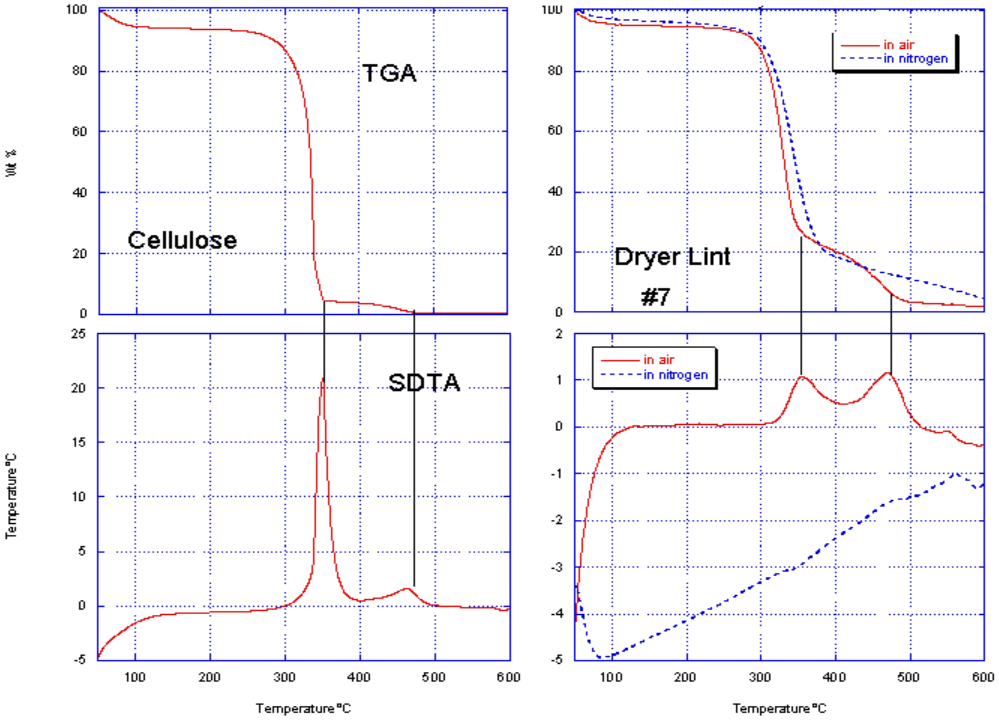


FIGURE D-1. TGA AND SDTA PLOTS FOR CELLULOSE AND DRYER LINT (#7)

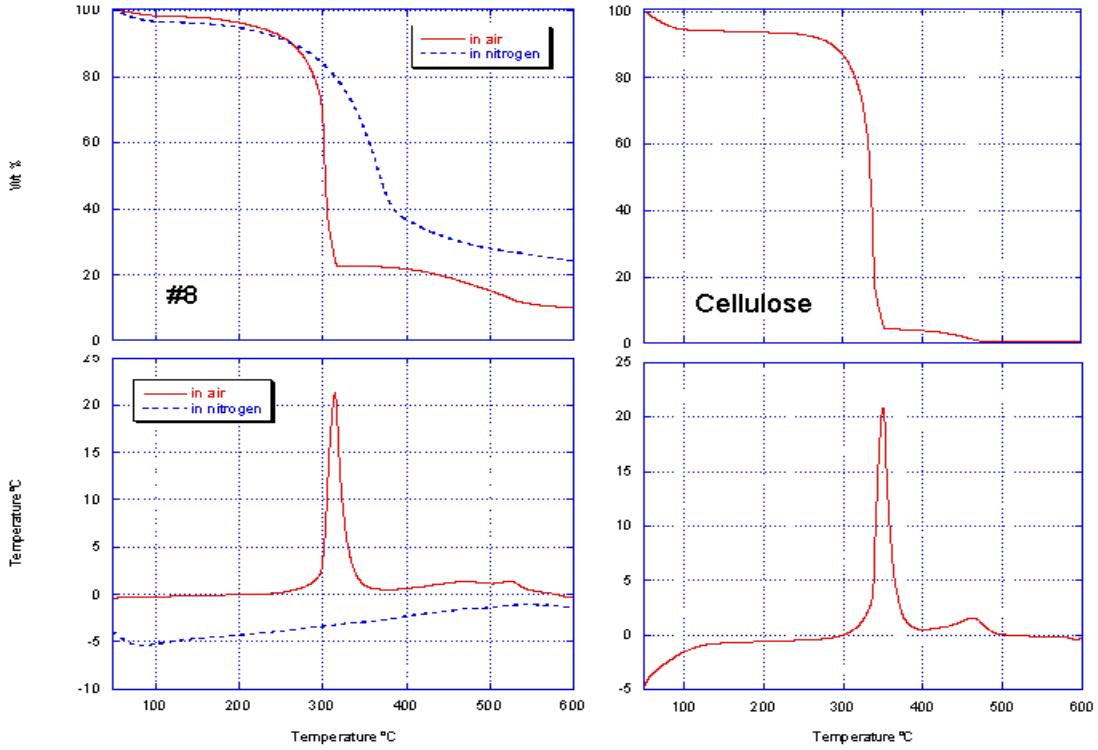


FIGURE D-2. TGA AND STDA PLOTS FOR SAMPLE #8 AND CELLULOSE

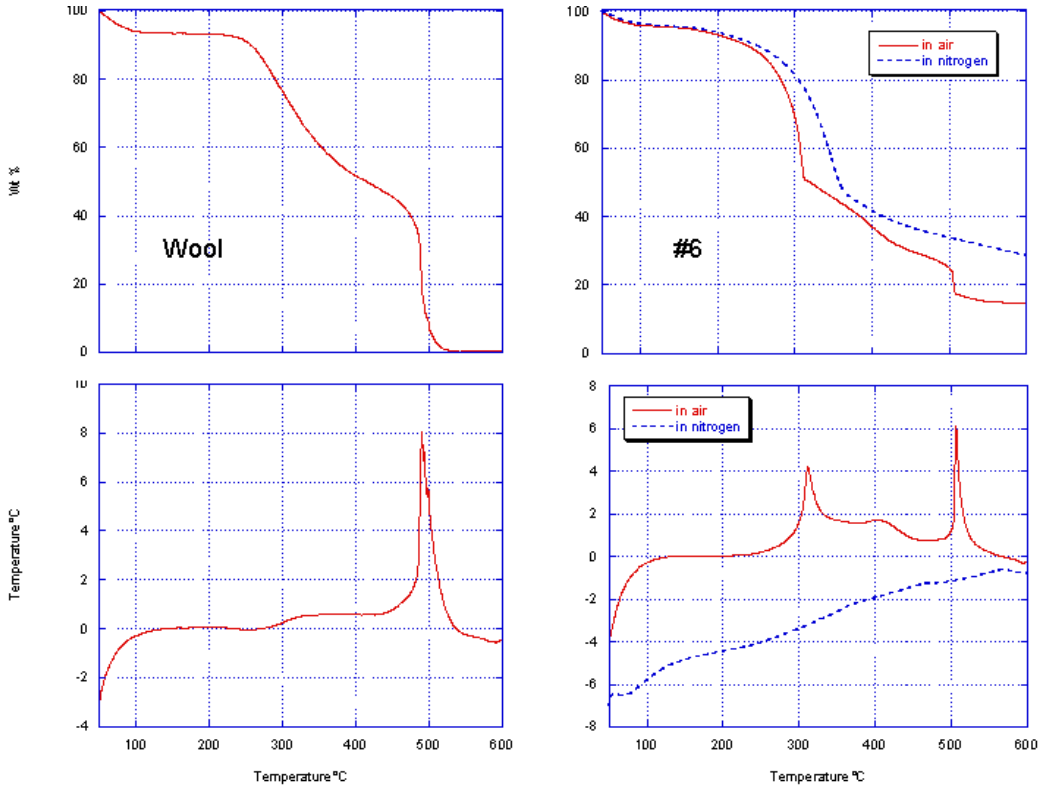


FIGURE D-3. TGA AND SDTA PLOTS FOR WOOL AND SAMPLE #6

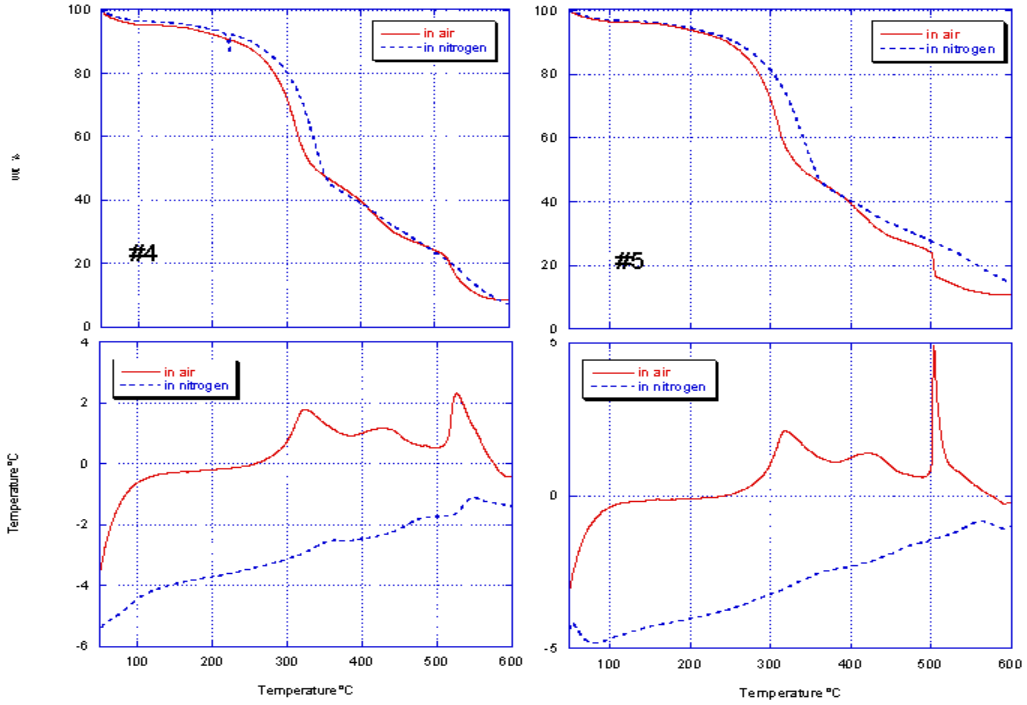


FIGURE D-4. TGA AND SDTA PLOTS FOR SAMPLES #4 AND #5

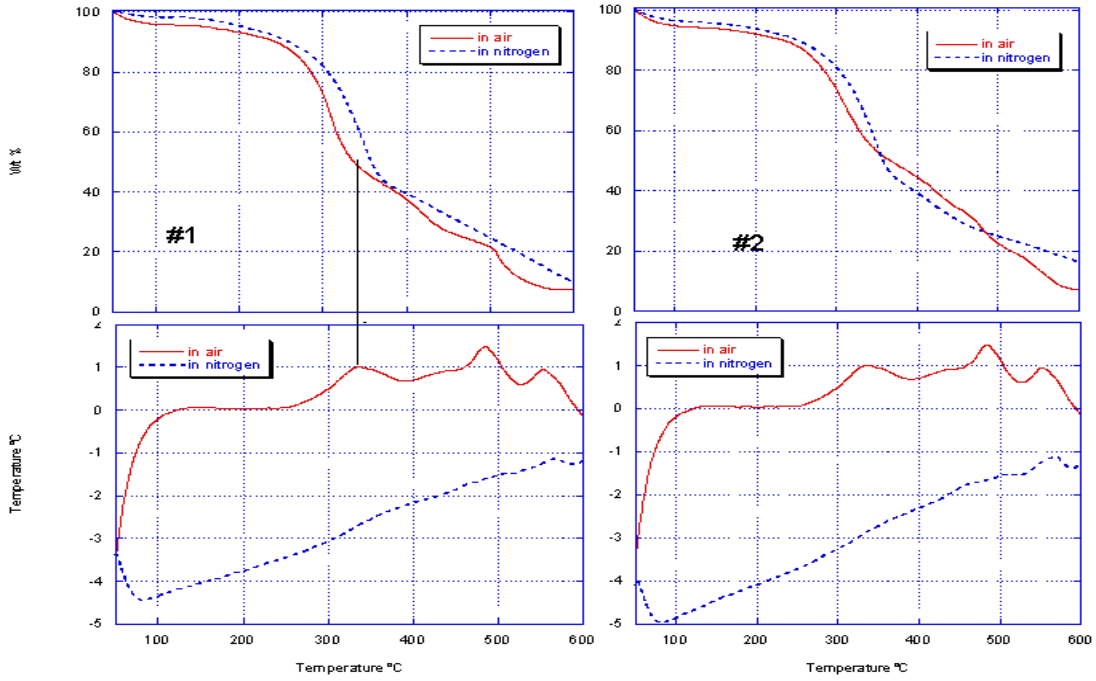


FIGURE D-5. TGA AND SDTA PLOTS OF SAMPLES #1 AND #2

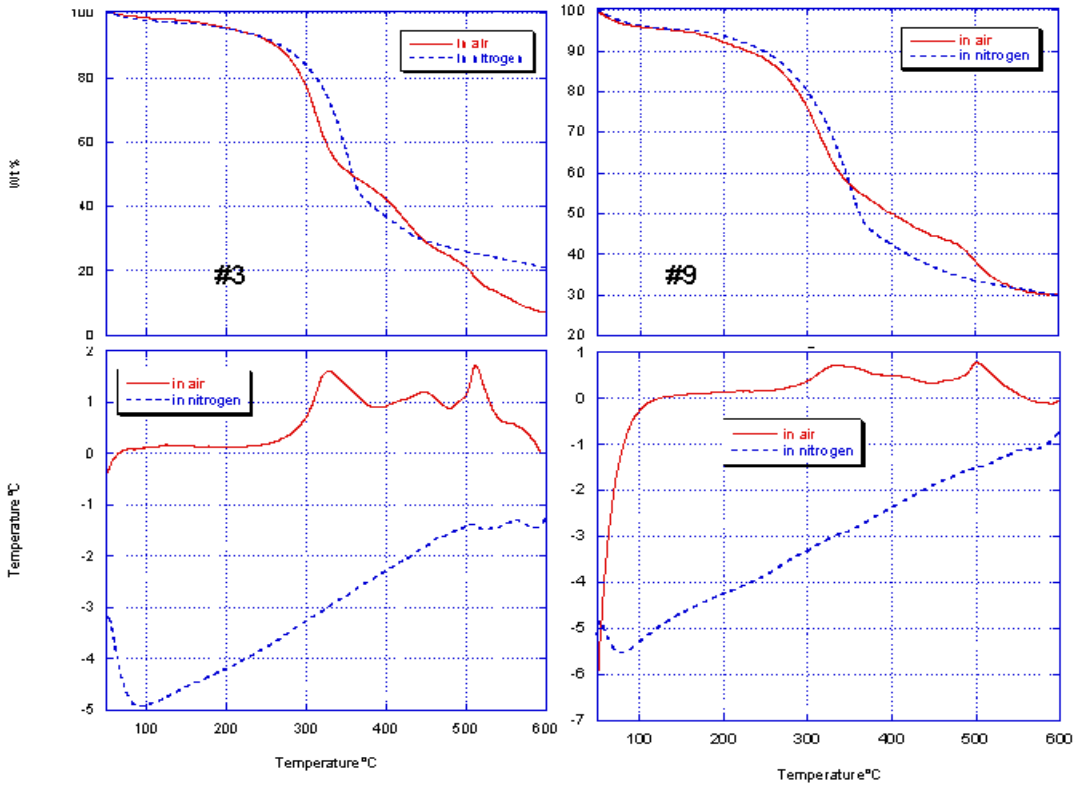


FIGURE D-6. TGA AND SDTA PLOTS OF SAMPLES #3 AND #9

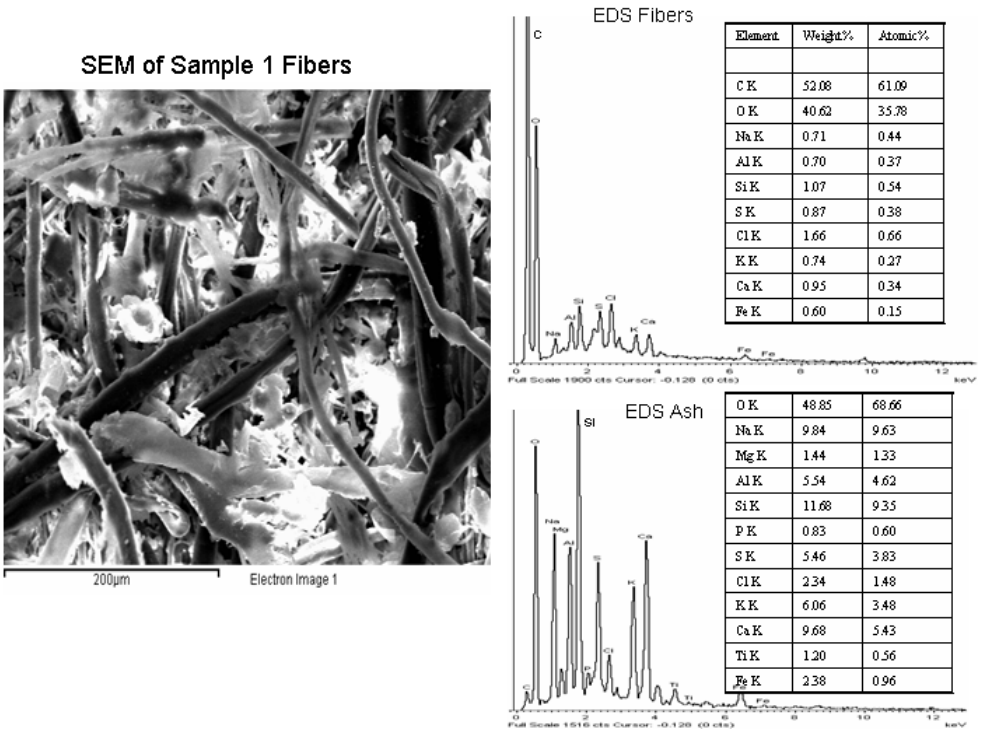


| Element | Weight% | Atomic% |
|---|---|---|
| | | |
| C K | 52.08 | 61.09 |
| O K | 40.62 | 35.78 |
| Na K | 0.71 | 0.44 |
| Al K | 0.70 | 0.37 |
| Si K | 1.07 | 0.54 |
| S K | 0.87 | 0.38 |
| Cl K | 1.66 | 0.66 |
| K K | 0.74 | 0.27 |
| Ca K | 0.95 | 0.34 |
| Fe K | 0.60 | 0.15 |

| | | |
|---|---|---|
| O K | 48.85 | 68.66 |
| Na K | 9.84 | 9.63 |
| Mg K | 1.44 | 1.33 |
| Al K | 5.54 | 4.62 |
| Si K | 11.68 | 9.35 |
| P K | 0.83 | 0.60 |
| S K | 5.46 | 3.83 |
| Cl K | 2.34 | 1.48 |
| K K | 6.06 | 3.48 |
| Ca K | 9.68 | 5.43 |
| Ti K | 1.20 | 0.56 |
| Fe K | 2.38 | 0.96 |

FIGURE D-7. SEM AND EDS ANALYSES OF SAMPLE #1 FIBERS AND ASH

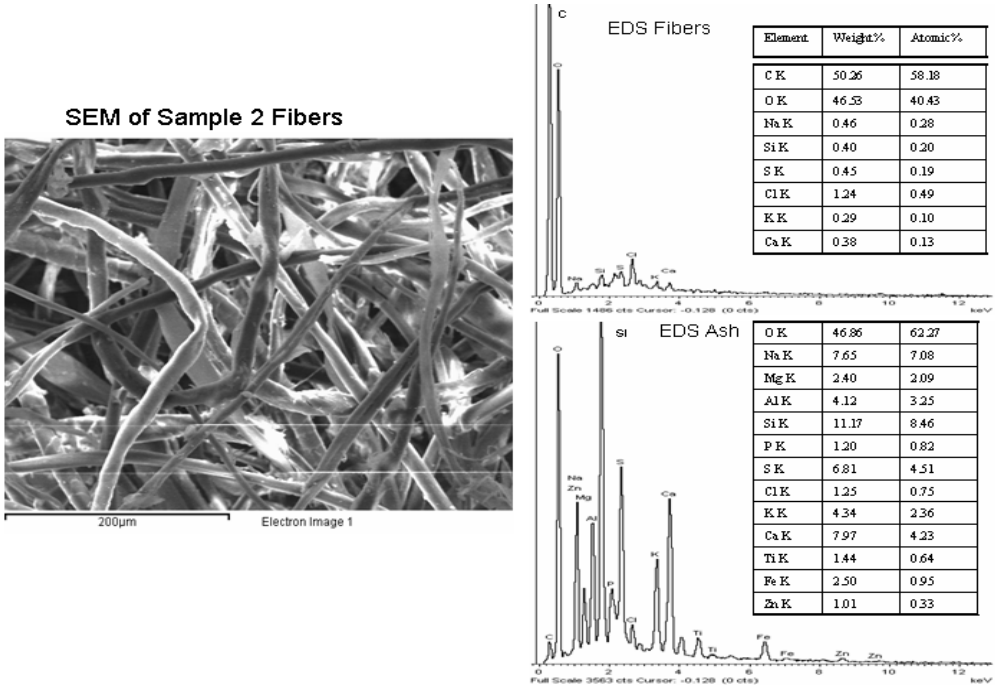


| Element | Weight% | Atomic% |
|---|---|---|
| C K | 50.26 | 58.18 |
| O K | 46.53 | 40.43 |
| Na K | 0.46 | 0.28 |
| Si K | 0.40 | 0.20 |
| S K | 0.45 | 0.19 |
| Cl K | 1.24 | 0.49 |
| K K | 0.29 | 0.10 |
| Ca K | 0.38 | 0.13 |

| | | |
|---|---|---|
| O K | 46.86 | 62.27 |
| Na K | 7.65 | 7.08 |
| Mg K | 2.40 | 2.09 |
| Al K | 4.12 | 3.25 |
| Si K | 11.17 | 8.46 |
| P K | 1.20 | 0.82 |
| S K | 6.81 | 4.51 |
| Cl K | 1.25 | 0.75 |
| K K | 4.34 | 2.36 |
| Ca K | 7.97 | 4.23 |
| Ti K | 1.44 | 0.64 |
| Fe K | 2.50 | 0.95 |
| Zn K | 1.01 | 0.33 |

FIGURE D-8. SEM AND EDS ANALYSES OF SAMPLE #2 FIBERS AND ASH

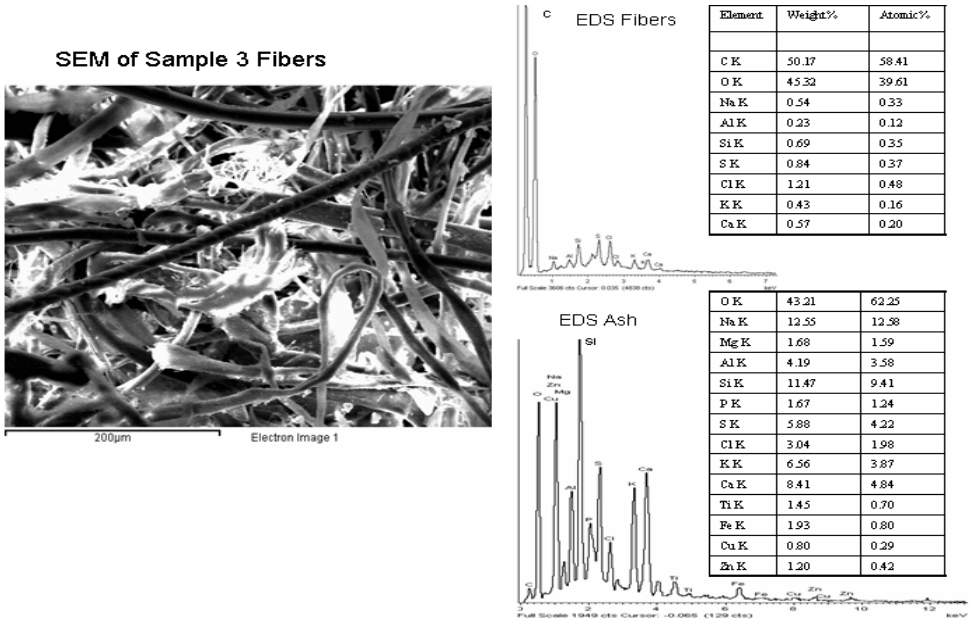


| Element | Weight% | Atomic% |
|---|---|---|
| | | |
| C K | 50.17 | 58.41 |
| O K | 45.32 | 39.61 |
| Na K | 0.54 | 0.33 |
| Al K | 0.23 | 0.12 |
| Si K | 0.69 | 0.35 |
| S K | 0.84 | 0.37 |
| Cl K | 1.21 | 0.48 |
| K K | 0.43 | 0.16 |
| Ca K | 0.57 | 0.20 |

| | | |
|---|---|---|
| O K | 43.21 | 62.25 |
| Na K | 12.55 | 12.58 |
| Mg K | 1.68 | 1.59 |
| Al K | 4.19 | 3.58 |
| Si K | 11.47 | 9.41 |
| P K | 1.67 | 1.24 |
| S K | 5.88 | 4.22 |
| Cl K | 3.04 | 1.98 |
| K K | 6.56 | 3.87 |
| Ca K | 8.41 | 4.84 |
| Ti K | 1.45 | 0.70 |
| Fe K | 1.93 | 0.80 |
| Cu K | 0.80 | 0.29 |
| Zn K | 1.20 | 0.42 |

FIGURE D-9. SEM AND EDS ANALYSES OF SAMPLE #3 FIBERS AND ASH

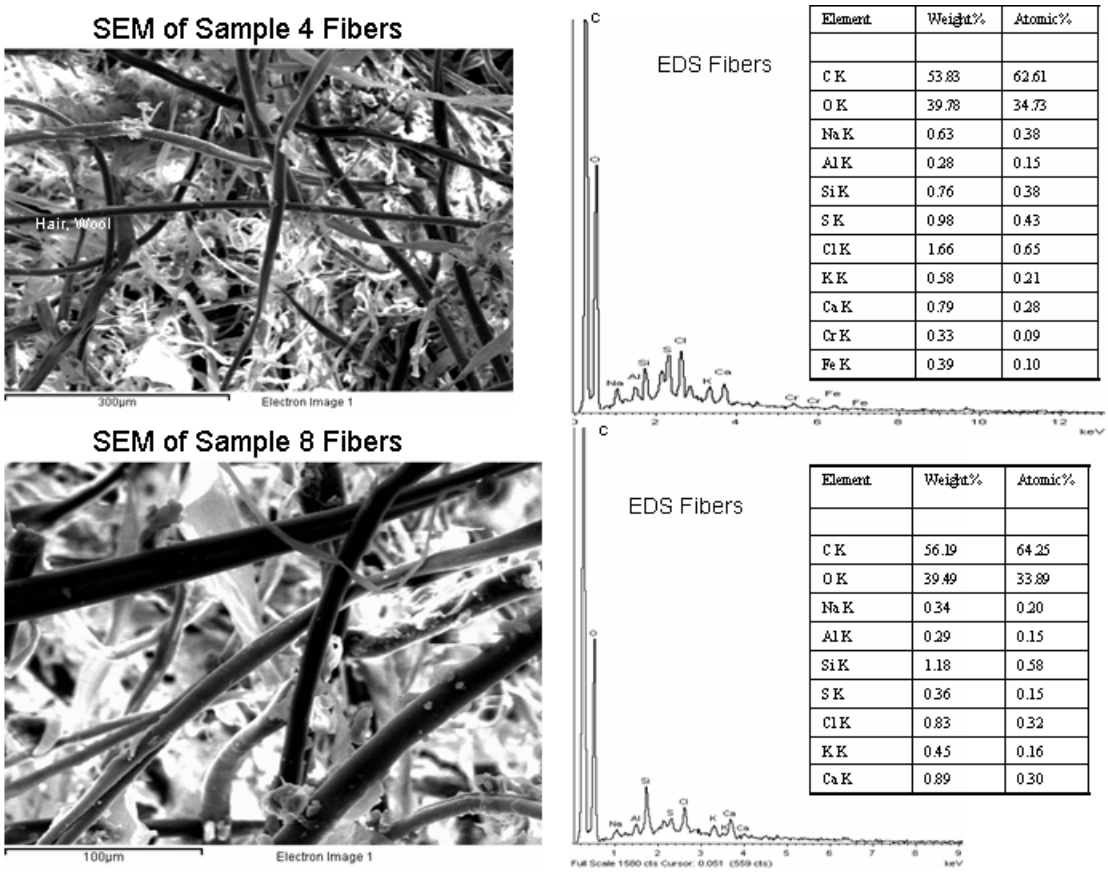


| Element | Weight% | Atomic% |
|---|---|---|
| | | |
| C K | 53.83 | 62.61 |
| O K | 39.78 | 34.73 |
| Na K | 0.63 | 0.38 |
| Al K | 0.28 | 0.15 |
| Si K | 0.76 | 0.38 |
| S K | 0.98 | 0.43 |
| Cl K | 1.66 | 0.65 |
| K K | 0.58 | 0.21 |
| Ca K | 0.79 | 0.28 |
| Cr K | 0.33 | 0.09 |
| Fe K | 0.39 | 0.10 |

| Element | Weight% | Atomic% |
|---|---|---|
| | | |
| C K | 56.19 | 64.25 |
| O K | 39.49 | 33.89 |
| Na K | 0.34 | 0.20 |
| Al K | 0.29 | 0.15 |
| Si K | 1.18 | 0.58 |
| S K | 0.36 | 0.15 |
| Cl K | 0.83 | 0.32 |
| K K | 0.45 | 0.16 |
| Ca K | 0.89 | 0.30 |

FIGURE D-10. SEM AND EDS ANALYSES OF SAMPLES #1 AND #8 FIBERS

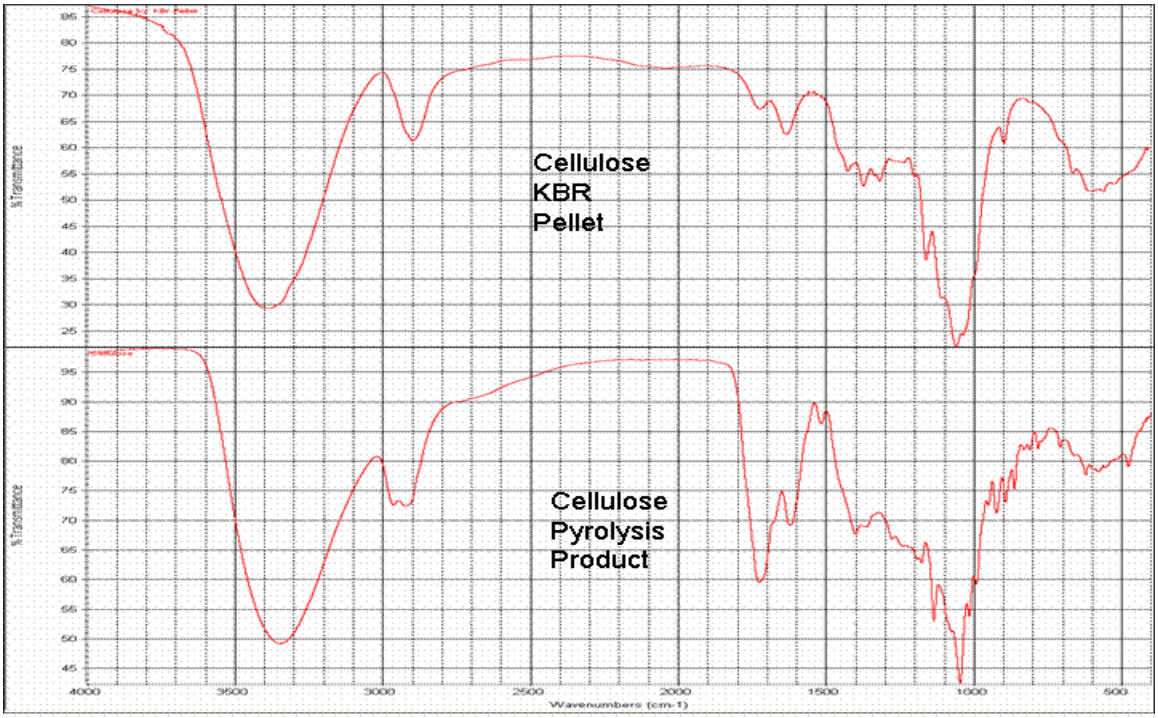


FIGURE D-11. FTIR SPECTRA OF CELLULOSE FIBERS AND PYROLYSIS PRODUCTS

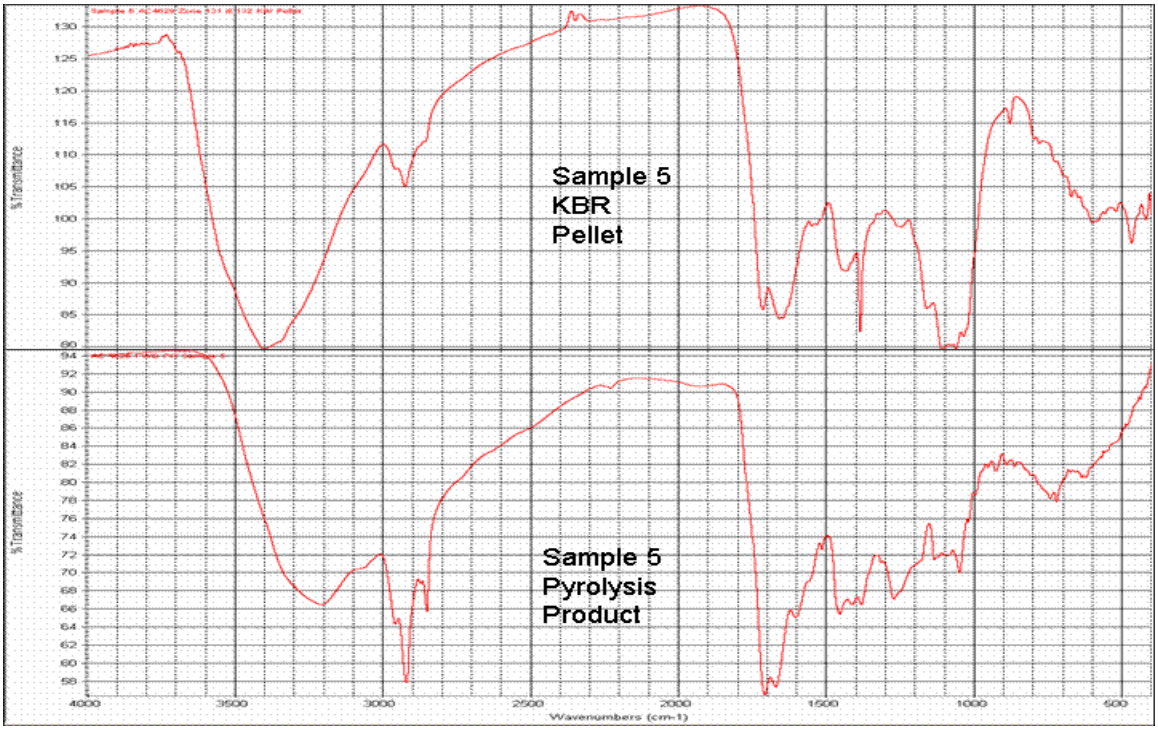


FIGURE D-12. FTIR SPECTRA OF SAMPLE #5 FIBERS AND PYROLYSIS PRODUCTS

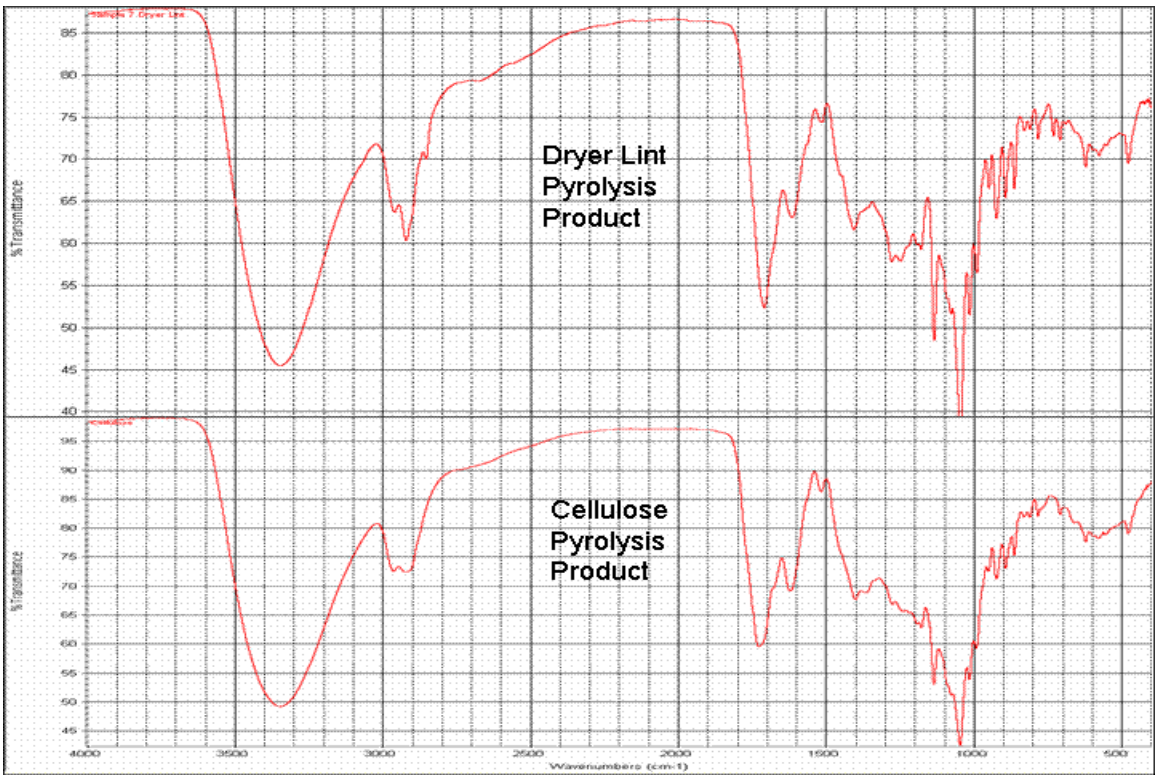


FIGURE D-13. FTIR SPECTRA OF DRYER LINT AND CELLULOSE PYROLYSIS PRODUCTS

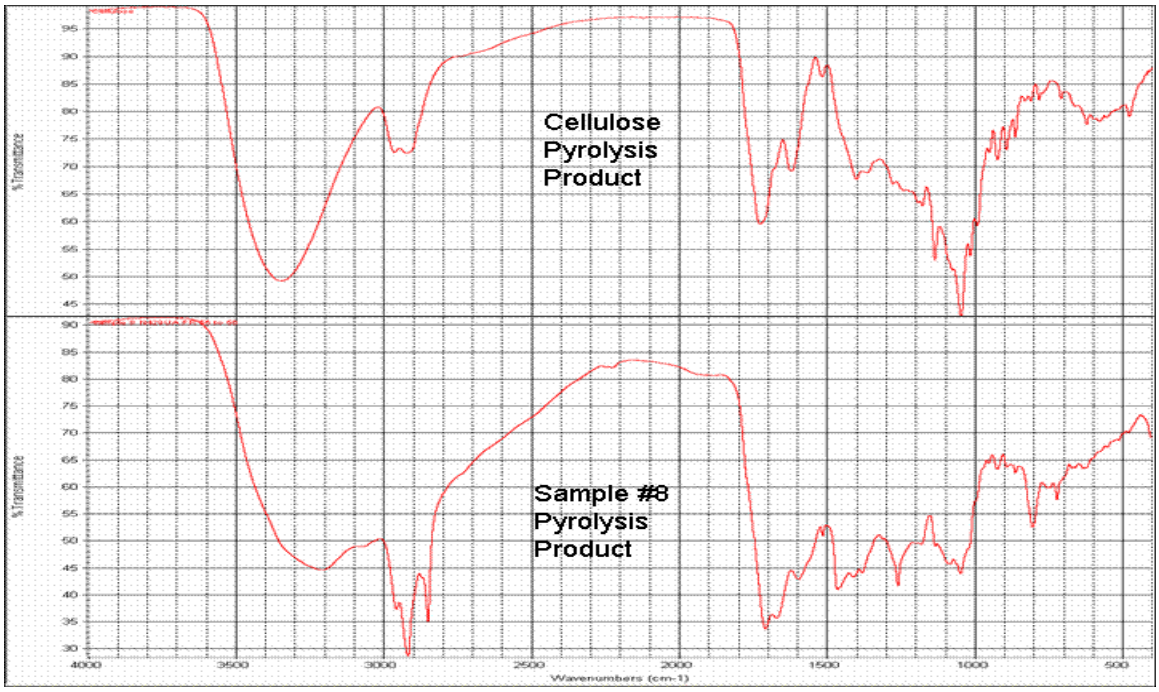


FIGURE D-14. FTIR SPECTRA OF CELLULOSE AND SAMPLE #8 PYROLYSIS PRODUCTS

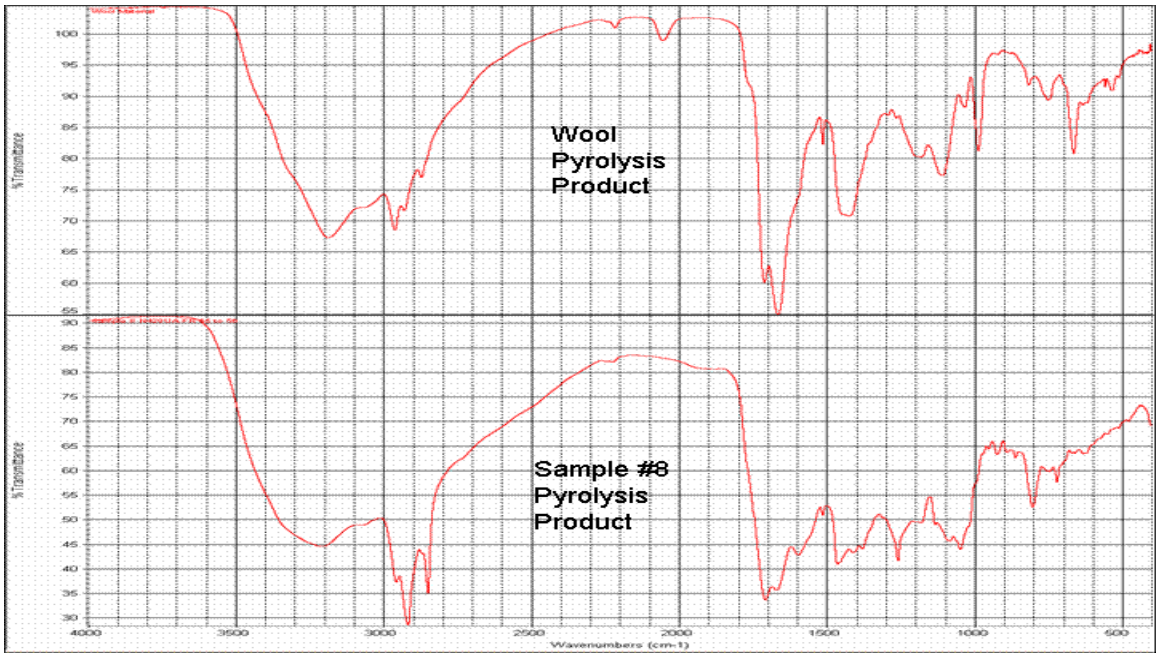


FIGURE D-15. FTIR SPECTRA OF WOOL AND SAMPLE #8 PYROLYSIS PRODUCTS

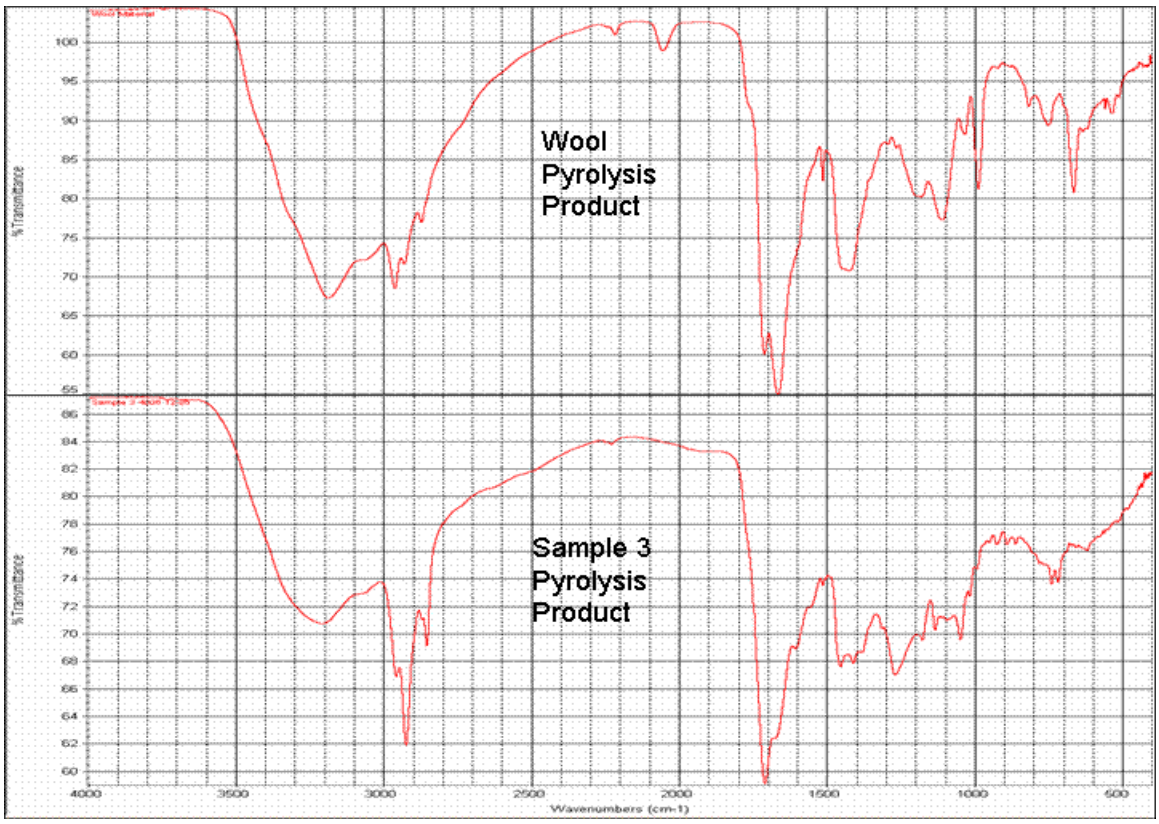


FIGURE D-16. FTIR SPECTRA OF WOOL AND SAMPLE #3 PYROLYSIS PRODUCTS

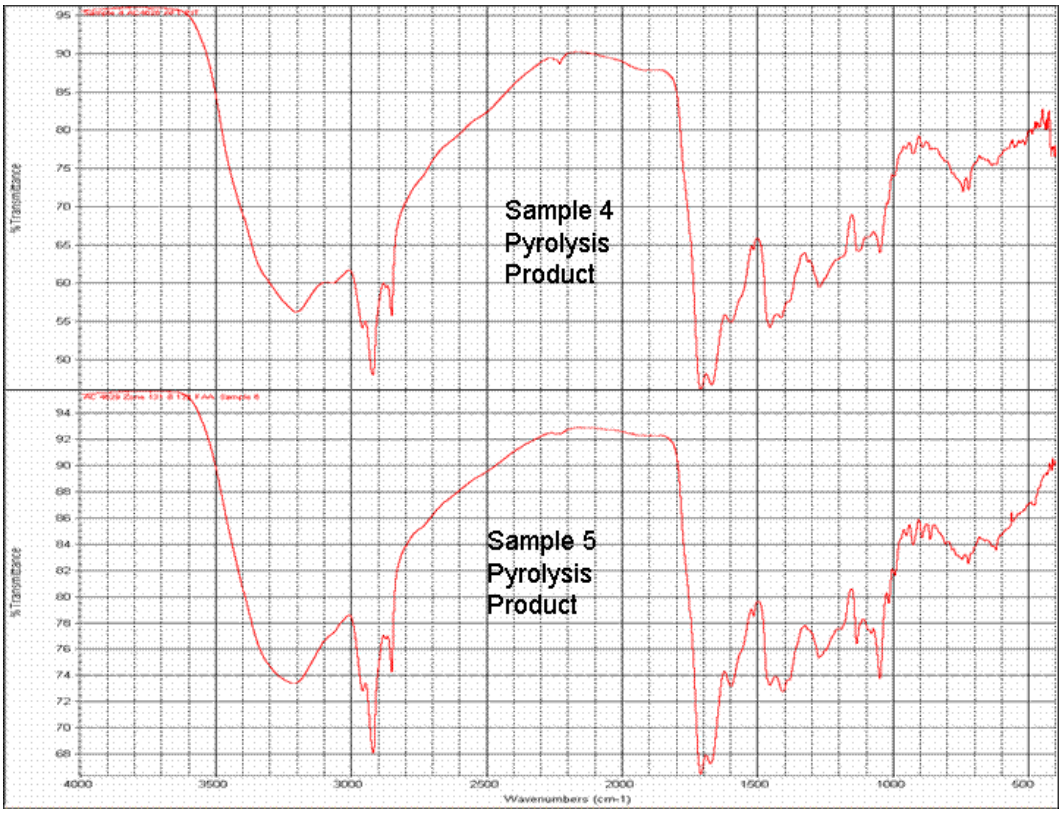


FIGURE D-17. FTIR SPECTRA OF SAMPLES #4 AND #5 PYROLYSIS PRODUCTS

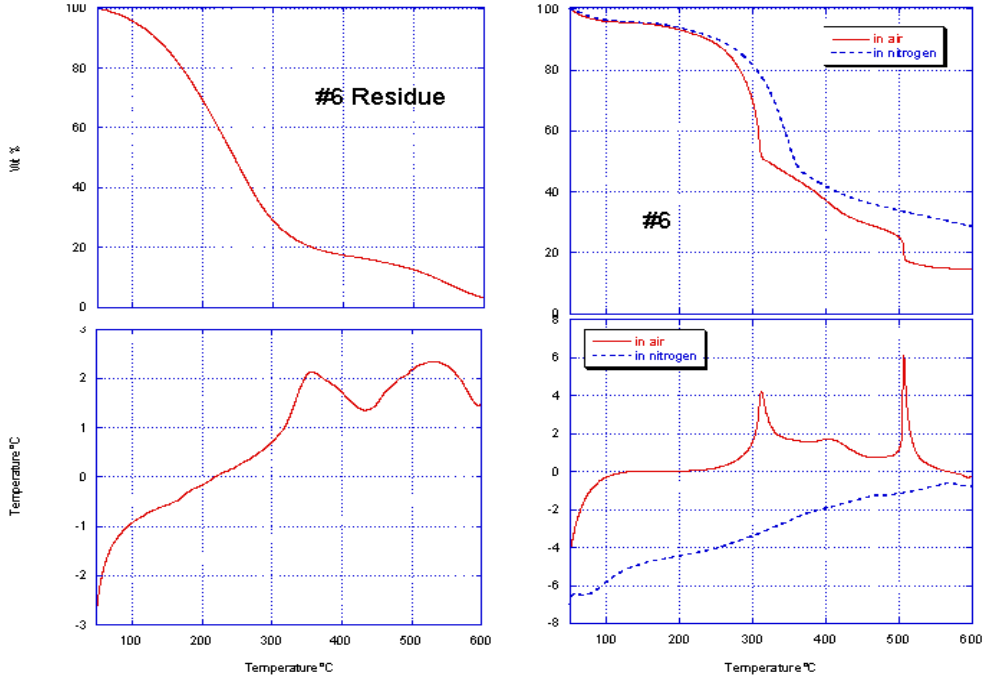


FIGURE D-18. TGA AND SDTA PLOTS OF SAMPLE #6 RESIDUE AND FIBERS

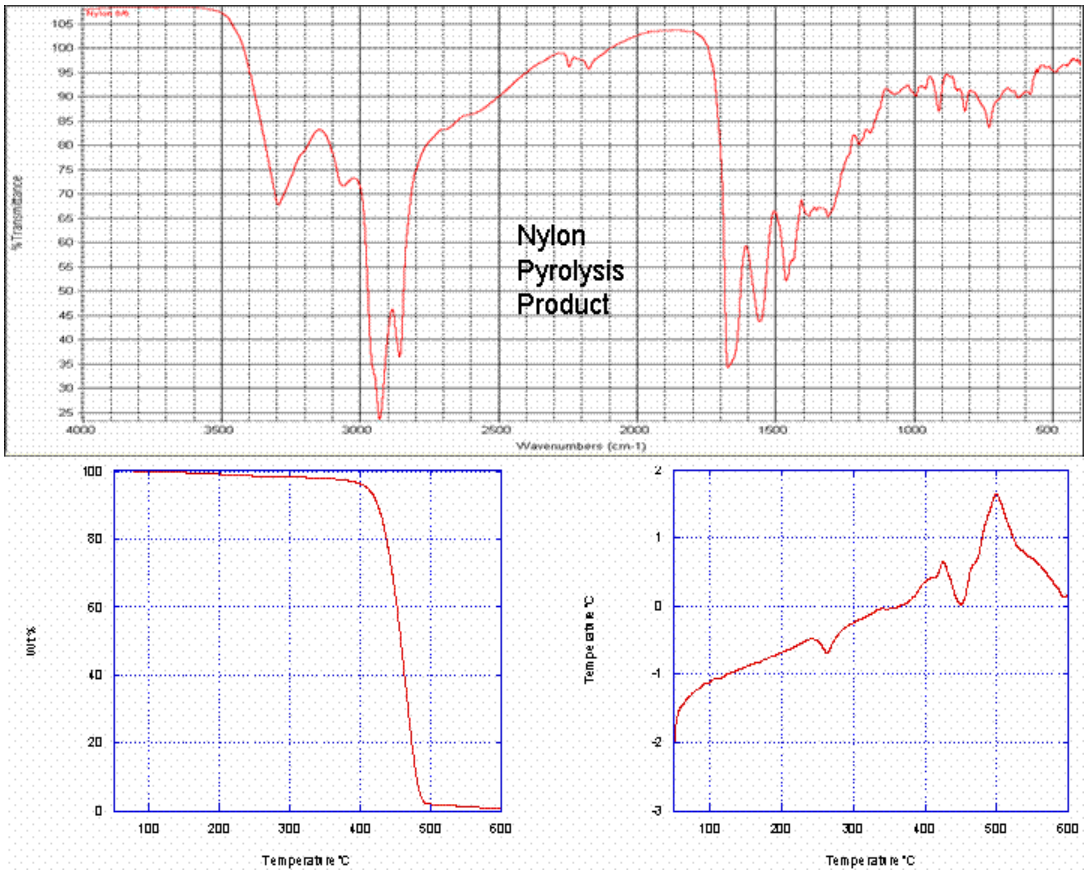


FIGURE D-19. FTIR, TGA AND SDTA ANALYSES OF NYLON

# APPENDIX E: PIEZO CABLE CHARACTERIZATION

## E.1 VIBRATION SHAKER

UDRI's LDS V850 Vibration System (Figure E-1) was used to perform the vibration testing. The frequency range was DC to 3000 Hz and the maximum sine and random vibration force rating was 5000 lbf. The vibration control software was VibControl Vibration Control System by m+p International using the HP 3565S expandable dynamic signal analyzer. Calibration of the LDS vibration system is traceable. The test fixture in figure D-2 was fabricated by modifying an existing aluminum fixture. The vertical section was replaced with 1" thick aluminum stock which was 13" high by 25" wide.

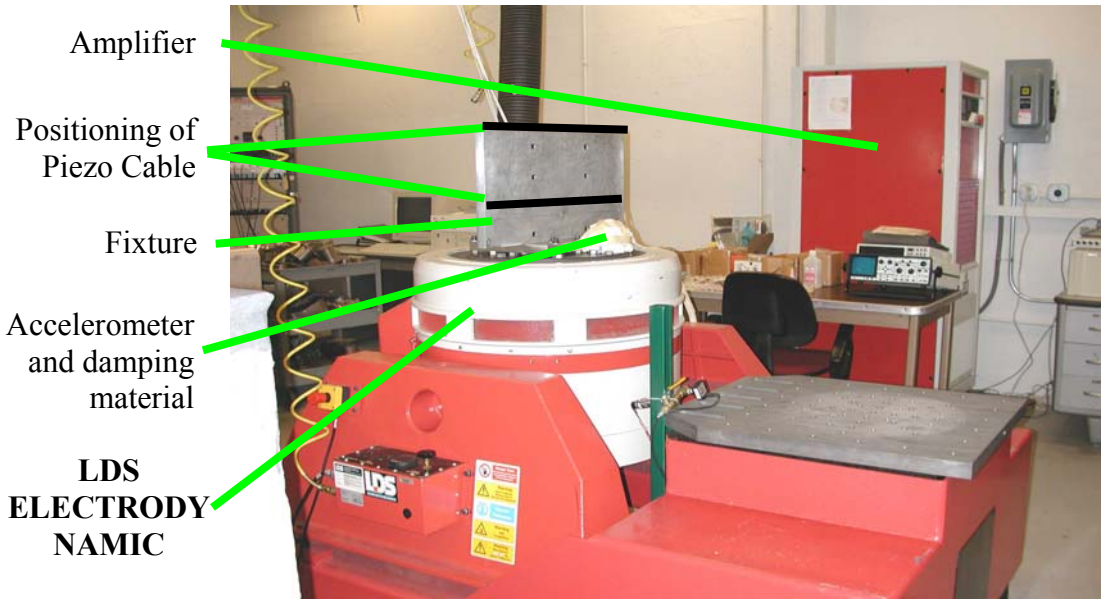


FIGURE E-1. LDS V850 VIBRATION SHAKER WITH TEST FIXTURE ATTACHED

## E.2 PIEZO CABLE.

The piezo cable for sensing the vibration signature was provided by Ormal Electronics Limited. The cable is normally used as a sensor for measuring vibration or displacement over a large area. Vibetek 10 has a medium sensitivity 1.0 pC/N (optimal) with a capacitance of 700 pF/meter. More specifications are provided in the table E-1.

TABLE E-1. SPECIFICATIONS OF VIBETEK PIEZO CABLE

| | |
|---|---|
| Outer diameter | 3.5 mm |
| Inner conductor diameter | 1.0 mm |
| Temperature range | -40 °C to 65 °C |
| Conductor resistance at 20 °C | 33 Ω/km (nominal) |
| Weight / unit length | 19 kg/km |
| Jacket material | Black weather resistant polyolefin |

## E.3 SIGNAL CONDITIONING CIRCUIT

The circuit shown in Figure E-2 was the final configuration used to condition the piezo) cable's signal output to the VibControl software. The circuit utilizes two voltage amplification stages to condition the signal as shown in figure E-3. The first stage has a voltage amplification of two, while the gain of the second stage is adjustable over a wide range (typically between 11 and 200).

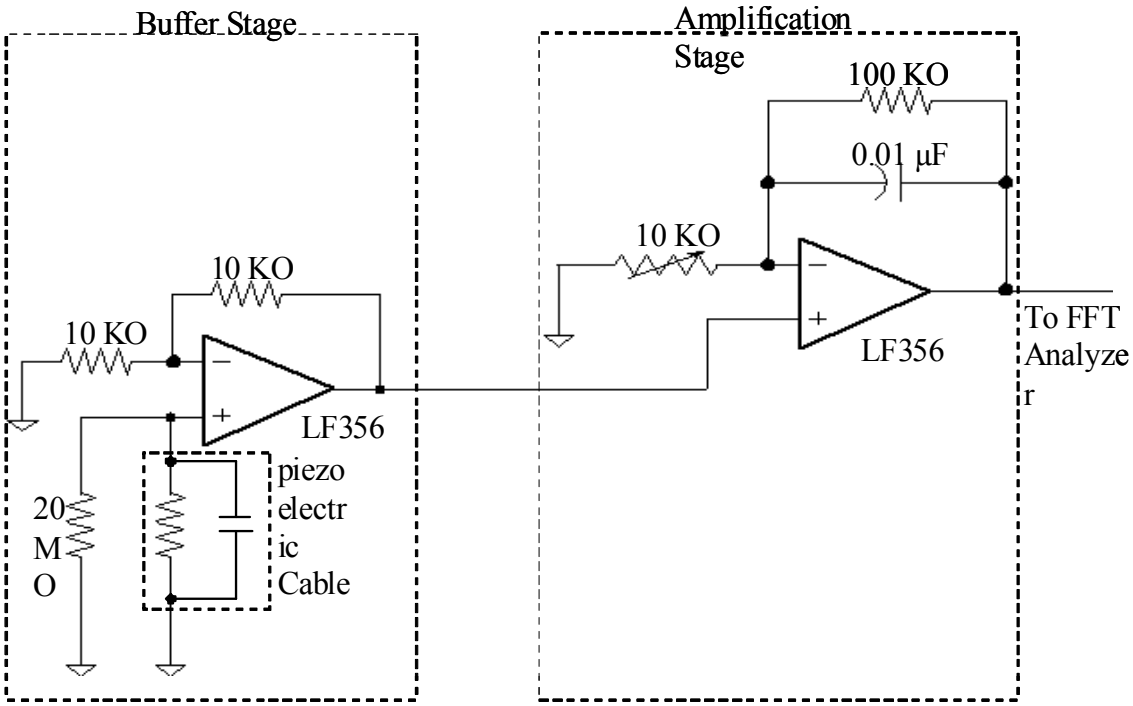


FIGURE E-2. SCHEMATIC OF SIGNAL CONDITIONING CIRCUIT

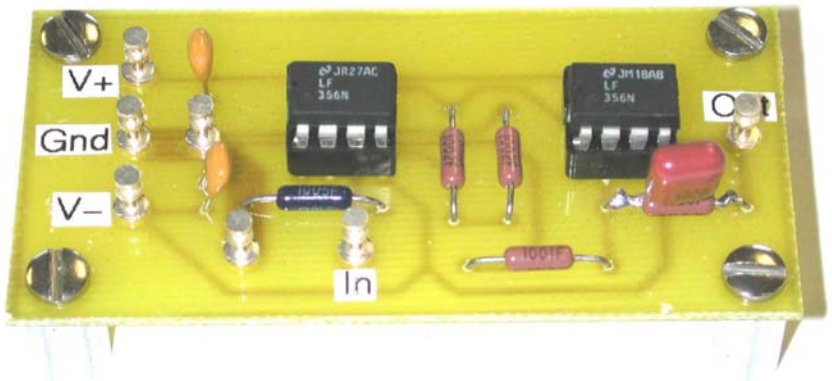


FIGURE E-3. ASSEMBLED SIGNAL CONDITIONING CIRCUIT

The circuit was installed on the test fixture in figure E-1, in lieu of a stationary bench, to eliminate external vibrations in the piezo cable. Batteries were used to provide DC power (as shown in figureE-4) to the signal conditioning circuit. The circuit was specifically built for

this test system and could be further adapted to fit actual situations in an aircraft. For longer cable runs, the sensitivity of this circuit would become too low because of the cable capacitance. This circuit would have to be changed to a charge amplifier to have the sensitivity and bandwidth required to work with longer cable runs.

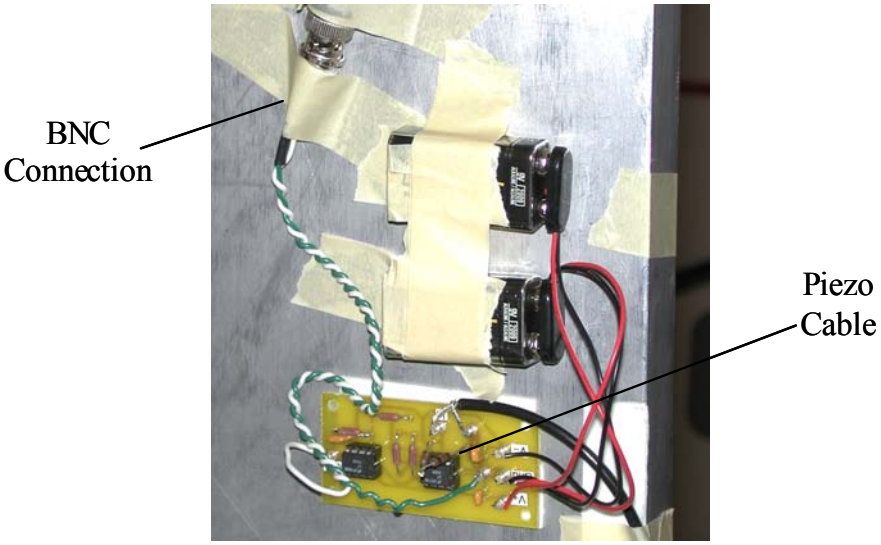


FIGURE E-4. SIGNAL CONDITIONER INSTALLED ON TEST FIXTURE

## E.4 VIBRATION PROFILES & TESTING

Random vibration testing was performed per RTCA / DO-160D Section 8 using fixed wing turbojet, turbofan, and propfan aircraft types. Aircraft fuselage zone applies to all equipment that is attached to frames, stringers, skin, brackets, and other fuselage structures. The test categories H, R, S, and T include standard and robust sine vibration, standard and robust random vibration, and high level short duration sine vibration. The actual vibration profiles are defined by curves C, C1, L, R, and Y. The random curves C (4 g RMS), C1 (6 g RMS), and C2 (8.5 g RMS) were tested because random vibration is the most normally encountered. Random curve C2 is identical to C except all values were increased by a factor of two. A sine profile was also used. The frequency range was from 10 Hz to 500 Hz while the acceleration levels used were 1 g, 2.5 g, and 5 g. A graphical representation of the random profiles is shown in Figure E-5.

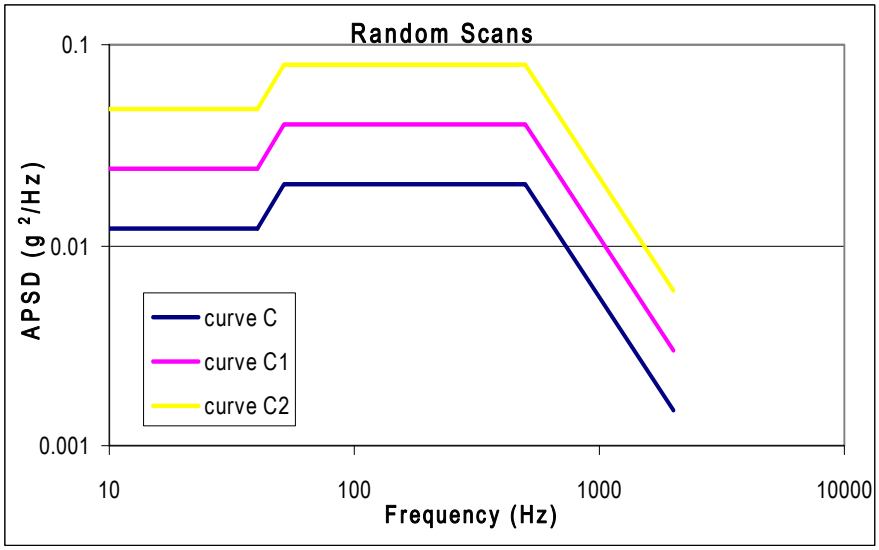


FIGURE E-5. RANDOM VIBRATION PROFILES C, C1, AND C2.

Random piezo cable sensitivities were evaluated at 50 mV/g, 100 mV/g, 150 mV/g, 200 mV/g, 250 mV/g, 500 mV/g, 1000 mV/g, and 1500 mV/g. Sine piezo cable sensitivities were set at 150 mV/g, 200 mV/g, and 250 mV/g.

The piezo cable was positioned along the top of the fixture or on the side in figure E-6. It was attached using instant glue at the ends and with tape across the entire length, at three points (ends and center) or at two points (ends). The piezo cable was tested on its own. No wiring bundle was used. A calibrated accelerometer controlled the shaker.

## E.5 VIBRATION CURVE PROFILE GENERAL PARAMETERS.

TABLE E-2. TEST PROFILE C GENERAL PARAMETERS

| | | | |
|---|---|---|---|
| Frequency Range: | 10 Hz - 2000 Hz | Max. Acceleration: | 12.4 g |
| Resolution: | 2 Hz | Max. Velocity: | 14.2 inDA/s |
| Selfchecklevel: | -12 dB | Max. Displacement: | 0.136 inDA |
| AWF: | 5 | RMS-Abort Limit: | 90 dB |
| Avg./Loop: | 5 | DOF : | 90 |
| Manual Mode: | Yes | Start Limit Check: | -12 dB |
| Control Strategie: | Maximum | RMS Value: | 4.13 g |

Stimulation

| Freq. [Hz] | Accel. [(g)²/Hz] | Slope type [-] | Alarm [dB] | | Aborts [dB] | |
|---|---|---|---|---|---|---|
| 10 | 0.012 | 0 dB/Oct | -1.5 | 3 | -3 | 6 |
| 40 | 0.012 | 6 dB/Oct | -1.5 | 3 | -3 | 6 |
| 51.7 | 0.02 | 0 dB/Oct | -1.5 | 3 | -3 | 6 |
| 500 | 0.02 | -6 dB/Oct | -3 | 3 | -6 | 6 |
| 2000 | 0.0015 | Slope | -3 | 3 | -6 | 6 |

Advanced Parameters:

| | |
|---|---|
| Averages per Loop: | 5 |
| Average weighting factor: | 5 |
| Degrees of freedom: | 90 |
| Line by line check startlevel: | -12 dB |
| Lower freq. Limit: | 10 Hz |
| Upper freq. Limit: | 2000 Hz |
| No of lines out of abort tol.: | 5 % |
| No of lines out of alarm tol.: | 10 % |
| Lower Alarm Limit (RMS): | -3 dB |
| Upper Alarm Limit (RMS): | -3 dB |
| Overall limit (RMS): | 90 dB |

Specimen :

| | |
|---|---|
| Shaker definition: | C:\VcpNT\Daten\LDS-3.shk |
| Max. input Voltage: | 2 V |
| Axial stiffness: | 0 N/m |

Masses:

| | | | |
|---|---|---|---|
| Moving coil mass: | 54 lbs | Fixture name: | modified cooler |
| Fixture weight: | 72 lbs | Specimen weight: | 5 lbs |
| Specimen name: | wiring harness | Items: | 1 |
| Total weight: | 131 lbs | | |

Schedule :

| | | |
|---|---|---|
| Level | 0 dB | 1:00:00 |
| Measurement | - | - |

Channel configuration information :

| No. | C W M | Sensitivity | Coupling | SysGain | Range | Mode | |
|---|---|---|---|---|---|---|---|
| 1 | C | 5 mV/g | Volt AC Gnd | 84.2 g/V | | - | - |
| 2 | M | 250 mV/g | Volt AC Gnd | - | 50 g | | - |

Channel Aborts:

| | | | | |
|---|---|---|---|---|
| 1 | C | 0.001 | 10 | g |
| 2 | M | - | - | - |

TABLE E-3. TEST PROFILE C1 GENERAL PARAMETERS

| | | | |
|---|---|---|---|
| Frequency Range: | 10 Hz - 2000 Hz | Max. Acceleration: | 17.5 g |
| Resolution: | 8 Hz | Max. Velocity: | 17.4 inDA/s |
| Selfchecklevel: | -12 dB | Max. Displacement: | 0.116 inDA |
| AWF: | 5 | RMS-Abort Limit: | 90 dB |
| Avg./Loop: | 5 | DOF : | 90 |
| Manual Mode: | Yes | Start Limit Check: | -12 dB |
| Control Strategie: | Maximum | RMS Value: | 5.83 g |

Stimulation

| Freq. [Hz] | Accel. [(g)²/Hz] | Slope type [-] | Alarm [dB] | | Aborts [dB] | |
|---|---|---|---|---|---|---|
| 10 | 0.024 | 0 dB/Oct | -1.5 | 3 | -3 | 6 |
| 40 | 0.024 | 6 dB/Oct | -1.5 | 3 | -3 | 6 |
| 51.7 | 0.04 | 0 dB/Oct | -1.5 | 3 | -3 | 6 |
| 500 | 0.04 | -6 dB/Oct | -3 | 3 | -6 | 6 |
| 2000 | 0.0025 | Slope | -3 | 3 | -6 | 6 |

Advanced Parameters:

| | |
|---|---|
| Averages per Loop: | 5 |
| Average weighting factor: 5 | |
| Degrees of freedom: | 90 |
| Line by line check startlevel: | -12 dB |
| Lower freq. Limit: | 10 Hz |
| Upper freq. Limit: | 2000 Hz |
| No of lines out of abort tol.: 10 % | |
| No of lines out of alarm tol.: 15 % | |
| Lower Alarm Limit (RMS): -3 dB | |
| Upper Alarm Limit (RMS): -3 dB | |
| Overall limit (RMS): | 90 dB |

Specimen :

| | |
|---|---|
| Shaker definition: | C:\VcpNT\Daten\LDS-3.shk |
| Max. input Voltage: | 2 V |
| Axial stiffness: | 0 N/m |

Masses:

| | | | |
|---|---|---|---|
| Moving coil mass: | 54 lbs | Fixture name: | modified cooler Fixture |
| weight: | 72 lbs | Specimen weight: | 5 lbs |
| Specimen name: | wiring harness | Items: | 1 |
| Total weight: | 131 lbs | | |

Schedule :

| | | |
|---|---|---|
| Level | 0 dB | 1:00:00 |
| Measurement | - | - |

Channel configuration information :

| No. | C W M | Sensitivity | Coupling | SysGain | Range | Mode | |
|---|---|---|---|---|---|---|---|
| 1 | C | 5 mV/g | Volt AC Gnd | 84.2 g/V | - | - | |
| 2 | M | 250 mV/g | Volt AC Gnd | - | 50 g | - | |

Channel Aborts:

| | | | | |
|---|---|---|---|---|
| 1 | C | 0.001 | 10 | g |
| 2 | M | - | - | - |

TABLE E-4. TEST PROFILE C2 GENERAL PARAMETERS

| | | | |
|---|---|---|---|
| Frequency Range: | 10 Hz - 2000 Hz | Max. Acceleration: | 24.8 g |
| Resolution: | 2 Hz | Max. Velocity: | 28.3 inDA/s |
| Selfchecklevel: | -12 dB | Max. Displacement: | 0.272 inDA |
| AWF: | 5 | RMS-Abort Limit: | 90 dB |
| Avg./Loop: | 5 | DOF : | 90 |
| Manual Mode: | Yes | Start Limit Check: | -12 dB |
| Control Strategies: | Maximum | RMS Value: | 8.26 g |

Stimulation

| Freq. [Hz] | Accel. [(g)²/Hz] | Slope type [-] | Alarm [dB] | | Aborts [dB] | |
|---|---|---|---|---|---|---|
| 10 | 0.0484 | 0 dB/Oct | -1.5 | 3 | -3 | 6 |
| 40 | 0.048 | 6 dB/Oct | -1.5 | 3 | -3 | 6 |
| 51.7 | 0.08 | 0 dB/Oct | -1.5 | 3 | -3 | 6 |
| 500 | 0.08 | -6 dB/Oct | -3 | 3 | -6 | 6 |
| 2000 | 0.006 | Slope | -3 | 3 | -6 | 6 |

Advanced Parameters:

| | |
|---|---|
| Averages per Loop: | 5 |
| Average weighting factor: | 5 |
| Degrees of freedom: | 90 |
| Line by line check startlevel: | -12 dB |
| Lower freq. Limit: | 10 Hz |
| Upper freq. Limit: | 2000 Hz |
| No of lines out of abort tol.: | 10 % |
| No of lines out of alarm tol.: | 15 % |
| Lower Alarm Limit (RMS): | -3 dB |
| Upper Alarm Limit (RMS): | -3 dB |
| Overall limit (RMS): | 90 dB |

Specimen :

| | |
|---|---|
| Shaker definition: | C:\VcpNT\Daten\LDS-3.shk |
| Max. input Voltage: | 2 V |
| Axial stiffness: | 0 N/m |

Masses:

| | | | |
|---|---|---|---|
| Moving coil mass: | 54 lbs | Fixture name: | modified cooler |
| Fixture weight: | 72 lbs | Specimen weight: | 5 lbs |
| Specimen name: | wiring harness | Items: | 1 |
| Total weight: | 131 lbs | | |

Schedule :

| | | |
|---|---|---|
| Level | 0 dB | 1:00:00 |
| Measurement | - | - |

Channel configuration information :

| No. | C | W | M | Sensitivity | Coupling | SysGain | Range | Mode | |
|---|---|---|---|---|---|---|---|---|---|
| 3 | | | M | 100 mV/g | Volt AC Gnd | - | 50 g | | - |
| 5 | | | C | 5.25 mV/g | Volt AC Gnd | 72.6 g/V | - | | - |

Channel Aborts:

| | | | | |
|---|---|---|---|---|
| 3 | M | - | - | - |
| 5 | C | 0.001 | 30 | g |

## TABLE E-5. TEST PROFILE SINE GENERAL PARAMETERS

| | | | |
|---|---|---|---|
| Starting freq.: | 10 Hz | Max. Acceleration: | 2.5 g |
| Damping: | 4 | Max. Velocity: | 30.7 inDA/s |
| Manual Mode: | Yes | Max. Displacement: | 0.489 inDA |
| No. Of Sweeps: | 1 | Test Duration: | 0:05:39 |
| Control Strategie: | Average | Sweep rate : | 1 Oct/min |
| Selfchecklevel: | -12 dB | Startup time : | 1 s |
| | | Shutdown time : | 1 s |

Stimulation

| Freq. [Hz] | Accel. [(g)²/Hz] | Veloc [inDA/s] | Displ [inDA] | Slope type [-] | Alarm [dB] | | Aborts [dB] | |
|---|---|---|---|---|---|---|---|---|
| 10 | 2.5 | 3.07e+01 | 4.89e-01 | Auto Acc | -3 | 3 | -9 | 9 |
| 500 | 2.5 | 6.15e+01 | 1.96e-04 | Auto Acc | -3 | 3 | -9 | 9 |

Specimen :

| | |
|---|---|
| Shaker definition: | C:\VcpNT\Daten\LDS-3.shk |
| Max. input Voltage: | 1.41 V |
| Axial stiffness: | 0 N/m |

Masses:

| | | | |
|---|---|---|---|
| Moving coil mass: | 54 lbs | Fixture name: | modified cooler Fixture |
| weight: | 72 lbs wiring harness | Specimen weight: Items: | 5 lbsSpecimen name: 1 |
| Total weight: | 131 lbs | | |

Channel Configuration Information :

| No. | C | W | M | Sensitivity | Coupling | SysGain | Range | Mode |
|---|---|---|---|---|---|---|---|---|
| 3 | | | M | 10 mV/g | Volt AC Flt | - | 100 g | - |
| 5 | | | C | 5.25 mV/g | Volt AC Flt | 98.3 g/V | - | - |

Channel Aborts:

| | | | | |
|---|---|---|---|---|
| 3 | M | - | - | g |
| 5 | C | - | 30 g | g |

## E.6 IN LAB VIBRATION MEASUREMENT GRAPHS - RANDOM

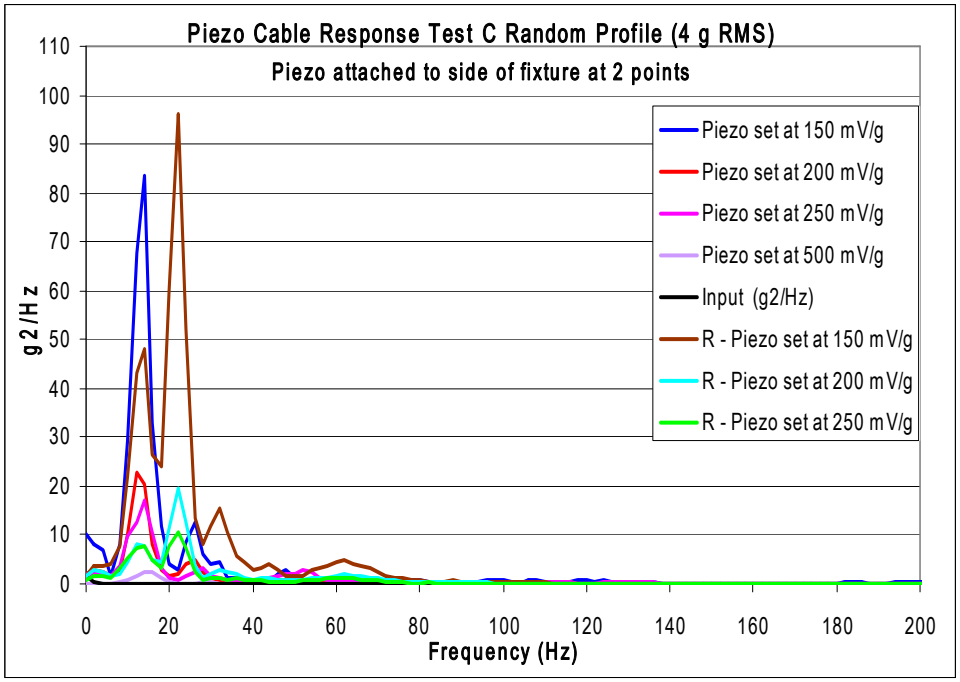


FIGURE E-6. 25" PIEZO CABLE ON SIDE OF FIXTURE 4 G

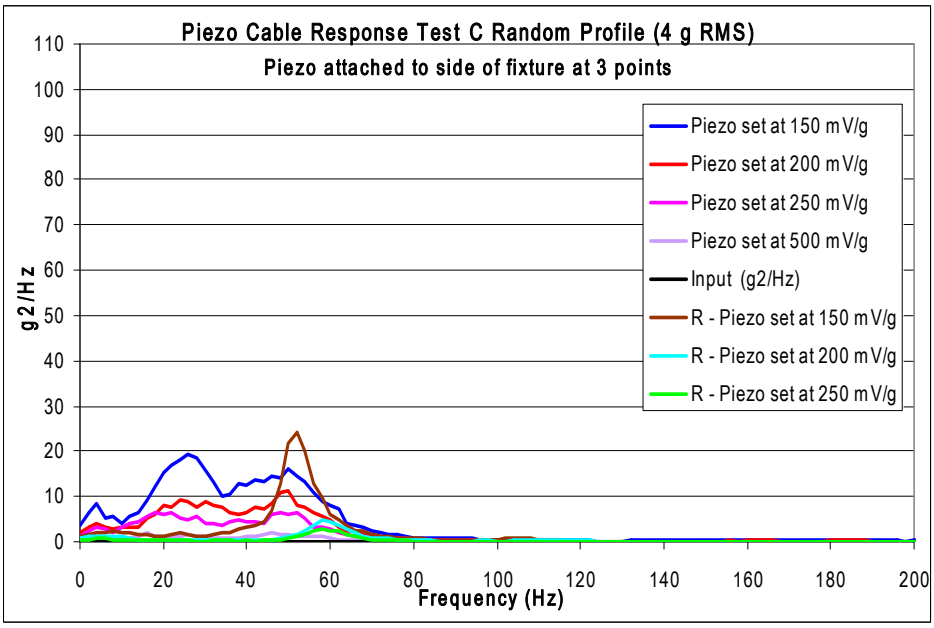


FIGURE E-7. 12.5" PIEZO CABLE ON SIDE OF FIXTURE 4 G

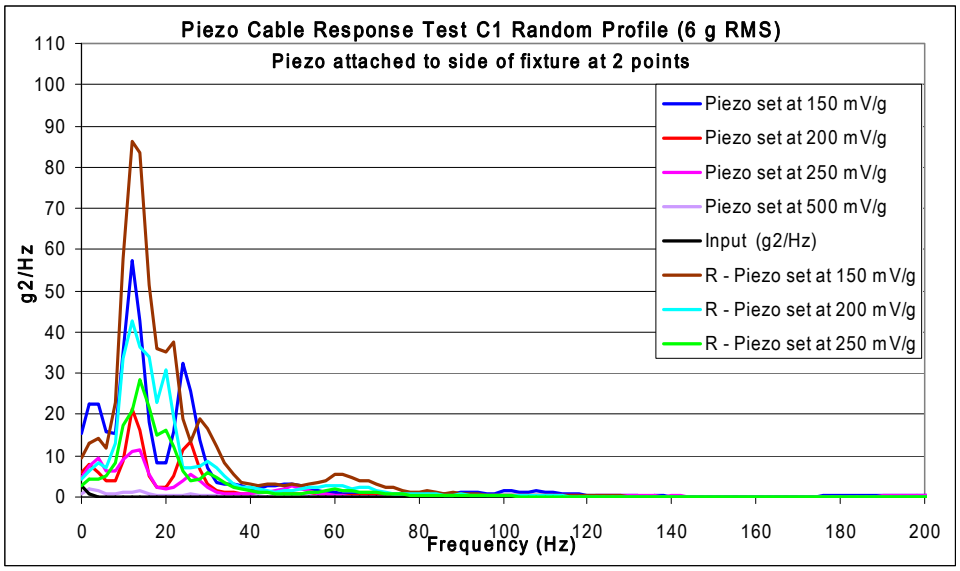


FIGURE E-8. 25" PIEZO CABLE ON SIDE OF FIXTURE 6G

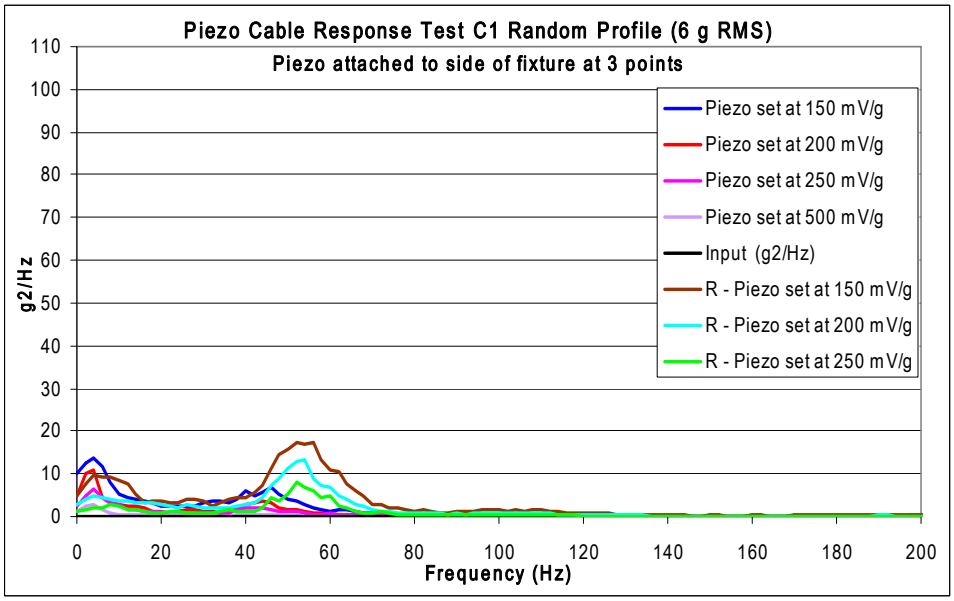


FIGURE E-9. 12.5" PIEZO CABLE ON SIDE OF FIXTURE 6 G

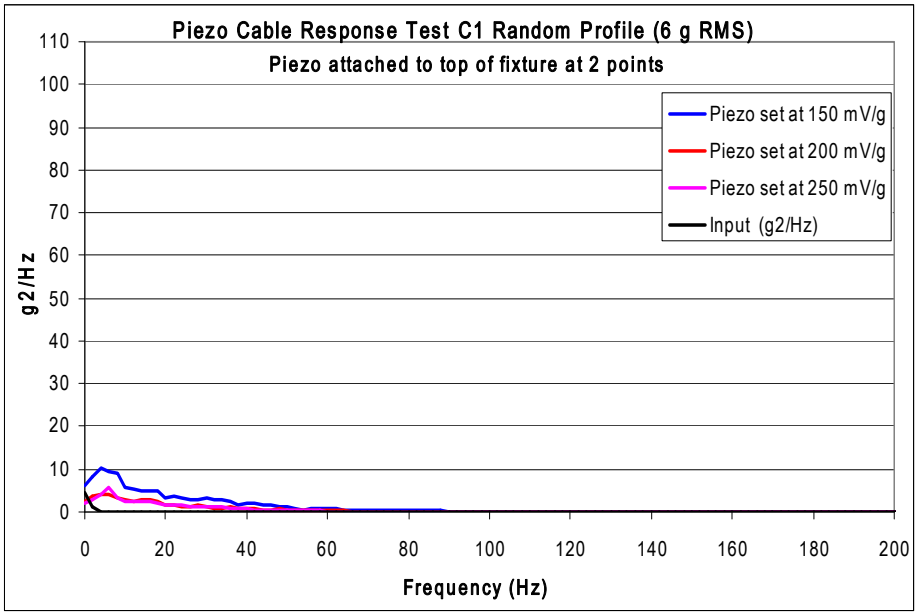


FIGURE E-10. 25" PIEZO CABLE ON TOP OF FIXTURE 6 G

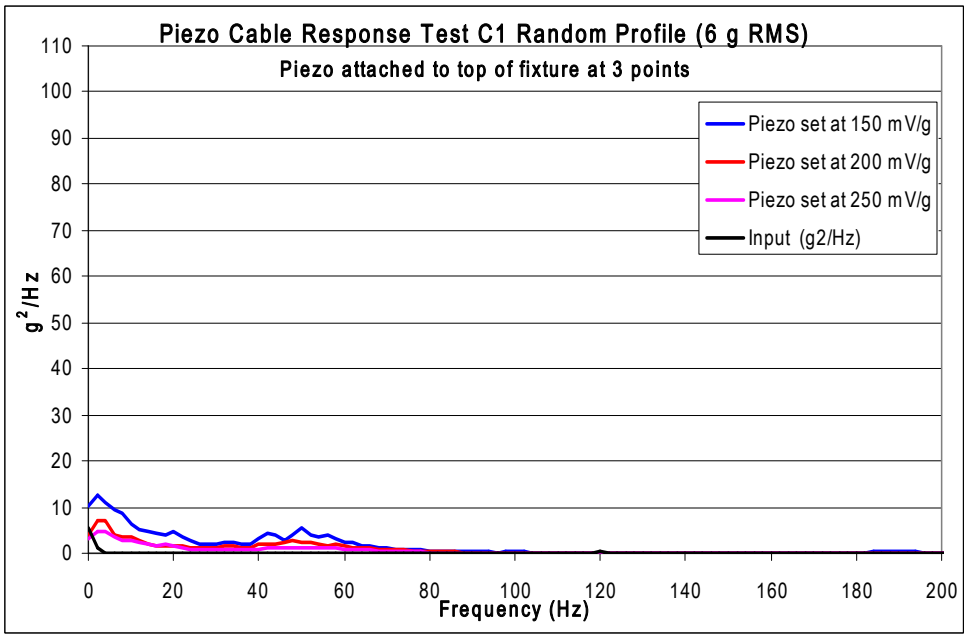


FIGURE E-11. 12.5" PIEZO CABLE ON TOP OF FIXTURE 6 G

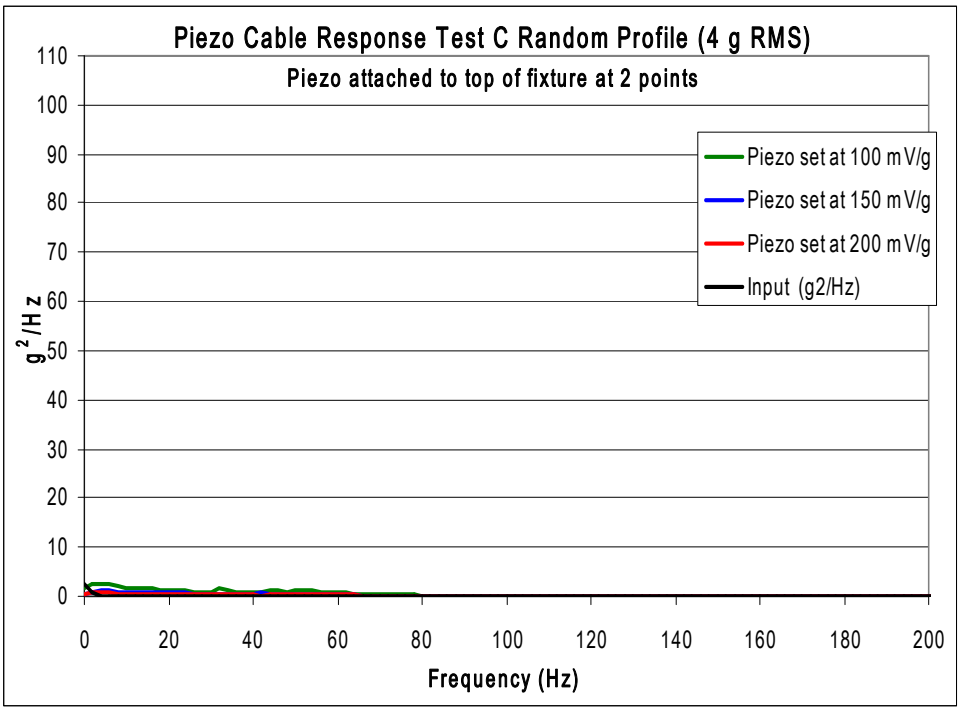


FIGURE E-12. 25" PIEZO CABLE ON TOP OF FIXTURE 4 G.

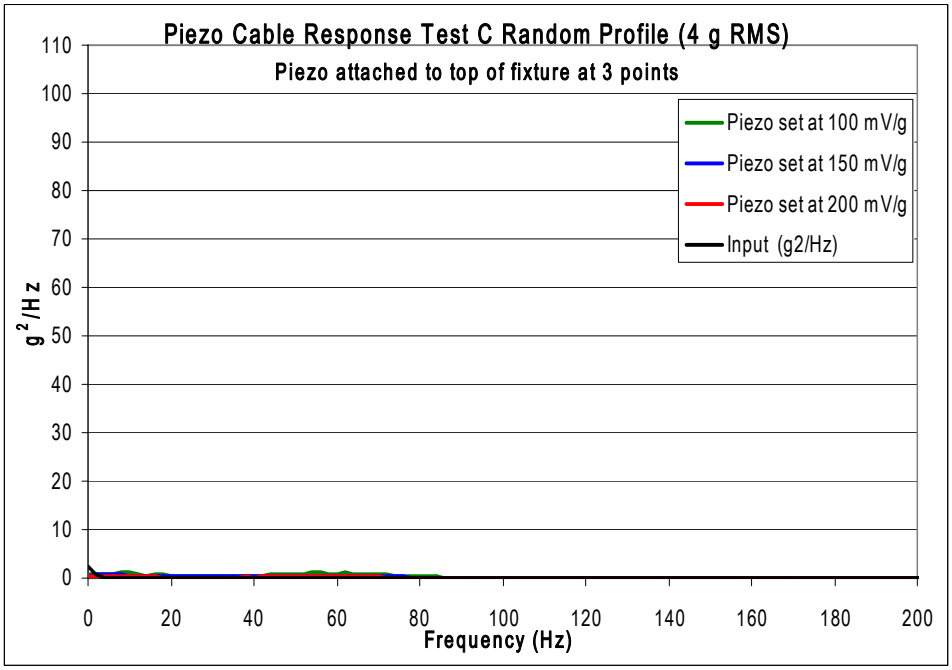


FIGURE E-13. 12.5" PIEZO CABLE ON TOP OF FIXTURE 4 G

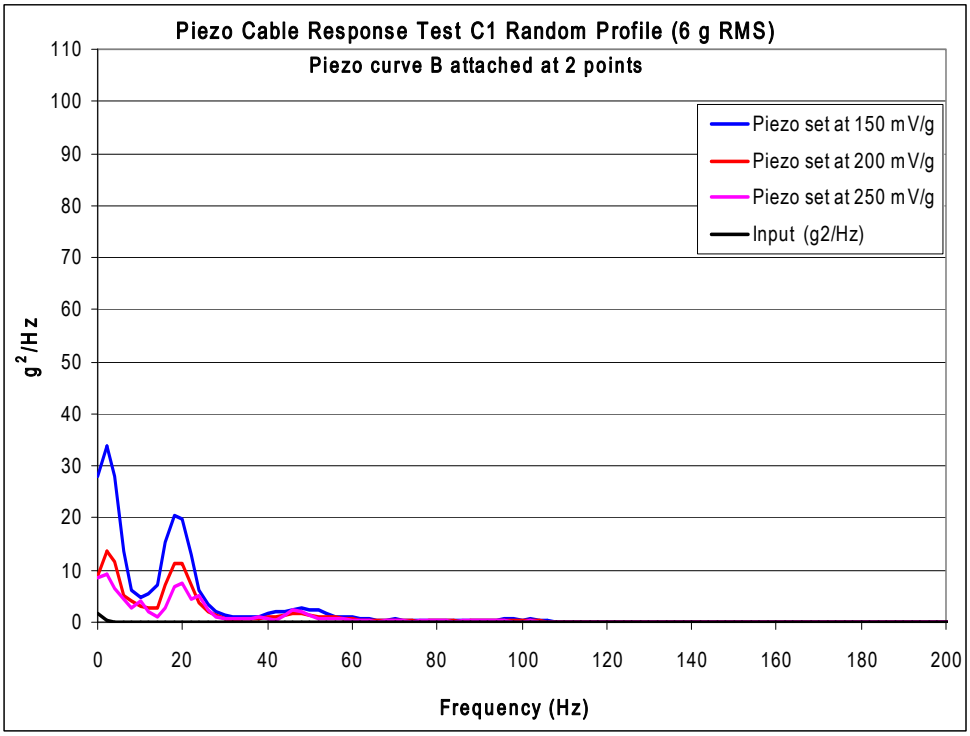


FIGURE E-14. 25" PIEZO CABLE IN CURVE B ON SIDE OF FIXTURE 6 G

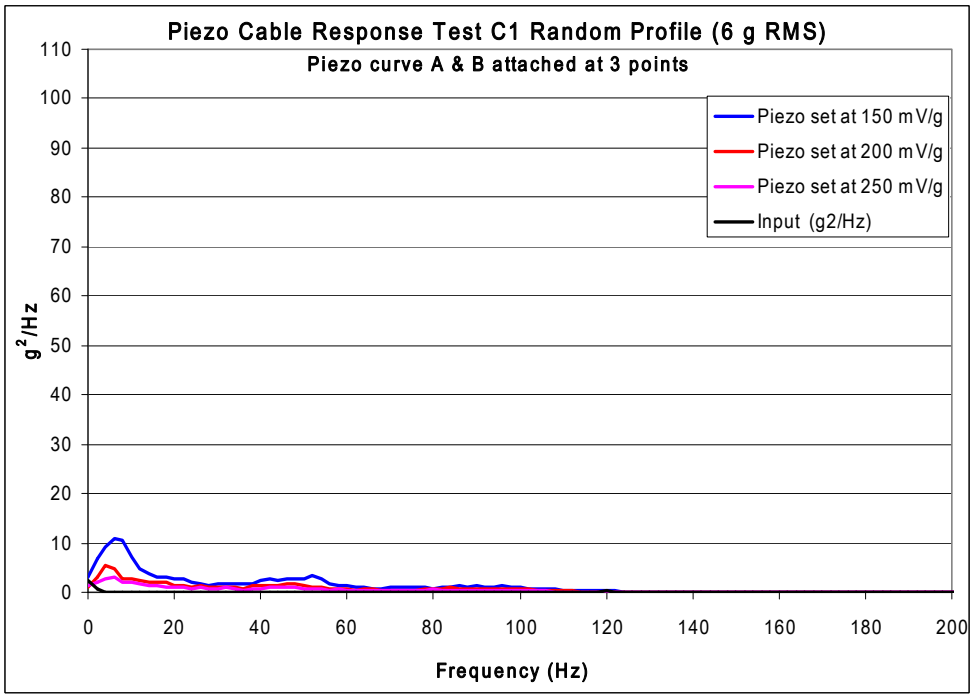


FIGURE E-15. 12.5" PIEZO CABLE IN CURVE B ON SIDE OF FIXTURE 6 G

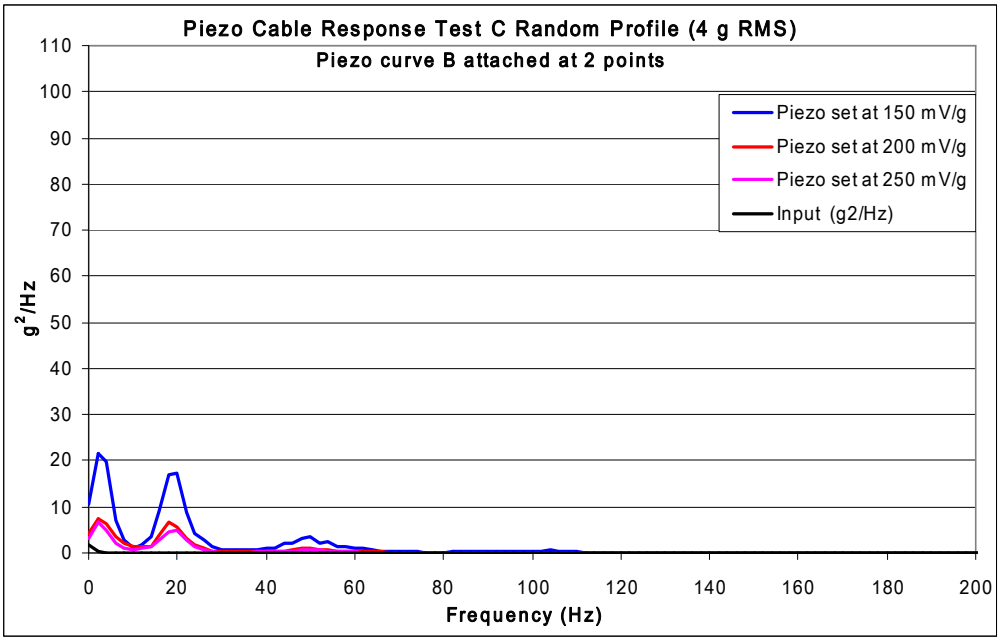


FIGURE E-16. 25" PIEZO CABLE IN CURVE B ON THE FIXTURE SIDE 4 G.

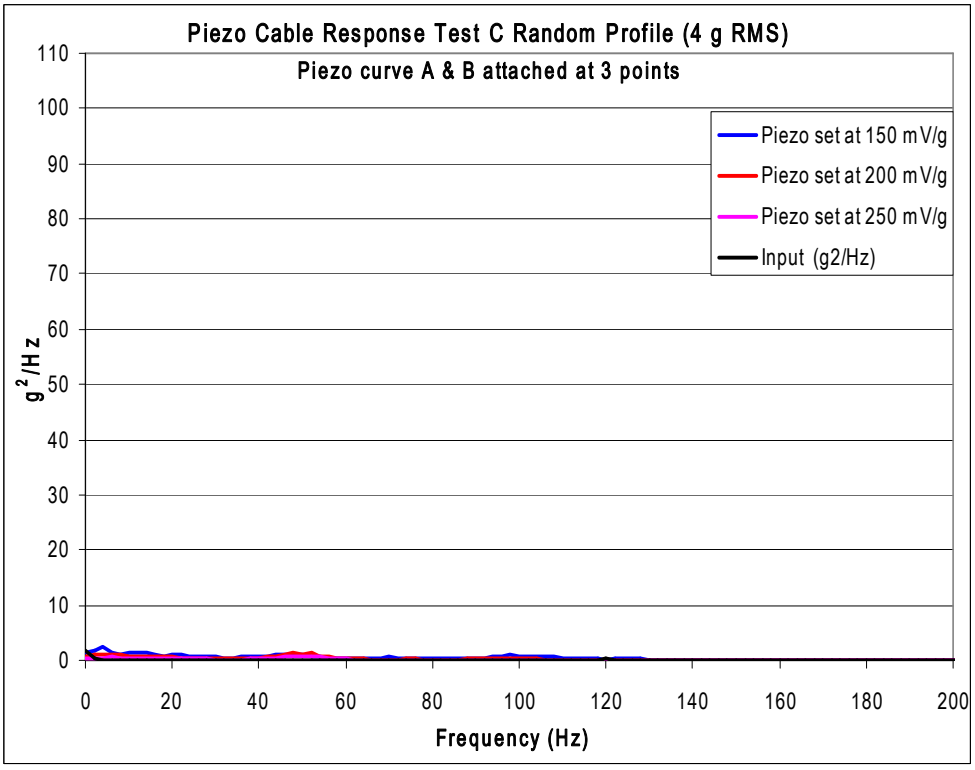


FIGURE E-17. 12.5" PIEZO CABLE IN CURVES A AND B ON SIDE OF FIXTURE 4G

## E.7 IN LAB VIBRATION MEASUREMENT GRAPHS – SINE WAVE

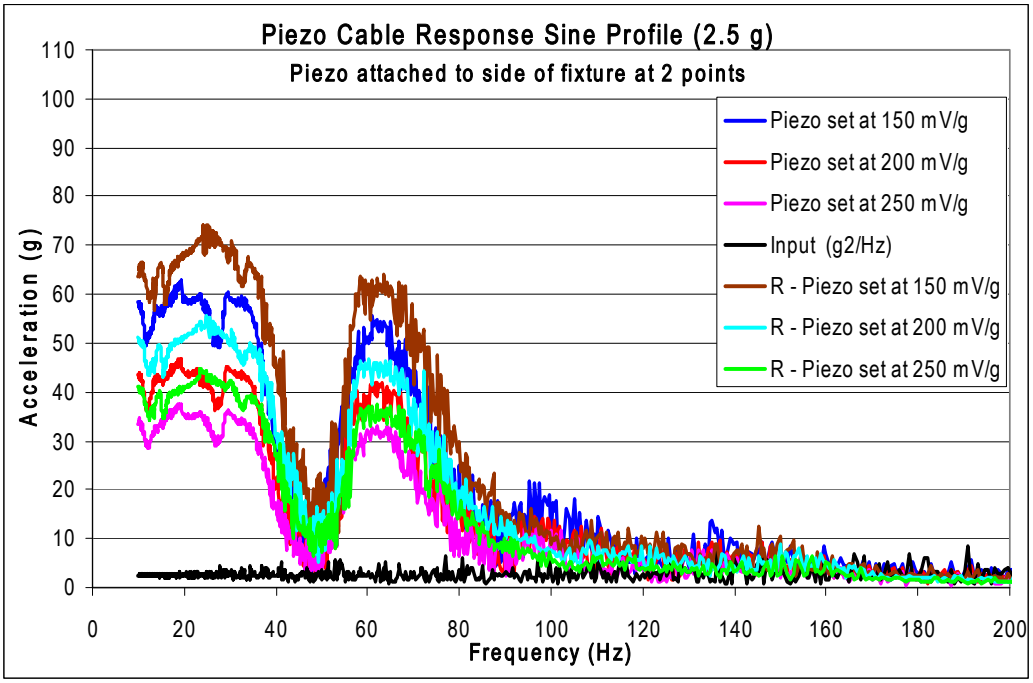


FIGURE E-18. 25" PIEZO CABLE ON SIDE OF FIXTURE 2.5 G

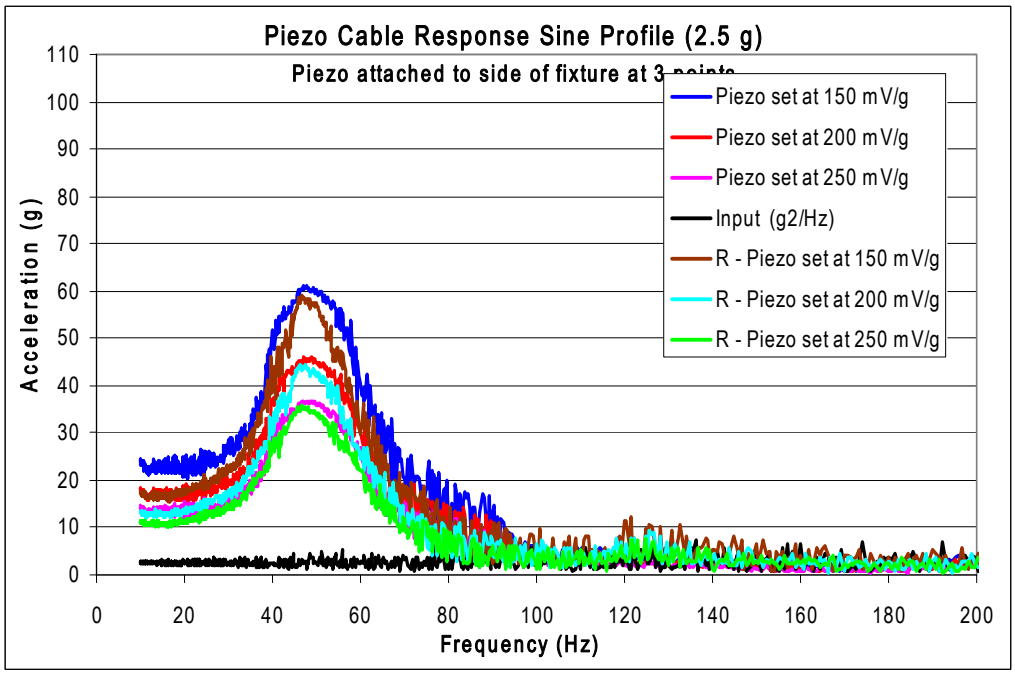


FIGURE E-19. 12.5" PIEZO CABLE ON SIDE OF FIXTURE 2.5 G

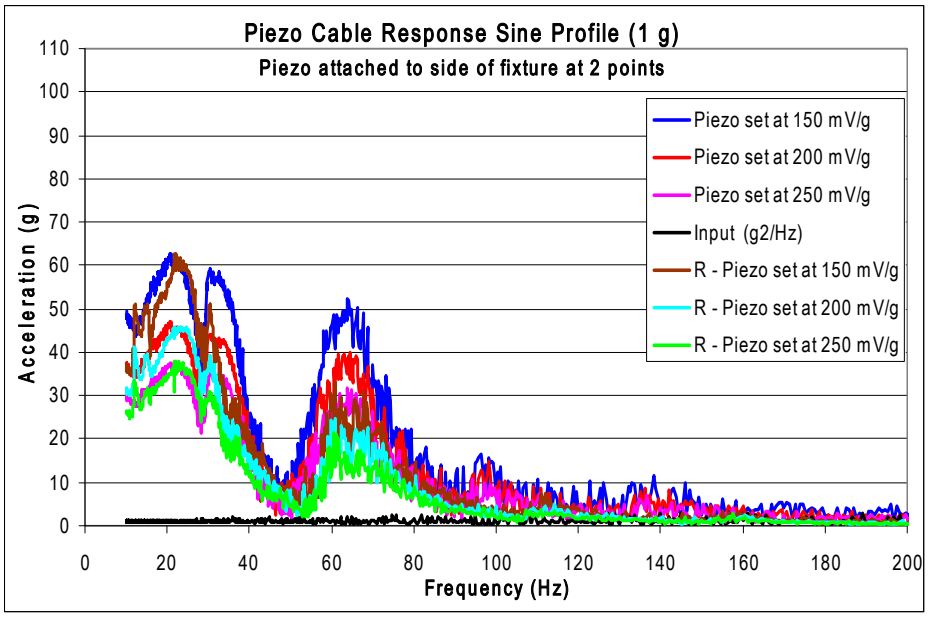


FIGURE E-20. 25" PIEZO CABLE ON SIDE OF FIXTURE 1G

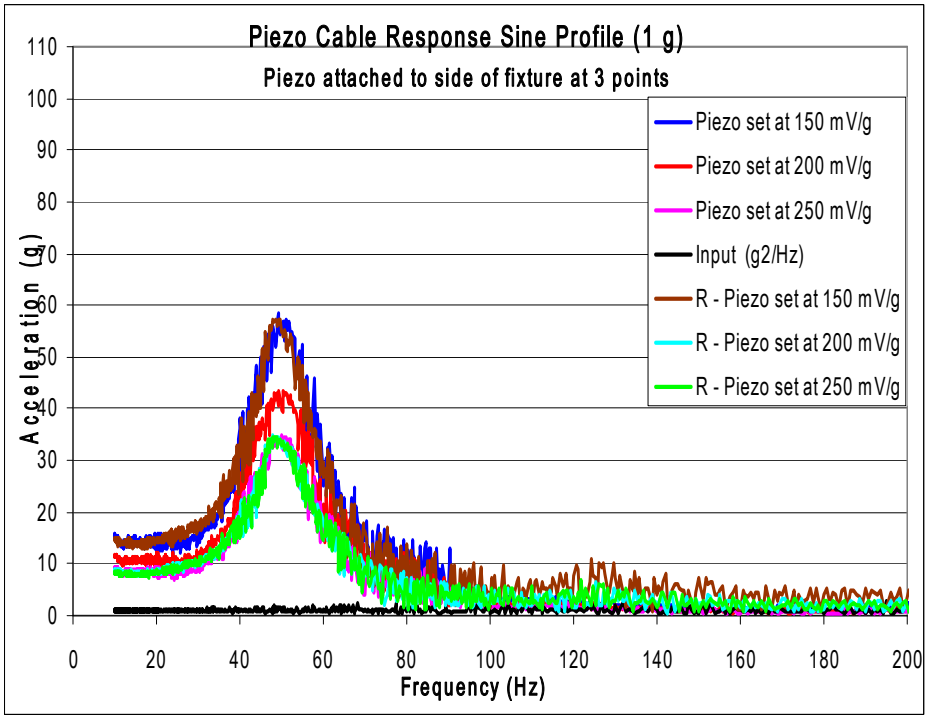


FIGURE E-21. 12.5" PIEZO CABLE ON SIDE OF FIXTURE 1G

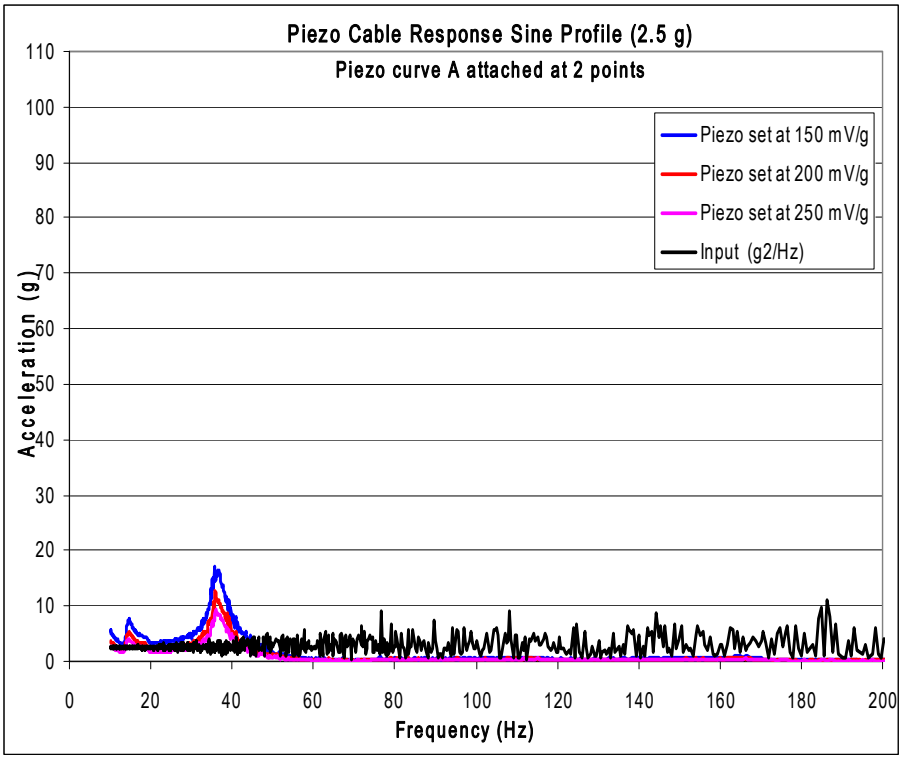


FIGURE E-22. 25" PIEZO CABLE IN CURVE A ON SIDE OF FIXTURE 2.5 G

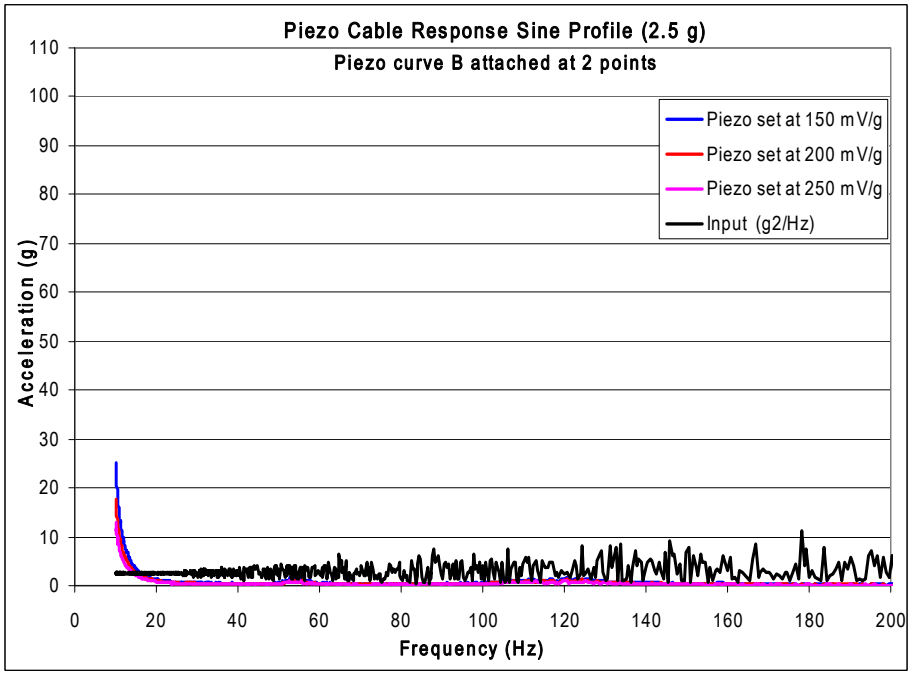


FIGURE E-23. 25" PIEZO CABLE IN CURVE B ON SIDE OF FIXTURE 2.5 G

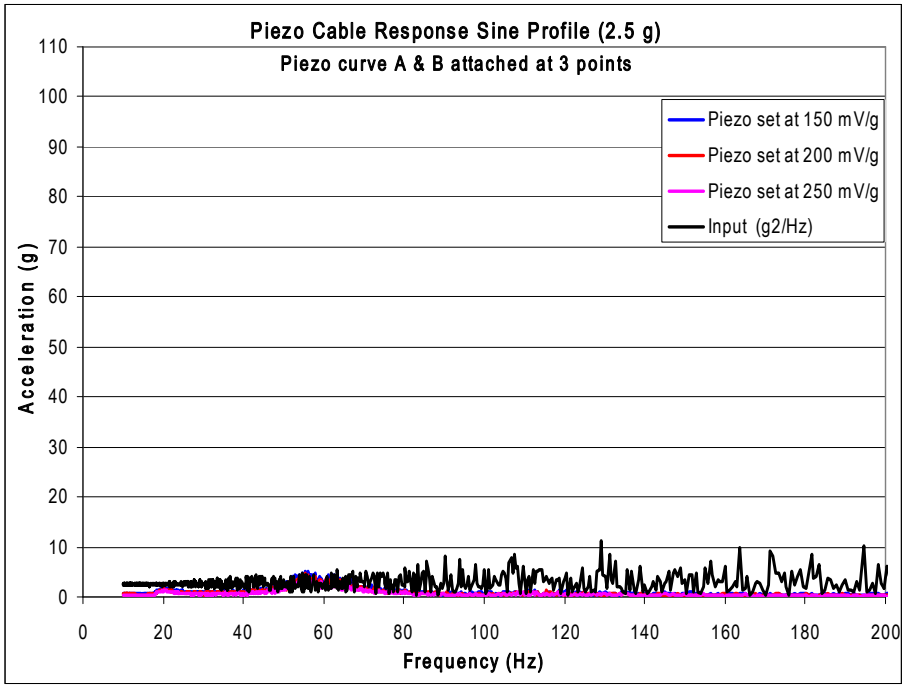


FIGURE E-24. 0.25" PIEZO CABLE IN CURVES A AND B ON SIDE OF FIXTURE 2.5 G

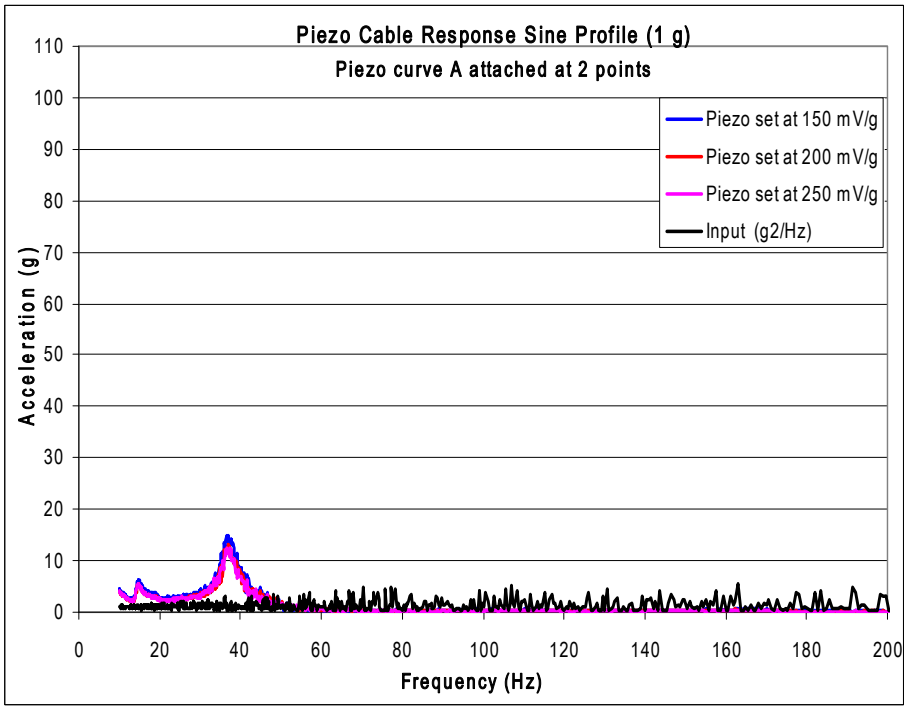


FIGURE E-25. 25" PIEZO CABLE IN CURVE A ON SIDE OF FIXTURE 1 G

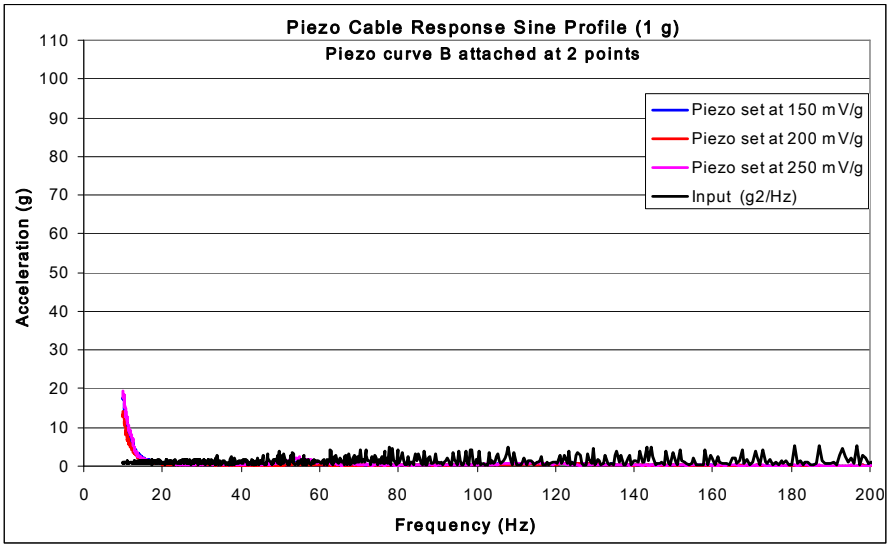


FIGURE E-26. 25" PIEZO CABLE IN CURVE B ON SIDE OF FIXTURE 1 G

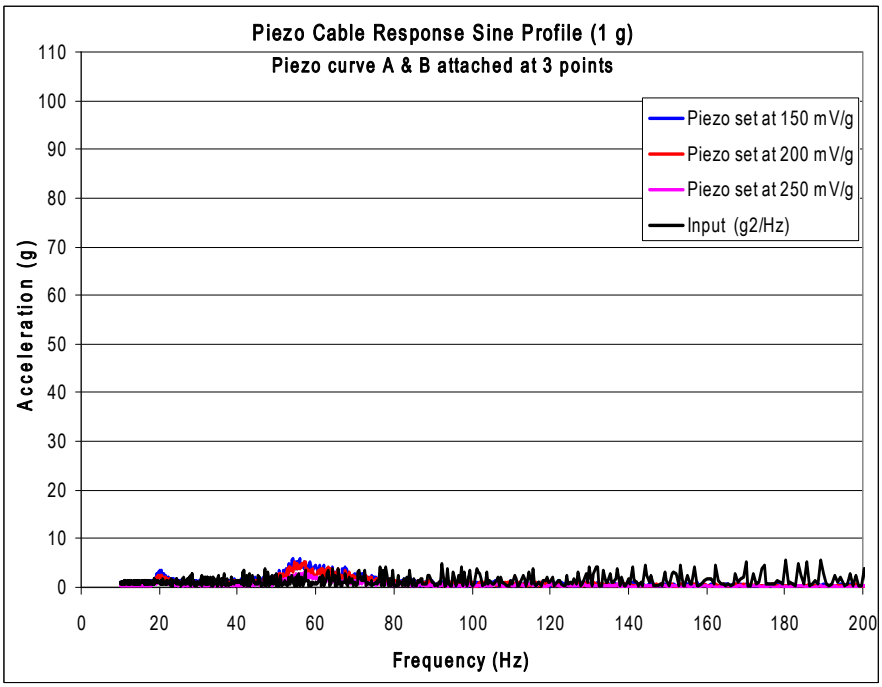


FIGURE E-27. 12.5" PIEZO CABLE IN CURVES A AND B ON SIDE OF FIXTURE 1 G

APPENDIX F-CONNECTOR DEGRADATION DETECTOR EXPERIMENTAL

## F.1 COIL MATERIALS AND DESCRIPTIONS.

Two basic types of coils were studied during the research. The first type of coil is shown in figure F-1 and was purchased or wound with a coil winder in the laboratory. For the laboratory version, fine gauge copper wire was wrapped around plastic tubing to produce the several hundred turn coils. Fine gauge wire with a large number of turns provides stronger signals than coarse gauge wire with a low number of turns. The commercial coils were not flexible but had the advantage that they could be affixed directly to the connector. The second type of coil is an "on-site wound" ten turn coil produced by winding an insulated wire with stripped ends around the wires to be monitored as shown in figure f-2.

FIGURE F-1. PICTURE OF A COMMERCIAL COIL

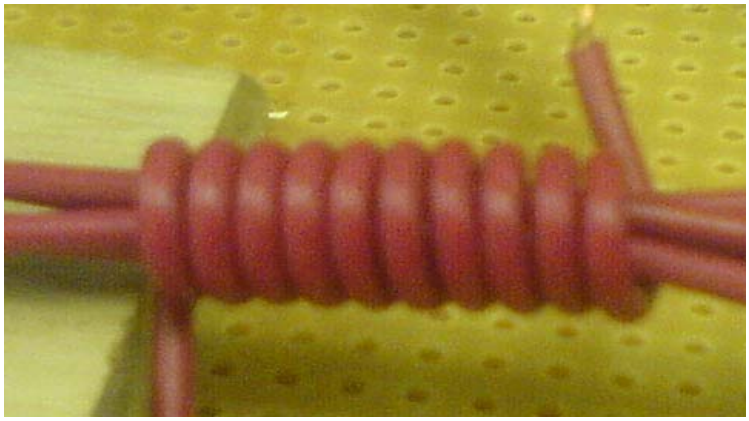

FIGURE F-2. ON-SITE, TEN WIND COIL

## F.2 CONNECTORS.

Commercially-available plastic connector shells and female and male gold plated copper alloy connector pins were procured and were put together for testing. The loose individual

pins allowed the flexibility to degrade these pins and then assemble them into the connector. Each connector shell has nine positions and four of them were connected to wires for this experiment.

A few male and female pins were assembled in as-purchased condition to form a "virgin connector" that was used for base line measurements. A few other pins were degraded by several different methods. Only the male parts of the connector pins were subjected to the degradation procedures. Two pins were degraded by dipping in a 40% nitric acid and water solution. One of the pins was degraded for about 2 minutes, while the second pin was degraded for 5 minutes. After dipping in nitric acid, the pins were rinsed in distilled water and dried in air. A third pin was hand rubbed with 500 grit sand paper until it lost its shine. The fourth connector pin was degraded using a mechanical vibration set up. The female portion was held stationary while the male pin was vibrated in contact with this pin for 15 minutes using a small displacement motion created by placing it into a fixture mounted to a vibrating loud speaker cone.

Wires approximately 2 feet long were soldered onto each connector pin and were labeled to identify each type of degradation. The ends of the wires were connected to switches to help in easy switching and avoid movement of any wires during the measurements as shown in figure F-3. For the prewound coils (laboratory wound and commercial shown in figure f-1), the ends of the four wires on the two sides of each connector were fed through the coils' center tubes before attaching to the switches. For the third set of tests, insulated wires were tightly wound around the four wires on the two sides of each connector (as shown in figure F-2) after the wires had been attached to the switches. The experimental set-up used to perform the connector degradation tests (performed one connector pin pair at a time) is shown in figure F-4.

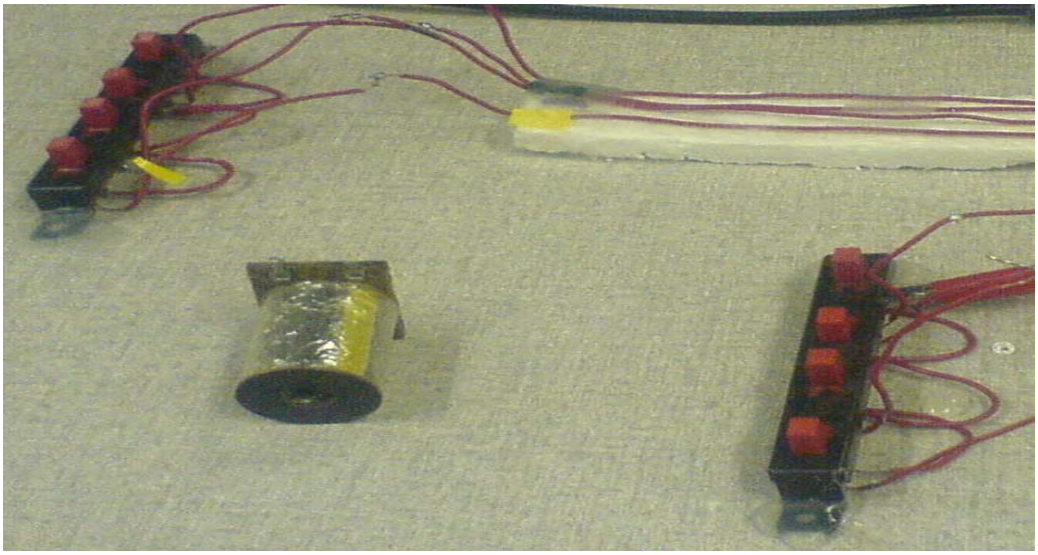

FIGURE F-3. SWITCHES USED TO CHANGE THE SIGNAL PASSING THROUGH THE FOUR WIRES

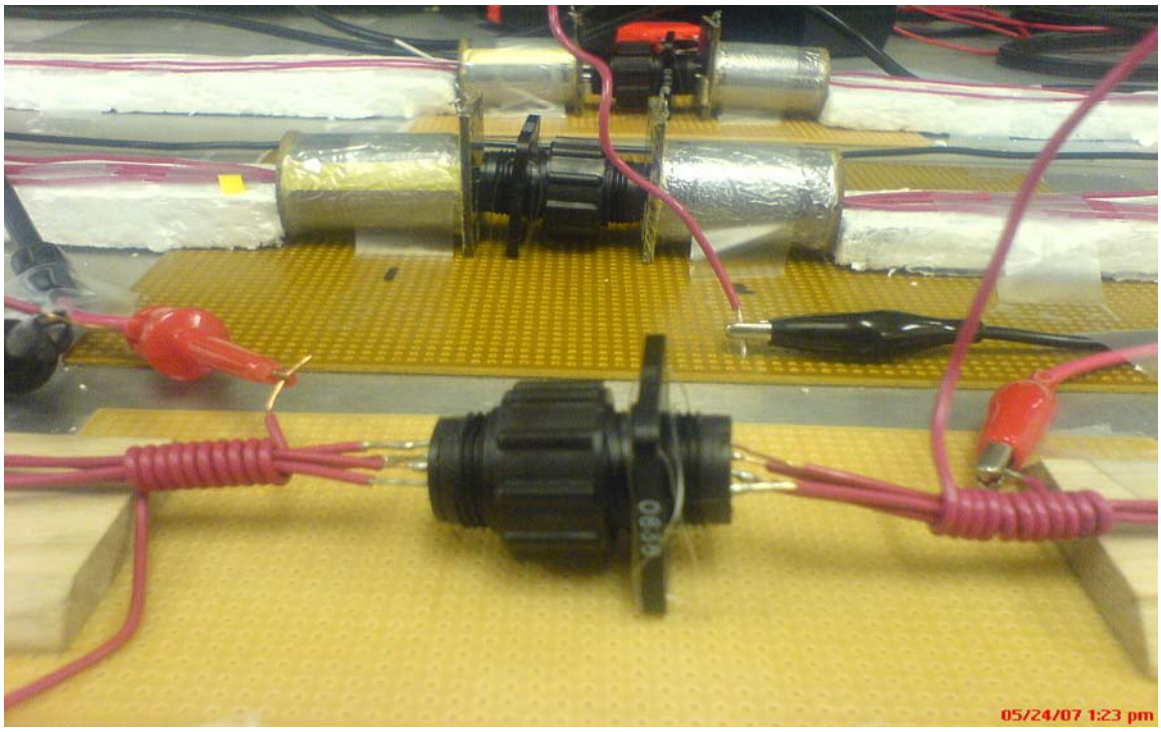


FIGURE F-4. EXPERIMENTAL SET-UPS FOR CONNECTOR DEGRADATION TESTS WITH THREE DIFFERENT COILS